Spectral Cohabitation and Interference Mitigation via Physical Radar Emissions

By

Gerald "Brandon" Ravenscroft

Submitted to the graduate degree program in Electrical Engineering and Computer Science and the Graduate Faculty of the University of Kansas in partial fulfillment of the requirements for the degree of Doctor of Philosophy.

_____

Dr. Shannon Blunt, Chairperson

_____

Dr. Chris Allen

_____

Dr. Jim Stiles

_____

Dr. Erik Perrins

_____

Dr. Chris Depcik

Date Defended: May 09, 2023

The dissertation committee for Gerald Brandon Ravenscroft certifies that
this is the approved version of the following dissertation:

Spectral Cohabitation and Interference Mitigation via Physical Radar Emissions

_____

Dr. Shannon Blunt, Chairperson

Date Approved: May 09, 2023

Abstract

Auctioning of frequency bands to support growing demand for high bandwidth 5G communications is driving research into spectral cohabitation strategies for next generation radar systems. The loss of radio frequency (RF) spectrum once designated for radar operation is forcing radar systems to either learn how to coexist in these frequency spectrum bands, without causing mutual interference, or move to other bands of the spectrum, the latter being the more undesirable choice. Two methods of spectral cohabitation are proposed and presented in this work, each taking advantage of recent developments in random frequency modulation (RFM) waveforms, which have the advantage of never repeating. RFM waveforms are optimized to have favorable radar waveform properties while also readily incorporating agile spectral notches. The first method of spectral cohabitation uses these spectral notches to avoid narrow-band RF interference (RFI) in the form of other spectrum users residing in the same band as the radar system, allowing both to operate while minimizing mutual interference. The second method of spectral cohabitation uses an optimization procedure to embed a communications signal into a dual-purpose radar/communications emission, thus allowing one waveform to serve both functions simultaneously. Both of these methods are presented and described in detail as well as being validated through simulation and physical open-air experimentation.

Acknowledgments

I would foremost like to thank my advisor, Dr. Shannon Blunt, and the professors in the Electrical Engineering and Computer Science Department at the University of Kansas including, but not limited to, Dr. Chris Allen, Dr. James Stiles, Dr. Erik Perrins, and Dr. Patrick McCormick for their patience, guidance, and willingness to impart knowledge during my time as an undergraduate and graduate student at the University of Kansas. I would also like to thank my fellow graduate students, both former and current, for their assistance and support in making this an enjoyable experience. I would also like to thank my many mentors during the various internships I participated in over the course of pursuing this degree. Finally, I would like to thank my mom, whose continuous and unwavering love and support along the way made this journey possible.

Table of Contents

List of Figures

List of Tables

Chapter 1: Introduction

Spectral congestion and competition in radar operating bands has become a topic of increasing concern in recent years [1-3]. Spectrum bands once allocated solely for radar operation are now being auctioned to support the growing demand for high bandwidth 5G communications [4], which has driven research into methods for radar and communications systems to coexist spectrally [5-11]. As the available spectrum continues to shrink, the burden shifts to radar systems to either coexist with communications systems operating in the same band or move to another region of the RF spectrum, often a less desirable choice. Furthermore, coexistence dictates the radar system does not interfere with the spectral neighbor while simultaneously avoiding interference from them [12, 13].

One approach to coexistence with communications systems has been the accommodation of narrowband communications in the radar operating band via the inclusion of spectral notches in random FM noise waveforms [14-17]. While mitigating interference caused by the narrowband communications signal, these waveforms also cause reduced interference to the communications system by placing as little energy as possible in its operating band via the spectral notch, while maintaining waveform coherence across the band. A similar approach was taken in [18] where a water-filling technique was used to design radar waveforms that accommodate legacy communications systems operating in the same spectral band as the radar system.

A more popular approach to coexistence has been the design of dual-function radar and communications (DRFC) systems, which seek to perform both the radar and communications functions with a single emission. An approach taken in [19] was to use pseudo random sequences for creation of phase-codes to create a noise-like emission which could serve both functions. Another approach using coding degrees of freedom via waveform phase modulation is that of [20-

27] where a continuous phase modulation (CPM) communications signal [28] is phase attached to a polyphase coded FM (PCFM) radar waveform [29] with a tunable modulation index parameter to adjust the performance tradeoff between functions. A dual-function radar and communications (DFRC) waveform design approach was taken in [30] by leveraging the combination of spread-spectrum multiple access (SS-MA) communications [31] with CPM. Another approach taken to the design of DFRC waveforms is to utilize spatial degrees of freedom as in [24, 32-35] to create a single multiple-input multiple output (MIMO) emission which can steer radar and communications beams independently, providing separability in spatial angle.

Two methods of spectral cohabitation between radar and communications waveforms are presented in this work. The first method seeks to actively accommodate and avoid interference from communications users emitting narrowband interference in the same operating band as the radar system. The second method designs a single, dual-purpose radar and communications emission to perform both the sensing and communications functions simultaneously. Each of these methods take advantage of a recently developed class of RFM waveforms known as pseudo random optimized FM (PRO-FM), which have favorable radar waveform properties such as constant amplitude, good spectral containment, and low autocorrelation sidelobes that further decohere when performing coherent processing. The first presented method creates spectral notches in PRO-FM waveforms, via a modification to the optimization procedure, to mitigate interference from in-band communications signals. The second method leverages the PRO-FM optimization routine to embed communications subcarriers into FM waveforms via a two-stage optimization procedure, providing an additional communications function, while maintaining the desirable qualities of PRO-FM waveforms for radar operation.

With the intention of providing motivation for the remainder of the work, and laying a solid foundation to build upon, Chapter 2 provides the background in basic radar and communications operation needed to substantiate content presented in subsequent chapters. Basic radar principles are introduced, and the most ubiquitous radar waveform, the linear frequency modulation (LFM) waveform, is defined to provide a baseline comparison for the other waveform types presented. The basic radar signal model is introduced, as well as matched filter pulse compression, in both continuous time and discrete representations. Doppler processing is described in detail as well as a clutter cancellation technique. A basic radar simulation is presented which demonstrates the techniques presented in the chapter. Finally, a brief introduction to wireless communications is given along with the definition of the orthogonal frequency division multiplexing (OFDM) waveforms, which forms the crux of 4G and 5G wireless communications.

Chapter 3 introduces random FM waveforms and describes their advantages and disadvantages over the traditional LFM waveform. The optimization procedure used to create PRO-FM waveforms is presented in detail. A modification to the optimization procedure is then made to allow the inclusion of spectral notches in the PRO-FM waveform with the goal of mitigating narrowband interference present in the radar operating band. Simulations are provided which demonstrate the utility of PRO-FM waveforms in radar operation both with and without spectral notches. The primary drawback to non-repeating RFM waveforms is introduced as well, range sidelobe modulation (RSM).

Chapter 4 then considers mitigation of spectral interference with notched PRO-FM waveforms. A joint-domain processing technique known as Non-Identical Multiple Pulse Compression (NIMPC) is derived and applied to all types of PRO-FM waveforms considered thus far in order to address the issue of RSM. Preservation of the spectral notch in the radar transmit

waveform by NIMPC is investigated as well. Another simulation is conducted to demonstrate the ability of NIMPC to compensate for RSM in RFM waveforms and preserve the capability of mitigating in-band interference. Results of physical open-air experimentation using a radar hardware testbed are presented that show the efficacy of PRO-FM waveforms and NIMPC filtering in a radar moving target indication (MTI) operating scenario.

Chapter 5 introduces a dual-function radar and communications waveform known as Tandem Hopped Radar and Communications (THoRaCs). Design of the THoRaCs waveform and optimization procedure are described in detail. Simulation results are provided showing the efficacy of the THoRaCs waveform in both radar and communications functions. Open-air experimentation results are presented once again using a radar testbed in an MTI operating scenario, showing the utility of THoRaCs as a radar waveform. A free-space communications experiment is presented which shows the capabilities of THoRaCs as a communications waveform. Finally, Appendix A provides summary tables for several radar and communications quality metrics presented in Chapter 5 and Appendix B provides a list of acronyms and their associated definitions.

Chapter 2: Radar and Communications Background

This chapter provides an introduction to the fundamental radar and communications principles needed to supply a solid foundation for the work presented in subsequent chapters. Since radar waveform design is a large component of the matter in this dissertation, thorough treatments of the radar waveform and its position in performing radar functions will be given. Signal processing techniques are also given due introduction as the radar waveforms designed in this work are tested with both simulated and physical radar operating scenarios. Since the crux of this dissertation is spectral cohabitation of radar systems with other users, namely narrowband communications, a brief introduction to wireless communications is also given.

The remainder of this chapter is laid out as follows. Section 2.1 introduces the basic operation of a radar system. Section 2.2 introduces the radar waveform and its function in a radar system. Section 2.3 describes the radar signal model and introduces pulse compression with both continuous time and discrete representations. Section 2.4 details Doppler processing methods for Doppler windowing and clutter cancellation. Section 2.5 ties together the concepts introduced so far in the chapter by applying them to a simple radar simulation example. Finally, Section 2.6 introduces the fundamental operation of wireless communications and how its goals differ from those of a radar system.

2.1 Basic Radar Operation

In the simplest sense, radar systems operate by transmitting electromagnetic energy towards a spatial region of interest and collecting the energy scattered back towards the radar system receiver (often called backscatter) from objects in that region [36]. The word "radar" is actually an acronym which stands for radio detection and ranging. As this name implies, the two primary goals of a radar system are 1) detect the presence of objects in the illuminated spatial region of interest and

2) determine the relative range of those objects to the radar system. While not a requirement, radar systems often use the same antenna to transmit and receive electromagnetic energy or use two separate antennas which are geographically close to one another. This type of operation is known as monostatic radar, which will be the focus of the work shown in this document. The diagram in Figure 1 shows a simplified illustration of the operation of a monostatic radar system.
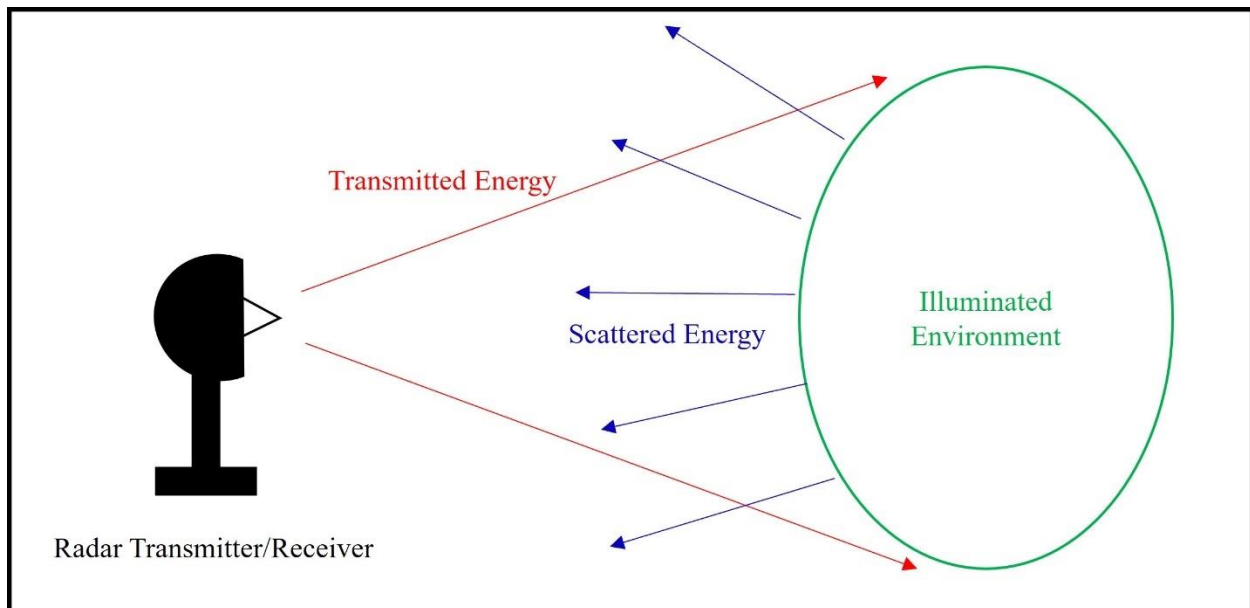
Figure 1: Illustration of basic monostatic radar operation

The transmitted energy, which is scattered back to, and collected by, the radar system receive antenna from objects in the illuminated environment will vary depending upon the number of objects and their relative electrical size, known as radar cross section (RCS), among many other factors. Relative distances from illuminated objects to the radar transmitter can be determined by (2.1)

$$R = \frac{c\Delta t}{2} \; ,$$

(2.1)

where R is the relative distance, c is the propagation speed of the electromagnetic energy, known as the speed of light and often approximated as 3 x 10^8 meters/second, and Δt is the round-trip

travel time from the radar transmitter to the object and back [36]. It is important to note that the modern radar system is a complex electrical system with many pieces working in harmony to achieve the desired function. The description of a radar system given thus far is highly simplified.

2.2 The Radar Waveform

The localized collection of energy transmitted by a radar system is commonly referred to as a signal, or waveform, terms which are often utilized interchangeably. These transmissions are contained within time intervals denoted as pulses, which are typically on the order of nanoseconds or microseconds in duration, known as the pulse width and commonly represented by the variable *T*. After a pulse is transmitted, it is followed by a listening interval, or dead time, in which the radar transmitter turns off and the receiver "listens" for, and collects, backscattered energy from the region illuminated by the radar pulse. Once this listening interval is complete, the radar transmitter will emit another pulse, followed by another listening interval. This repetition occurs at intervals known as the pulse repetition interval (PRI), which typically lasts on the order tens to hundreds of microseconds. The inverse of the PRI, known as the pulse repetition frequency (PRF), describes how frequently each PRI is repeated. The backscatter from a specified number of pulses (and thus PRIs) is collected into a section of data known as a coherent processing interval (CPI), which can be on the order of tens to thousands to PRIs, where various processing techniques can be employed to determine the composition of the illuminated region of interest. Figure 2 provides an illustration of these different timing components common to a pulsed radar system. Radar systems can operate in pulsed or continuous waveform (CW) modes, but only pulsed operation is considered here. The primary difference for a CW radar system from that of the pulsed system described thus far, and that depicted in Figure 2, is that the CW system transmits continuously, as the name implies, and performs the listening task simultaneously with the transmit task. Additional

concerns (which will not be covered here) must be addressed when operating a radar in a CW mode, possibly limiting the available applications of the system [36].
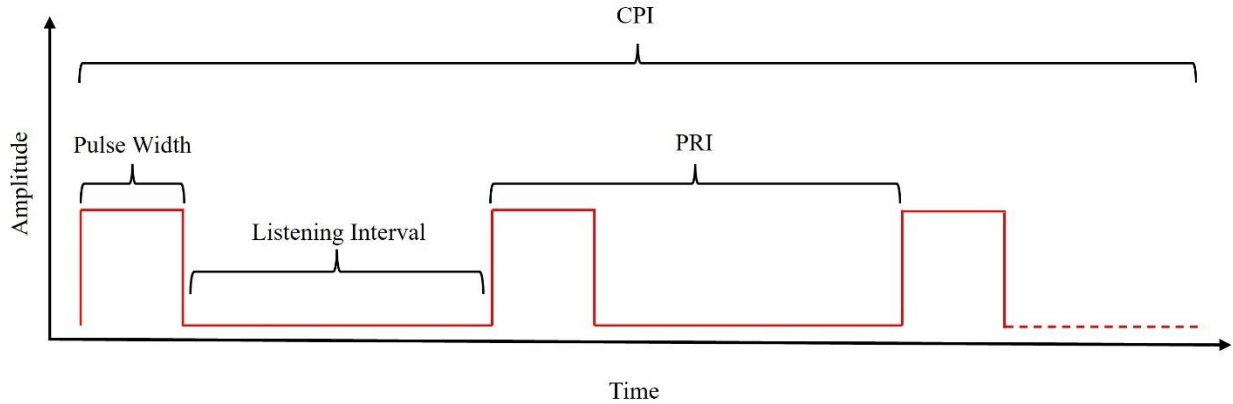
Figure 2: Timing diagram of basic pulsed radar operation

Early radar systems, and some simple modern systems, utilize a simple transmit pulse that is characterized solely by its amplitude and pulse-duration, such as a time-gated or CW tone (single frequency). Simple pulses, however, are limited in their utility. Further examining this limitation, first consider the Rayleigh range resolution, commonly referred to as just range resolution, of a simple radar pulse given by

$$\Delta R = \frac{cT}{2},$$
(2.2)

or equivalently for a simple pulse in terms of the pulse bandwidth, *B*, by

$$\Delta R = \frac{c}{2B}.$$
(2.3)

Equations (2.2) and (2.3) are equivalent for a simple pulse because the pulse bandwidth is equal to the inverse of the pulse duration [36], however it is important to note that (2.3) is also applicable for non-simple pulses, which will be discussed in more detail later in this section. Range resolution dictates how close two objects illuminated by the radar waveform can be, while still being discerned as two separate objects at the receiver. Objects farther apart than ΔR will be discerned

as two separate objects, while objects closer together than ΔR cannot be discerned as two separate objects [36]. Equation (2.2) dictates that a pulse must be short in duration in order to have better, meaning finer, range resolution.

Now consider the energy contained within the simple pulse, which is directly proportional to the pulse duration, T. Radar detection performance is improved by illuminating objects of interest with large amounts of energy, such that sufficient energy is scattered back the radar receiver to allow for detection. Radar detection is thus improved by having transmit pulses which are long in duration. However, this is in direct competition with the range resolution requirement. This conflict highlights the tradeoff, or coupling, between pulse transmit energy (and thus receive detection capability) and range resolution quality for a simple radar pulse [37].

As a method to decouple transmit energy and resolution, modulated pulses are typically used in radar systems. Modulating the phase or frequency of a pulsed waveform can increase the bandwidth of the waveform, and thus make the range resolution finer according to (2.3), for a fixed pulse duration without giving up transmitted energy, which hinders the detection capability of the radar system. Many types of phase and frequency modulated waveforms exist for different types of radar systems, but the most ubiquitous is the LFM waveform. A common benchmark of a modulated waveform is the product of the bandwidth, B, and pulse duration, T, aptly named the time-bandwidth product and represented by BT. Since simple (unmodulated) pulses have a bandwidth and pulse duration which are direct reciprocals of one another, their time bandwidth product is simple $BT = 1$.

Radar transmit waveforms are often defined by the complex valued, continuous-time baseband representation [37]

$$s(t) = a(t) e^{j\theta(t)}, \tag{2.4}$$

where $s(t)$ is the continuous-time waveform, $a(t)$ is the time-varying pulse amplitude envelope, and $\theta(t)$ is the continuous-time phase function of the waveform. Radar systems often operate to detect objects at very far distances, on the order of tens or hundreds of kilometers. A radar transmitter can therefore emit very high-power electromagnetic radiation, on the order of tens or hundreds of kilowatts, or more. The amplifiers used in these high-power transmitters subsequently operate in a "saturated" mode, which greatly improves the power efficiency of the amplifier ([36, 38]). However, operation in saturation precludes the use of any amplitude modulation (AM) in the transmit amplifier. The pulse amplitude envelope $a(t)$ in (2.4) is therefore unity for all time t and the waveform can be characterized by the phase function $\theta(t)$ and frequency function $f(t)$, which is proportional to the first derivative of the phase function [37]. Constant amplitude waveforms such as these are known as frequency modulated (FM) waveforms.

Utilizing the form of (2.4), LFM waveforms are defined as

$$s_{\text{LFM}}(t) = e^{j\pi\left(\frac{B}{T}\right)t^2}, \tag{2.5}$$

for bandwidth B and pulse duration T. The LFM phase function is thus simply defined as

$$\theta_{\text{LFM}}(t) = \pi\left(\frac{B}{T}\right)t^2, \tag{2.6}$$

and the instantaneous frequency function of an LFM waveform is given by

$$f(t) = \frac{1}{2\pi}\frac{d\theta(t)}{dt} = \left(\frac{B}{T}\right)t, \tag{2.7}$$

in units of Hertz for a time variable of seconds [37]. An LFM waveform will sweep linearly though the frequencies which define the bandwidth, B, starting from time $t = 0$ and ending at time $t = T$. Figure 3 shows the power spectrum of an LFM waveform with time-bandwidth product $BT = 200$. The power spectrum is estimated using a fast Fourier transform (FFT) of the time-domain

waveform given by (2.5), which has been oversampled by a factor of 4, thus allowing for more spectral roll-off to be captured in the power spectrum estimate of the signal, a practice which is common in radar signal processing.
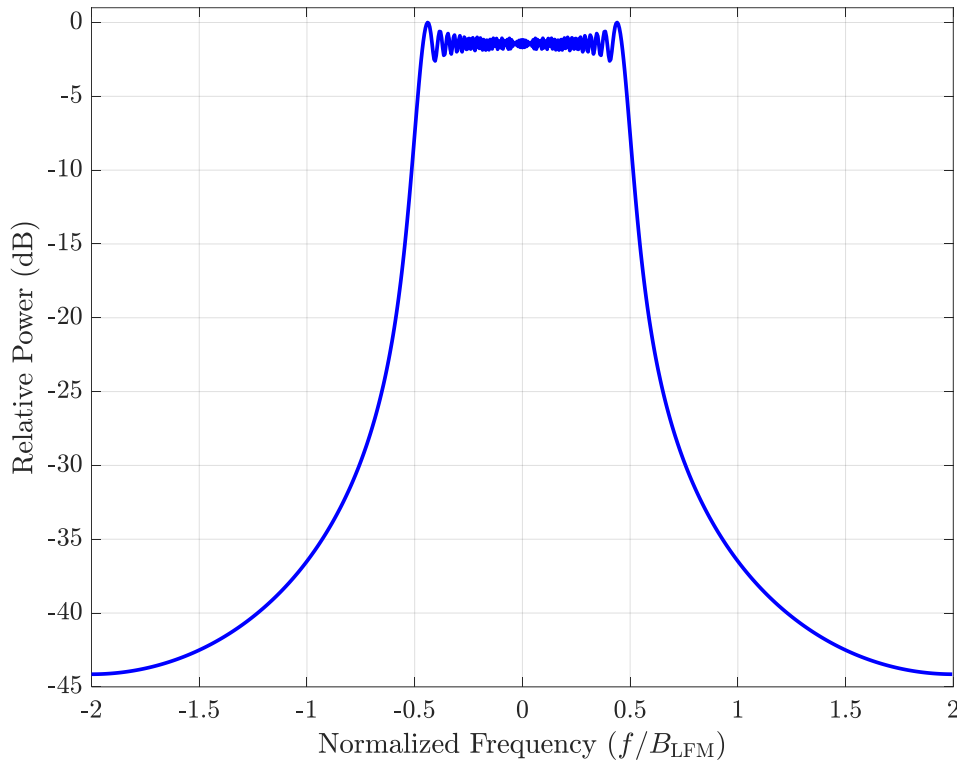
Figure 3: Power spectrum of an LFM waveform with $BT = 200$

Visible in the LFM power spectrum of Figure 3 is the compactness of the power spectrum, meaning that power is tightly located within B (denoted as B_{LFM} in Figure 3) and the spectrum rolls-off rapidly for frequencies greater than B. This is a very desirable trait for a radar waveform as it limits the amount of interference caused to, and received from, spectrally neighboring electromagnetic systems. The compact spectrum also allows the radar receiver to capture a smaller bandwidth when capturing the signal, which eases requirements on the receiver system. A compact power spectrum, along with a well-defined phase function and ease of implementation, make LFM waveforms the standard for most radar systems. However, as will be shown in Chapter 3, many benefits can be garnered from other types of FM waveforms that cannot be realized with the LFM.

2.3 The Radar Signal Model and Pulse Compression

The transmission of a radar waveform, along with subsequent capture of backscattering from an illuminated environment, as depicted in Figure 1, can be modeled mathematically with a continuous-time convolution as

$$y_r(t) = \int_{-\infty}^{\infty} s(t-\tau)x(\tau)d\tau + n(t) , \qquad (2.8)$$

for $y_r(t)$ the backscattering energy captured at the radar receiver, $s(t)$ the signal emitted from the radar transmitter, $x(t)$ the complex impulse response of the region of interest illuminated by the transmit signal, and $n(t)$ the complex, additive white Gaussian noise (AWGN) representative of the thermal noise inherent to the radar receiver electronics (ignoring other sources of thermal noise, which are often negligible). In practical application, the integration limits of (2.8) extend over the finite duration of the transmission PRI, or radar receiver's listening interval. The complex impulse response $x(t)$ will contain both objects of interest, for example a moving vehicle, and objects which are not of interest, denoted as clutter, such as trees and buildings which may need to be removed via filtering operations to uncover the objects of interest.

Estimation of the complex impulse response of the illuminated environment from $y_r(t)$ in (2.8) is typically performed via a filtering operation denoted as pulse compression for modulated radar waveforms. The pulse compression filter typically utilized is the matched filter (MF), which is represented as the time-reversed complex conjugate of the transmit waveform

$$w_{\mathrm{MF}}(t) = s^*(-t), \qquad (2.9)$$

where $w_{\mathrm{MF}}(t)$ is the matched filter, $s(-t)$ indicates time reversal of the transmitted waveform, and * denotes complex conjugation. Applying the matched filter in (2.9) to the received signal in (2.8) via correlation yields

$$\hat{x}(\tau) = \int_{-\infty}^{\infty} s^*(t-\tau) y_r(t) dt, \qquad (2.10)$$

where $\hat{x}(t)$ is the estimate of the complex scattering environment illuminated by the radar transmit signal. This estimate will differ from the true $x(t)$ via two important consequences, 1) corruption by the AWGN process $n(t)$ and 2) the pulse compression sidelobes associated with application of the matched filter in (2.9). Pulse compression sidelobes are a by-product of the filtering process in (2.10) and transmit waveform $s(t)$, which will also dictate the sidelobe structure of the estimate. Consideration of pulse compression sidelobes is important as radar operations often deal with high dynamic ranges in illuminated environments, and sidelobes from pulse compressed large RCS scatterers can obscure the estimates of nearby, smaller RCS scatterers.

A method for determining the pulse compression sidelobe structure of a waveform is the via direction calculation of the autocorrelation response, $r(t)$, as

$$r(\tau) = \int_{-\infty}^{\infty} s^*(t-\tau) s(t) dt, \qquad (2.11)$$

where it can be noted that $s(t)$ in (2.11) simply replaces $y_r(t)$ in (2.10). The autocorrelation response is useful in that it lends insight into the pulse compression structure of transmitted waveform $s(t)$ when the matched filter is applied to obtain an estimate of the complex impulse response of a hypothetical point scatterer. The matched filter is not the only filtering method that can be utilized to obtain as estimate of $\hat{x}(t)$, but it is the mostly commonly used method in most radar systems and serves as an important benchmark for other filtering methods.

Figure 4 shows the autocorrelation response of an LFM waveform with $BT = 200$, whose power spectrum was depicted in Figure 3. The time axis is normalized to the pulse width of the signal, representing the full sidelobe response of a hypothetical point scatterer corresponding to time t (i.e. $x(t = 0) = 1$ in (2.8)). The power axis has been normalized to 1 and represented on a

decibel scale, which is common in radar signal processing due to the high dynamic range of most radar applications. Figure 5 shows the same autocorrelation response but zoomed in on the mainlobe region on the plot (i.e., near $t = 0$). Two important attributes of the LFM autocorrelation can be discerned from Figure 4 and Figure 5. First, the LFM autocorrelation has a first sidelobe with a peak of about 13 dB below the mainlobe. Subsequent sidelobes beyond this roll-off with increasing t with an amplitude structure as dictated by a $\sin(t)/t$, or $\text{sinc}(t)$ function as time increases [37]. This sidelobe structure shows how a large RCS scatterer can obscure closely located smaller RCS scatterers, even though they would normally be separable as indicated by the range resolution of the pulse in (2.3). Second, the first null on either side of the mainlobe occurs at $1/BT = 0.005$, indicating the mainlobe has a width of $2/(BT) = 0.010$. This shows that the resolution of the LFM waveform after pulse compression is inversely proportional to the time-bandwidth product, which agrees with (2.3).
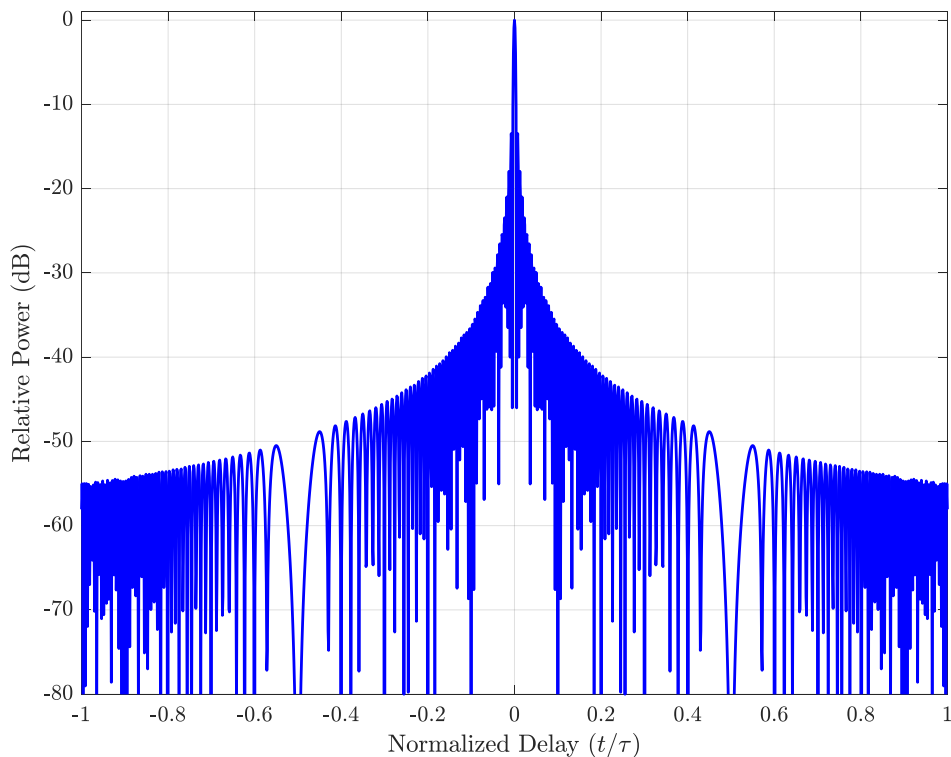
Figure 4: Autocorrelation of an LFM waveform with $BT = 200$
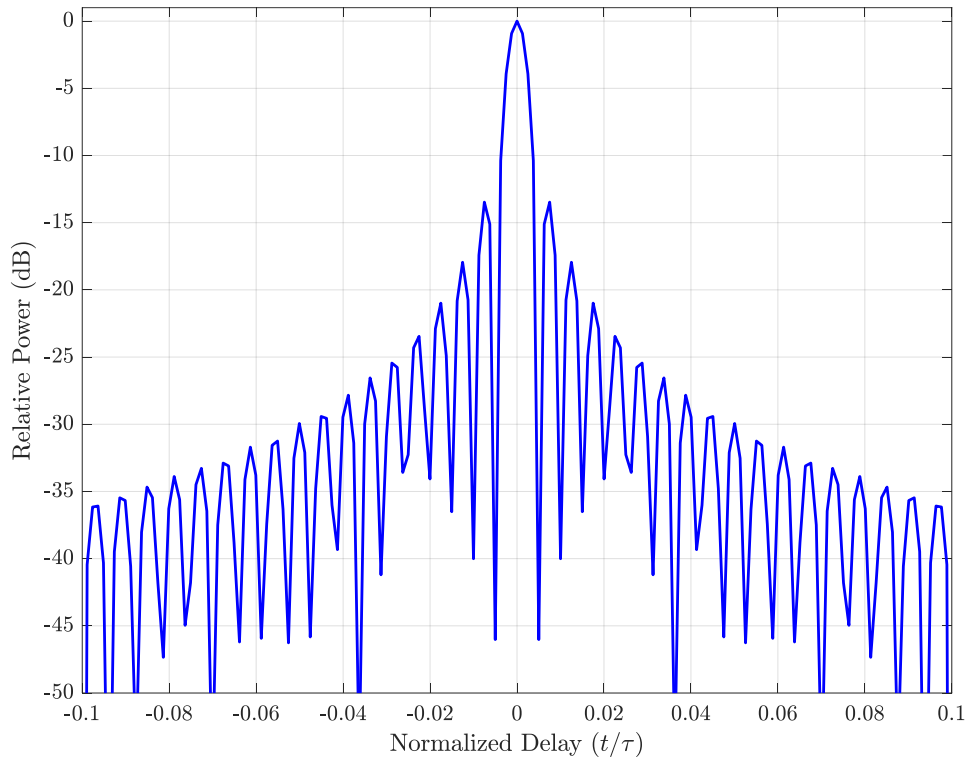
Figure 5: Autocorrelation of an LFM waveform with $BT = 200$ (mainlobe detail view)

Discrete representations of signals are typically used when performing radar signal processing, as the signal captured at the radar receiver is typically in a digital form after passing through an analog to digital converter (ADC). As such, the radar transmit waveform and subsequent filtering operations previously described can be converted to a discrete form. The modulated continuous time radar waveform of pulse duration T and bandwidth B can be discretized into the length N vector **s** as

$$\mathbf{s} = \begin{bmatrix} s(1) & s(2) & \cdots & s(N) \end{bmatrix}^{T} = \begin{bmatrix} s_1 & s_2 & \cdots & s_N \end{bmatrix}^{T}, \tag{2.12}$$

for $(\bullet)^{T}$ the vector-matrix transpose operation. The discrete waveform **s** is a discretized version of $s(t)$ with a sampling period of T_s such that $N = T/T_s$ is the total number of points in the discrete waveform. It is important to note that the sampling frequency $f_s = 1/T_s$ must be sufficiently larger than B (at least 2 times, in fact, according to the Nyquist sampling theorem [39]) in order to prevent aliasing. As was shown in Figure 3, it is common to oversample the discrete-time representation

of the radar signal such that a sufficient amount of the power spectrum roll-off can be captured as to ascertain its characteristics. In (2.12), the number of discrete points in the waveform can also be written as $N = (BT)K$, for BT the time-bandwidth product and K the oversampling factor (typically with respect to the 3-dB bandwidth of the waveform power spectrum).

A discrete form of the continuous-time convolution described in (2.8) can be formed by first considering the backscattered energy captured at the radar receiver for a single discrete delay index, l. This discretized convolution can be represented mathematically as

$$y_r(l) = \sum_{n=1}^{N} s(n) x(l-n+1) + n(l), \tag{2.13}$$

where the lag, or delay, variable l has replaced the continuous time variable t and the discrete summation has replaced the continuous-time convolution integral. In (2.13), $x(l)$ is the complex scattering amplitude at index l, and $n(l)$ is a single sample of AWGN. Now, collect N samples of the complex scattering amplitude at delay l to yield the vector-matrix representation of the scattering energy captured at the radar receiver as

$$\mathbf{y}_r(l) = \begin{bmatrix} y(l) & \cdots & y(l+N-1) \end{bmatrix}^T = \mathbf{S}\mathbf{x}(l) + \mathbf{n}(l), \tag{2.14}$$

where $\mathbf{x}(l)$ is the length $(2N-1)$ vector represented by

$$\mathbf{x}(l) = \begin{bmatrix} x(l-N+1) & \cdots & x(l+N-1) \end{bmatrix}^T, \tag{2.15}$$

and $\mathbf{n}(l)$ is an N x 1 vector of AWGN samples. The waveform matrix $\mathbf{S}$ is an N x $(2N-1)$ Toeplitz matrix consisting of delay shifted versions of the discretized transmit waveform such as to allow convolution of the transmit waveform $\mathbf{s}$ with $\mathbf{x}(l)$ and is represented as

$$\mathbf{S} = \begin{bmatrix} s_N & \cdots & \cdots & s_1 & 0 & \cdots & 0 \\ 0 & \ddots & & \vdots & \ddots & \ddots & \vdots \\ \vdots & \ddots & \ddots & \vdots & & \ddots & 0 \\ 0 & \cdots & 0 & s_N & \cdots & \cdots & s_1 \end{bmatrix}. \tag{2.16}$$

The N x 1 vector $\mathbf{y}_r(l)$ therefore contains a collection of N contiguous samples of backscattered energy from the illuminated environment corresponding to delay l.

A discretized and normalized version of the matched filter represented in (2.9) is given by

$$\mathbf{w}_{\mathrm{MF}}(l) = \mathbf{w}_{\mathrm{MF}} = \frac{\mathbf{s}}{\mathbf{s}^H \mathbf{s}}, \tag{2.17}$$

where the absence of the delay variable l after the first equality is due to the delay-independent nature of the matched filter. The normalization term in the denominator of (2.17) is equivalent to the total power in the signal and is often utilized in discrete radar signal processing to maintain relative signal power levels. The discrete matched filter is applied to the scattering energy captured at the radar receiver in order to obtain an estimate of the complex scattering amplitude at delay l via

$$\hat{x}_{\mathrm{MF}}(l) = \mathbf{w}_{\mathrm{MF}}^H \mathbf{y}(l). \tag{2.18}$$

The discrete matched filter is applied to $\mathbf{y}_r(l)$ for all indices of l in which an estimate is desired, forming a composite range profile estimate based upon a single transmitted pulse. Each index l typically corresponds to a range cell since the time elapsed from the transmitter emission to the reception of the backscattered energy is used to determine the range of the cell with respect to the radar system, as described in (2.1). It should be noted that the matrix multiplication in (2.18) is typically not used to perform pulse compression matched filtering, but rather a mathematically equivalent process using the FFT and inverse fast Fourier transform (IFFT) is performed in the frequency domain to achieve reduced computational complexity [40]. As the timescale for which range cells are collected and estimated is on the order of a radar PRI, this dimension is often denoted as the "fast-time", or "fast-frequency", dimension. Figure 6 shows a representation of the fast-time dimension in each column consisting of a collection of L range cells. The complex

amplitude of a contiguous group of L range cells (the columns in Figure 6) is estimated using the filtering process described in (2.12) – (2.18).

2.4 Doppler Processing and Clutter Cancellation

The discrete collection of backscattered energy can be repeated for multiple PRI intervals, often for all M pulses or PRIs present in a radar CPI. Each of these collections, represented as the columns in Figure 6, are arranged sequentially in the order which they are captured. Collected in this manner, a discrete radar data matrix is formed containing L range cells, or rows, and M pulses/PRIs, or columns, as depicted in Figure 6. As the time scale for which multiple pulses/PRIs are captured is on the order of a radar CPI, this dimension is referred to as the "slow-time", or "slow-frequency" dimension. Each cell in the discrete radar data matrix will thus have both a fast-time and slow-time component, as shown with the cell highlighted in Figure 6.
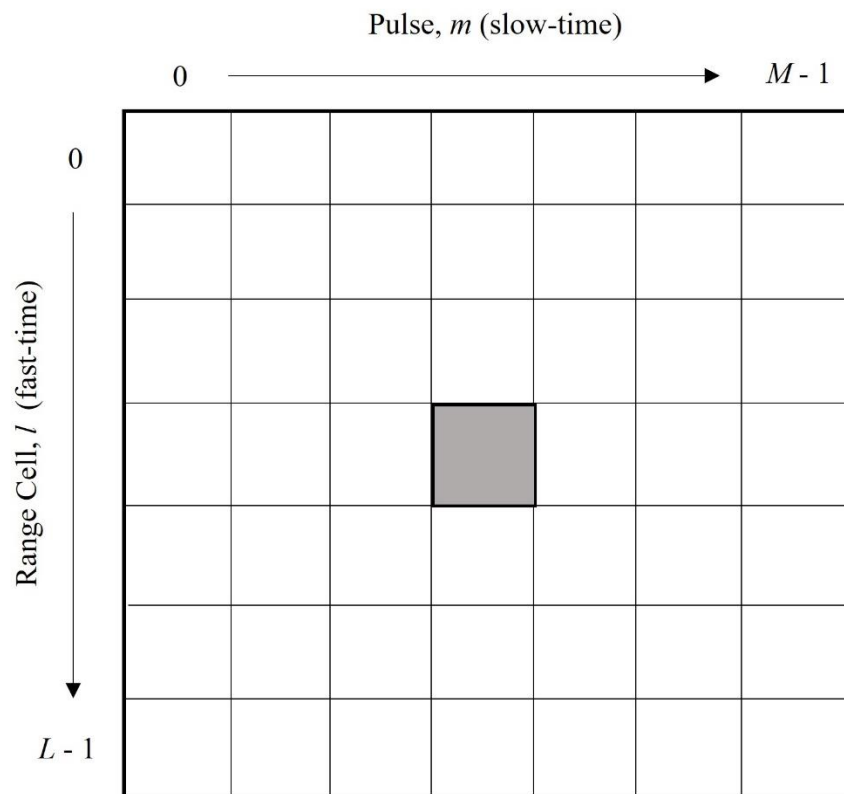
Figure 6: Discrete representation of radar data matrix with a single joint fast-time/slow-time cell highlighted

While many scatterers in the illuminated region of interest will remain stationary (often denoted as clutter) over the M pulses/PRIs in the CPI, the presence of scatterers that are moving relative to the radar system platform is also possible. Scatterers moving radially with respect to the radar system platform over the CPI will impart a Doppler shift to the transmitted waveform given by the radial velocity of the scatterer, υ_r, and the wavelength of the transmitted waveform, λ, as

$$f_D = \frac{2\upsilon_r}{\lambda},$$
(2.19)

where f_D is the Doppler frequency shift imparted onto the transmitted waveform by the scatter, in units of Hertz (Hz). Whereas the complex scattering amplitude in each range cell is estimated via a fast-time filtering operation (e.g., matched filter pulse compression), the Doppler shift for scatterers in each range cell over the CPI is estimated via a slow-time filtering operation often referred to as a Doppler filter.

Estimating the Doppler frequency of scatterers in the illuminated environment starts with first collecting the M estimates of the complex scattering at range delay l into the M x 1 vector $\hat{\mathbf{x}}_{\mathrm{MF}}(l)$. The normalized Doppler estimate for range cell l is then formed via application of the Doppler filter as

$$\hat{\mathbf{x}}_{\mathrm{MF,DP}}(l) = \left(\frac{1}{M} \mathbf{W}_{\mathrm{DP}}^H \right) \hat{\mathbf{x}}_{\mathrm{MF}}(l),$$
(2.20)

for $(\bullet)^H$ the Hermitian, or conjugate-transpose operation, and the matrix $\mathbf{W}_{\mathrm{DP}}$ containing P columns of the length-M Doppler steering vectors

$$\mathbf{v}(\theta) = \left[1 \quad e^{j2\pi\theta(1)} \quad e^{j2\pi\theta(2)} \quad \cdots \quad e^{j2\pi\theta(M-1)} \right]^T,$$
(2.21)

for P discretized values of normalized Doppler frequencies θ on the interval $\theta \in [-1/2, +1/2]$. The value of P is usually chosen as an integer multiple of M as $P = K_D M$ for some Doppler

oversampling factor K_D, as to prevent loss of estimated Doppler energy due to straddling loss [37].

The Doppler estimation in (2.20) produces the length-P vector $\hat{\mathbf{x}}_{MF,DP}(l)$ with estimated Doppler

frequencies from scatterers at range cell l. Repeating (2.20) for a set of L range cells produces the

L x P matrix $\hat{\mathbf{X}}_{MF,DP}$ commonly referred to as the range-Doppler (RD) map. The Doppler filter

$\mathbf{W}_{DP}$ is in fact a discrete Fourier transform (DFT) which is usually implemented to perform

Doppler filtering with the more efficient, but mathematically equivalent, FFT.

Akin to how the autocorrelation response lends insight into the pulse compression sidelobe

structure of a transmitted waveform when the matched filter is applied to obtain the impulse

response estimate of a hypothetical point scatterer (as shown for the LFM in Figure 4 and Figure

5), the point spread function (PSF) extends this insight into the Doppler dimension to determine

the structure of the Doppler response for a hypothetical point scatterer at an arbitrary range cell

with zero Doppler frequency over a CPI of M pulses. Even though the hypothetical point scatterer

has zero Doppler frequency, the Doppler sidelobe structure will generalize to any non-zero

Doppler frequency. Figure 7 depicts the PSF for the LFM waveform with $BT = 200$, whose

autocorrelation response is shown in Figure 4, over a CPI of $M = 1000$ pulses with a Doppler

oversampling factor of $K_D = 10$ for a total of $P = 10,000$ discrete normalized Doppler frequencies

in the DFT. Note that the Doppler oversampling factor can be arbitrary, and will depend upon the

application, but a relatively large value was shown here as to provide fine Doppler detail in the

PSF. The Doppler frequency axis is normalized to the PRF, as the unambiguous Doppler

measurement limit, $f_{D,max}$, of a pulsed radar system is determined by the PRF as $f_{D,max} = \pm\,PRF/2$

[36]. The peak power of the PSF is normalized to unity and represented on a decibel scale, as with

the autocorrelation. It is important to note that the zero-Doppler cut of Figure 7 is identical to the

LFM autocorrelation shown in Figure 4. Figure 8 zooms into the delay and frequency axes to show a detailed view of the mainlobe region of the PSF.
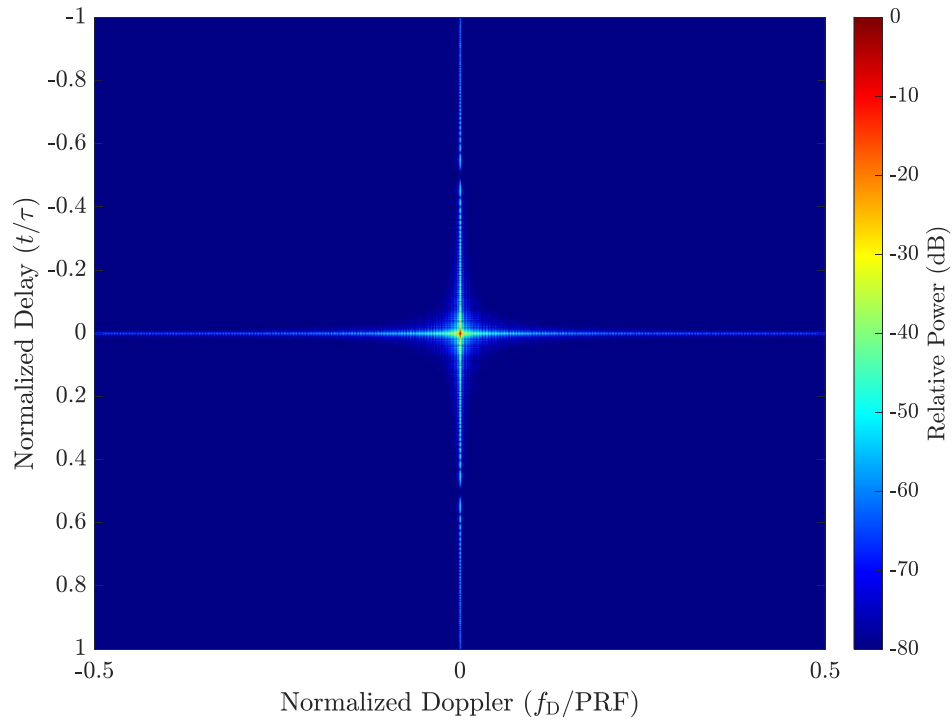
Figure 7: Point Spread Function of an LFM waveform with $BT = 200$ and a CPI of $M = 1000$ pulses
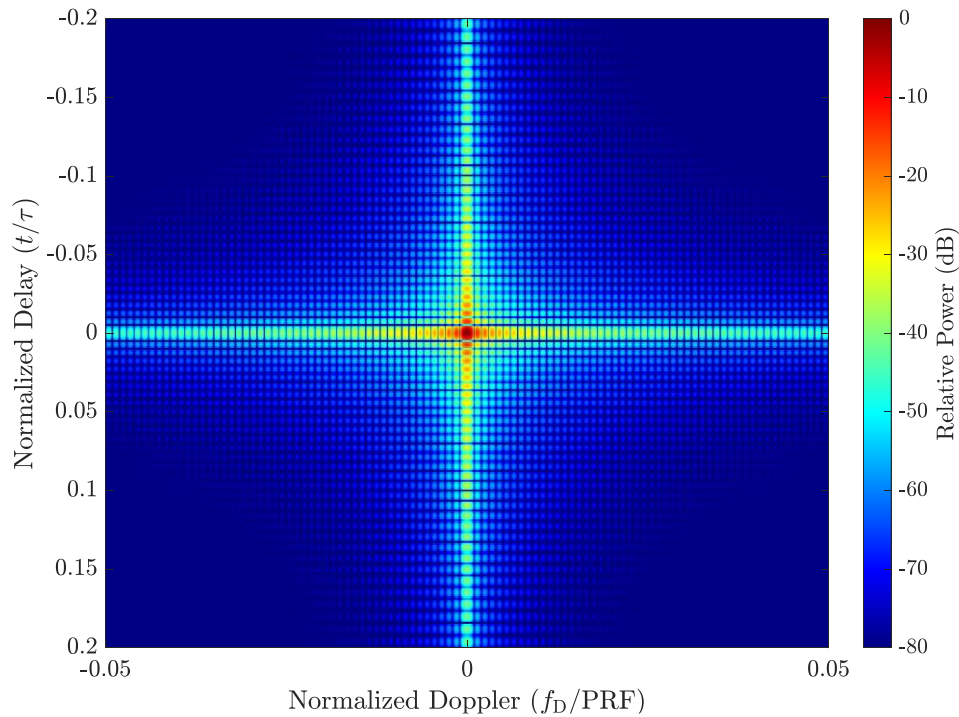
Figure 8: Point Spread Function of an LFM waveform with $BT = 200$ and a CPI of $M = 1000$ pulses (mainlobe detail view)

A common practice in Doppler processing is to apply a slow-time weight to the collection of M responses at each range cell before the Doppler filtering operation [36]. This is known as Doppler tapering or windowing and is performed with a simple modification to (2.20) as

$$\hat{\mathbf{x}}_{\text{MF,DP}}(l) = \left(\frac{1}{M} \mathbf{W}_{\text{DP}}^{H} \right) (\hat{\mathbf{x}}_{\text{MF}}(l) \odot \mathbf{b}) \ , \tag{2.22}$$

for the length M discrete windowing function $\mathbf{b}$ and $\odot$, the Hadamard, or element-wise, multiplication operation. Figure 9 shows a comparison between two types of Doppler windows. The first (blue trace) is a rectangular, or non-tapering (same as not applying a taper since all values of the function are one), window and the second (red trace) is a Taylor window with five nearly-constant sidelobe levels adjacent to the mainlobe and a maximum sidelobe level of approximately -50 dB relative to the mainlobe peak [41]. The Taylor window has been normalized to have the same peak as the rectangular window for ease of comparison. The plots in Figure 9 depict the Doppler sidelobe structure for a hypothetical point scatterer at an arbitrary range cell with zero Doppler frequency that has been windowed with each type of windowing function. Comparing the two plots in Figure 9, the first noticeable difference is the peak sidelobe level of about -13 dB relative to the mainlobe peak for the rectangular window with a sidelobe roll-off structure dictated by a $\sin(x)/x$ or $\text{sinc}(x)$ function, whereas the Taylor window has a first mainlobe peak value of about -50 dB (as designed) with an overall peak at the fifth sidelobe of about -47.5 dB relative to the mainlobe peak. This illustrates how a Doppler window can be used to suppress sidelobes from a large scatterer to uncover smaller scatterers located at the same range cell with Doppler frequencies close to the larger scatterer. The second noticeable difference is the loss of Doppler resolution associated with the Taylor window as indicated by a widening of the mainlobe in Figure 9. This resolution loss is one of the two primary tradeoffs with Doppler windowing, the other being a loss in the signal-to-noise ratio (SNR) of the estimated response. Due to the normalization, this

is not immediately discernible in Figure 9, but it is still present. According to [36], this Taylor window has an SNR loss of about 1.5 dB relative to a rectangular window with a Doppler resolution loss of about 52% compared to a rectangular window. These two tradeoffs are typically accepted, however, for such a large reduction in Doppler sidelobe levels. It is worth noting that the blue trace in Figure 9 is equivalent to the zero-delay cut of the LFM PSF shown in Figure 7 and Figure 8. All Doppler processed results presented in the remainder of this document will be accompanied by an indication of whether or not Doppler windowing was utilized.
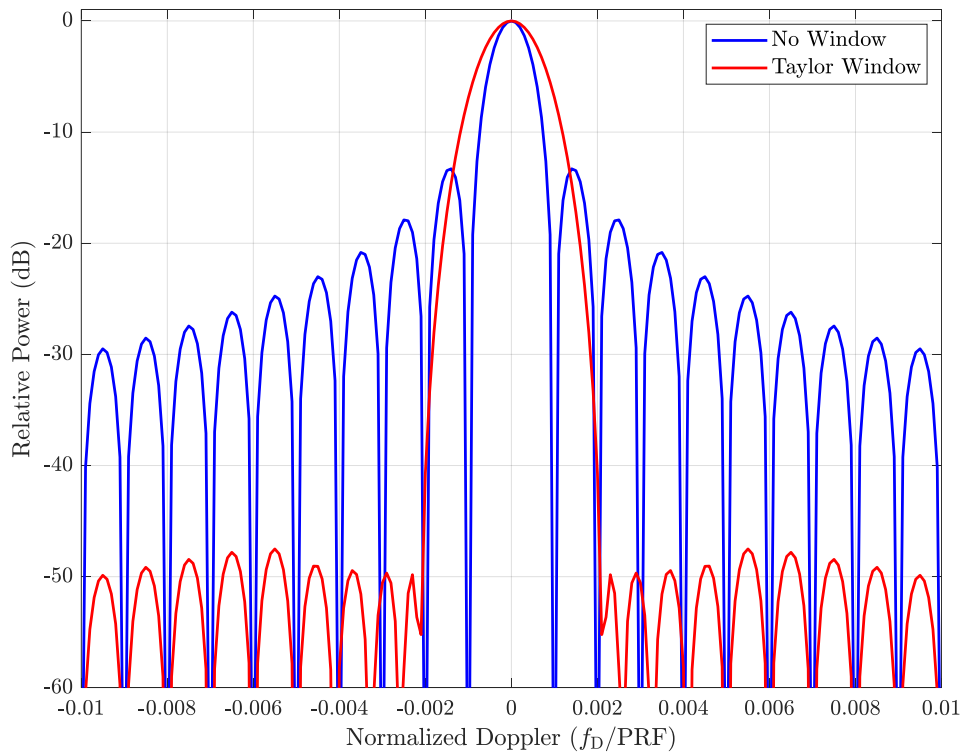
Figure 9: Comparison of a rectangular (or lack thereof) Doppler tapering window (blue) with a Taylor window consisting of five nearly constant-level sidelobes adjacent to the mainlobe and maximum sidelobe level of approximately -50 dB relative to the mainlobe peak

Another common practice in radar processing is the application of clutter cancellation for objects in the illuminated region which are not of interest. These objects are often stationary scatterers and can be natural or man-made. Clutter often has more backscatter energy than

scatterers of interest and can obscure them if they have a Doppler frequency close to that of the clutter. Clutter cancellation is applied through a simple modification to (2.22) as

$$\hat{\mathbf{x}}_{\mathrm{MF,DP,CC}}(l) = \left(\frac{1}{M} \mathbf{W}_{\mathrm{DP}}^{H} \right) \left(\hat{\mathbf{x}}_{\mathrm{MF}}(l) \odot \mathbf{b} \right) \mathbf{P}_{\perp} \tag{2.23}$$

where $\mathbf{P}_{\perp}$ is the M x M orthogonal projection matrix which projects away from the Doppler frequency subspace of the clutter that is to be cancelled. As indicated by (2.23), multiplication with the orthogonal projection matrix occurs *after* multiplication of the range profile estimates with a Doppler window. The orthogonal projection matrix is formed by first considering the Doppler DFT matrix, whose columns are described in (2.21). Denote the collection of P length-M Doppler steering vectors into the M x P DFT Matrix $\mathbf{A}_{\mathrm{DFT}}$. Next, perform a singular value decomposition (SVD) on this DFT matrix as

$$\mathrm{SVD}(\mathbf{A}_{\mathrm{DFT}}) = \mathbf{U} \boldsymbol{\Sigma} \mathbf{V}^{H}, \tag{2.24}$$

where the multiplicand of interest on the right-hand side of (2.24) is the unitary matrix $\mathbf{U}$, which has dimension M x M and forms an orthonormal basis for the DFT matrix. Collecting the first Z columns of $\mathbf{U}$, corresponding to the first Z singular values from the SVD decomposition of the DFT matrix, and number of DFT steering vectors which sufficiently characterize the Doppler frequency extent of the clutter, into the M x Z matrix $\mathbf{B}$, the orthogonal projection matrix is formed as

$$\mathbf{P}_{\perp} = \mathbf{I}_{M} - \mathbf{B} \left(\mathbf{B}^{H} \mathbf{B} \right)^{-1} \mathbf{B}^{H}, \tag{2.25}$$

for $\mathbf{I}_{M}$ the M x M identity matrix. All Doppler processed results presented in the remainder of this document will be accompanied by an indication of whether or not clutter cancellation was utilized.

2.5 Basic Radar Simulation Example

A basic simulation of pulsed radar operation is presented here as a means to tie together the concepts presented thus far of basic radar operation, pulse compression, Doppler processing, Doppler windowing, and clutter cancellation. The simulated radar waveform is an LFM waveform with $BT = 50$ and $K = 2$ for $N = 100$ total discrete points. The illuminated environment of interest, denoted by the impulse response $x(t)$ in (2.8), is formed by creating a clutter profile which is generated randomly as a complex Gaussian process with power of -30 dB relative to the peak transmit power of the LFM waveform and zero Doppler frequency. Note that it is common for clutter to have non-zero Doppler frequency components in practice, but that is not the case for this simplified simulation. After generating a clutter profile, three scatterers are added to this environment, characterized by their range index, power relative to the peak transmit power, and normalized Doppler frequency. The characteristics of these three scatterers are summarized in Table 1. Scatterer and clutter powers considered in this simulation are representative of the high dynamic range associated with most radar applications, where the range of powers associated can vary by many tens to a hundred or more orders of magnitude.

Table 1: Scatterer parameters for basic radar simulation

	Relative Power (dB)	Range Index, L	Normalized Doppler (f_D/PRF)
Scatterer 1	-60	250	0.10
Scatterer 2	-50	250	-0.25
Scatterer 3	-55	400	0.10

This impulse response of the simulated environment is convolved with the radar transmit waveform, as described mathematically in (2.13), and AWGN noise is added with a power of -50 dB relative to the peak transmit power to simulate thermal noise in the radar receiver. A total of M = 100 pulses are transmitted and their backscatter collected to form the CPI.

The pulse compression matched filter is applied as described in (2.18) and Doppler processing is performed as described in in (2.20). The resulting range-Doppler map is shown in Figure 10 with the three estimated scatters circled in red. As is evident, the highest power region of the illuminated environment is the clutter which is located at zero Doppler frequency. The three scatterers are still visible on the RD map, with their range indices, normalized Doppler frequencies and relative power levels well-estimated by the pulse compression matched filter and Doppler processing. However, for clutter with non-zero Doppler frequencies and scatterers with smaller relative powers, it is easy to see how the latter would be easily obscured by the presence of uncancelled clutter. The application of pulse compression matched filtering and Doppler filtering in this type of scenario is often referred to as MTI, a common function of pulsed radar systems [36].
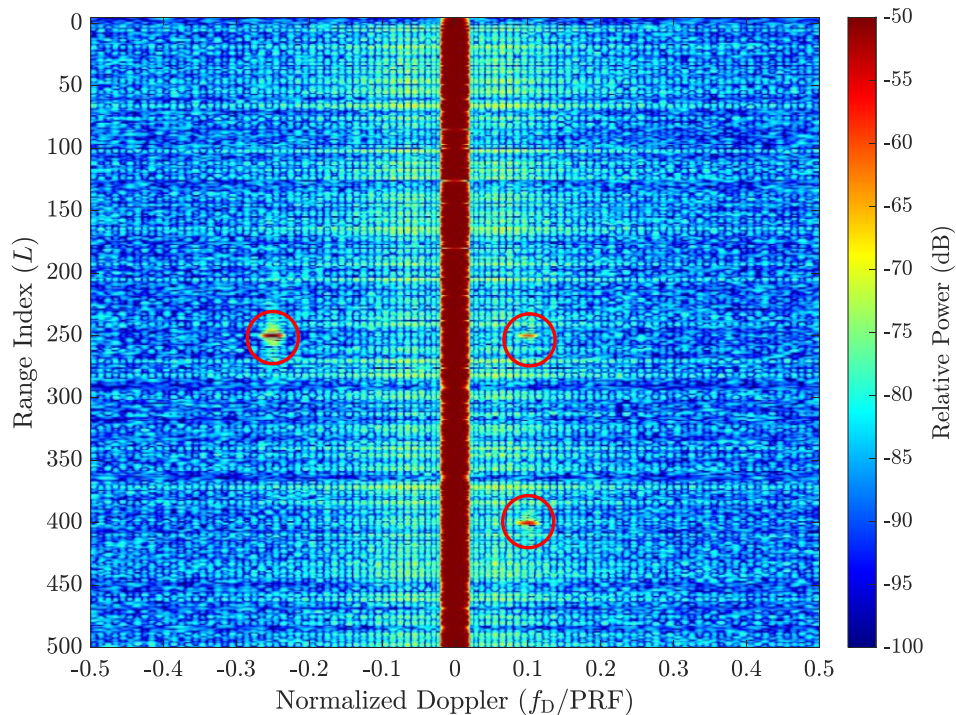
Figure 10: Range-Doppler map of illuminated environment of interest via a basic radar simulation

Next, the processing is extended by applying clutter cancellation as described by (2.23) with $Z = 11$ singular values for the clutter cancellation and a rectangular Doppler window. The

resulting RD map is shown in Figure 11. Immediately noticeable is the absence of clutter in the

RD map, being replaced by a "notch" due to the application of clutter cancellation. The three

scatterers are much more readily discernible in this RD map. Finally, the Doppler window depicted

in Figure 9 is added to the processing procedure, along with clutter cancellation. The resulting RD

map is shown in Figure 12. It is readily noticed that the Doppler sidelobes of each scatterer have

essentially disappeared into the noise floor. The expected loss in resolution is also presented as a

widening of the Doppler mainlobe for each scatterer. Finally, the loss in SNR caused by the

Doppler window can also be noticed as a slight increase in the noise floor of the RD map when

comparing to the rectangular window of Figure 11.
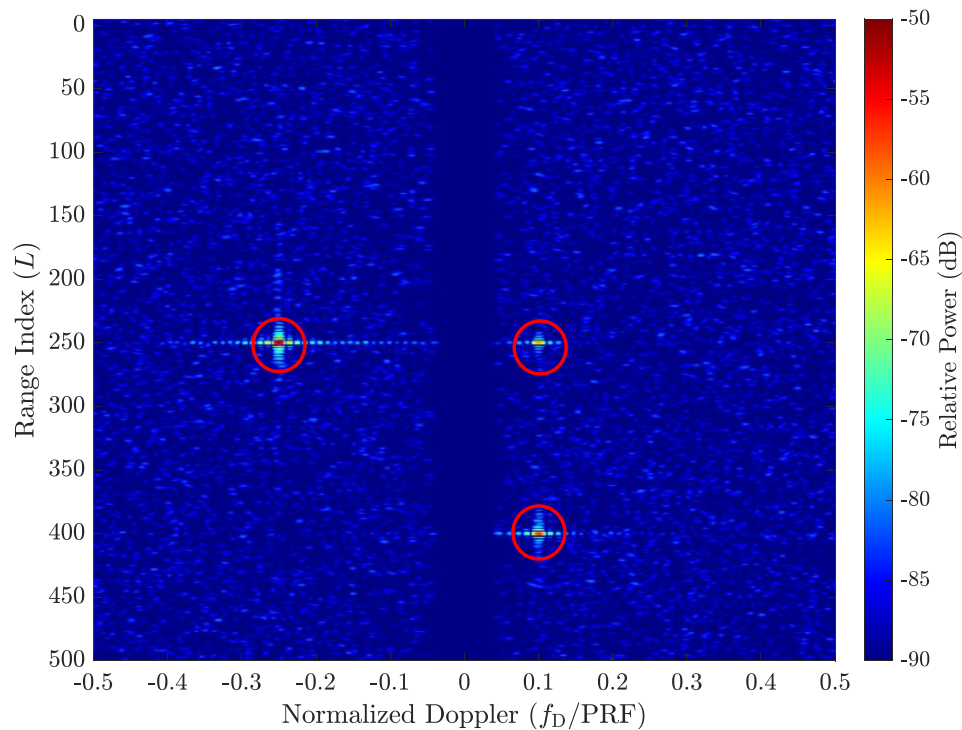
Figure 11: Range-Doppler map, with the addition of clutter cancellation, of illuminated environment of interest via a basic radar simulation
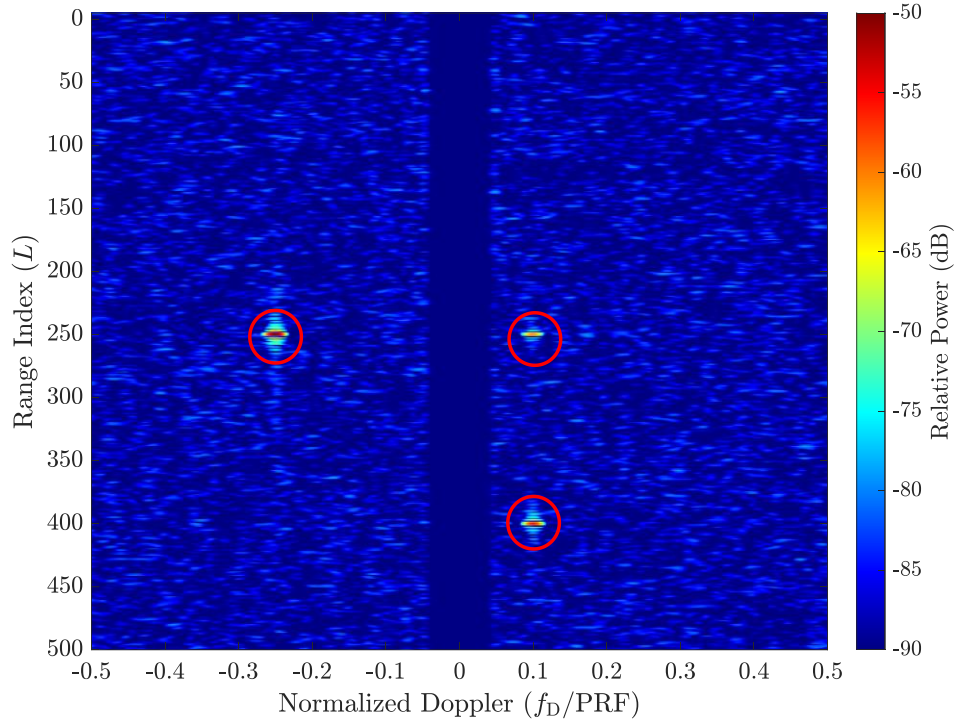
Figure 12: Range-Doppler map, with the addition of clutter cancellation and a Taylor Doppler window, of illuminated environment of interest via a basic radar simulation

Before closing this introduction to basic radar operation, a note on signal processing gain is warranted. An added benefit to the use of pulse compression waveforms is the pulse compression gain obtained by matched filtering, which is defined as the waveform time-bandwidth product, BT [36]. This per-pulse gain stems from the coherent processing applied by the pulse compressed matched filter to the backscatter collected at the radar receiver (both scatterers of interest and clutter), which is illuminated by the known radar transmit waveform. Since the thermal noise present in the radar receiver system is typically AWGN, and thus incoherent with the radar transmit waveform, an SNR gain of BT is obtained for each compressed pulse (note that this assumes the signal bandwidth captured at the radar receiver is the same as the noise bandwidth, which is typical in practice). Further processing gain is obtained by performing coherent Doppler processing over a set of M pulses in a CPI. Thus, the total SNR gain obtained by combining pulse compression and Doppler processing is equal to MBT. Note that since the signal captured at the radar receiver will

contain both scatterers of interest and clutter, a gain in the clutter-to-noise ratio (CNR) of *MBT* is also realized.

2.6 Basics of Wireless Communications

Fundamentally, the goal of wireless communications is to transmit information electromagnetically between two points, often denoted as the transmitter and receiver. Figure 13 shows a diagram of the basic operation of wireless communications.
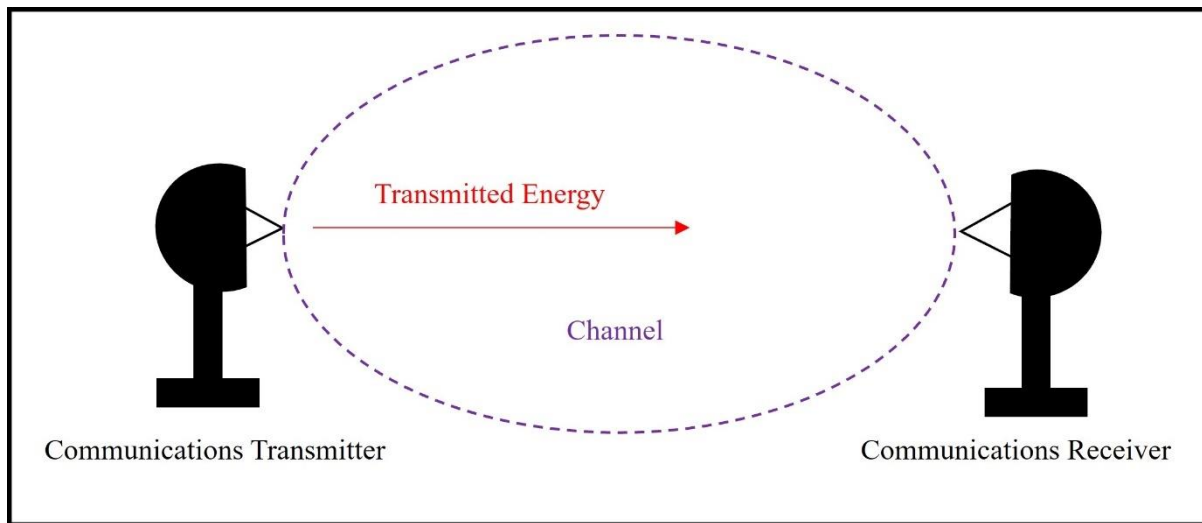
Figure 13: Diagram of basic wireless communications operation

Where the goal of radar operation is to estimate the complex scattering amplitude of the region illuminated by the radar transmitter such as to ascertain the presence of scatterers, the goal of a wireless communications system is to transmit information through the illuminated medium such that it can be accurately retrieved at the intended communications receiver. This requires estimation of the propagation medium, commonly known as the channel, for the purpose of removing, or cancelling, its effects on the signal captured by the receiver [42]. In addition to compensating for channel effects, communications systems often employ various error correction coding strategies to increase the likelihood of the receiver successfully determining the information sent by the transmitter [43].

The information transmitted by a communications signal takes the form of a complex symbol on a communications constellation. Examples of three different quadrature amplitude modulation (QAM) constellations are shown in Figure 14, 4-QAM, 16-QAM and 64-QAM, where the numbers in front of "QAM" represent the number of complex symbols in the constellation. Each symbol typically represents a mapping to a sequence of binary bits, the information which is desired to be transmitted. For R symbols in a communications constellation, a total of $\log_2(R)$ bits of information can be conveyed by each symbol. Therefore, modulating a communications signal with a symbol from a larger constellation will allow information to be conveyed at a faster rate. However, since communications signals are corrupted by both the propagation channel and thermal noise present in the receiver system, errors in channel estimation and cancellation, along with low SNR environments, will result in an increased chance in error when demodulating the embedded symbol at the communications receiver. The more symbols present on the constellation, the more likely a demodulation error will occur at the communications receiver for a given SNR and channel estimation and cancellation accuracy. Therefore, densely populated constellations are typically reserved for high SNR operation environments and/or error correction coding schemes which provide robustness to challenging propagation environments.

Since communications constellations contain multiple amplitude levels (as shown in Figure 14), and the transmitted communications signal is the superposition of many individually modulated signals, communications signals are typically not constant amplitude, and therefore are precluded from the high-power amplification typical of radar systems. This major drawback is addressed with an optimization scheme introduced in Chapter 5. While constant amplitude communications modulation schemes do exist, such as CPM [28], they are typically limited in their applications, such as CPM in aeronautical telemetry [44].

Many different modulation schemes exist for wireless communications, but the only method introduced here (due to its relevance in Chapter 5) is OFDM. The goal of OFDM is to avoid the intersymbol interference (ISI) incurred by many linear modulation schemes when transmitting signals through a channel. OFDM avoids ISI by choosing the modulating waveforms to be the eigenfunction of the channel, which are complex exponentials for a linear time invariant (LTI) channel [42]. The continuous-time, complex baseband representation of an OFDM signal can be given by

$$s(t) = \sum_{n=1}^{N} B[n] \, e^{j2\pi f_n t} I[0,T](t),$$ (2.26)

where $B[n]$ is the complex constellation symbol transmitted by the modulating complex exponential at subcarrier frequency f_n, and $I[0,T]$ is a time-gating function which is unity for $0 \leq t \leq T$, and zero elsewise [42]. Consequently, (2.26) indicates that the transmitted OFDM signal will be the superposition of N complex exponential functions, each residing at a single subcarrier frequency f_n and modulating a single information bearing symbol $B[n]$ for the duration T of the signal. Due to ease of implementation and channel estimation and equalization, OFDM is a popular modulation scheme and forms the basis for 4G and 5G commercial communications standards [45].
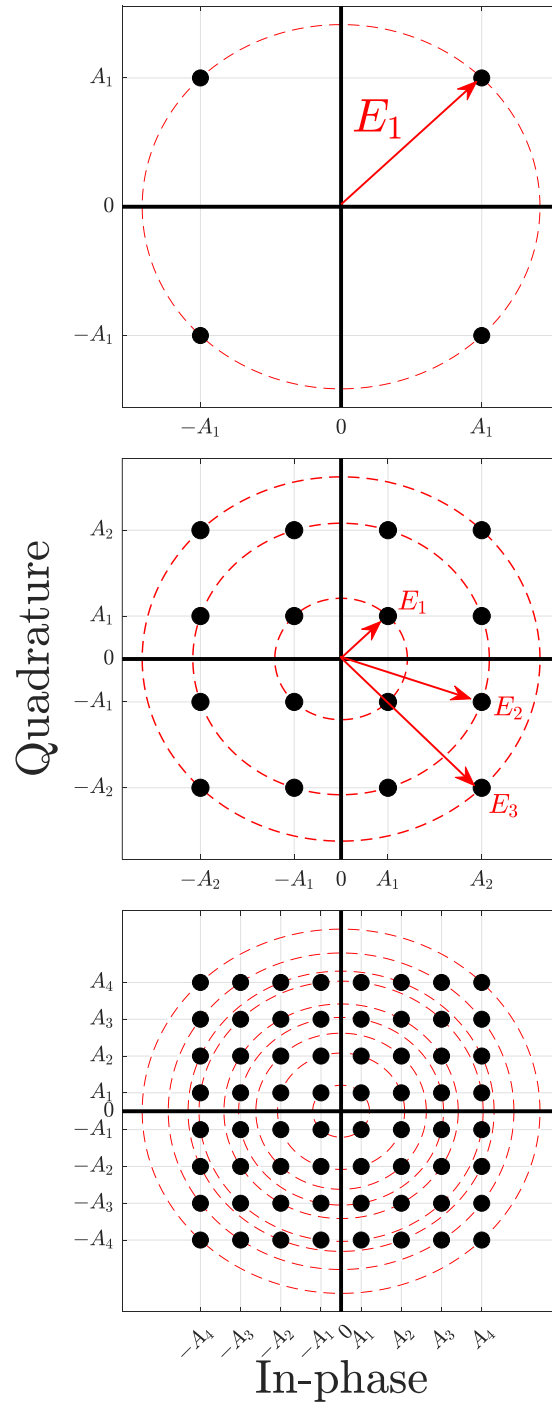
Figure 14: Examples of 4-QAM (top), 16-QAM (middle) and 64-QAM (bottom) symbol constellations, with associated amplitude rings, common to communications

Chapter 3: Random FM Waveforms

This chapter provides an introduction to RFM waveforms and highlights some of their key characteristics and advantages, while also analyzing the tradeoffs incurred with their use as radar waveforms. Design of a specific class of RFMs is discussed and its utility as radar waveforms is assessed through simulation. Although a single RFM optimization technique is presented here which relies on an alternating projections optimization routine [16, 17, 46, 47], many other strategies have been explored in recent years to design separate classes of RFM waveforms with varying applications including PCFM [29, 48-54], analytical spectrum notching via the PCFM framework [55], spectral notching in RFM waveforms for modest DAC rates [56], wideband FM MIMO [57, 58], dual-polarized RFM [59], frequency and time template error [60, 61], complementary RFM waveforms [62], non-linear radar [63, 64] and stochastically defined RFM waveforms [65], among others.

The remainder of this chapter is laid out as follows. Section 3.1 gives an introduction to RFM waveforms, along with a brief history, and discusses some of their advantages and tradeoffs. Section 3.2 introduces a class of RFM waveforms which is utilized heavily in later chapters. A description of the optimization procedure is given along with simulation results. Sections 3.3 and 3.4 then explore placing spectral notches into this class of RFM waveforms and analyzes the tradeoffs with additional simulation results. Finally, Section 3.5 briefly considers placing spectral notches into LFM waveforms and assesses the impact of such.

3.1 Introduction to Random FM Waveforms

While a relatively new and emerging radar paradigm, the application of random FM, or FM noise, waveforms for radar operation is rooted in a patent issued in 1980 [66]. Subsequent work in [67] expanded upon the concept of RFM waveforms by modulating the frequency of radar waveforms

with white noise processes. Theoretical analysis of RFM waveforms was presented in [68, 69] with the assumption of Gaussian distributed white noise process driving the random modulation of the waveform frequency. RFM waveforms can be thought of as a specific case of noise radar [70], in which the randomness is present only in the FM component of the signal [71], therefore maintaining a constant amplitude and remaining amenable to high-power amplification.
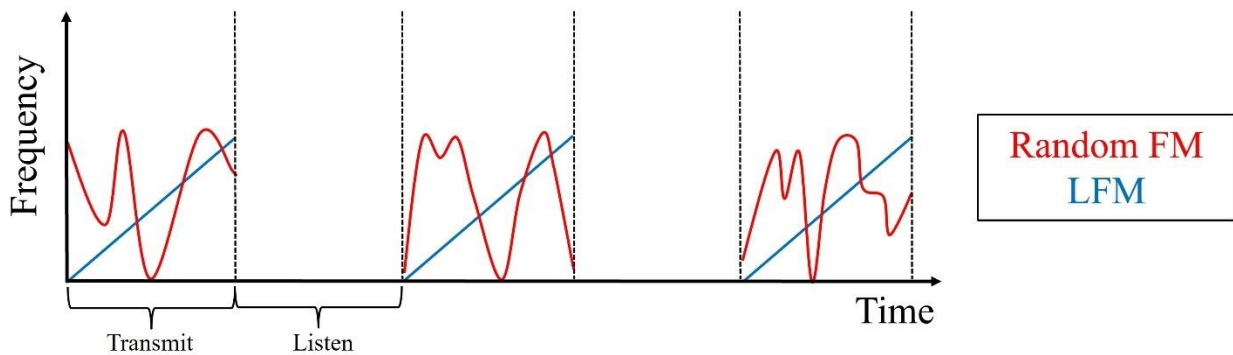
Figure 15: Example representation of the frequency behavior of a pulsed RFM waveform as compared to that of a pulsed LFM waveform

An example of the frequency characteristic of an RFM is shown in Figure 15. As expected, the waveform possesses an unpredictable and random (hence the name) time-frequency structure. This is in stark contrast to the ubiquitous LFM waveform, which has easily discernible structure as shown in Figure 15 and well-defined frequency and phase structure, as given by (2.6) – (2.7). Although the phase/frequency structure of the RFM waveform is random in nature, they can still possess smooth phase trajectories through proper design, thus providing good spectral containment, as shown later in this chapter. Furthermore, careful RFM design yields waveforms with very desirable autocorrelation properties. Peak sidelobe levels in the autocorrelation response of a single pulse better than $-10 \log_{10} (BT)$ dB are achieved in practice, with levels on the order of $-20 \log_{10} (BT)$ dB achievable through proper design [71-73]. Furthermore, coherent slow-time

processing of M waveforms will yield an additional sidelobe level reduction of $10 \log_{10}(M)$ as the sidelobes combine coherently across different random FM pulses, while the autocorrelation mainlobe remains coherent [71].

In addition to increased complexity in designing of the random FM waveform, another tradeoff with traditional LFM waveforms is incurred. Due to the unique, non-repeating structure of the pulse compression sidelobes, slow-time processing induces an RSM effect on high-powered clutter and scatterers of interest [23, 74] in the illuminated environment, which is not incurred with the use of repeated waveforms. This undesirable RSM is caused by a nonstationarity (essentially a coupling between the fast-time and slow-time dimensions) in the collection of received backscatter energy in the radar CPI, and cannot be mitigated with standard clutter cancellation techniques, as depicted in (2.23). The presence of RSM can often be severe and obscure scatterers in the illuminated scene. Examples of this are shown later in this chapter, and in Chapter 4, where a technique to mitigate RSM is also presented.

3.2 PRO-FM Waveforms

A new class of random FM waveforms known as PRO-FM was introduced in [46, 47]. PRO-FM waveforms are randomly initialized and optimized to have good spectral containment via matching to a desired power spectrum template, along with desirable autocorrelation properties, while still being FM (and thus constant amplitude) in nature. Since the initialization is random, optimized PRO-FM waveforms will retain unique sidelobe structures on a per-pulse basis which will combine incoherently when performing Doppler processing. The two competing optimization goals of matching to a desired spectrum template and retaining constant amplitude represent non-overlapping solution sets and pose a nonconvex optimization problem. Optimization of PRO-FM

waveforms therefore consists of two alternating projections steps akin to the Gerchberg-Saxton algorithm originally developed for phase retrieval in image processing [75].

Consider the optimization of a set of M pulsed PRO-FM waveforms with time-bandwidth product BT. The discretized waveform for each pulse m is initialized as $s_{0,m}$ using either a random phase code or the PCFM framework [29], the latter of which possesses smoother phase transitions and thus reduces the number of optimization iterations required for desirable PRO-FM waveforms to be produced. After initialization, each waveform is subjected to L sequential iterations of the two alternating projections steps ([46, 47])

$$\mathbf{r}_{l+1,m} = \mathbb{F}^{-1}\left\{\mathbf{g} \odot \exp\left(j\angle\mathbb{F}\{\mathbf{s}_{l,m}\}\right)\right\} \tag{3.1}$$

and

$$\mathbf{s}_{l+1,m} = \mathbf{u} \odot \exp\left(j\angle\mathbf{r}_{l+1,m}\right). \tag{3.2}$$

In the optimization routine of (3.1) and (3.2), F and F^{-1} denote the Fourier and inverse Fourier transforms, respectively. The desired frequency spectrum template $|G(f)|$ (corresponding to power spectrum template $|G(f)|^2$) is discretized and represented by the length N vector $\mathbf{g}$. The vector $\mathbf{u}$ is a discretized rectangular window with length N. The pulse number is represented by m. Finally, $\odot$ represents a Hadamard product and $\angle\,(\bullet)$ retrieves the phase of the argument.

The first step of the alternating projection procedure in (3.1) works to match the frequency spectrum of the optimized waveform to the desired frequency spectrum template represented by $|G(f)|$ (and therefore the desired power spectrum template $|G(f)|^2$ as well). This power spectrum template is chosen to be Gaussian in nature, as the associated autocorrelation will have zero sidelobes in theory due to the Fourier relationship between the power spectrum density and the autocorrelation function. In practice, however, the sidelobes will not be zero, but will be very low. The resulting waveform $\mathbf{r}_{l+1,m}$ from the first alternating projections step in (3.1) will not be

constant amplitude, so the second step of the procedure in (3.2) serves to remove all amplitude modulation from the waveform. This operation will distort the spectrum of the first alternating projections step, so the procedure is repeated for K iterations until a satisfactory result is obtained.

The power spectrum template used for the PRO-FM alternating projections optimization is represented by the Gaussian power spectral template [76]

$$G(f) = A\exp\left(-\frac{1}{2}\left|\frac{f-\gamma}{\sigma}\right|^{\eta}\right), \tag{3.3}$$

where A is an arbitrary scaling factor, f is the independent frequency variable, σ is the standard deviation, γ represents the center of the function (typically 0 for the normalized frequencies in which PRO-FM waveform spectra are represented), and η is a tunable parameter that determines the order of the Gaussian power spectral template, and thus the spectral compactness. A value of $\eta = 2$ represents a standard Gaussian power spectrum, while values of $\eta > 2$ represent a super Gaussian (SG) power spectrum. Originating from the field of optics [77], a SG spectrum has much sharper roll-off than a standard Gaussian spectrum. The initial PRO-FM representation in [46, 47] only considered a standard Gaussian template ($\eta = 2$), but this was extended to SG in [76, 78] where analysis and physical experimentation demonstrated that SG power spectrum templates could be incorporated into the design of RFM waveform to achieve more compact spectral roll-off, at the cost of losing some of the sidelobe decoherence when performing slow-time processing across a set of M pulses.

Maintaining a fair comparison across different SG power spectra with varying powers (dictated by η) is accomplished by keeping a consistent 3-dB bandwidth. It can be shown [76] that this can be achieved by selecting the standard deviation in (3.3) as

$$\sigma = \frac{(B/2)}{\left(2\ln(2)\right)^{1/\eta}},$$

(3.4)

for the parameters $A = 1$ and $\gamma = 0$ (representative of PRO-FM design). It is important to note that the power spectrum template defined in (3.3) is represented as $|G(f)|^2$, where the function utilized in the PRO-FM optimization procedure in (3.1) is a discretized version of the spectrum template $|G(f)|$ (note the difference of a power of 2). Figure 16 shows a comparison of SG spectral template functions $|G(f)|$ as defined in (3.3) and (3.4) for values of $\eta = 2, 4, 8$ and 16. The 3-dB bandwidth, B, of the template spectra is denoted as well. As expected, increasing the value of η provides a more compact spectrum template. This means that more of the optimized PRO-FM waveform power spectrum will reside within the 3-dB bandwidth. Judicious choice of the standard deviation parameter in (3.4) has ensured that all of the spectrum templates in Figure 16 maintain the same 3-dB bandwidth.

The PRO-FM optimization procedure described in (3.1) and (3.2) is used to optimize $M = 1000$ waveforms with time-bandwidth product $BT = 200$, oversampling factor $K = 4$ (so $N = 800$ discrete points in each waveform) for $L = 100$ iterations. Each of the four different super Gaussian templates shown in Figure 16 are considered to generate optimized PR0-FM waveforms with varying degrees of spectral compactness to assess the associated tradeoffs. Figure 17 shows the root-mean-square (RMS) power spectra of each of these optimized PRO-FM waveforms along with their associated SG spectral template $|G(f)|$. Performing the RMS across all M waveforms gives an indication of the characteristics of a single waveform by reducing variance. RMS is a useful representation for RFM waveform design and will be used throughout this chapter and the rest of this document. Illustrated by Figure 17 is more spectral compactness for increasing SG spectrum template order. The optimized waveform spectra match their spectral templates well
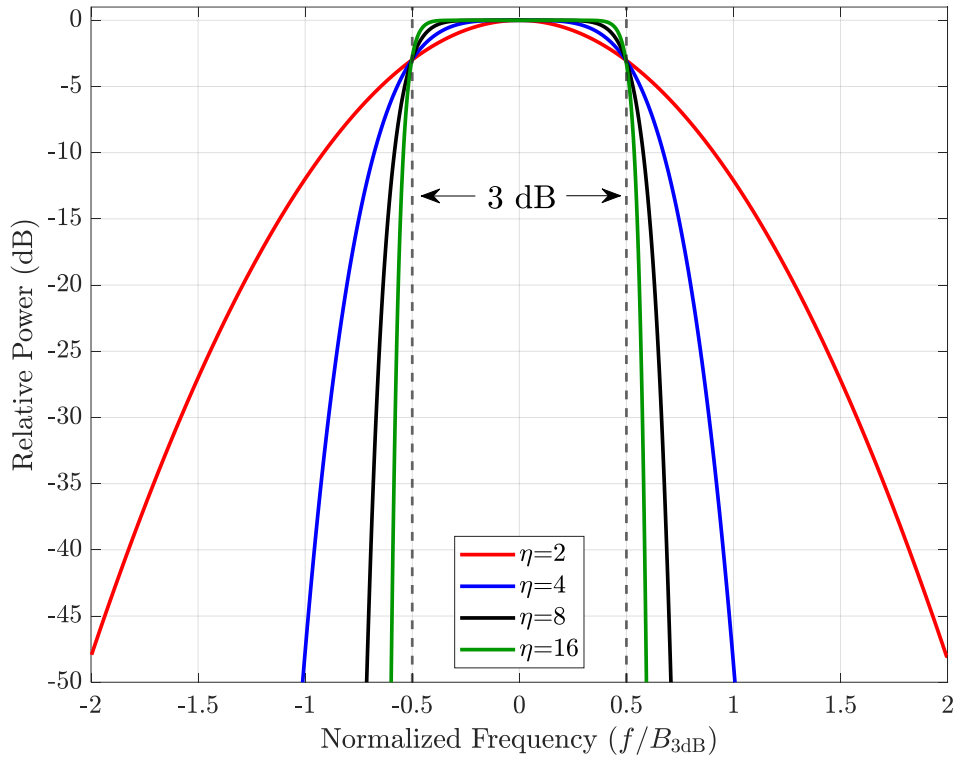
Figure 16: Frequency spectrum templates with orders of η = 2, 4, 8 and 16 utilized for optimization of PRO-FM waveforms

within the 3-dB bandwidth, with more deviation occurring as the spectrum rolls off. The RMS spectrum of the waveforms optimized with η = 2 roll-off to a value of about -25 dB relative to the peak where the other values of η flatten out at about -32 dB relative to the peak. Figure 18 shows a detail view of the 3-dB bandwidth of all RMS shown in Figure 17. All optimized waveform spectra have the same 3-dB bandwidth, with larger values of η associated with more of the power spectrum being contained within. It should be noted that the results in Figure 17 and Figure 18 for η = 2 agree with those first observed in [47].
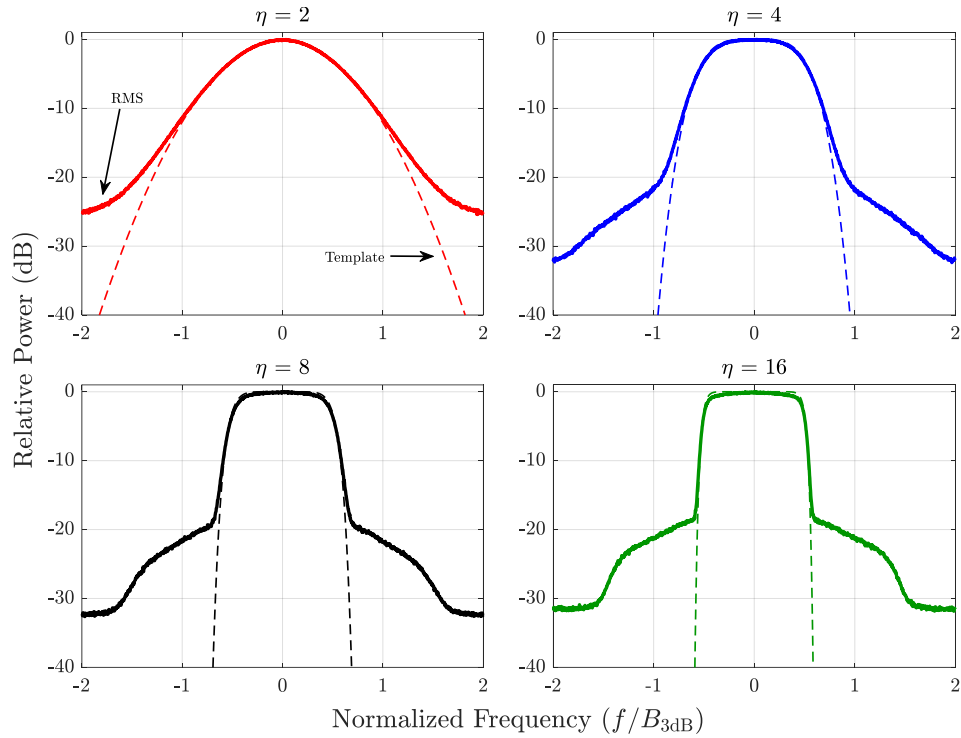
Figure 17: RMS power spectrum for $M = 1000$ optimized PRO-FM waveforms with $BT = 200$ and $\eta = 2$, 4, 8 and 16 with associated spectral templates
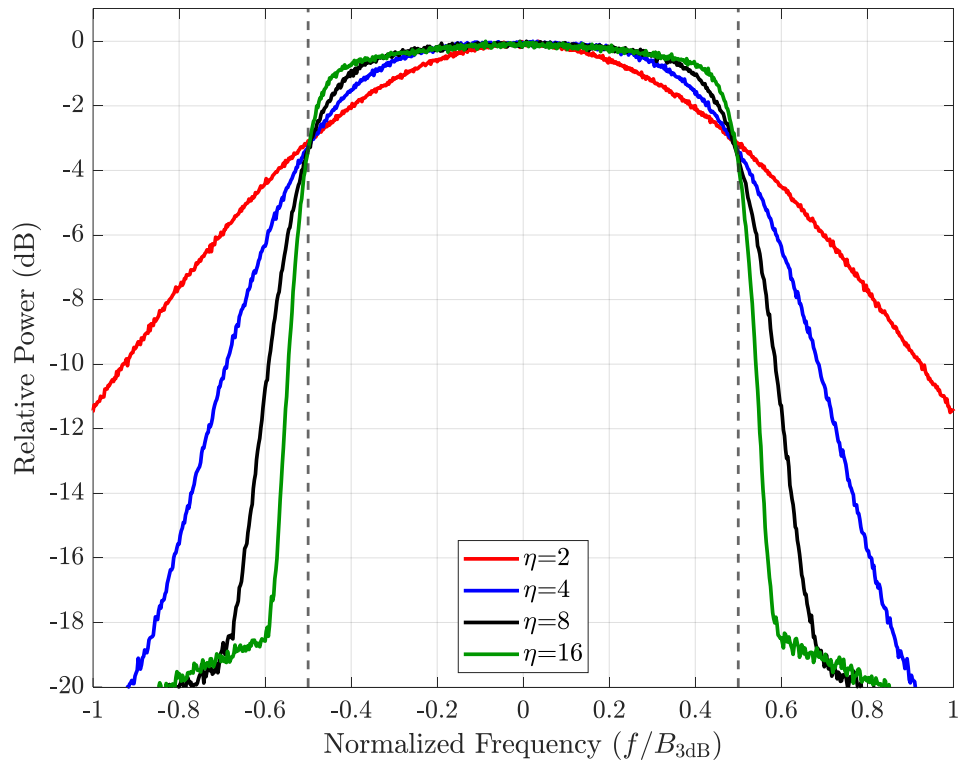
Figure 18: RMS power spectrum 3-dB detail for $M = 1000$ optimized PRO-FM waveforms with $BT = 200$ and $\eta = 2$, 4, 8 and 16

The autocorrelation responses of the optimized PRO-FM waveform sets are considered next. Figure 19 shows the RMS and mean autocorrelations responses for the optimized PRO-FM waveforms. While the RMS representation is a form of incoherent combination across the M optimized waveforms, the mean is a coherent combination across all M optimized waveforms (i.e., Doppler processing). Noted first is that the RMS autocorrelation responses exhibit peak levels of about -35.8 dB, -34.1 dB, -33.3 dB and -33.0 dB (relative to the mainlobe peak) for values of $\eta = 2, 4, 8$ and 16, respectively. This increasing peak sidelobe level illustrates the first tradeoff for improved spectral compactness. However, each autocorrelation achieves a peak sidelobe level between $-10 \log_{10}(200) \approx$ -23 dB and $-20 \log_{10}(200) \approx$ -46 dB as previously predicted. The mean autocorrelation for each waveform exhibits a coherent integration gain (due to incoherently combining sidelobes) on the order of $10 \log_{10}(1000) = 30$ dB, once again as expected. This reduction in autocorrelation sidelobes via coherent combination across the M pulses in the set of optimized waveforms highlights the true power and potential of PRO-FM waveforms.

Another notable feature in Figure 19 is the broadening of the autocorrelation mainlobe for increasing values of η. This is explored in more detail in Figure 20 where it is noticed that persistent sidelobes near-in to the mainlobe (often denoted as "shoulder lobes") begin to manifest for larger values of η. These shoulder lobes persist for each optimized waveform in the set and thus do not decohere when performing coherent processing. Furthermore, larger values of η translate to a higher number of persistent shoulder lobes. The level of these shoulder lobes will decrease before rolling off into the autocorrelation floor, but this roll-off is more gradual as the value of η becomes larger, as depicted in Figure 20. This presence of persistent shoulder lobes highlights the second tradeoff for improved spectral compactness.
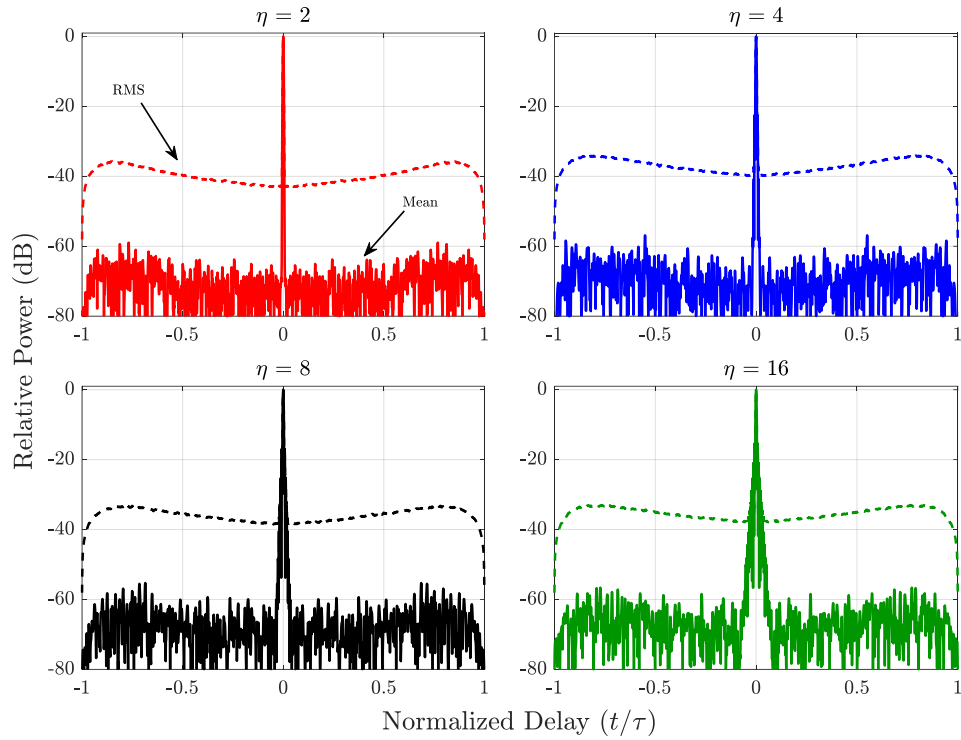
Figure 19: RMS and mean (coherent) autocorrelation for $M = 1000$ optimized PRO-FM waveforms with $BT = 200$ and $\eta = 2, 4, 8$ and 16
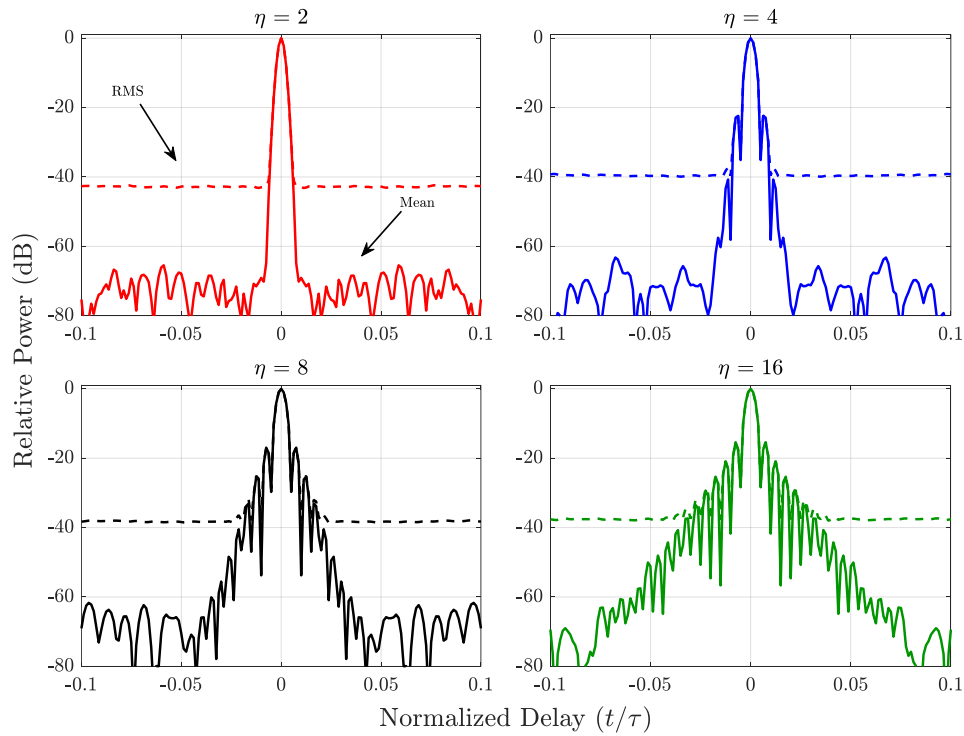
Figure 20: RMS and mean (coherent) autocorrelation mainlobe detail for $M = 1000$ optimized PRO-FM waveforms with $BT = 200$ and $\eta = 2, 4, 8$ and 16

Figure 21 shows a detail plot of the RMS autocorrelation mainlobe region for each case shown in Figure 19 and Figure 20, with the goal of comparing the resolution of each case provided by the autocorrelation mainlobe width. It is apparent that all cases retain almost identical mainlobe widths, with $\eta = 2$ having an essentially negligible narrower width.
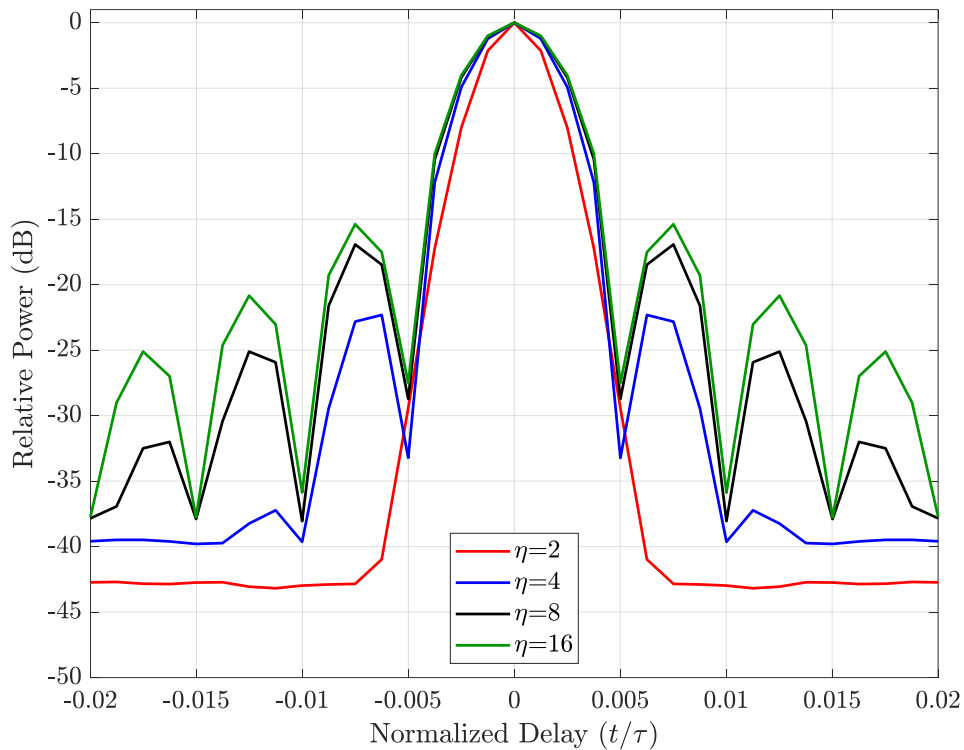
Figure 21: RMS autocorrelation mainlobe detail for $M = 1000$ optimized PRO-FM waveforms with $BT = 200$ and η = 2, 4, 8 and 16

As means to assess the joint range-Doppler performance of the optimized PRO-FM waveforms, a PSF is formed for each of the four optimized waveform sets as was shown for the LFM in Figure 7. As was the case for the LFM, a Doppler oversampling factor of $K_D = 10$ is used when performing Doppler processing across the set of $M = 1000$ optimized pulses. A Doppler window was not used to generate each PSF as the core behavior can be obscured with the application of a Doppler taper to the PSF. Figure 22 shows the PSF generated for each waveform set. When comparing to the LFM PSF in Figure 7, the first noticeable differences is the higher

background floor, which increases in value as η becomes larger. This is the RSM previously described caused by the incoherent combination of the sidelobes when performing Doppler processing. The next notable feature is the lack of range/time sidelobes for the PSF plot of each PRO-FM waveform when compared to the LFM. This is expected from the results obtained in Figure 19, where in fact the zero-Doppler cut across time for each of the PSFs in Figure 22 is equivalent to its counterpart mean autocorrelation depicted in Figure 19. A closer look at the delay/Doppler mainlobe region of each PSF is provided in Figure 23. The shoulder lobes present in Figure 19 are once again present here, where it is noticed that each shoulder lobe is associated with a smearing of energy across Doppler, which becomes more severe for larger values of η. This is another form of RSM and can become quite severe as will be shown in more detail later in this chapter. It is clear how this smearing of energy could obscure scatterers of interest when relatively high RCS clutter and scatterers are present in an illuminated scene of interest, highlighting yet another tradeoff for improved spectral compactness in PRO-FM waveforms.

A useful metric for comparing the background floor of various waveform PSFs was introduced in [79] and is once again utilized here. The PSF metric is defined as

$$\delta = \frac{1}{n(L)n(\Omega_D)} \sum_{\ell \in L} \sum_{\omega_D \in \Omega_D} \rho(\ell, \omega_D)$$

for $\ell \neq 0 \pm \Delta\ell, \quad \omega_D \neq 0 \pm \Delta\omega_D$

$$(3.5)$$

The PSF is represented by $\rho(\ell, \omega_D)$ where the delay and Doppler mainlobe widths are represented by $\Delta\ell$ and $\Delta\omega_D$, respectively. The quantities L and Ω_D represent the extent of the PSF in normalized delay and Doppler, respectively. The normalization terms $n(L)$ and $n(\Omega_D)$ represent the cardinality (or total number of values present) of the sets of delay and Doppler values being summed across. This metric basically determines the mean power value of the PSF outside of the

delay and Doppler mainlobe regions (essentially ignoring their values), which are excluded since they represent the standard delay and Doppler sidelobe response while the focus is on the RSM which occurs in the remainder of the PSF. The metric defined in (3.5) is applied to all PSFs generated in this chapter and represented on a decibel scale, with a summary being provided in Table 2. As a point of reference, the value of δ for the LFM PSF shown in Figure 7 is -97.2 dB. The PSFs shown in Figure 22 for values of $\eta = 2$, 4, 8 and 16 have δ values of -70.5 dB, -67.9 dB, -66.9 dB, and -66.5 dB respectively, once again showing that the background floor increases due to worsening RSM as the value of η increases.
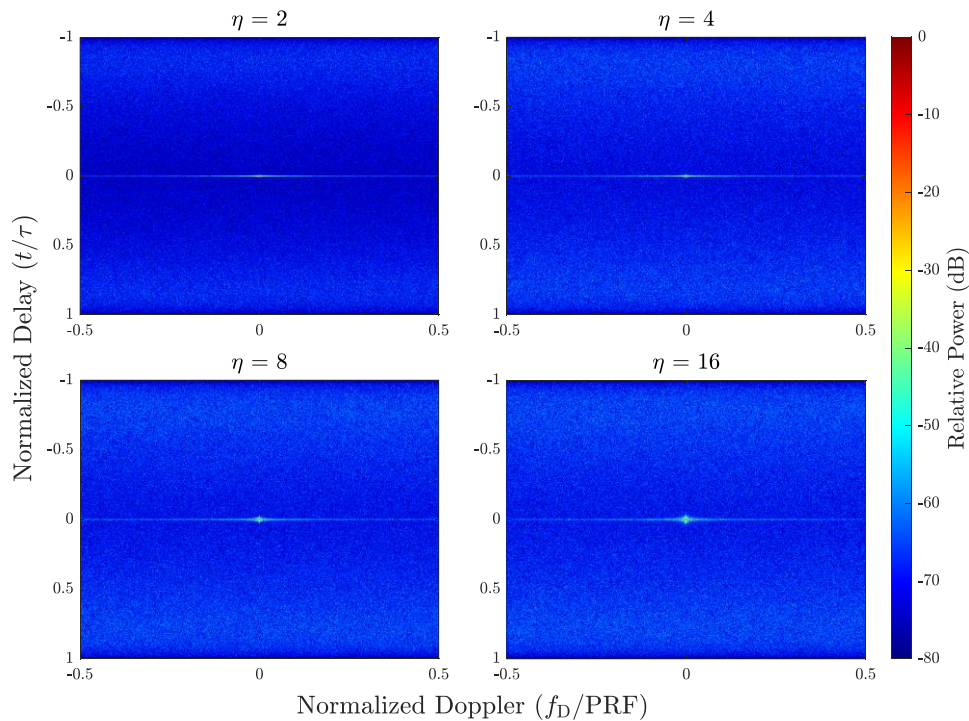
Figure 22: PSF for $M = 1000$ optimized PRO-FM waveforms with $BT = 200$ and $\eta = 2$, 4, 8 and 16 (no Doppler windowing)
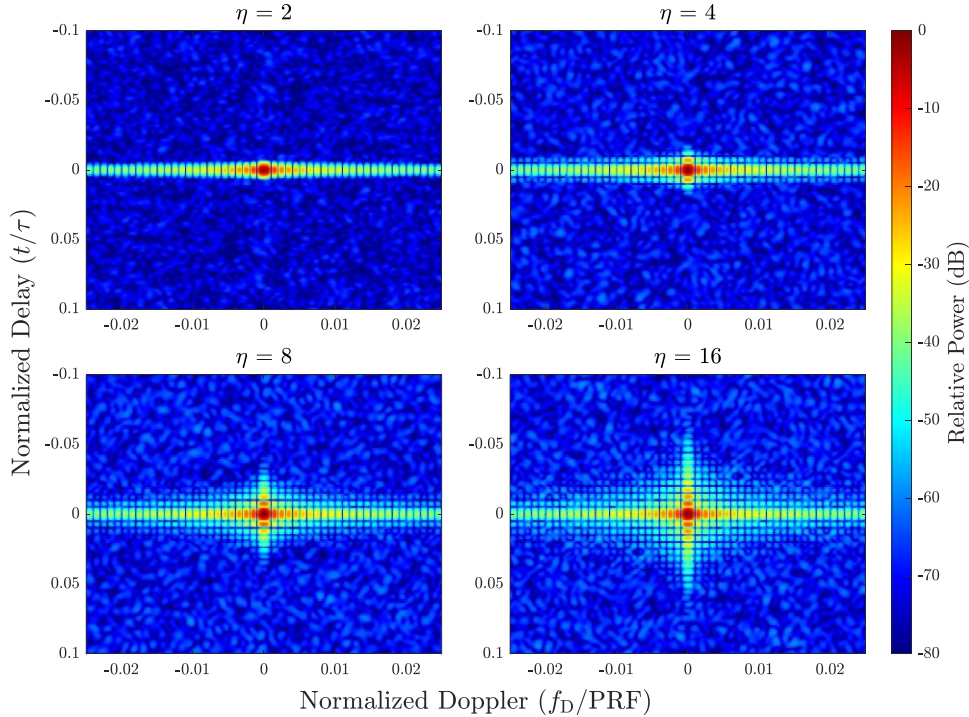
Figure 23: PSF mainlobe detail for $M = 1000$ optimized PRO-FM waveforms with $BT = 200$ and $\eta = 2$, 4, 8 and 16 (no Doppler windowing)

3.3 Stationary Spectral Notches in PRO-FM Waveforms

Mitigation of narrowband interference present in the radar operating frequency spectrum was considered by expanding the optimization framework of PRO-FM in [16, 17] to include spectral notches, which are essentially regions of the frequency spectrum where little power as possible is present. Remaining coherent across the frequency spectrum requires some small amount of power to be present in the notch region in order to maintain a single transmit waveform with a consistent transmit center frequency. The PRO-FM optimization procedure of (3.1) and (3.2) is easily modified to include spectral notches via modification of the desired spectrum template as

$$|G(f)| = 0 \text{ for } f \in \Omega, \tag{3.6}$$

which is a null constraint for Ω the desired frequencies in which the spectral notch is to be placed. This constraint can contain one or more sets of contiguous frequencies to create multiple spectral

notches. One of the main tradeoffs of incorporating a rectangular spectral notch as dictated by (3.6) is the creation of a $\sin(x)/x$ roll-off in the autocorrelation sidelobe response.

An effective means to deal with this tradeoff is the inclusion of a tapering region around each notch. Tapering in the spectral notch region can be incorporated via

$$|G(f)| = \begin{cases} h_{\mathrm{L}}(f) & \text{for} \quad f \in \Omega_{\mathrm{L}} \\ 0 & \text{for} \quad f \in \Omega \\ h_{\mathrm{U}}(f) & \text{for} \quad f \in \Omega_{\mathrm{U}} \end{cases}, \tag{3.7}$$

for the lower, Ω_{L}, and upper, Ω_{U}, frequency regions around the spectral notch and the taper applied to the lower, $h_{\mathrm{L}}(f)$, and upper, $h_{\mathrm{U}}(f)$, frequency regions, respectively. Smoothing the transition between each spectral notch and its surrounding spectral content helps to mitigate degradation to the autocorrelation sidelobe response of the optimized waveform. While any continuous function for $h_{\mathrm{L}}(f)$ and $h_{\mathrm{U}}(f)$ can be chosen, the use of a Tukey function has been shown to work well [16]. Figure 24 shows the inclusion of a single spectral notch into the templates of Figure 16, centered at normalized frequency $3B/8$ with a width of $B/10$ and a Tukey taper region of width $B/16$ on either side of the notch. Figure 25 shows a detail view of the 3-dB bandwidth of the spectrally notched templates. The depth of the notch in each spectral template is set to 60 dB below the peak of the waveform spectrum.
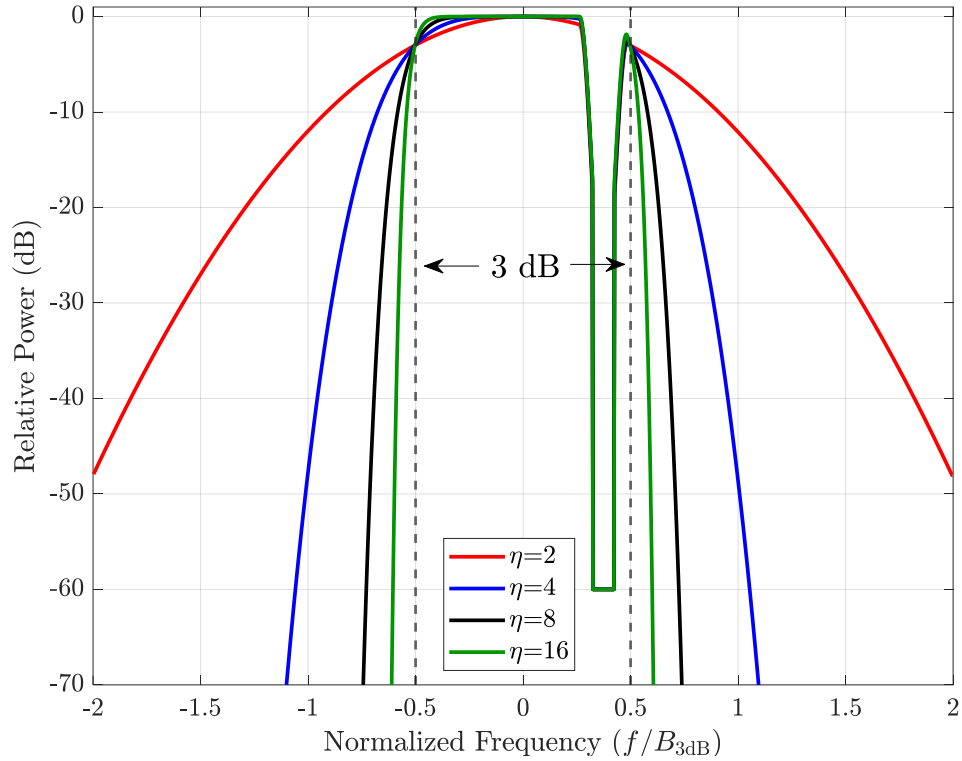
Figure 24: Frequency spectrum templates with orders of η = 2, 4, 8 and 16 with a spectral notch centered at $3B/8$ with width $B/10$ and taper of size $B/16$ utilized for optimization of Notched PRO-FM waveforms
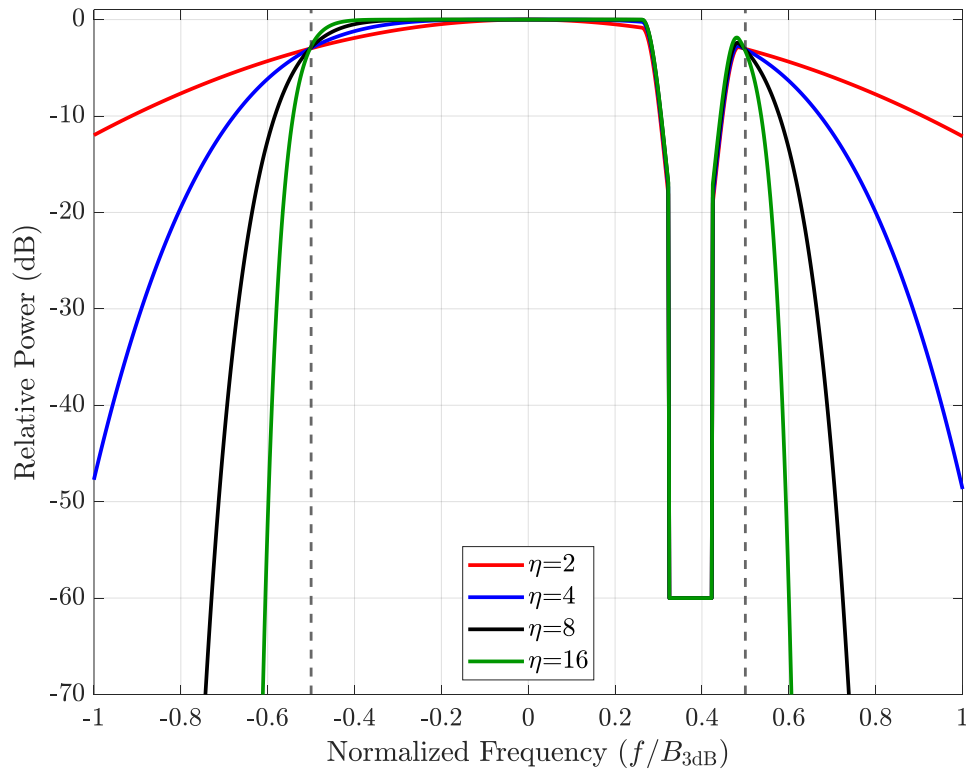
Figure 25: Frequency spectrum templates (3-dB bandwidth detail) with orders of η = 2, 4, 8 and 16 with a spectral notch centered at $3B/8$ with width $B/10$ and taper of size $B/16$ utilized for optimization of Notched PRO-FM waveforms

Incorporating spectral notches via (3.6), with or without the inclusion of tapers as in (3.7), has been shown to create spectral notches which are about 20 dB deep when compared to the surrounding spectrum power of the waveform around the notch. This may suffice for some applications, but the spectral notches can be made deeper via a technique denoted as reiterative uniform weighting optimization (RUWO) [80], which is applied after the completion of the two alternating projections steps in (3.1) and (3.2). Denote the mth optimized waveform after L iterations of (3.1) and (3.2) as $\mathbf{s}_{L,m}$ and set this equal to $\mathbf{x}_{0,m}$. The spectral notch in $\mathbf{s}_{L,m}$ is then deepened via P iterations of

$$\mathbf{x}_{p,m} = \exp\left(j\angle\left(\mathbf{W}^{-1}\mathbf{x}_{p-1,m}\right)\right), \tag{3.8}$$

where $\mathbf{W}$ is an $N \times N$ structured covariance matrix. Formation of $\mathbf{W}$ is achieved via

$$\mathbf{W} = \mathbf{B}\mathbf{B}^{H} + \delta\mathbf{I}, \tag{3.9}$$

for the $N \times N$ identity matrix $\mathbf{I}$ and diagonal loading factor δ used to avoid an ill-conditioned matrix inverse, and $N \times Q$ matrix of discretized steering vectors $\mathbf{B}$

$$\mathbf{B} = \begin{bmatrix} 1 & 1 & \cdots & 1 \\ e^{j2\pi f_0} & e^{j2\pi f_1} & \cdots & e^{j2\pi f_{Q-1}} \\ \vdots & \vdots & \ddots & \vdots \\ e^{j2\pi f_0(N-1)} & e^{j2\pi f_1(N-1)} & \cdots & e^{j2\pi f_{Q-1}(N-1)} \end{bmatrix}, \tag{3.10}$$

where the spectral notch regions Ω of (3.7), non-inclusive of Ω_L and Ω_U, are discretized into Q frequency values denoted f_q.

Assessing the impact of incorporating a spectral notch into optimized PRO-FM waveforms begins with optimizing $M = 1000$ waveforms with time-bandwidth product $BT = 200$, oversampling factor $K = 4$ (so $N = 800$ discrete points in each waveform) for $L = 100$ iterations of (3.1) and (3.2). A single spectral notch is inserted into the frequency spectrum template $|G(f)|$ as shown in Figure 24, where each template is considered to generate notched PRO-FM waveforms.

After completing $L = 100$ iterations of (3.1) and (3.2), RUWO is performed via (3.8) for $P = 100$ iterations to deepen the spectral notch in each optimized waveform.
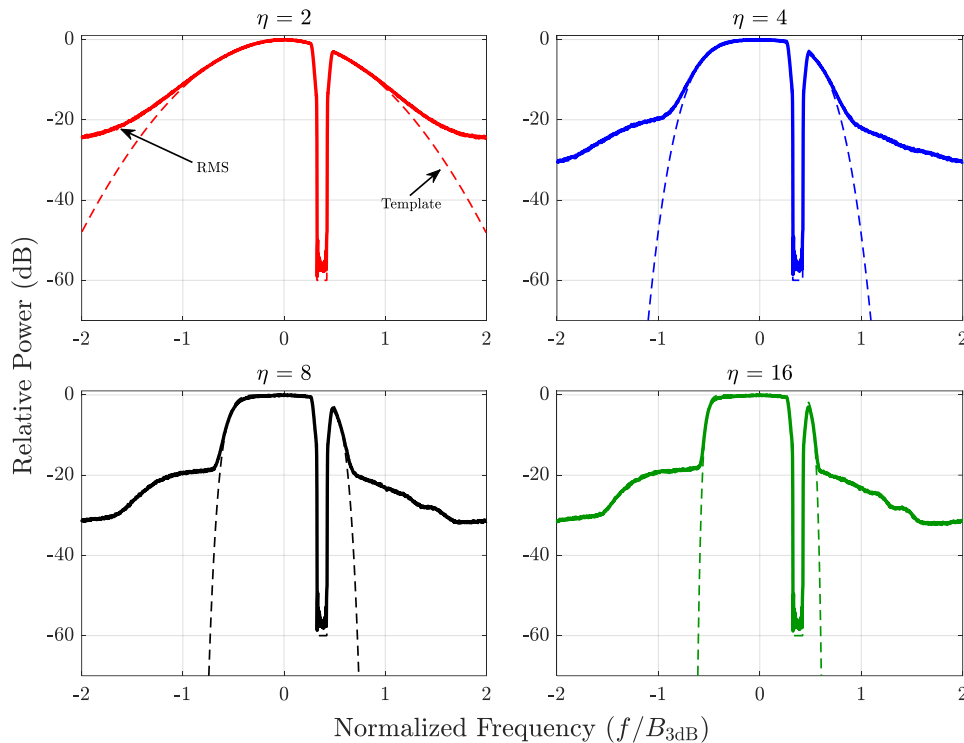
Figure 26: RMS power spectrum for $M = 1000$ optimized PRO-FM waveforms with $BT = 200$ having a single spectral notch deepened with RUWO and $\eta = 2, 4, 8$ and 16 with associated spectral templates

Figure 26 shows the RMS power spectrum of each optimized notched PRO-FM waveform along with the associated spectrum template used to optimize them. It is noticed that the application of RUWO results in spectral notches that are about 57 dB deep when compared to the spectrum peak, regardless of the value of η. This is almost as deep as the designed -60 dB for the spectral template notch. When comparing the RMS power spectra in Figure 26 to those of the notch-free case in Figure 17, a degradation to the spectral roll-off is noticed with the inclusion of a spectral notch. For $\eta = 2$, the RMS spectrum roll-off level is about 0.5 dB higher with the inclusion of a spectral notch, while the spectral roll-off level is about 1.8 dB, 1.6 dB and 0.3 dB higher for values of $\eta = 4, 8$ and 16, respectively. The inconsistency in increase of spectral-off for increasing η can be explained by the asymmetric roll-off observed for frequencies closer to the spectral notch, as the

spectral roll-off is hindered more for normalized frequencies greater than zero than those less than zero, which makes sense when considering the location of the spectral notch. With a non-symmetric distribution of spectral power, it is harder to make a direct comparison of spectral roll-between waveforms with and without notches. It is intuitive that the spectral roll-off is adversely impacted as removal of the energy in the spectral notch region of the FM waveform dictates that it must be placed somewhere else in the spectrum.

Figure 27 shows the optimized RMS spectra from Figure 26 plotted together for a direct comparison. All four waveform spectra hold their adherence to the spectrum template within the 3-dB bandwidth, even with the inclusion of a spectral notch. For larger values of η, the asymmetry noticed in the waveform spectrum roll-off is exacerbated. Figure 28 shows a detail view of Figure 27 in the 3-dB bandwidth region. Smooth transitions around the spectral notch region are maintained, even for large values of η, due to the inclusion of the Tukey spectral taper into the spectral template.
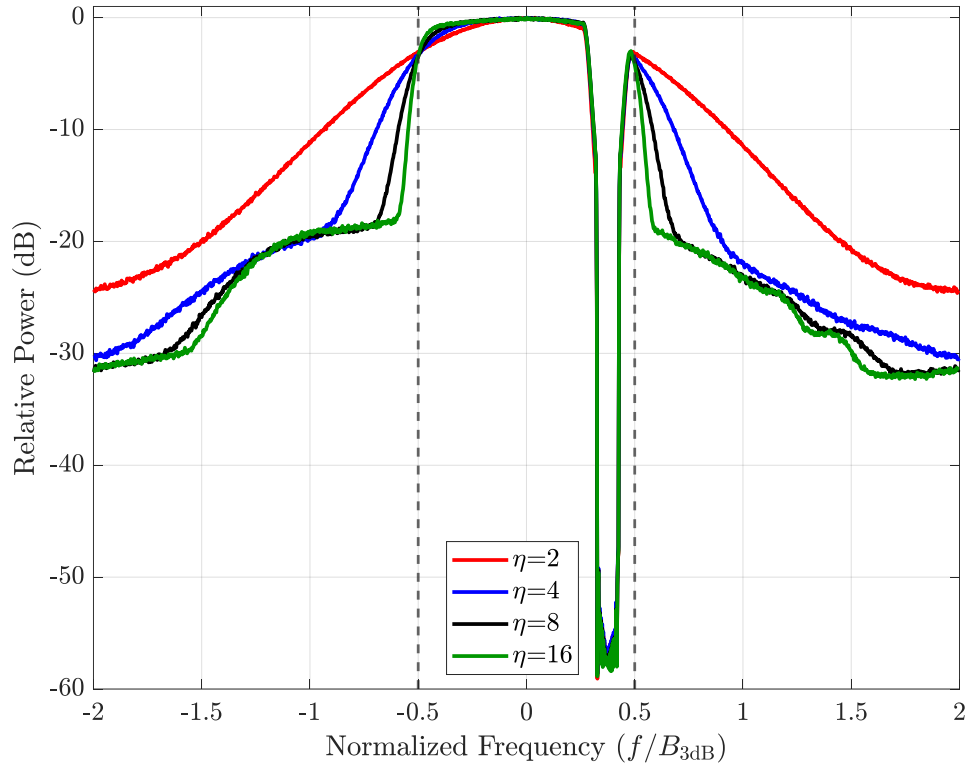
Figure 27: RMS power spectrum comparison for $M = 1000$ optimized PRO-FM waveforms with $BT = 200$ having a single spectral notch deepened with RUWO and $\eta = 2$, 4, 8 and 16
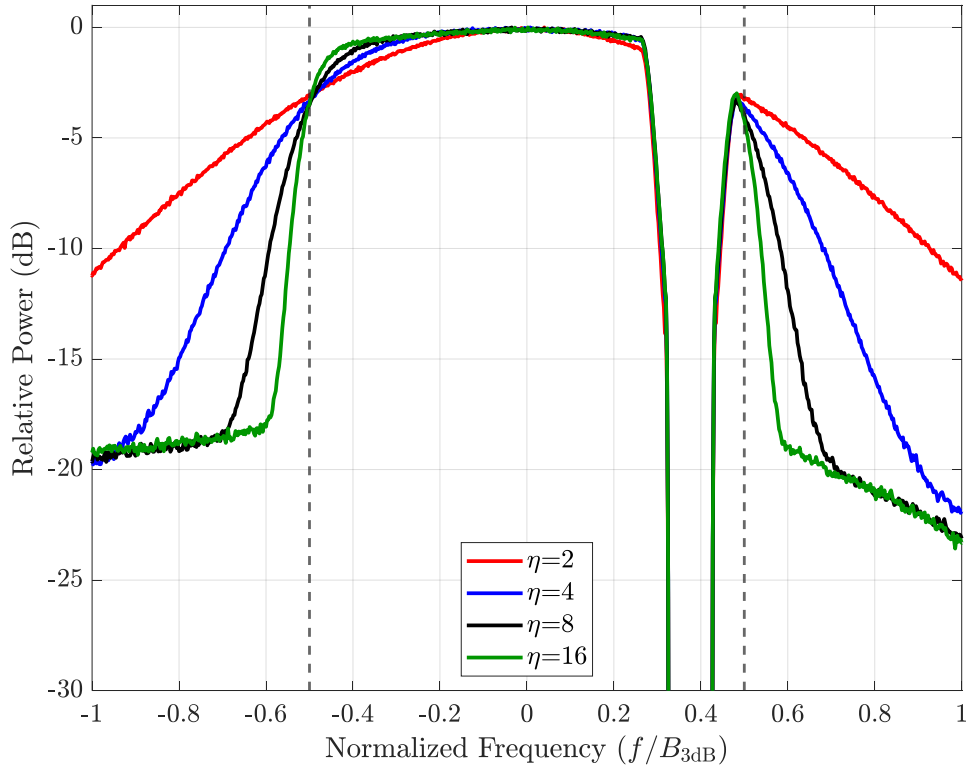
Figure 28: RMS power spectrum comparison detail view for $M = 1000$ optimized PRO-FM waveforms with $BT = 200$ having a single spectral notch deepened with RUWO and $\eta = 2$, 4, 8 and 16

The mean and RMS autocorrelation of the optimized, spectrally notched PRO-FM waveforms are considered in Figure 29. The peak sidelobe level of the RMS autocorrelation of each spectrally notched waveform is on par with its notch-free counterpart, with increases in peak sidelobe level of about 0.8 dB for the spectrally notched waveforms for all cases of η. The coherent mean autocorrelation for each spectrally notched waveform also compares well to its notch-free counterpart, with the spectrally notched waveforms exhibiting an increase in the peak of the mean sidelobe level of about 1 dB for all cases of η. The most obvious difference between the spectrally notched and notch-free waveform autocorrelations is the exacerbation of the shoulder lobes. For the notch-free waveform with $\eta = 2$, no shoulder lobes were present, where they are now observed for the spectrally notched counterpart. In fact, the inclusion of the spectral notch heightens the severity of autocorrelation shoulder lobes for each case of η.

Figure 30 shows a mainlobe detail view of the mean and RMS autocorrelations shown in Figure 29. When comparing the notch-free waveforms to the notched waveforms, a disruption of the roll-off structure of the shoulder lobes can be noticed for notched waveforms. Inclusion of a spectral notch causes the autocorrelation shoulder lobes to be more irregularly spaced and wider than their notch-free counterparts. Regardless of this irregularity, the spectrally notched shoulder lobes are more severe and their impact on RSM will be assessed via their PSFs. Figure 31 shows a mainlobe detail view of the RMS autocorrelation of the spectrally notched waveforms. For η values of 4, 8 and 16, the mainlobes are nearly identical while for $\eta = 2$ the mainlobe appears slightly narrower, as it did for the notch free case of Figure 21.
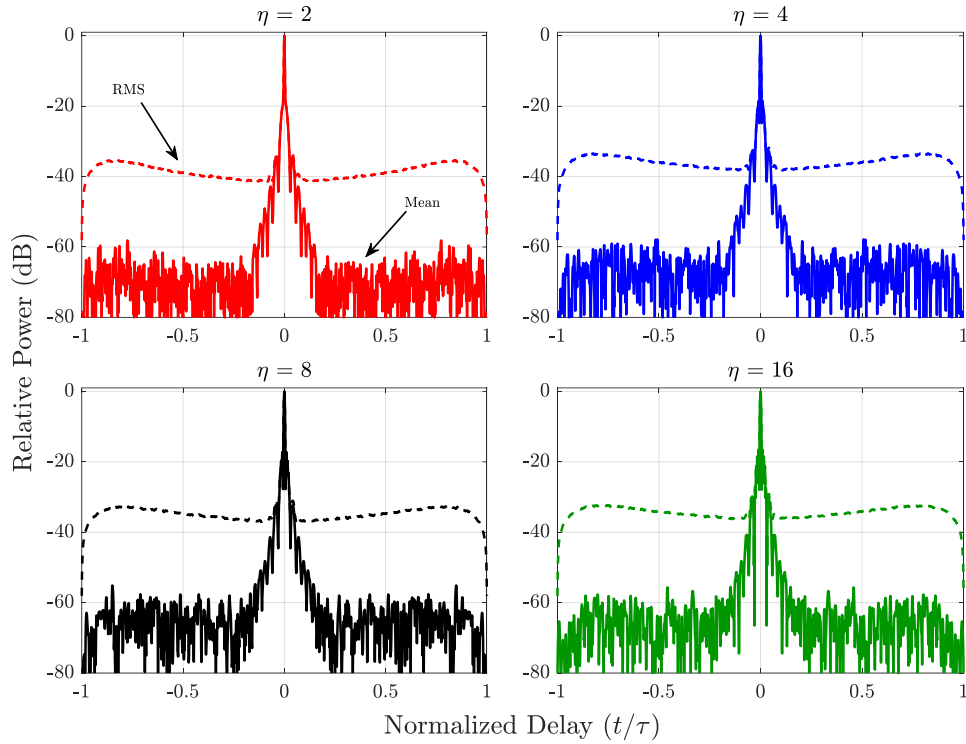
Figure 29: RMS and mean (coherent) autocorrelation for $M = 1000$ optimized PRO-FM waveforms with $BT = 200$ having a single spectral notch deepened with RUWO and $\eta = 2, 4, 8$ and 16
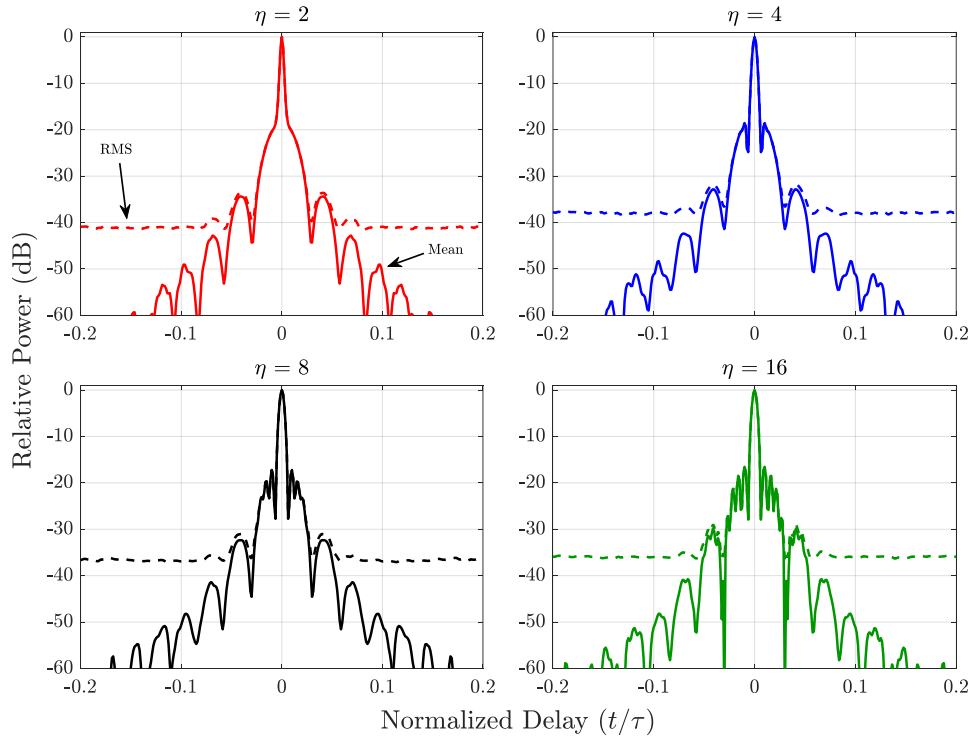
Figure 30: RMS and mean (coherent) autocorrelation mainlobe detail view for $M = 1000$ optimized PRO-FM waveforms with $BT = 200$ having a single spectral notch deepened with RUWO and $\eta = 2, 4, 8$ and 16
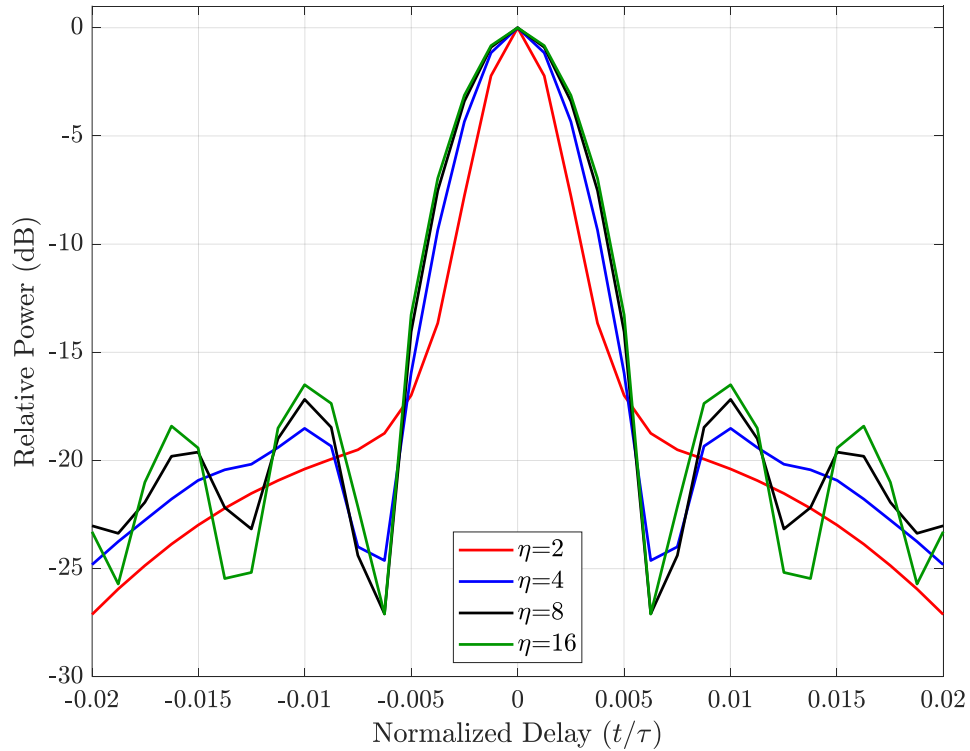
Figure 31: RMS autocorrelation mainlobe detail view for $M = 1000$ optimized PRO-FM waveforms with $BT = 200$ having a single spectral notch deepened with RUWO and $\eta = 2$, 4, 8 and 16

A point spread function is generated for each optimized, spectrally notched PRO-FM waveform case in same manner as the notch free case. Each point spread function is shown in Figure 32 with a mainlobe detail view shown in Figure 33. Comparing the notch free waveforms in Figure 22, a significant increase in the background floor, and thus degree of RSM, is noticed. In fact, the PSFs shown in Figure 32 for values of $\eta = 2$, 4, 8 and 16 have δ values of -69.7 dB, -67.1 dB, -66.0 dB, and -65.5 dB respectively, once again showing that the background floor increases due to worsening RSM as the value of η increases. These values of δ signify increases over their notch-free counterparts of 0.8 dB, 0.8 dB, 0.9 dB and 1.0 dB, demonstrating consistent degradation with the inclusion of a spectral notch across all cases of η.
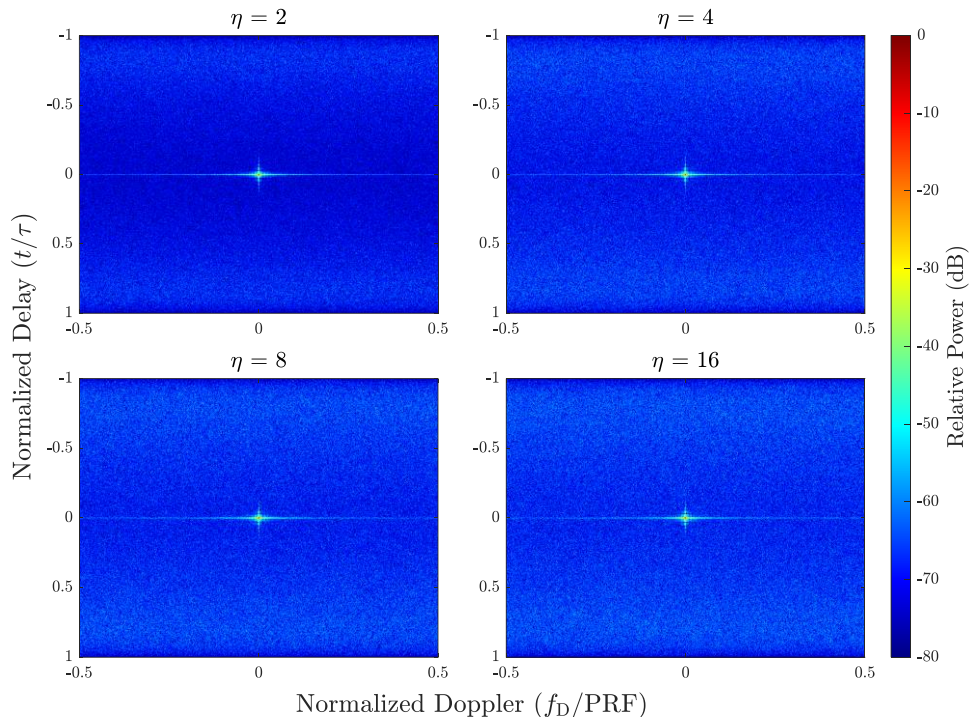
Figure 32: PSF for $M = 1000$ optimized PRO-FM waveforms with $BT = 200$ having a single spectral notch and $\eta = 2, 4, 8$ and 16 (no Doppler windowing)
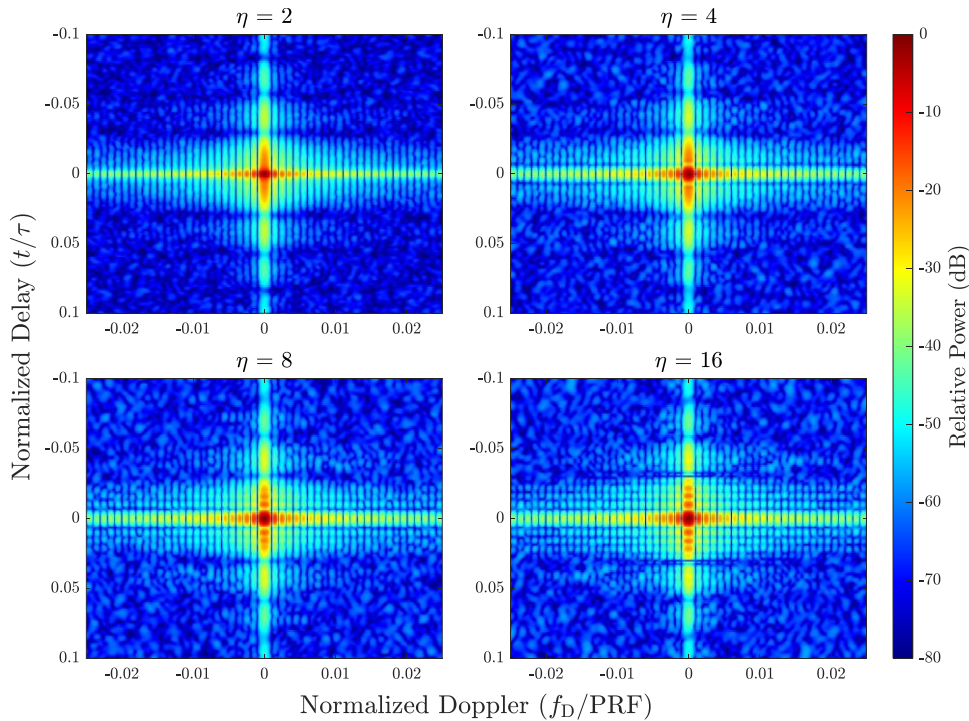
Figure 33: PSF mainlobe detail view for $M = 1000$ optimized PRO-FM waveforms with $BT = 200$ having a single spectral notch and $\eta = 2, 4, 8$ and 16 (no Doppler windowing)

3.4 Hopping Spectral Notches in PRO-FM Waveforms

Spectral notches (and their associated tapers) placed into the PRO-FM optimization framework via (3.7) do not have to remain static on a pulse-wise basis. The spectral location, width and taper can be modified on a per-pulse basis, requiring modification of the spectral template definition in (3.7) for each successive change, along with reformation of the structured covariance matrix in RUWO via (3.9) and (3.10) for changes in the Q discretized frequency values f_q. Adjusting the location of the spectral notch can be useful when trying to avoid spectrally agile narrowband interference, such as spectrally hopping OFDM waveforms and other forms of frequency hopping communications [31].

In order to assess the impact of a hopping spectral notch on the RSM of the waveform CPI, three different hopping cases are considered in which the spectral notch changes its center frequency location every 100 pulses, every 10 pulses or every single pulse. This corresponds to 10, 100 and 1000 unique spectral notch center frequency locations, respectively, during the $M = 1000$ pulse CPI. The spectral notch hops randomly to a new location when it has persisted for the requisite number of pulses in each case and is not allowed to occupy a center frequency more than once, ensuring the notch covers all available locations within the 3-dB bandwidth during the CPI. The 3-dB bandwidth of the Gaussian spectral template is divided into the appropriate number of unique notch locations for each case, where the same four values of η = 2, 4, 8 and 16 are considered for each case. As with the stationary notch, the width of each notch is $B/10$ and a Tukey taper region of width $B/16$ is present on either side of the notch. Figure 34 shows the case where the spectral notch can occupy 10 different locations, persisting at each for 100 pulses before randomly hopping to a different, previously unoccupied notch center location. As with the other PRO-FM waveforms considered so far, each waveform has $BT = 200$, oversampling factor $K = 4$

and $L = 100$ iterations of the alternating projections in (3.1) and (3.2) are performed for each waveform with $P = 100$ iterations of RUWO in (3.8) being performed to deepen the spectral notch.
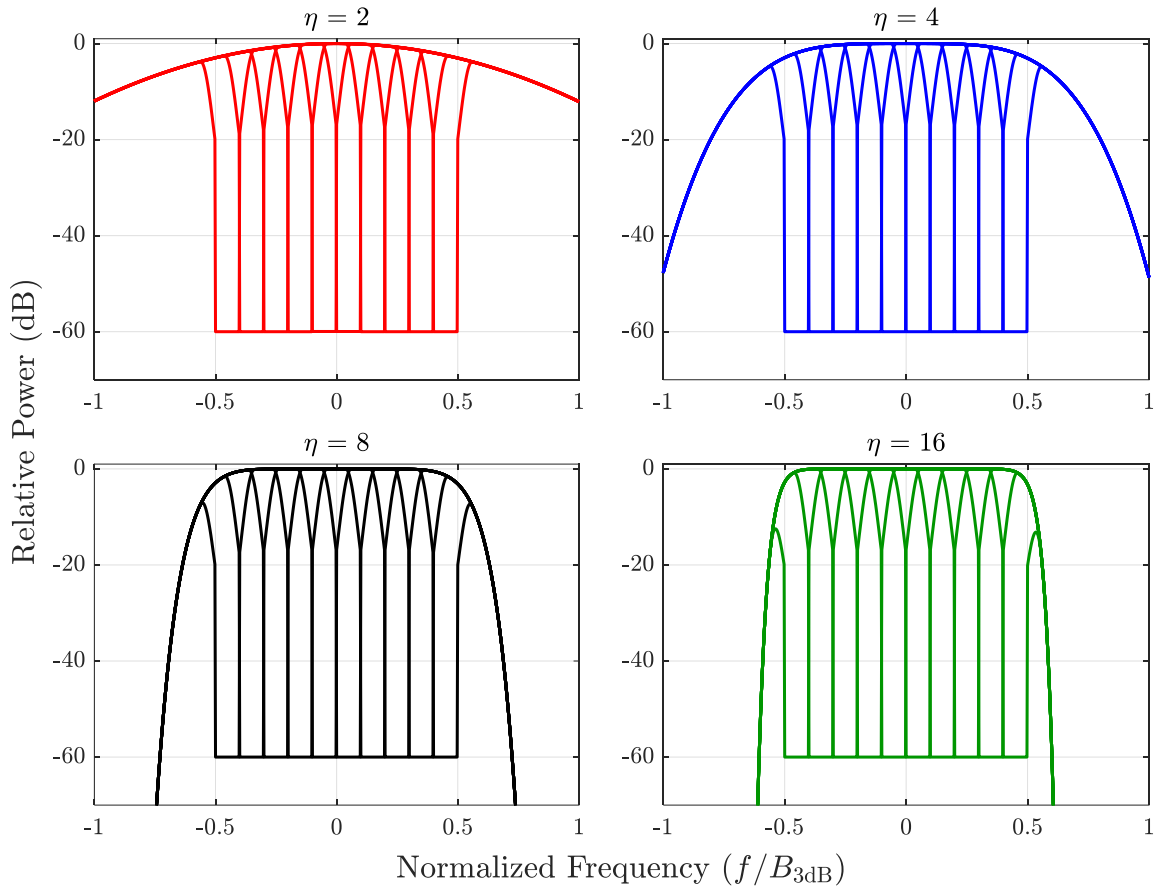
Figure 34: Frequency spectrum templates with orders of $\eta = 2$, 4, 8 and 16 with 10 possible spectral notch locations each having width $B/10$ and taper of size $B/16$ corresponding to a persistence of 100 pulses each in the $M = 1000$ pulse CPI

RMS spectrum plots across the $M = 1000$ pulses will not be shown for any case of the hopping spectral notch, as the random hopping will serve to essentially average out the spectral notch over the CPI. Mean and RMS autocorrelation plots will not be shown either, with the focus being placed directly on the PSF and the RSM caused by hopping the spectral notch during the CPI.

Figure 35 shows the PSF for the case of the spectral notch hopping every 100 pulses, or 10 times total, during the CPI. A similar degree of RSM is noticeable when comparing to the stationary notch case. The PSFs for this case have δ values of -69.4 dB, -66.8 dB, -65.8 dB, and -65.3 dB for $\eta = 2$, 4, 8 and 16, respectively, representing increases over their respective stationary

notch counterparts of 0.3 dB, 0.3 dB, 0.2 dB and 0.2 dB. Although the RSM level has not changed

significantly, observing the mainlobe detail of the PSF in Figure 36 shows that the range-Doppler

sidelobe structure has changed significantly for the spectrally hopped case. The concentration of

power has shifted from the delay and Doppler sidelobes to the region immediately surrounding the

mainlobe of the hypothetical point scatterer, where the concentration is slightly higher along the

Doppler dimension.
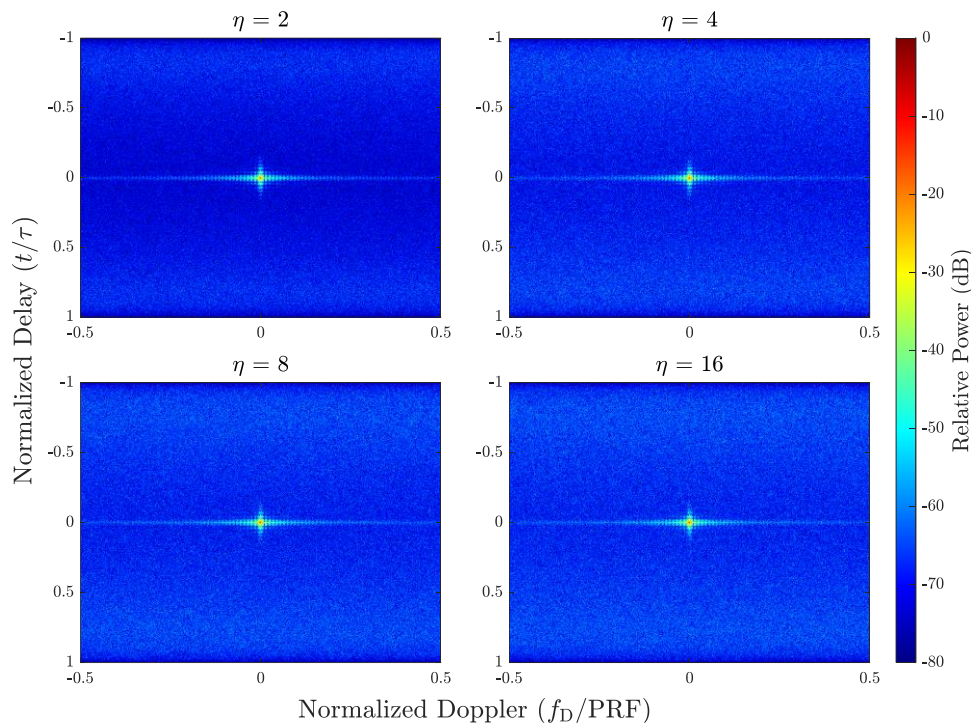
Figure 35: PSF for $M = 1000$ optimized PRO-FM waveforms with $BT = 200$ having a spectral notch hopping location every 100 pulses and $\eta = 2$, 4, 8 and 16 (no Doppler windowing)

Figure 37 shows the PSF for the case of the spectral notch hopping every 10 pulses, or 100 times

total, during the CPI. Further change in the structure of the RSM is noticed when increasing the

hopping frequency as the energy of the PSF has begun to spread out more in Doppler, forming a

band that persists for almost the entire extent of normalized Doppler frequencies. The PSFs for

this case have δ values of -68.9 dB, -66.3 dB, -65.4 dB, and -65.0 dB for $\eta = 2$, 4, 8 and 16,

respectively, representing increases over their respective 100 pulse hopped notch counterparts of

0.5 dB, 0.5 dB, 0.4 dB and 0.3 dB, representing another modest increase. The mainlobe detail of the PSF in Figure 38 confirms the further smearing of the power along the Doppler dimension, with the most severe being concentrated near the mainlobe before fizzling out towards the extreme ends of the Doppler spectrum, as visible in Figure 37. The impact of a spectrally hopped notch on the degree of RSM is starting to become clear, but now the frequency of spectral hopping is taken to the extreme.
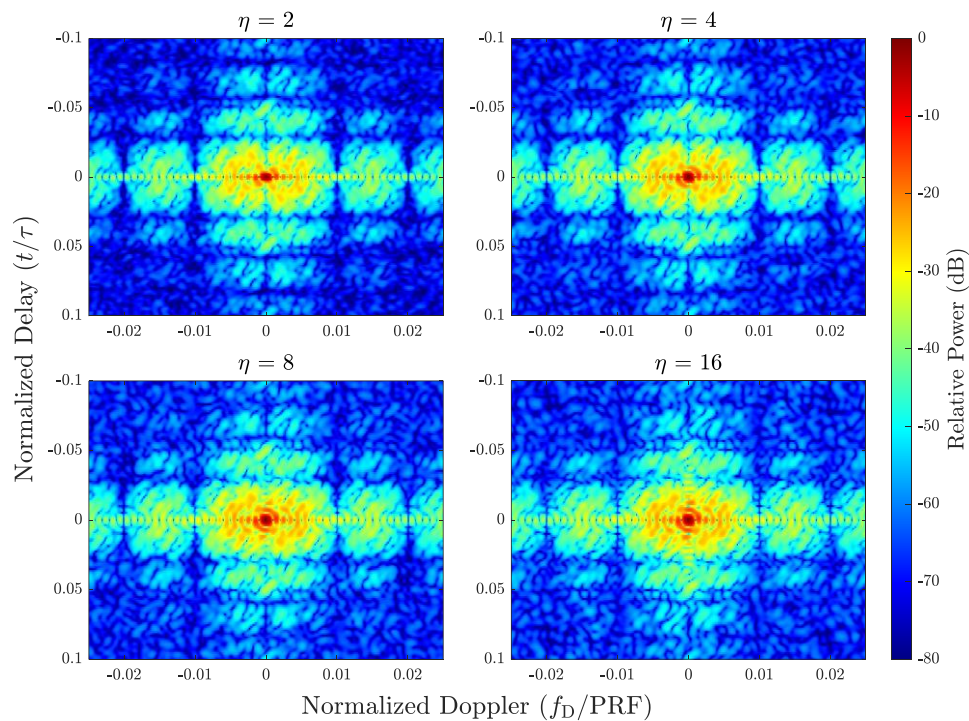
Figure 36: PSF mainlobe detail view for $M = 1000$ optimized PRO-FM waveforms with $BT = 200$ having a spectral notch hopping location every 100 pulses and $\eta = 2$, 4, 8 and 16 (no Doppler windowing)
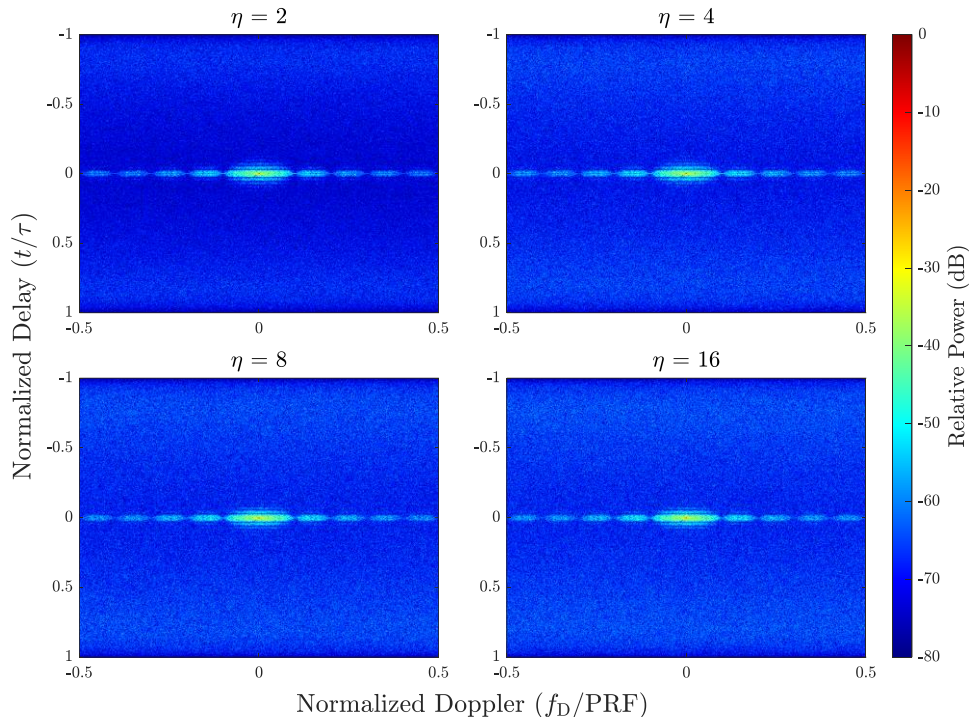
Figure 37: PSF for $M = 1000$ optimized PRO-FM waveforms with $BT = 200$ having a spectral notch hopping locations every 10 pulses and $\eta = 2$, 4, 8 and 16 (no Doppler windowing)
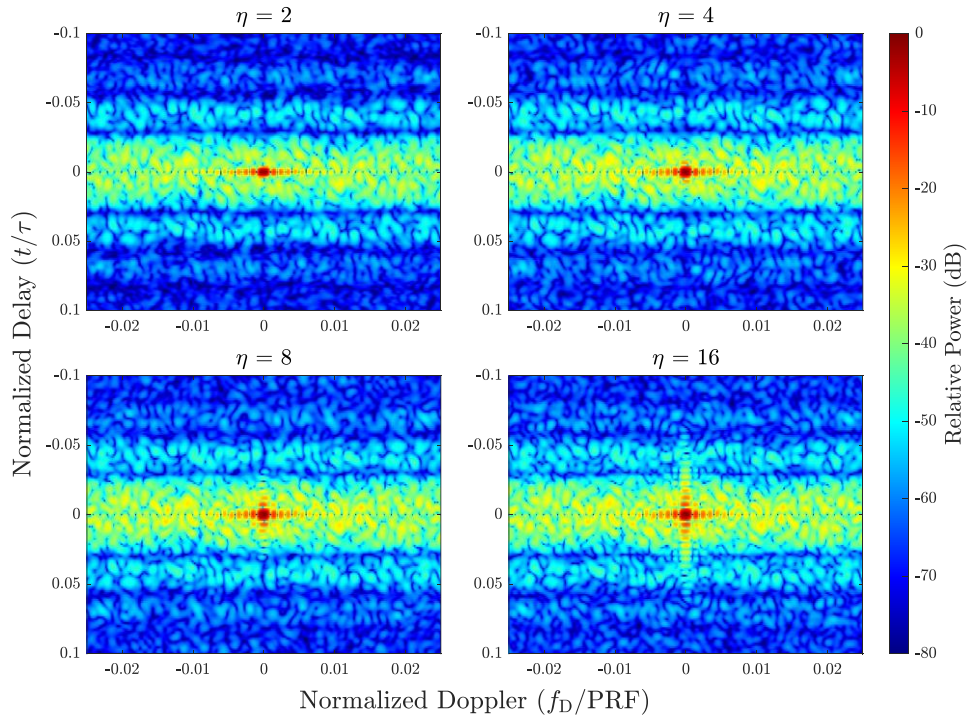
Figure 38: PSF mainlobe detail view for $M = 1000$ optimized PRO-FM waveforms with $BT = 200$ having a spectral notch hopping locations every 10 pulses and $\eta = 2$, 4, 8 and 16 (no Doppler windowing)

Figure 39 shows the PSF for the case of the spectral notch hopping every single pulse, or 1000 times total, during the CPI. The smearing of the energy across Doppler due to RSM is now about equal across the Doppler spectrum, forming a solid band. The PSFs for this case have δ values of -68.2 dB, -65.8 dB, -65.0 dB, and -64.5 dB for η = 2, 4, 8 and 16, respectively, representing increases over their respective 10 pulse hopped notch counterparts of 0.7 dB, 0.5 dB, 0.4 dB and 0.5 dB, representing another modest increase. The mainlobe detail of the PSF in Figure 40 shows the power of the Doppler band is almost constant even near-in to the mainlobe.

These results show that even more problematic than the slight increase in δ across the gamut of hopping spectral notch persistence (increases of 1.0 – 1.5 dB for all values of η when ranging from a stationary spectral notch to hopping locations every pulse) is the structure of the smearing due to RSM. As the hopping rate is increased, the RSM energy around the PSF mainlobe region is progressively smeared across Doppler in an essentially equal magnitude band. This increased degree of RSM due to a hopping spectral notch has been found to be caused by a modulation of the pulse compression mainlobe, in addition the changing sidelobe structure, from pulse to pulse when performing coherent integration across the CPI. However, the aggregate impact will still be referred to as RSM. This will cause issues when attempting to discern small RCS scatterers when adjacent in Doppler to large RCS scatterers such as clutter. The key takeaway from this section is that more change in the frequency spectrum on a pulse-to-pulse basis within the CPI results in a higher degree of RSM when applying standard matched filter pulse compression and Doppler processing with projection-based clutter cancellation.

Table 2: Summary of PSF RMS metric δ for each waveform case of Chapter 3

	$\eta = 2$	$\eta = 4$	$\eta = 8$	$\eta = 16$
PRO-FM	-70.5	-67.9	-66.9	-66.5
Notched PRO-FM	-69.7	-67.1	-66.0	-65.5
10 Hop Notched PRO-FM	-69.4	-66.8	-65.8	-65.3
100 Hop Notched PRO-FM	-68.9	-66.3	-65.4	-65.0
1000 Hop Notched PRO-FM	-68.2	-65.8	-65.0	-64.5
LFM	-97.2			
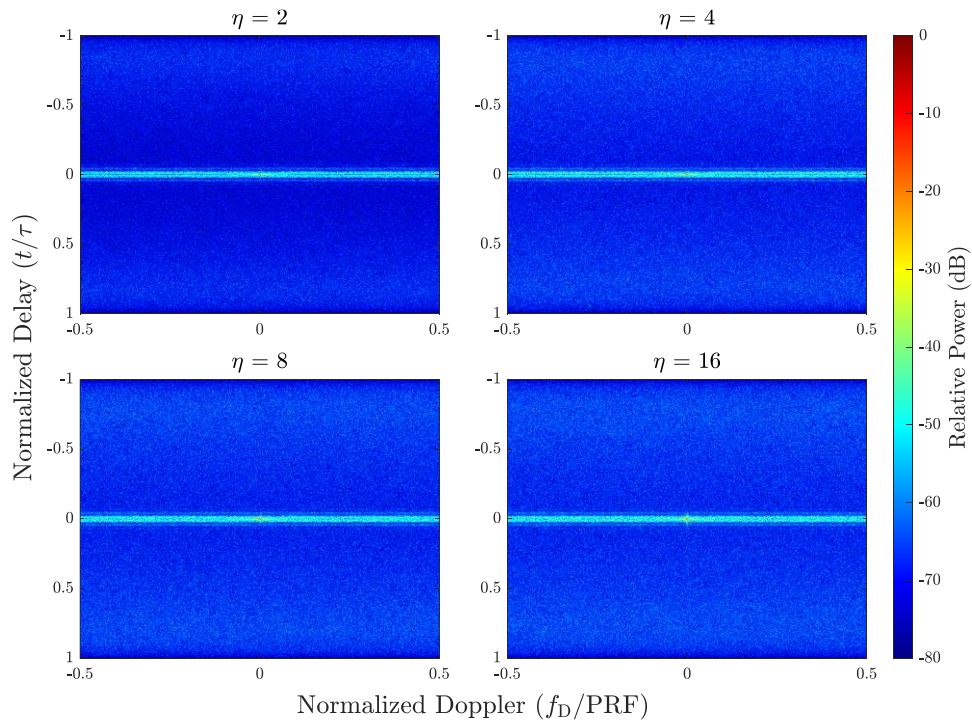
Figure 39: PSF for $M = 1000$ optimized PRO-FM waveforms with $BT = 200$ having a spectral notch hopping locations every single pulse and $\eta = 2, 4, 8$ and 16 (no Doppler windowing)
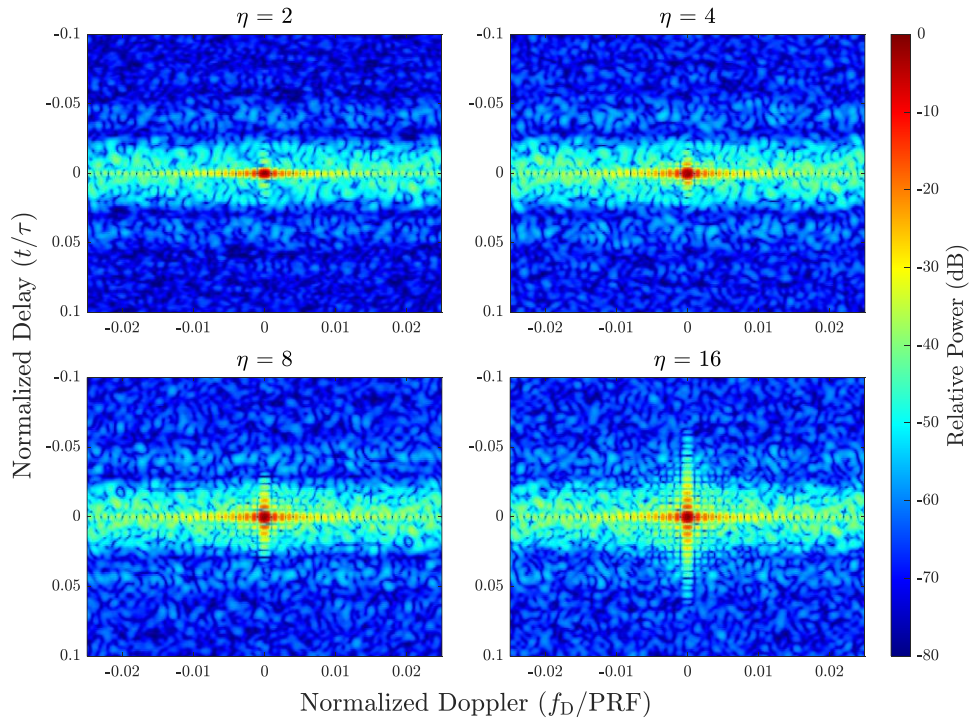
Figure 40: PSF mainlobe detail view for $M = 1000$ optimized PRO-FM waveforms with $BT = 200$ having a spectral notch hopping locations every single pulse and $\eta = 2, 4, 8$ and 16 (no Doppler windowing)

3.5 Spectral Notches in LFM Waveforms

For the sake of demonstrating a point, the result of placing a spectral notch in an LFM waveform is shown. This has been previously explored in [81, 82] using iterative algorithms and further explored using RUWO in [83], of which the results are shown here. Since the deepening of a spectral notch in an RFM waveform using RUWO maintains the constant amplitude nature of the waveform, it is logical to think that it can be applied to an LFM waveform to create a spectral notch. RUWO is performed for 100 iterations to insert a stationary spectral notch into an LFM waveform with $BT = 200$, centered at normalized frequency $3B/8$ with a width of $B/10$, as in the notched PRO-FM case.

Figure 41 shows the power spectrum of the RUWO notched LFM waveform and a standard LFM waveform. Note that every notched LFM waveform will have an identical spectrum as RUWO always begins with the same initialization, a standard LFM waveform. Therefore, the RMS

spectrum across a CPI of *M* pulses will be identical to that of a single pulse. Inclusion of the spectral notch causes severe distortion to the LFM spectrum, including spikes in the power level surrounding the notch and a significant increase in sidelobe roll-off. The autocorrelation of the notched LFM and standard LFM is shown in Figure 42. Inclusion of a spectral notch severely degrades the autocorrelation, increasing the sidelobe level across all delay with many large sidelobes near-in to the mainlobe. Furthermore, since each notched LFM is identical, these sidelobes will persist and not be averaged down by coherent integration. The results shown here, which generally agree with what was presented in [81, 82], highlight the problem with using an iterative algorithm such as RUWO to insert a spectral notch into a set of LFM waveforms with identical initializations.
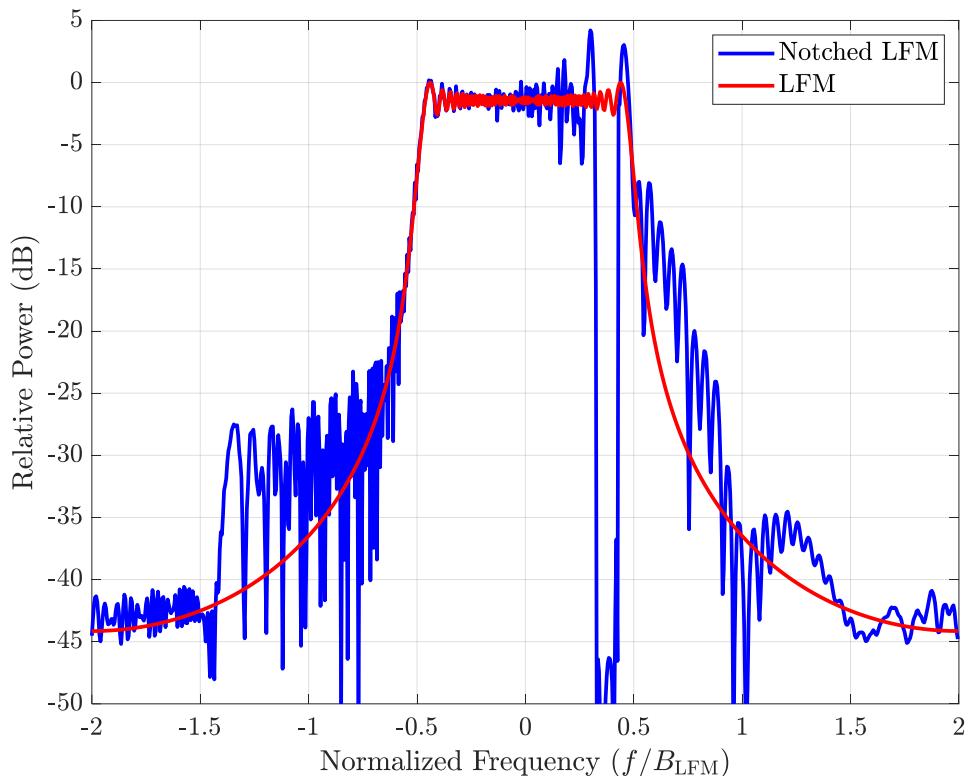
Figure 41: Power spectrum of LFM waveform with $BT = 200$ both with and without a spectral notch inserted at $3B/8$ of width $B/10$ using RUWO
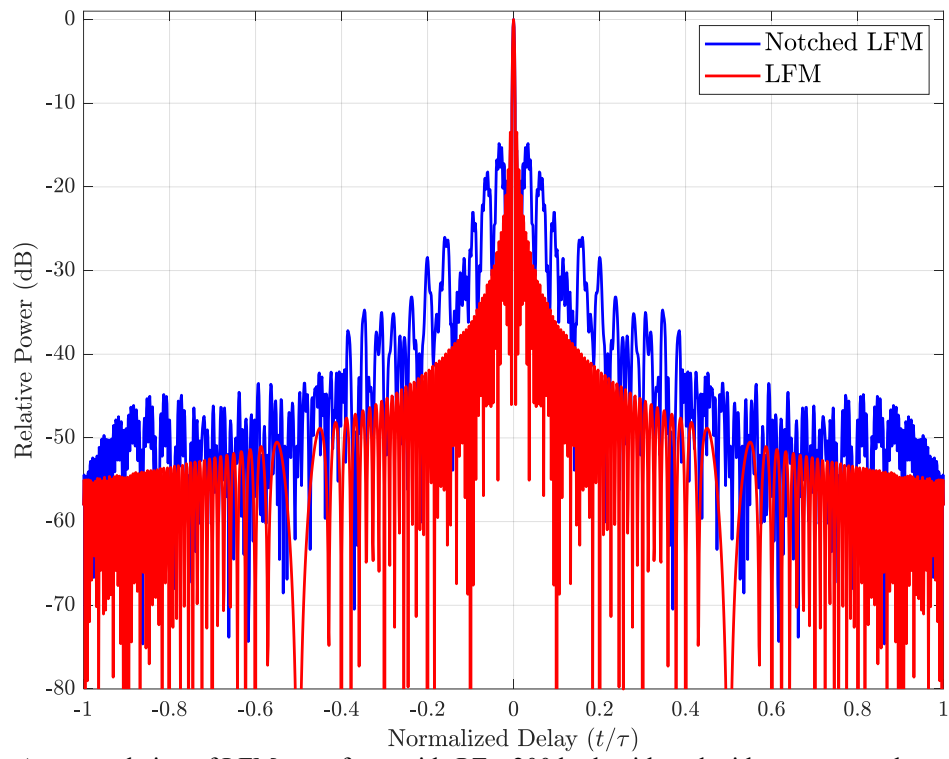
Figure 42: Autocorrelation of LFM waveform with *BT* = 200 both with and without a spectral notch inserted at 3*B*/8 of width *B*/10 using RUWO

Chapter 4: Mitigation of Narrowband Interference via Spectral Notches in FM Waveforms

4.1 Introduction

The groundwork laid in Chapter 3 is expanded upon in this chapter. Chapter 3 showed that PRO-FM waveforms with SG spectra are a powerful tool for radar operation due to their good spectral containment and sidelobe reduction during coherent combination across a CPI. Results presented in Chapter 3 also showed that spectral notches can be placed in PRO-FM waveforms optimized to have SG spectra and that the waveforms can be redesigned to change the spectral notch location arbitrarily. The primary drawback to this class of waveforms is the RSM introduced by the incoherent sidelobe structure when performing coherent combination, which is only exacerbated by introduction of a hopping spectral notch during the CPI. This chapter presents a new processing method to account for this RSM and proves its efficacy, along with that of PRO-FM waveforms, via physical experimentation.

The remainder of this chapter is laid out as follows. Section 4.2 introduces a processing strategy to account for RSM and provides a mathematical derivation. Section 4.3 applies this new processing technique to spectrally notched PRO-FM waveform via a simple simulation. Section 4.4 then extends this simulation to include the presence of narrowband interference and assess the mitigation capability of the notched waveform and new processing technique. Section 4.5 rounds out the chapter by demonstrating the efficacy of PRO-FM waveforms, with and without spectral notches, and the new processing technique on actual hardware via physical experimentation using a radar testbed for an MTI operating mode.

4.2 Compensation for RSM via Joint-Domain Processing

Although moderate success was found for compensation of RSM using the least-squares mismatched filter (LS-MMF) [79] and a clutter filling approach [84, 85], addressing the RSM

which dominated the results in Chapter 3 requires more capable processing than these approaches, or standard matched filter pulse compression and Doppler processing with projection-based clutter cancellation, can provide. A joint range-Doppler domain processing technique known as NIMPC was first introduced in [86] for the application of stepped LFM waveforms, which transmit an LFM waveform at varying center frequencies throughout the CPI in order to synthesize a larger bandwidth than can be achieved with a single waveform transmission. Noticing that NIMPC was successful in suppressing clutter in this application, its utility was extended to hopping spectral notches in PRO-FM waveforms to avoid spectrally agile narrowband interference in [87]. NIMPC performs joint range-Doppler processing while easily allowing deterministic (i.e., non-adaptive) clutter cancellation via a structured covariance matrix.

Constructing the joint-domain NIMPC filter begins with collecting the backscattered signal for M pulses in a CPI corresponding to a range cell l into the discretized row vector

$$\mathbf{y}(l) = \begin{bmatrix} y_0(l) & y_1(l) & \cdots & y_m(l) & \cdots & y_{M-1}(l) \end{bmatrix}. \tag{4.1}$$

Each mth element in this vector is defined by

$$y_m(l) = \sum_{\theta} \left[\mathbf{x}_\theta^T(l)\mathbf{s}_m e^{jm\theta} \right] + n(l), \tag{4.2}$$

for the vector

$$\mathbf{x}_\theta(l) = [x(l,\theta) \quad x(l-1,\theta) \quad \cdots \quad x(l-N+1,\theta)]^T \tag{4.3}$$

which is a collection of N complex scattering coefficients (both objects of interest and clutter) corresponding to Doppler phase shift θ that convolves with the mth pulsed waveform at delay l. The waveform transmitted for the mth pulse is denoted as $\mathbf{s}_m$ and $n(l)$ is a sample of complex AWGN. Collecting N fast-time samples of the received signal in (4.3) yields the matrix representation

$$\mathbf{Y}(l) = \sum_\theta \left[\mathbf{X}_\theta(l)\left(\mathbf{S} \odot \mathbf{V}_\theta\right)\right] + \mathbf{N}(l) . \tag{4.4}$$

The $N \times M$ matrix $\mathbf{V}_\theta$ consists of M Doppler steering vectors and is formed as

$$\mathbf{V}_\theta = \mathbf{1}_{N\times 1}[1 \quad e^{j\theta} \quad e^{j2\theta} \quad \cdots \quad e^{j(M-1)\theta}], \tag{4.5}$$

for the $N \times 1$ vector of ones $\mathbf{1}_{N \times 1}$. The matrix $\mathbf{N}(l)$ is an $N \times M$ collection of AWGN samples and $\odot$ is the Hadamard product. The $N \times M$ matrix $\mathbf{S}$ contains all transmitted waveforms in the CPI and the $N \times M$ matrix $\mathbf{X}_\theta(l)$ is composed of the complex scattering values for the $2N - 1$ range cells surrounding $x(l,\theta)$ and is formed as

$$\mathbf{X}_\theta(l) = \begin{bmatrix} x(l,\theta) & x(l-1,\theta) & \cdots & x(l-N+1,\theta) \\ x(l+1,\theta) & x(l,\theta) & \cdots & x(l-N+2,\theta) \\ \vdots & \vdots & \ddots & \vdots \\ x(l+N-1,\theta) & x(l+N-2,\theta) & \cdots & x(l,\theta) \end{bmatrix} . \tag{4.6}$$

To facilitate the formation of a joint-domain filter, the received signal matrix in (4.4) can be formed into a length-NM single vector via use of the vectorization operation as defined as

$$\tilde{\mathbf{y}}(l) = \text{vec}\left\{\mathbf{Y}(l)\right\} = \text{vec}\left\{\sum_\theta \left[\mathbf{X}_\theta(l)\left(\mathbf{S} \odot \mathbf{V}_\theta\right)\right] + \mathbf{N}(l)\right\} \tag{4.7}$$

which simply consists of stacking the first column of the matrix onto the second column and repeating in a likewise fashion for all columns in the matrix. With the received signal matrix now in a convenient format, a normalized joint-domain range-Doppler steering vector for Doppler θ is formed as

$$\mathbf{w}_\theta = \frac{1}{NM}\text{vec}\left\{\mathbf{S} \odot \mathbf{V}_\theta\right\} . \tag{4.8}$$

This filter can be applied to the received signal vector in (4.7) to form the NIMPC estimate of the complex scatterer at $x(l,\theta)$ by

$$\hat{x}_{\text{NIMPC}}(l,\theta) = \mathbf{w}_\theta^H \, \tilde{\mathbf{y}}(l) . \tag{4.9}$$

If the filter in (4.9) is applied sequentially for all range cells l and Doppler values θ, a result identical to that of applying sequential pulse compression and Doppler processing is obtained, albeit without the inclusion of clutter cancellation or Doppler windowing. The primary advantage of the NIMPC filter is a multiplicative increase in the degrees of processing freedom that can be used to incorporate clutter cancellation. This advantage is indeed taken for the RSM problem caused by coupling of the range and Doppler domains with a spectrally notched waveform whose notch location changes throughout the CPI, as was demonstrated in Chapter 3.

The NIMPC framework allows for easy modification of the joint-domain filter in (4.9) to include clutter cancellation for desired Doppler values θ. The first step is to form a structured range-Doppler covariance matrix $\mathbf{R}$ as

$$\mathbf{R} = \mathbf{P}_\phi \, \mathbf{P}_\phi^H + \varepsilon \mathbf{I} \,, \tag{4.10}$$

for diagonal loading factor ε and identity matrix $\mathbf{I}$ to prevent ill-conditioning of the matrix inverse where $\mathbf{P}_\phi$ is defined as

$$\mathbf{P}_\phi = \begin{bmatrix} \mathbf{c}^\phi_{-(N-1)} & \mathbf{c}^\phi_{-(N-1)+1} & \cdots & \mathbf{c}^\phi_0 & \cdots & \mathbf{c}^\phi_{(N-1)-1} & \mathbf{c}^\phi_{(N-1)} \end{bmatrix}, \tag{4.11}$$

$\mathbf{c}_n{}^\phi$ is formed as

$$\mathbf{c}^\phi_n = \mathrm{vec}\left(\mathbf{S}_n \odot \mathbf{V}_\phi\right), \tag{4.12}$$

with $\mathbf{S}_n$ defined by

$$\mathbf{S}_n = \begin{cases} \begin{bmatrix} \mathbf{s}^n_0 & \mathbf{s}^n_1 & \cdots & \mathbf{s}^n_{M-1} \end{bmatrix} & \text{for} \quad 0 \le n \le N-1 \\ \begin{bmatrix} \mathbf{s}^n_0 & \mathbf{s}^n_1 & \cdots & \mathbf{s}^n_{M-1} \end{bmatrix} & \text{for} \quad -(N-1) \le n \le 0 \end{cases}, \tag{4.13}$$

and

$$\mathbf{s}^n_m = \begin{cases} \begin{bmatrix} \mathbf{0}^T_n & s_m(0) & \cdots & s_m(N-1-n) \end{bmatrix} & \text{for} \quad 0 \le n \le N-1 \\ \begin{bmatrix} s_m(|n|) & \cdots & s_m(N-1) & \mathbf{0}^T_{|n|} \end{bmatrix} & \text{for} \quad -(N-1) \le n \le 0 \end{cases}, \tag{4.14}$$

in which $s_m(n)$ is the nth sample of the mth pulse and $\mathbf{0}_n$ is an n x 1 vector of zeros. The middle

column $\mathbf{c}_0{}^\phi$ of $\mathbf{P}_\phi$ corresponds to the contribution of clutter in the desired range cell, whereas the

other $2(N\text{-}1)$ columns correspond to contributions from clutter in the surrounding range cells, thus

accounting for the RSM. The clutter cancelled NIMPC estimate for range cell l and Doppler value

θ is then formed as

$$\hat{x}_{NIMPC-C}\left(l,\theta\right) = \tilde{\mathbf{w}}_\theta^H \tilde{\mathbf{y}}(l), \tag{4.15}$$

where

$$\tilde{\mathbf{w}}_\theta = \frac{\mu}{NM}\mathbf{R}^{-1}\Big[\,\mathrm{vec}\big([\mathbf{S}\odot\mathbf{V}_\theta]\big)\Big], \tag{4.16}$$

is the clutter whitened NIMPC filter and μ is an arbitrary scale factor. The matrix $\mathbf{P}_\phi$ contains

versions of the Doppler steering vectors to account for all possible delay shifts of each discretized

transmit waveform associated with Doppler values ϕ of the clutter that are desired to be cancelled.

The clutter notch can be extended to account for clutter-Doppler spread by placing multiple closely

spaced notches i.e., replacing $\mathbf{P}_\phi$ in (4.10) with $\tilde{\mathbf{P}}_\phi = \begin{bmatrix} \mathbf{P}_{\phi_0} & \mathbf{P}_{\phi_1} & \cdots & \mathbf{P}_{\phi_{Q-1}} \end{bmatrix}$ where Q is the total

number of notches. Each notch requires $2N\text{-}1$ degrees of freedom (or $Q(2N\text{-}1)$ total) and may

necessitate the use of additional pulses to increase the available degrees of freedom, given by the

product NM for $N = (BT)K$ the total number of discrete points in each waveform.

A note of the computational cost of calculating the NIMPC filter in (4.16) is warranted.

The costliest step of the NIMPC procedure is to invert the covariance matrix formed in (4.10).

This matrix has dimensions of NM x NM and will require on the order of $(NM)^3$ complex operations

(denoted as $O(NM)^3$ in order notation) to calculate the inverse. Although not described here,

methods exist to reduce the computational complexity and storage requirements of this matrix

inverse (by exploiting the structure of the covariance matrix), and subsequent formation and

application of the NIMPC filter. These techniques are described in [88] along with application to physically collected radar waveforms.

4.3 Simulation of Joint-Domain Processing to Spectrally Notched FM Waveforms

Application of NIMPC to PRO-FM waveforms, both with and without spectral notches, is explored in this section via a simple radar simulation like that presented in Chapter 2. The simulated radar waveforms each have $BT = 50$ and $K = 2$ for $N = 100$ total discrete points with a CPI of $M = 100$ pulses. The illuminated environment of interest is formed by creating a clutter profile which is generated randomly as a complex Gaussian process and power scaled such that the CNR after coherent processing gain is approximately 30 dB. The clutter profile has only a zero Doppler frequency component. Note that it is common for clutter to have non-zero Doppler frequency components in practice, but that is not the case for this simplified simulation.

After generating the clutter profile, a single scatterer is added to this environment, characterized by a range index of $l = 50$ (for a possible $L = 100$ range bins), power of -50 dB relative to the peak transmit power, and normalized (by the PRF) Doppler frequency of 0.25. The impulse response of this simulated environment is convolved with the radar transmit waveform CPI, and AWGN noise is added with its power scaled such that the SNR after coherent processing gain is approximately 20 dB. Five different radar waveform transmit CPIs are considered for this simulation, 1) LFM, 2) PRO-FM, 3) PRO-FM with a stationary spectral notch, 4) PRO-FM with a spectral notch which hops every 10 pulses (corresponding to 10 total hops during the CPI), and 5) PRO-FM with a spectral notch which hops every single pulse (corresponding to 100 total hops during the CPI). Each value of super Gaussian template order considered in Chapter 3 is considered here as well ($\eta = 2, 4, 8$ and 16). A static random number generator (RNG) seed is used to generate

random clutter and noise for each waveform test case and value of η, such that a fair comparison can be made across all cases.

Two processing methods are applied to form RD maps for each waveform test case. First, standard matched filter pulse compression followed by Doppler processing and projection-based clutter cancellation with $Z = 17$ principal singular values is performed. A Doppler window taper is not utilized for this processing method. This first processing method will be referred to as "standard" or "matched filter". Second, joint-domain processing with clutter cancellation is performed via NIMPC using $Q = 3$ clutter notches. Though direct comparison of the projection-based clutter cancellation technique and that incorporated into NIMPC are not directly comparable, the projection-based clutter notch is much wider than that of NIMPC (as will be apparent in the simulation results) due to the smearing of the clutter caused by the RSM of the mostly rapidly hopping spectral notch case with the need to form a clutter notch wide enough to sufficiently cancel. This second processing method will henceforth be referred to as simply "NIMPC". The true location of the scatterer is indicated for each RD map by a red circle.

A modified version of the PSF metric, δ, in (3.5) is used to calculate the mean residual power after processing for each RD map. The excluded regions for calculating this mean power are the delay and Doppler mainlobe regions for the scatterers, similar to how the delay and Doppler mainlobes were excluded for the PSFs, as well as the Doppler values corresponding to the region of the clutter notch formed by the projection-based clutter cancellation technique (since it is wider than the NIMPC clutter notch), which was not considered with the PSFs. A summary of all δ values is provided in Table 3.

As a means of comparison and to establish a baseline case, the first waveform simulation case considered is the LFM. Figure 43 shows the RD map when performing standard processing

and Figure 44 shows the result using NIMPC. In both cases, the scatterer is easily discernable, and the estimated power is almost exactly the true value of -50 dB. Aside from the difference in clutter notch width, there is essentially no difference in the background level of the RD maps. This makes sense as the LFM waveform CPI is consistent across each pulse and no RSM in anticipated. This result shows that NIMPC can perform equivalent processing to the standard procedure for a static CPI of transmit waveforms, and while NIMPC is not detrimental, it is also not really necessary in this case due to the increased computational complexity. The background floor values for this case are -71.3 dB for standard processing, and -71.1 dB for NIMPC.
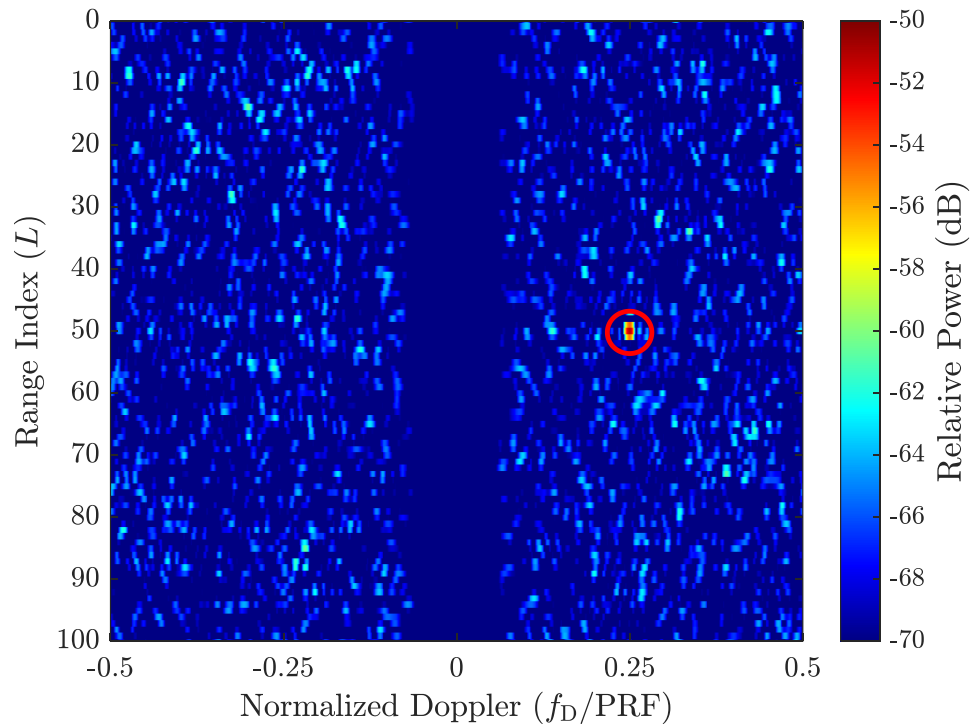
Figure 43: RD map of simulation for an LFM transmit waveform CPI using standard processing and projection-based clutter cancellation
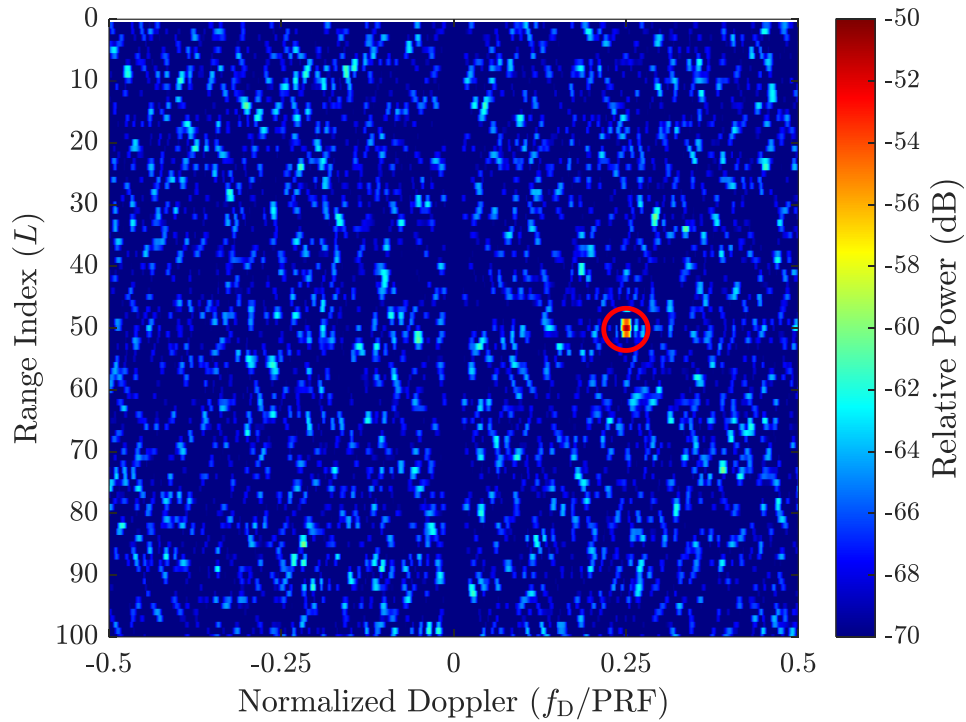
Figure 44: RD map of simulation for an LFM transmit waveform CPI using NIMPC with clutter cancellation

The radar waveform test case considered next is that of a CPI of PRO-FM waveforms without a spectral notch. Figure 45 shows the RD map using standard processing and Figure 46 shows the RD map using NIMPC, each for all cases of η considered. In the standard processing case, the scatterer is visible for all η, although the RSM floor increases for increasing η. The values of δ for Figure 45 are -69.7 dB, -69.2 dB, -68.3 dB and -68.0 dB for values of $\eta = 2, 4, 8$ and 16, respectively. The background floor in Figure 46 is essentially identical for all cases, showing that NIMPC processing has effectively eliminated the RSM caused by the waveform agile CPI. The values of δ for Figure 46 are -71.1 dB, -71.2 dB, -71.2 dB and -71.1 dB for values of $\eta = 2, 4, 8$ and 16, respectively, representing consistent values for all cases and significant improvements as compared to standard processing.
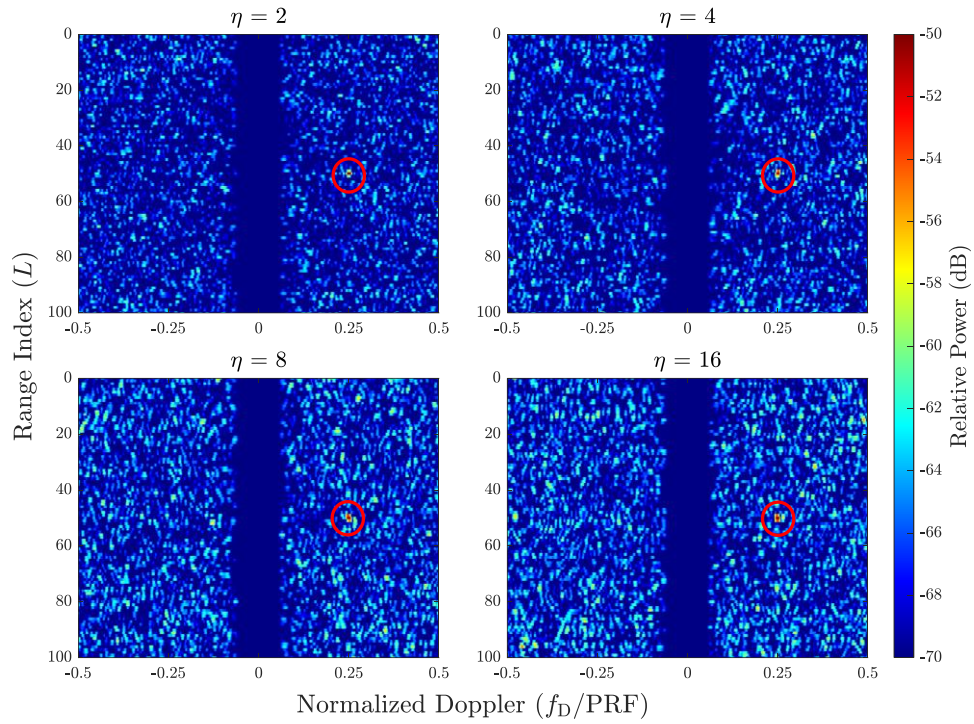
Figure 45: RD maps of simulation for a CPI of PRO-FM waveforms with η = 2, 4, 8 and 16 using standard processing and projection-based clutter cancellation
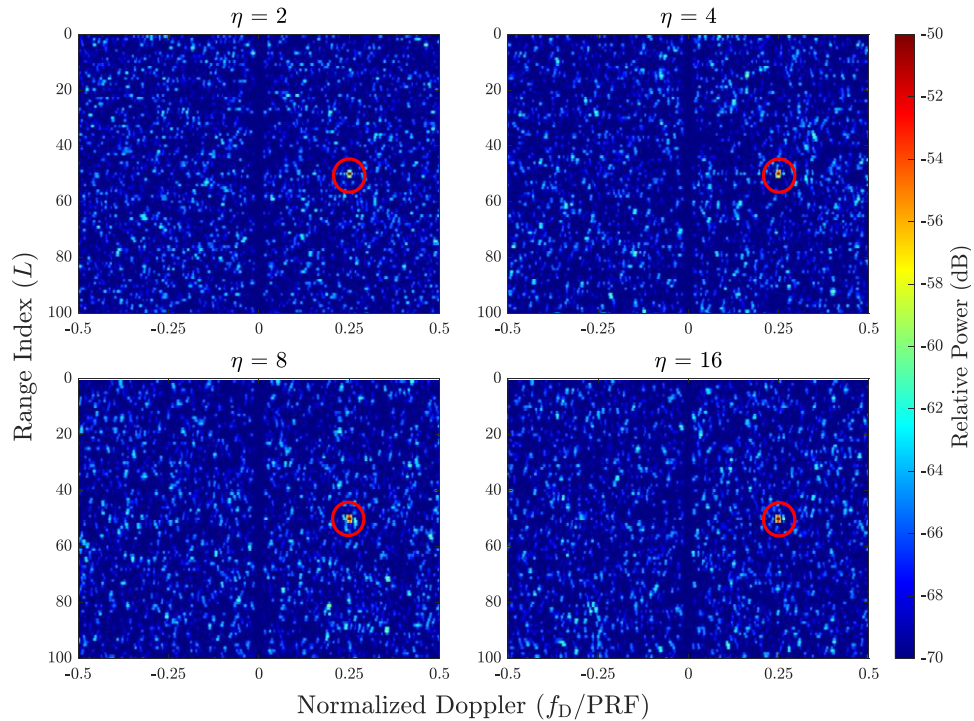
Figure 46: RD maps of simulation for a CPI of PRO-FM waveforms with η = 2, 4, 8 and 16 using standard processing and NIMPC with clutter cancellation

The radar waveform test case considered next is that of a CPI of PRO-FM waveforms with a stationary spectral notch centered at normalized frequency $3B/8$ with a width of $B/10$ and a Tukey taper region of width $B/16$ on either side of the notch. Figure 47 shows the RD map using standard processing and Figure 48 shows the RD map using NIMPC, each for all cases of η considered. In the standard processing case, the scatter is visible for all η, although the RSM floor increases for increasing η and the scatterer is close to being obscured for $\eta = 16$. The values of δ for Figure 47 are -69.2 dB, -68.3 dB, -67.4 dB and -67.1 dB for values of $\eta = 2, 4, 8$ and 16, respectively. The background floor in Figure 48 is essentially identical for all cases, showing that NIMPC processing has once again effectively eliminated the RSM caused by the waveform agile CPI. The values of δ for Figure 48 are -71.2 dB, -71.1 dB, -71.1 dB and -71.1 dB for values of $\eta = 2, 4, 8$ and 16, respectively, representing consistent values, and nearly identical results to that of the notch-free PRO-FM waveform case, as well as significant improvements when compared to standard processing.
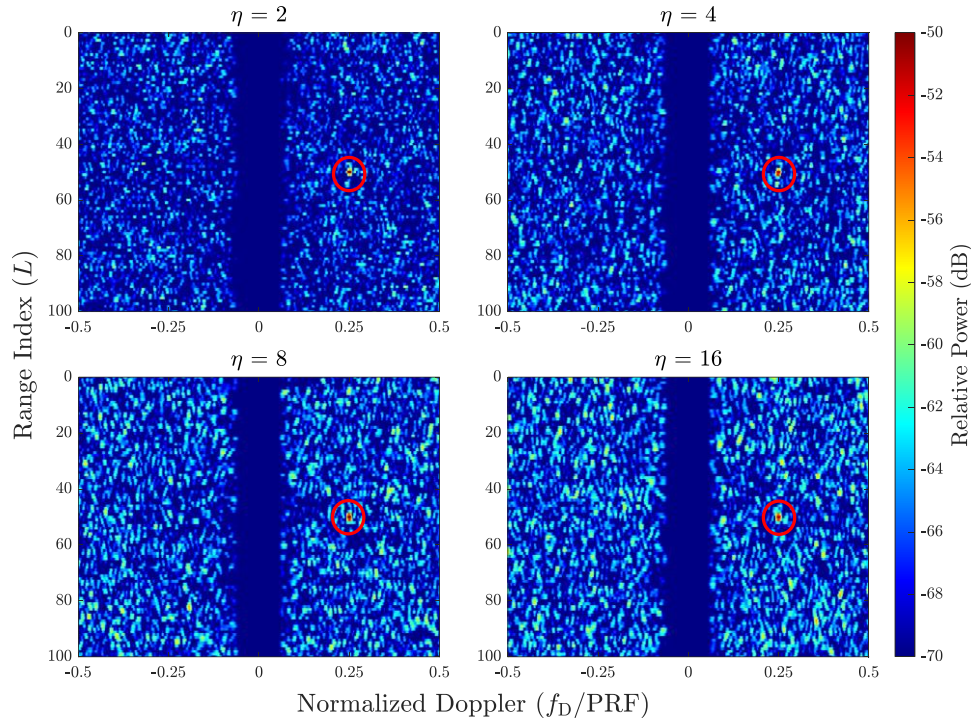
Figure 47: RD maps of simulation for a CPI of PRO-FM waveforms with a stationary notch and η = 2, 4, 8 and 16 using standard processing and projection-based clutter cancellation
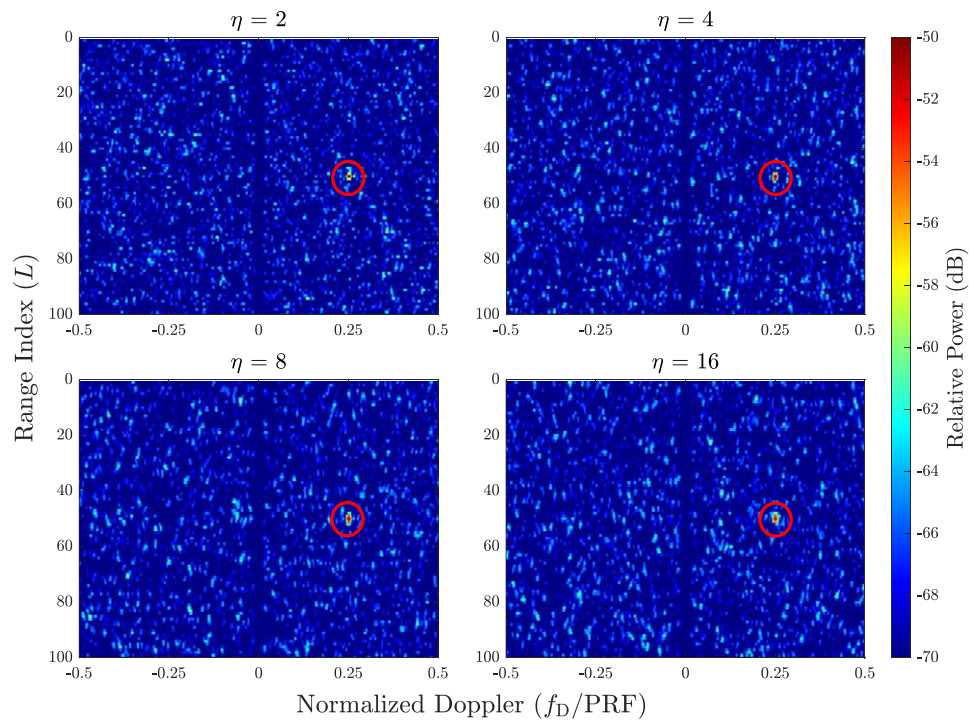
Figure 48: RD maps of simulation for a CPI of PRO-FM waveforms with a stationary notch and η = 2, 4, 8 and 16 using standard processing and NIMPC with clutter cancellation

The next test case is that of a CPI of PRO-FM waveforms with a spectral notch that hops 10 times during the CPI, persisting at each location for 10 pulses. Figure 49 shows the RD map using standard processing and Figure 50 shows the RD map using NIMPC. In the standard processing case, the scatterer has now become obscured for almost each value of η. The values of δ for Figure 49 are -68.4 dB, -67.5 dB, -66.7 dB and -67.5 dB for values of η = 2, 4, 8 and 16, respectively. The background floor in Figure 50 is essentially identical for all cases, showing that NIMPC processing has once again effectively eliminated the RSM caused by the waveform agile CPI. The values of δ for Figure 50 are -71.1 dB, -71.2 dB, -71.2 dB and -71.2 dB for values of η = 2, 4, 8 and 16, respectively, representing consistent values, and nearly identical results to that of the stationary notched PRO-FM waveform case, as well as significant improvements when compared to standard processing.
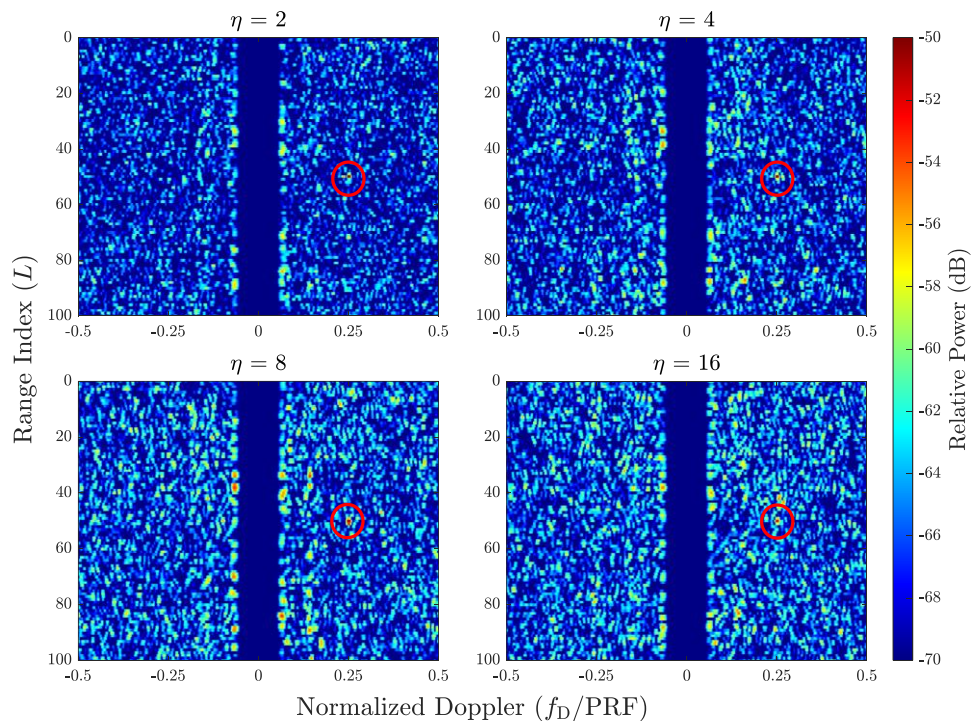
Figure 49: RD maps of simulation for a CPI of PRO-FM waveforms with a hopping notch changing locations every 10 pulses and η = 2, 4, 8 and 16 using standard processing and projection-based clutter cancellation
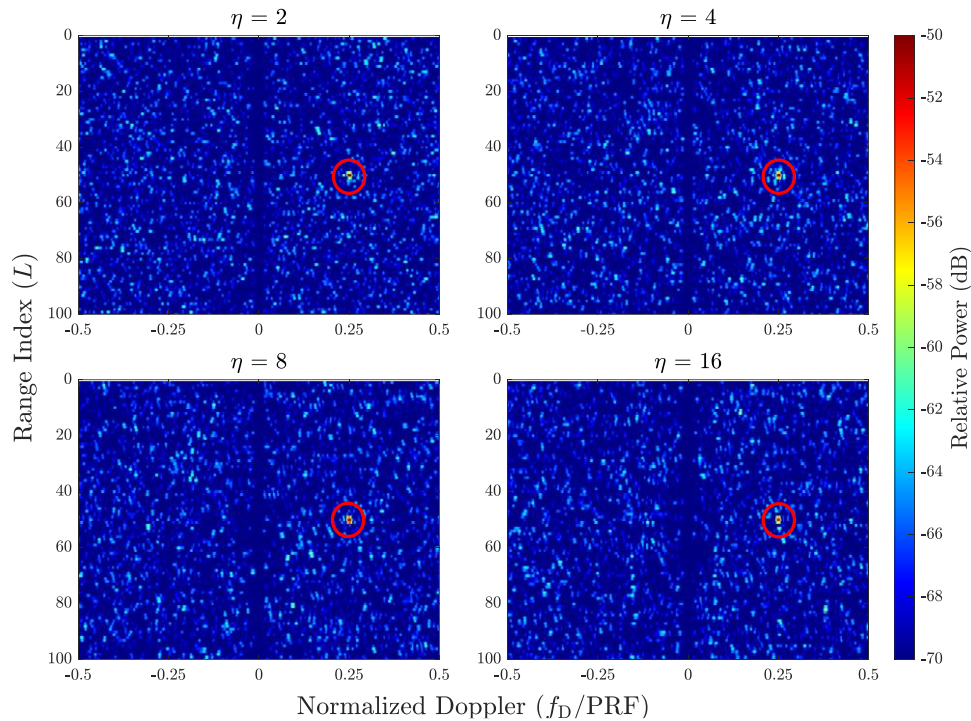
Figure 50: RD maps of simulation for a CPI of PRO-FM waveforms with a hopping notch changing locations every 10 pulses and η = 2, 4, 8 and 16 using NIMPC with clutter cancellation

The final test case is that of a CPI of PRO-FM waveforms with a spectral notch that hops 100 times during the CPI, changing locations every single pulse. Figure 51 shows the RD map using standard processing and Figure 52 shows the RD map using NIMPC. In the standard processing case, the scatterer is now obscured for all values of η as the RSM has become severe. The values of δ for Figure 51 are -65.4 dB, -64.3 dB, -63.7 dB and -63.4 dB for values of η = 2, 4, 8 and 16, respectively. The background floor in Figure 50 is essentially identical for all cases, showing that NIMPC processing has once again effectively eliminated the RSM caused by the waveform agile CPI. The values of δ for Figure 52 are -71.1 dB, -71.1 dB, -71.2 dB and -71.1 dB for values of η = 2, 4, 8 and 16, respectively, representing consistent values once again, and nearly identical results to all other PRO-FM waveform cases, as well as significant improvements when compared to standard processing.
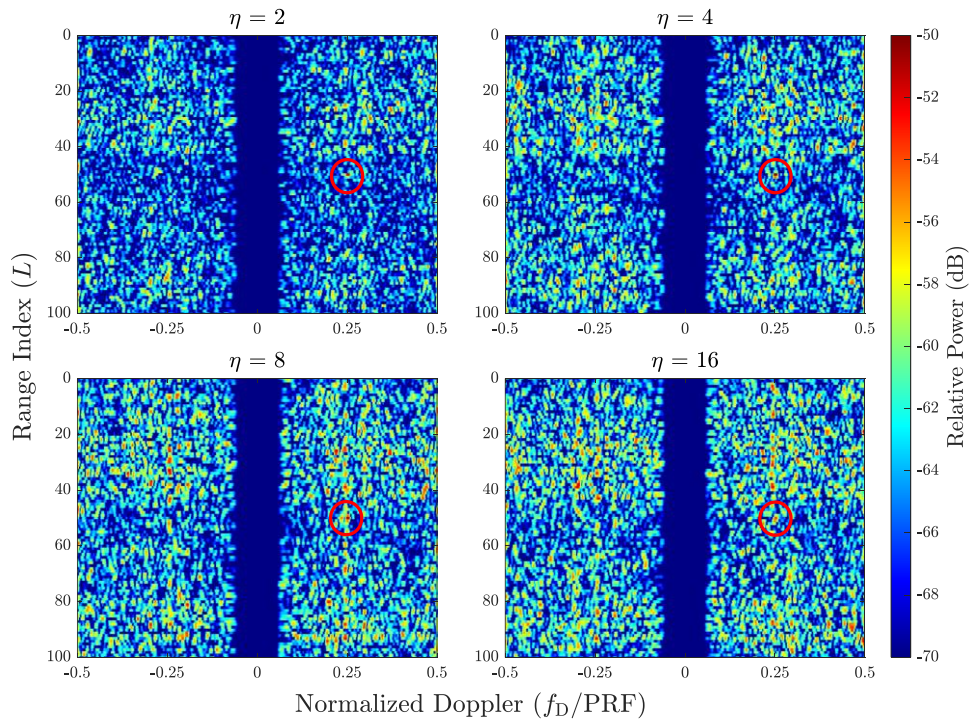
Figure 51: RD maps of simulation for a CPI of PRO-FM waveforms with a hopping notch changing locations every single pulse and η = 2, 4, 8 and 16 using standard processing and projection-based clutter cancellation
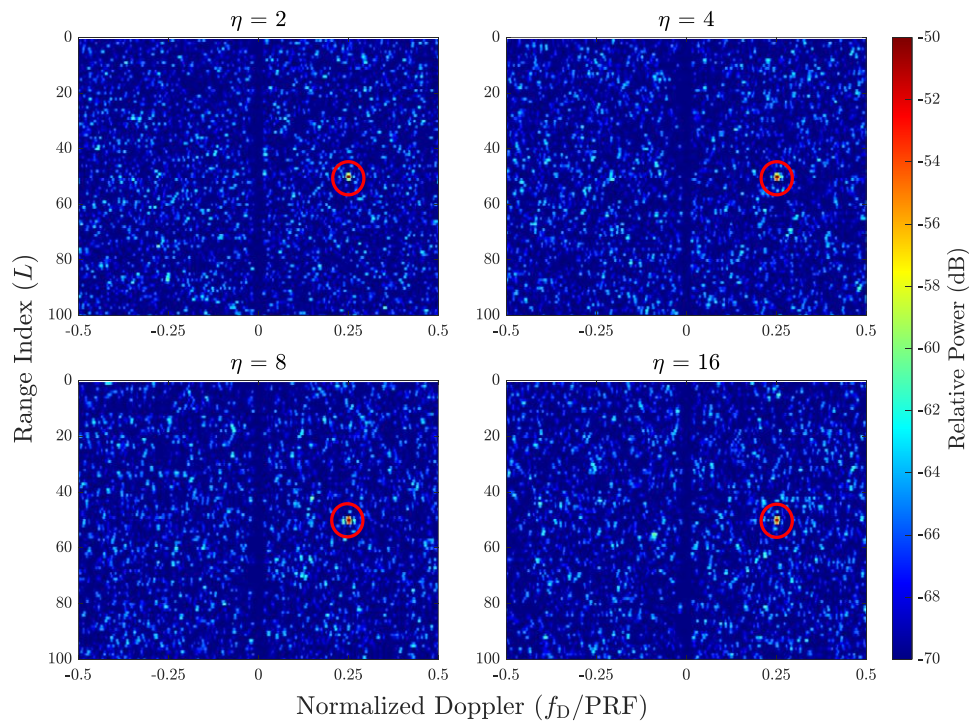
Figure 52: RD maps of simulation for a CPI of PRO-FM waveforms with a hopping notch changing locations every single pulse and η = 2, 4, 8 and 16 using NIMPC with clutter cancellation

As the purpose of the spectral notch in a PRO-FM is to mitigate narrowband interference, it is important to make sure the NIMPC filter preserves the spectral notch, otherwise the reduction in RSM benefits observed so far would be meaningless for notched PRO-FM applications. To ensure spectral notch preservation, the frequency spectrum of the NIMPC filter must be assessed. This is achieved by observing the RMS power spectrum of the NIMPC filters across each value of Doppler frequency θ considered in the simulation. Figure 53 shows the RMS spectrum of the NIMPC filter plotted along with the waveform spectrum for the notch-free PRO-FM waveform case shown in Figure 45 and Figure 46. Clearly, the NIMPC filter RMS spectrum is almost identical to that of the PRO-FM waveform in each case, showing that the spectral compactness is preserved for larger values of η.
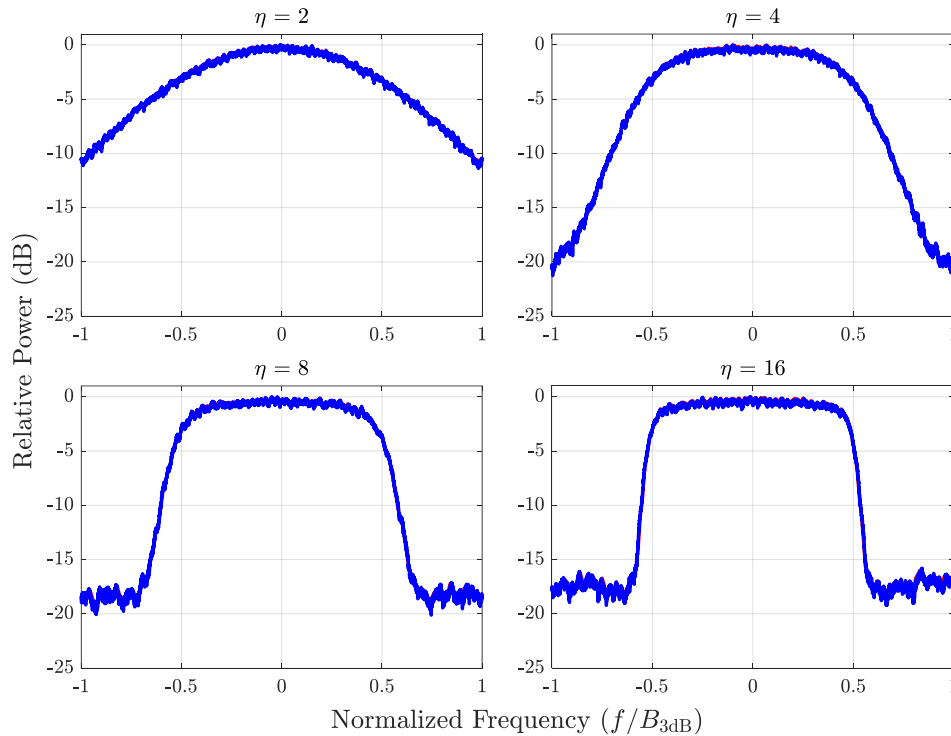
Figure 53: RMS Spectrum of NIMPC filter (blue) and waveform (red) for PRO-FM waveform simulation case with $\eta = 2, 4, 8$ and 16

Figure 54 shows the RMS spectrum of the NIMPC filter and waveform for the stationary notched PRO-FM case shown in Figure 47 and Figure 48. The RMS spectrum of the NIMPC filter

preserves the spectral notch to a depth of about -32 dB whereas the RMS notch depth of the optimized waveform is about -40 dB, showing a slight degradation in the notch depth caused by the NIMPC filter. This result shows that NIMPC filtering mostly preserves the spectral notches placed in PRO-FM waveforms and will subsequently reject narrowband interference to an extent similar to the standard matched filter of the notched PRO-FM waveform (where the notched PRO-FM waveform and its associated matched filter have identical spectra). It is noted that the spectral notch depth of about 40 dB this simulation case is about 15 dB lower than the notched PRO-FM waveform depicted in Figure 26 of Chapter 2. Th reason for this discrepancy is the difference in waveform BT considered in each case. The results of Chapter 2 used a per-waveform BT of 200 while the simulations presented thus far in this chapter use a per-waveform BT of 50, representing fewer degrees of design freedom for the alternating projections and RUWO optimization procedures, and thus a shallower notch depth is achieved. The reason for reduction of waveform dimensionality in this chapter is due to the computational requirement demand of NIMPC processing, although enough dimensionality has been preserved to show the true capabilities of NIMPC in these simulations.
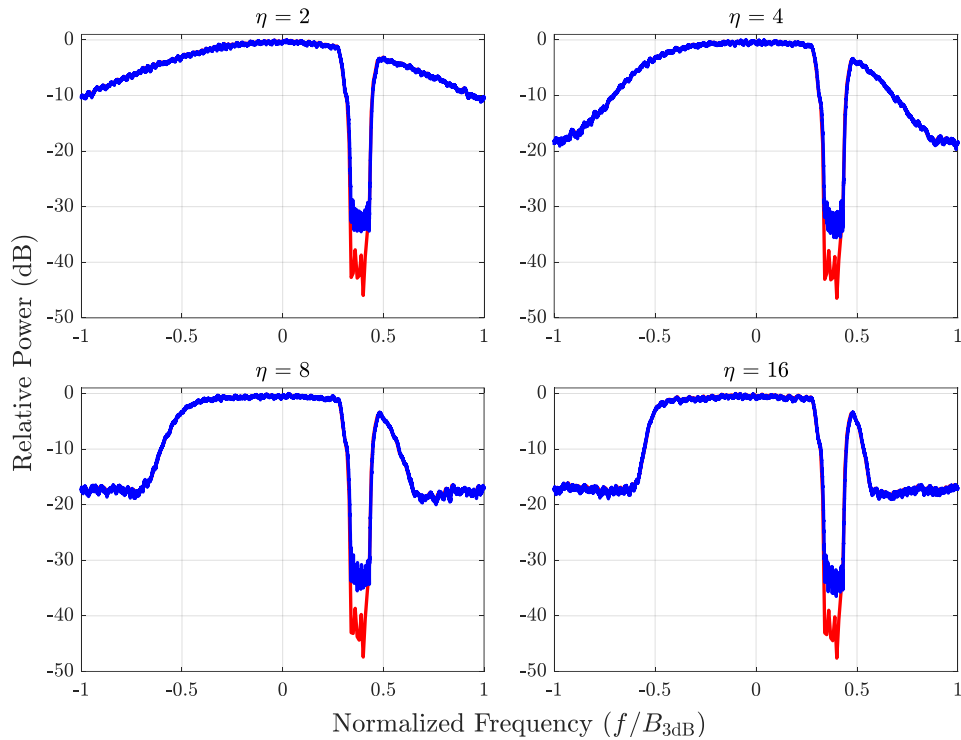
Figure 54: RMS Spectrum of NIMPC filter **(**blue) and waveform (red) for Notched PRO-FM waveform simulation case with η = 2, 4, 8 and 16

4.4 Extension of Joint-Domain Processing Simulation to Interference Environments

With knowledge that NIMPC processing preserves most of the spectral notch depth in PRO-FM waveforms, the simulations of the previous section are extended here to include the presence of narrowband interference in the radar operating band. The narrowband interference takes the form of an OFDM signal of spectral width $B/20$ comprised of subcarriers modulating a single communications symbol taken randomly from a 64-QAM constellation (see Figure 14). An artificial noise floor is added to the OFDM interference signal such that peak spectral power of the signal is about 60 dB relative to the noise floor (before being power scaled). The interference signal is added to the received signal after the impulse response of the simulated environment is convolved with the radar transmit waveform CPI, and before thermal noise is added. The OFDM interference signal is power scaled such that the signal-to-interference ratio (SIR) is -20 dB at the

radar receiver. Beyond the addition of narrowband interference, the simulations in this section, including processing, are the same as those of Section 3 of this chapter.

For the case of the LFM waveform CPI, the OFDM interference signal is spectrally stationary throughout the CPI. This is depicted in Figure 55 where the RMS spectrum of the LFM transmit waveform (before convolution with the impulse response of the simulated scattering environment) is shown along with the RMS spectrum of the power scaled OFDM interference signal. In the case of the notch-free PRO-FM and stationary-notched PRO-FM cases, the OFDM interference is spectrally stationary throughout the CPI as shown in Figure 56 and Figure 57, respectively, for each case of η. For the two hopping spectrally notched PRO-FM cases, the spectral notch hops in tandem with the OFDM interference, representing an optimal scenario in which the radar system is able to sense the interference and design a new spectrally notched PRO-FM waveform immediately. This represents a "cognitive behavior" of the radar system, which is not discussed in this work but is explored in detail in [6, 83, 85, 89-104].
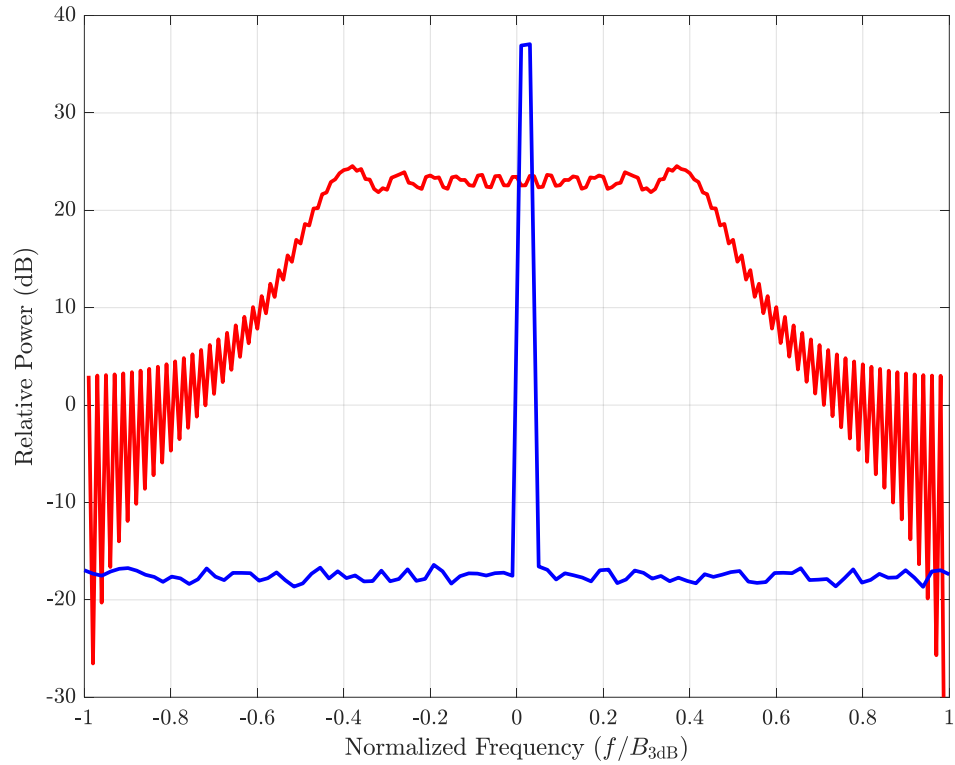
Figure 55: RMS spectrum of transmit LFM waveform and power scaled OFDM interference signal
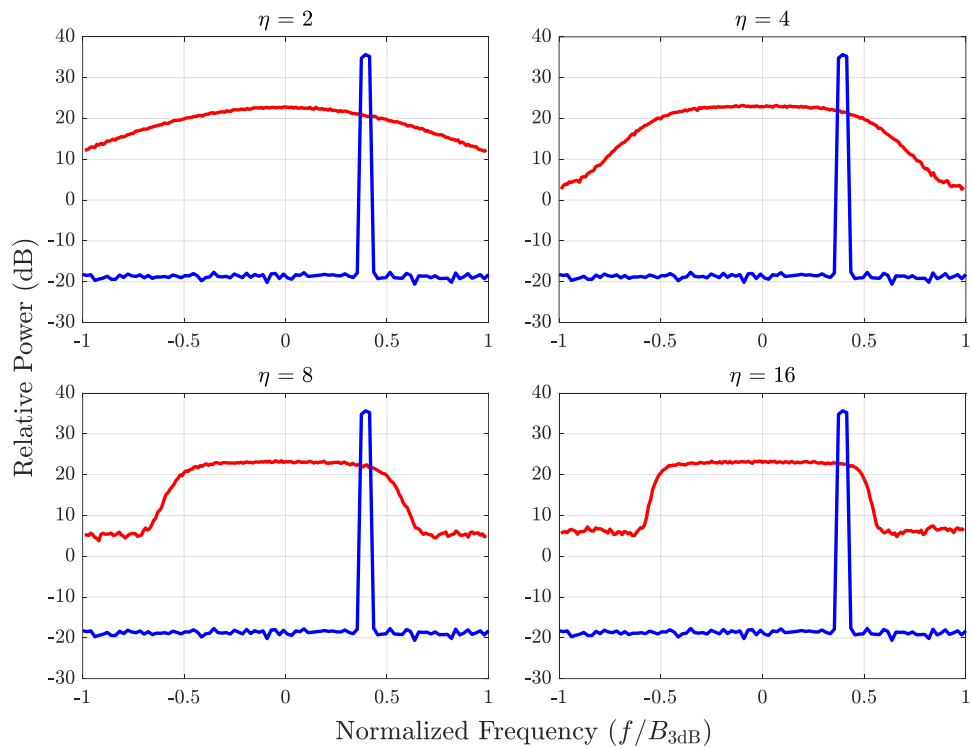
Figure 56: RMS spectrum of transmit notch-free PRO waveform and power scaled OFDM interference signal for η = 2, 4, 8 and 16
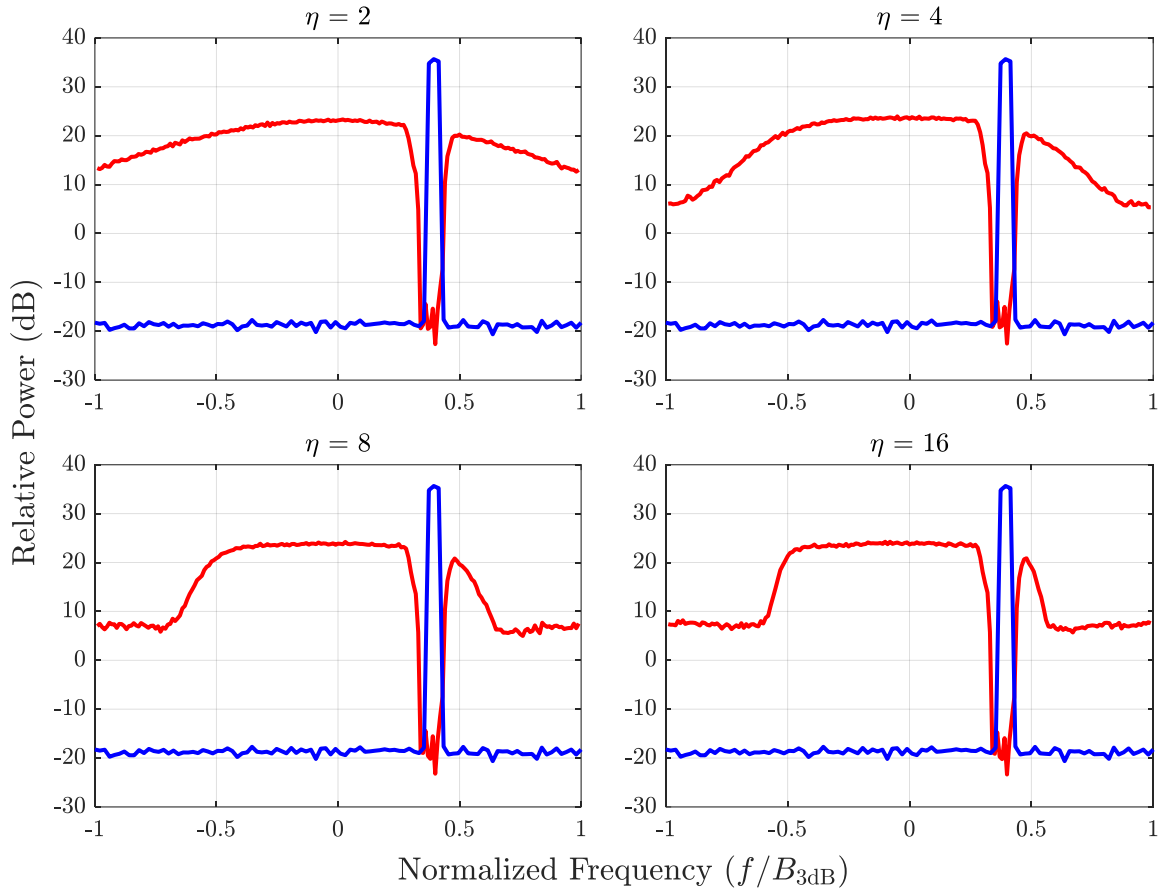
Figure 57: RMS spectrum of transmit spectrally notched PRO waveform and power scaled OFDM interference signal for η = 2, 4, 8 and 16

Figure 58 shows the RD map when performing standard processing and Figure 59 shows the result using NIMPC for the simulation of a CPI of LFM waveforms when the narrowband OFDM interference is introduced. In both cases, the scatterer is no longer discernible against the interference floor established by the presence of the interference. As anticipated, NIMPC does not provide any benefit in the presence of in-band interference when the transmit waveform itself is not designed itself to mitigate in-band interference. The background floor values of δ for this case are nearly identical at -63.6 dB for standard processing, and -63.5 dB for NIMPC, representing severe degradation over the interference-free simulation counterpart.
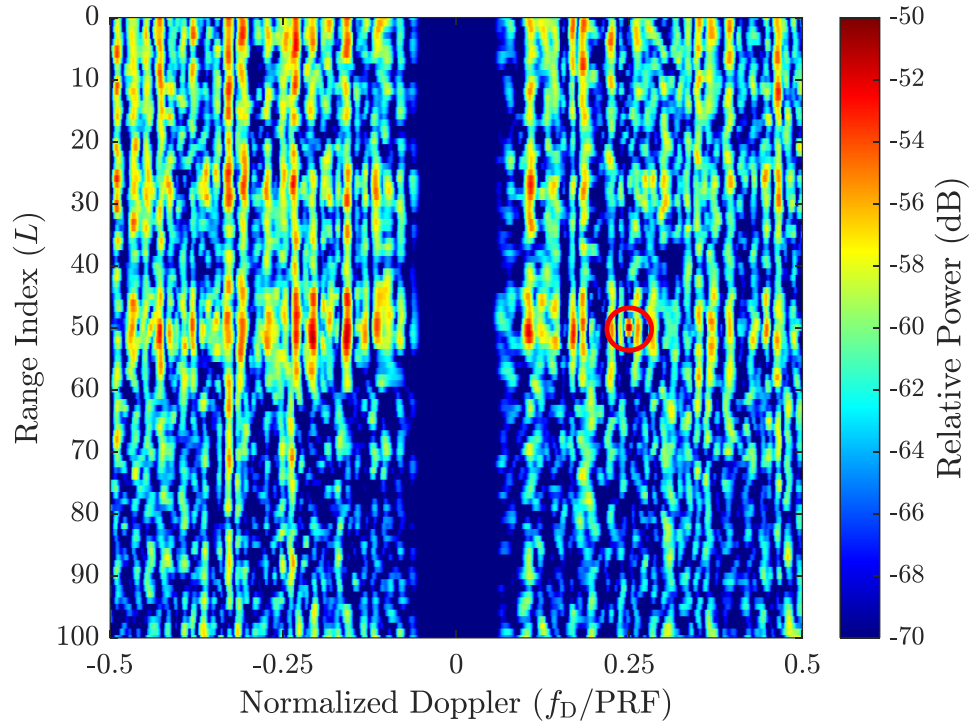
Figure 58: RD map of simulation for an LFM transmit waveform plus CPI plus stationary OFDM interference using standard processing and projection-based clutter cancellation
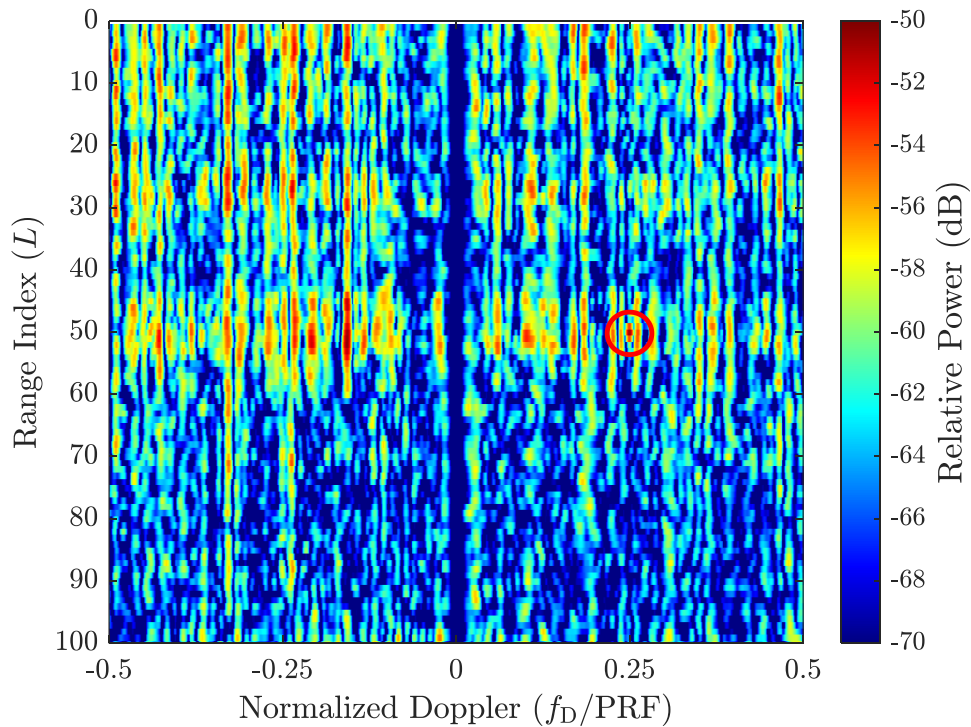
Figure 59: RD map of simulation for an LFM transmit waveform CPI plus stationary OFDM interference using NIMPC with clutter cancellation

Figure 60 shows the RD map using standard processing and Figure 61 shows the RD map using NIMPC for the simulation of a CPI of PRO-FM waveforms without a spectral notch, each for all cases of η considered, when the narrowband OFDM interference is introduced. Once again, the scatterer is no longer discernible against the interference floor established by the presence of the interference and NIMPC does not provide any benefit in the presence of in-band interference when the transmit waveform itself is not designed itself to mitigate in-band interference. The values of δ for Figure 60 are -62.3 dB, -61.5 dB, -60.9 dB and -60.4 dB for values of $\eta = 2, 4, 8$ and 16, respectively, where the values of δ for Figure 61 are -62.4 dB, -61.6 dB, -61.1 dB and -60.6 dB for values of $\eta = 2, 4, 8$ and 16, respectively, again representing severe degradation over the interference-free simulation counterpart in Section 3.
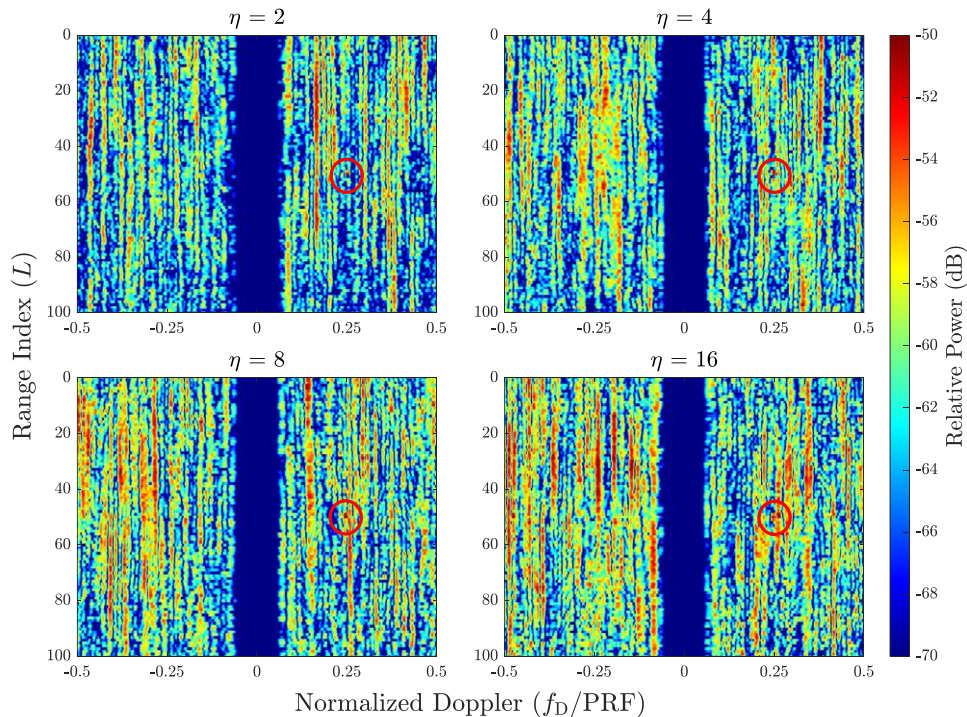
Figure 60: RD maps of simulation for a CPI of PRO-FM waveforms plus stationary OFDM interference with $\eta = 2$, 4, 8 and 16 using standard processing and projection-based clutter cancellation
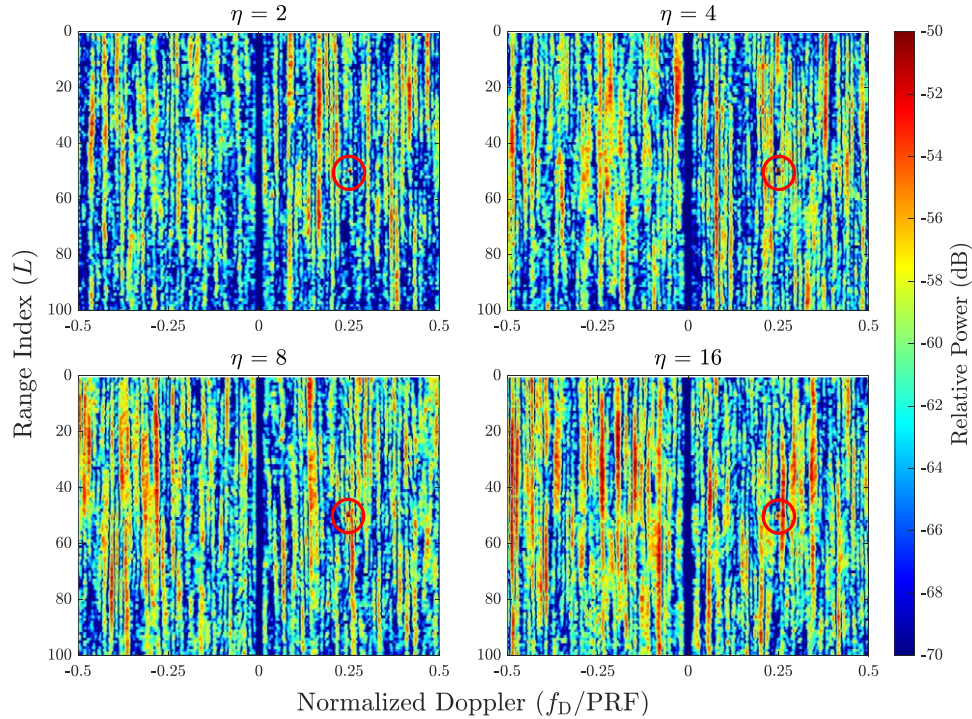
Figure 61: RD maps of simulation for a CPI of PRO-FM waveforms plus stationary OFDM interference with $\eta = 2$, 4, 8 and 16 using standard processing and NIMPC with clutter cancellation

Figure 62 shows the RD map using standard processing for the simulation of a CPI of PRO-FM waveforms with a stationary spectral notch, for all cases of η considered, when the narrowband OFDM interference is introduced. The scatterer is now discernible for η values of 2 and 4 and starts to become obscured for values of 8 and 16. The addition of a spectral notch in the PRO-FM waveform to accommodate the interference has helped significantly, but the RSM is still detrimental when standard processing is used. The values of δ for Figure 62 are -68.7 dB, -67.9 dB, -67.1 dB and -66.7 dB for values of $\eta = 2$, 4, 8 and 16, respectively. These represent degradations caused by the introduction of interference of 0.5 dB, 0.4 dB, 0.3 dB and 0.4 dB, respectively, over the interference-free counterpart in Section 3, indicating that the spectral notch has mitigated most of the interference power.
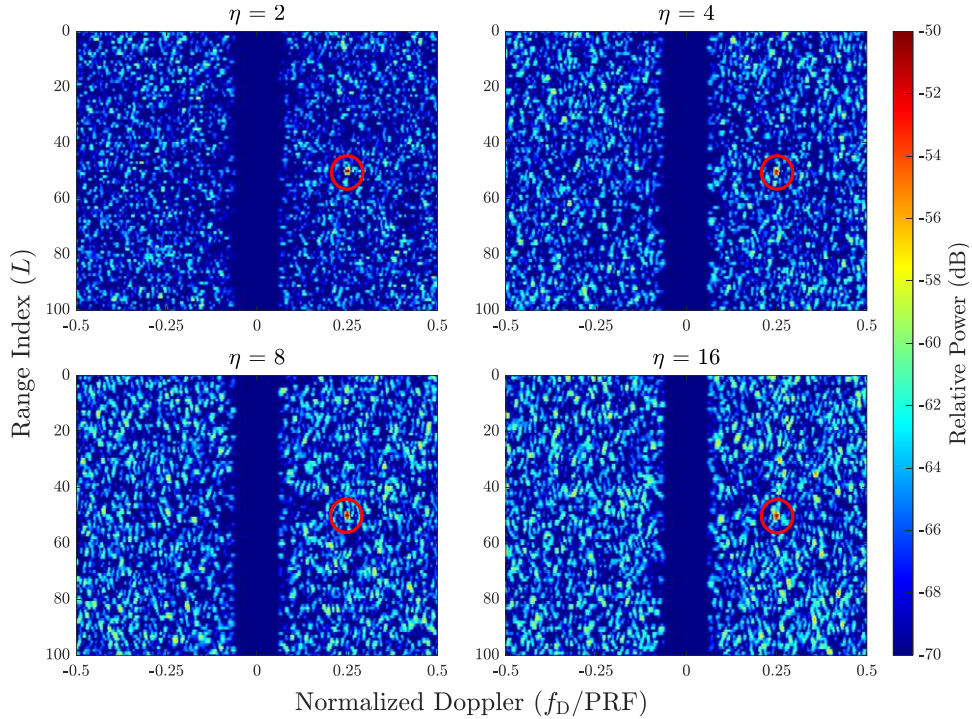
Figure 62: RD maps of simulation for a CPI of PRO-FM waveforms with a stationary notch plus stationary OFDM interference and η = 2, 4, 8 and 16 using standard processing and projection-based clutter cancellation

Figure 63 shows the RD map using NIMPC for the simulation of a CPI of PRO-FM waveforms with a stationary spectral notch, for all cases of η considered, when the narrowband OFDM interference is introduced. The scatterer is now clearly visible in an all cases, showing that NIMPC processing has successfully accounted for the RSM, while maintaining the spectral notch of the waveform to mitigate the interference. The values of δ for Figure 63 are -70.5 dB, -70.2 dB, -70.4 dB and -70.2 dB for values of η = 2, 4, 8 and 16, respectively. These represent improvements of 1.8 dB, 2.3 dB, 3.3 dB and 3.5 dB, respectively, over the standard processing case and degradations of 0.7 dB, 0.9 dB, 0.7 dB and 0.9 dB, respectively, over the interference free counterpart in Section 3, demonstrating preservation of the spectral notch in the PRO-FM waveform to mitigate interference.
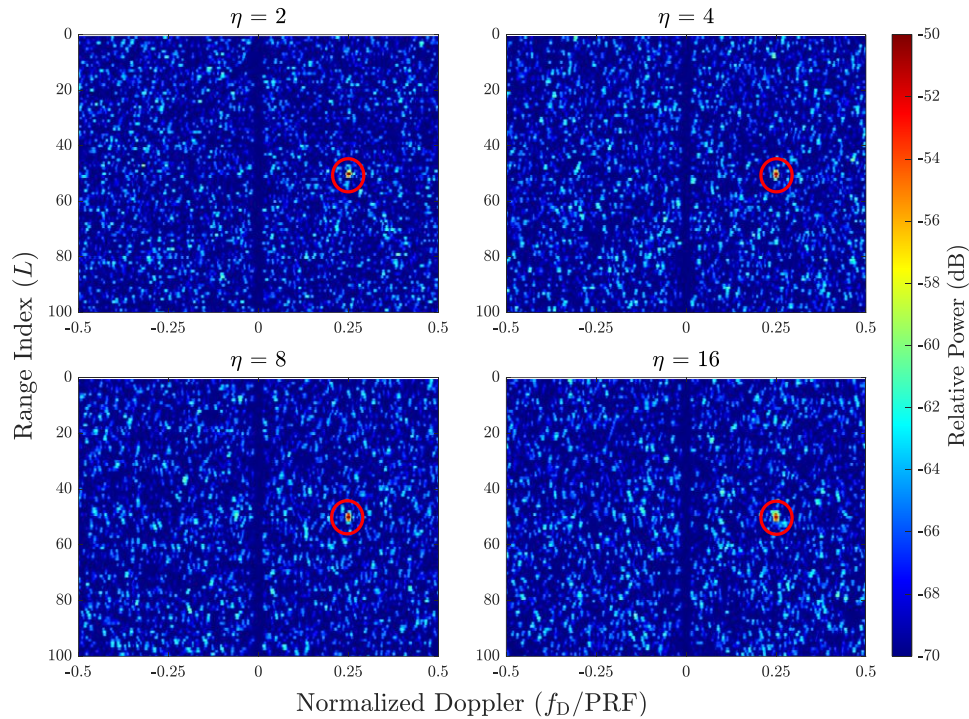
Figure 63: RD maps of simulation for a CPI of PRO-FM waveforms with a stationary notch plus stationary OFDM interference and $\eta = 2$, 4, 8 and 16 using standard processing and NIMPC with clutter cancellation

Figure 64 shows the RD map using standard processing for the simulation of a CPI of PRO-FM waveforms with a spectral notch that hops 10 times during the CPI, persisting at each location for 10 pulses, to accommodate the introduction of spectrally hopping narrowband OFDM interference, for all cases of η considered. The scatterer is now somewhat discernible for $\eta = 2$ and is obscured for values of $\eta = 4$, 8 and 16. While the spectral notch is hopping to avoid the spectrally agile interference successfully, the severity of the RSM has become detrimental enough to obscure the scatterer. The values of δ for Figure 64 are -67.8 dB, -67.0 dB, -66.3 dB and -66.0 dB for values of $\eta = 2$, 4, 8 and 16, respectively. These represent degradations caused by the introduction of hopping interference of 0.6 dB, 0.5 dB, 0.4 dB and 0.5 dB, respectively, over the interference-free counterpart indicating that the spectral notch has mitigated most of the interference power, although the scatterer is still obscured due to RSM and residual, unmitigated interference.
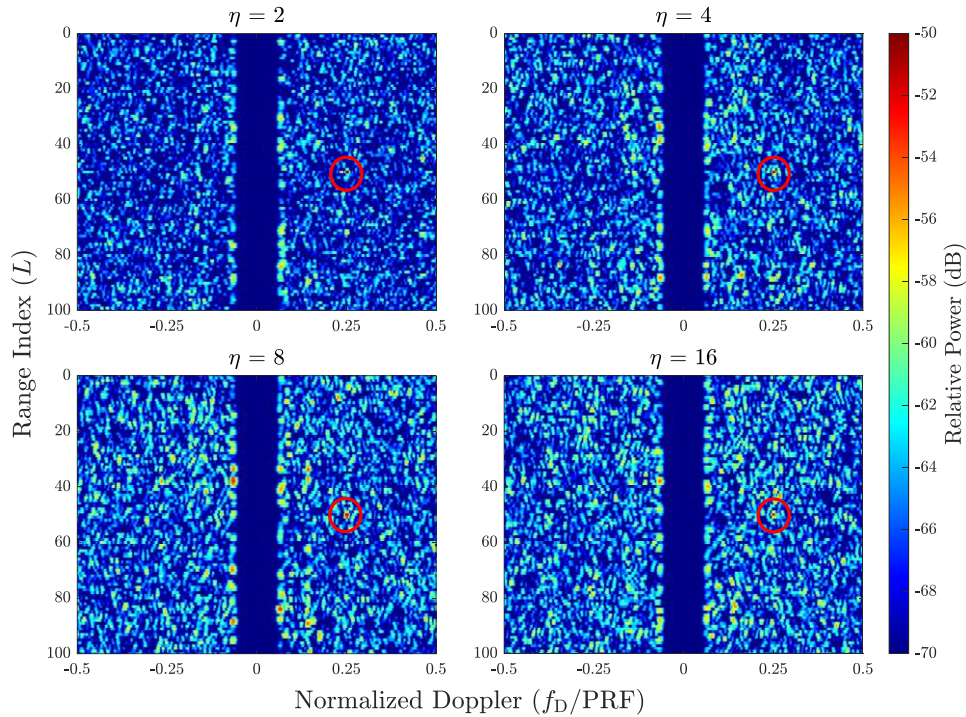
Figure 64: RD maps of simulation for a CPI of PRO-FM waveforms with a hopping notch changing locations every 10 pulses plus hopping OFDM interference and $\eta = 2, 4, 8$ and 16 using standard processing and projection-based clutter cancellation

Figure 65 shows the RD map using NIMPC for the simulation of a CPI of PRO-FM waveforms with a spectral notch that hops 10 times during the CPI, persisting at each location for 10 pulses, to accommodate the introduction of spectrally hopping narrowband OFDM interference, for all cases of η considered. The scatterer is now clearly visible in an all cases, showing that NIMPC processing has successfully accounted for the RSM, while maintaining the spectral notch of the waveform to mitigate the interference. The values of δ for Figure 65 are -70.1 dB, -70.0 dB, -69.9 dB and -69.9 dB for values of $\eta = 2, 4, 8$ and 16, respectively. These represent improvements of 2.3 dB, 3.0 dB, 3.6 dB and 3.9 dB, respectively, over the standard processing case and degradations of 1.0 dB, 1.2 dB, 1.3 dB and 1.3 dB, respectively, over the interference free counterpart in Section 3, demonstrating preservation of the hopping spectral notch in the PRO-FM waveform (although not preserving quite to the degree of the stationary notch PRO-FM waveform case) to mitigate interference.
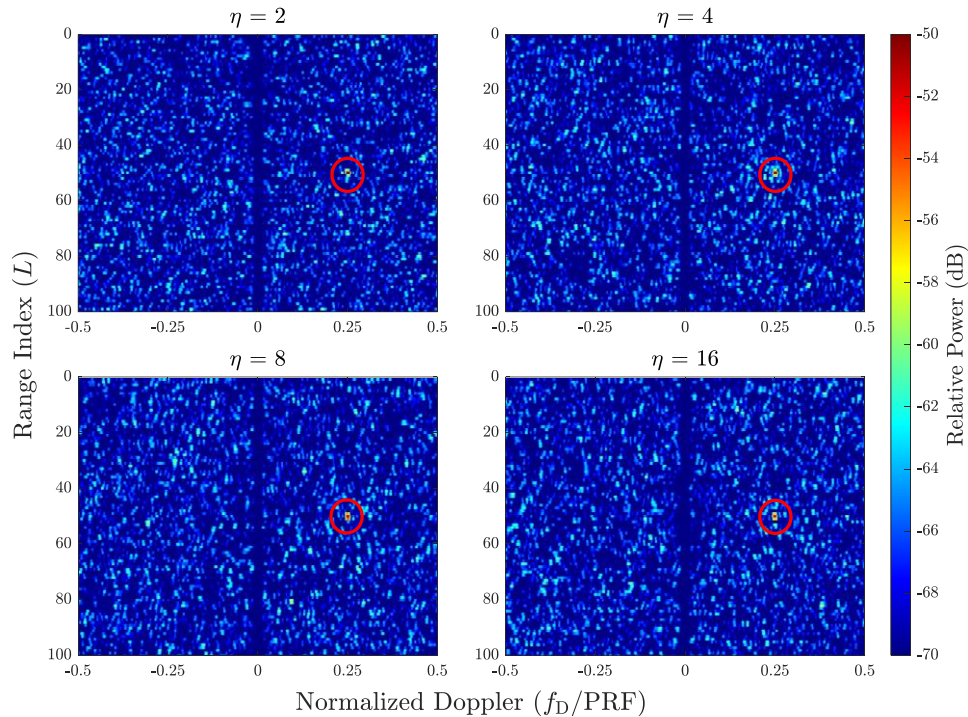
Figure 65: RD maps of simulation for a CPI of PRO-FM waveforms with a hopping notch changing locations every 10 pulses plus hopping OFDM interference and η = 2, 4, 8 and 16 using NIMPC with clutter cancellation

Figure 66 shows the RD map using standard processing for the simulation of a CPI of PRO-FM waveforms with a spectral notch that hops 100 times during the CPI, persisting at each location for one pulse, to accommodate the introduction of spectrally hopping narrowband OFDM interference, for all cases of η considered. The scatterer is completely obscured for each case of η showing that once again, while the spectral notch is hopping to avoid the spectrally agile interference successfully, the severity of the RSM is detrimental enough to obscure the scatterer. The values of δ for Figure 66 are -65.1 dB, -64.1 dB, -63.5 dB and -63.2 dB for values of η = 2, 4, 8 and 16, respectively. These represent degradations caused by the introduction of hopping interference of 0.3 dB, 0.2 dB, 0.2 dB and 0.2 dB, respectively, over the interference-free counterpart indicating that the spectral notch has mitigated most of the interference power, although the scatterer is still obscured due to RSM.
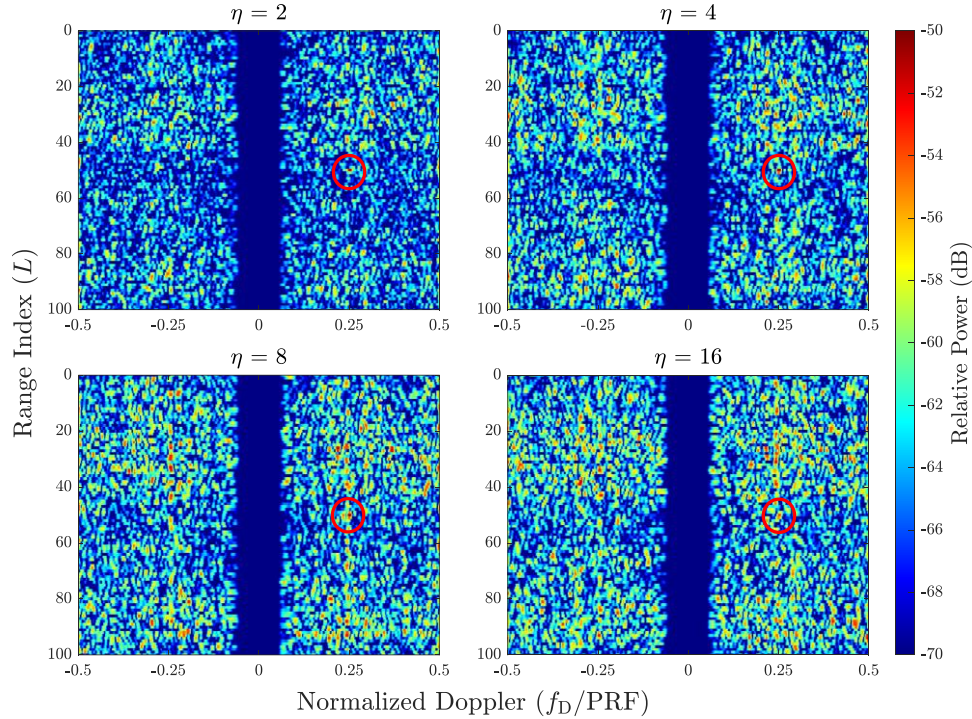
Figure 66: RD maps of simulation for a CPI of PRO-FM waveforms with a hopping notch changing locations every single pulse plus hopping OFDM interference and $\eta = 2, 4, 8$ and 16 using standard processing and projection-based clutter cancellation

Figure 67 shows the RD map using NIMPC for the simulation of a CPI of PRO-FM waveforms with a spectral notch that hops 100 times during the CPI, persisting at each location for 1 pulse, to accommodate the introduction of spectrally hopping narrowband OFDM interference, for all cases of η considered. The scatterer is clearly visible in an all cases, showing that NIMPC processing has successfully accounted for the RSM, while maintaining the spectral notch of the waveform to mitigate the interference. The values of δ for Figure 67 are -70.2 dB, -70.1 dB, -70.1 dB and -70.0 dB for values of $\eta = 2, 4, 8$ and 16, respectively. These represent improvements of 5.1 dB, 6.0 dB, 6.6 dB and 6.8 dB, respectively, over the standard processing case and degradations of 0.9 dB, 1.0 dB, 1.1 dB and 1.1 dB, respectively, over the interference free counterpart in Section 3, demonstrating preservation of the hopping spectral notch in the PRO-FM waveform to mitigate interference, to about the same degree as the case where the spectral notch hopped 10 times during the CPI, persisting at each location for 10 pulses.
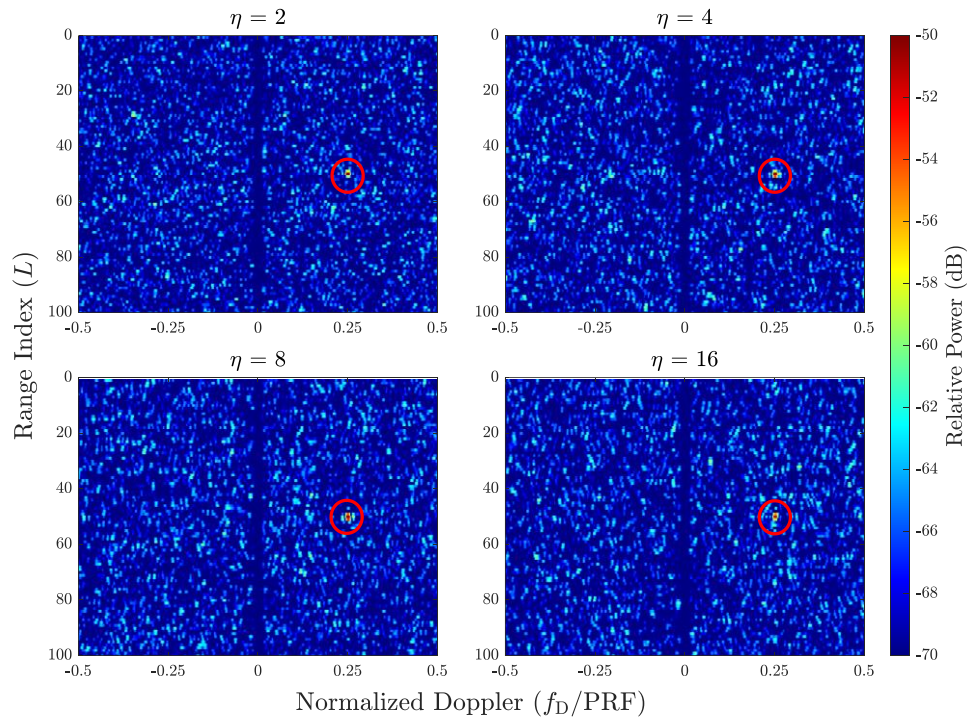
Figure 67: RD maps of simulation for a CPI of PRO-FM waveforms with a hopping notch changing locations every single pulse plus hopping OFDM interference and $\eta = 2$, 4, 8 and 16 using NIMPC with clutter cancellation

Table 3 provides a summary of the δ metric values presented in the simulation results of Sections 3 and 4 of this chapter.

Table 3: Summary of δ values for each simulation case of Sections 3 and 4 of Chapter 4

	Matched Filter			
	$\eta = 2$	$\eta = 4$	$\eta = 8$	$\eta = 16$
PRO-FM w/o Stationary Interference	-69.7	-69.2	-68.3	-68.0
PRO-FM w/ Stationary Interference	-62.3	-61.5	-60.9	-60.4
Notched PRO-FM w/o Stationary Interference	-69.2	-68.3	-67.4	-67.1
Notched PRO-FM w/ Stationary Interference	-68.7	-67.9	-67.1	-66.7
10 Hop Notched PRO-FM w/o Hopping Interference	-68.4	-67.5	-66.7	-66.5
10 Hop Notched PRO-FM w/ Hopping Interference	-67.8	-67.0	-66.3	-66.0
100 Hop Notched PRO-FM w/o Hopping Interference	-65.4	-64.3	-63.7	-63.4
100 Hop Notched PRO-FM w/ Hopping Interference	-65.1	-64.1	-63.5	-63.2
LFM w/o Stationary Interference	-71.3			
LFM w/ Stationary Interference	-63.6			

	NIMPC			
	$\eta = 2$	$\eta = 4$	$\eta = 8$	$\eta = 16$
PRO-FM w/o Stationary Interference	-71.1	-71.2	-71.2	-71.1
PRO-FM w/ Stationary Interference	-62.4	-61.6	-61.1	-60.6
Notched PRO-FM w/o Stationary Interference	-71.2	-71.1	-71.1	-71.1
Notched PRO-FM w/ Stationary Interference	-70.5	-70.2	-70.4	-70.2
10 Hop Notched PRO-FM w/o Hopping Interference	-71.1	-71.2	-71.2	-71.2
10 Hop Notched PRO-FM w/ Hopping Interference	-70.1	-70.0	-69.9	-69.9
100 Hop Notched PRO-FM w/o Hopping Interference	-71.1	-71.1	-71.2	-71.1
100 Hop Notched PRO-FM w/ Hopping Interference	-70.2	-70.1	-70.1	-70.0
LFM w/o Stationary Interference	-71.1			
LFM w/ Stationary Interference	-63.5			

4.5 Experimental Evaluation of NIMPC in Addressing RSM

The efficacy of joint-domain processing with NIMPC to address RSM from spectrally hopping notches in PRO-FM waveforms accommodating narrowband interference in the operating band is now assessed using physical radar emissions and loopback captured OFDM interference in an MTI scenario, as was first demonstrated in [83, 96, 102]. Figure 68 shows a picture of the experimental radar testbed setup utilized for the MTI operation. Vehicles travelling north and south on Iowa Street near the intersection of 23rd Street in Lawrence, KS are illuminated with low power emissions (~ 21 dBm at the input to the transmit antenna) to perform the MTI function. The vehicle

traffic is oriented mostly radially with radar testbed transmit and receive antennas. Figure 69 provides a summary diagram (non-comprehensive) of the radar testbed setup.
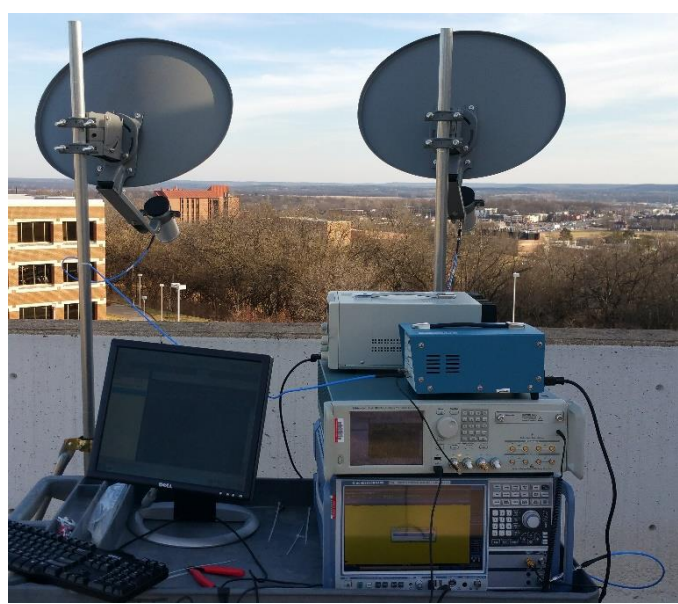
Figure 68: Picture of experimental testbed setup on the roof of Nichols Hall at the University of Kansas with illuminated intersection of 23rd and Iowa Streets visible approximately 1.1 km away from the testbed
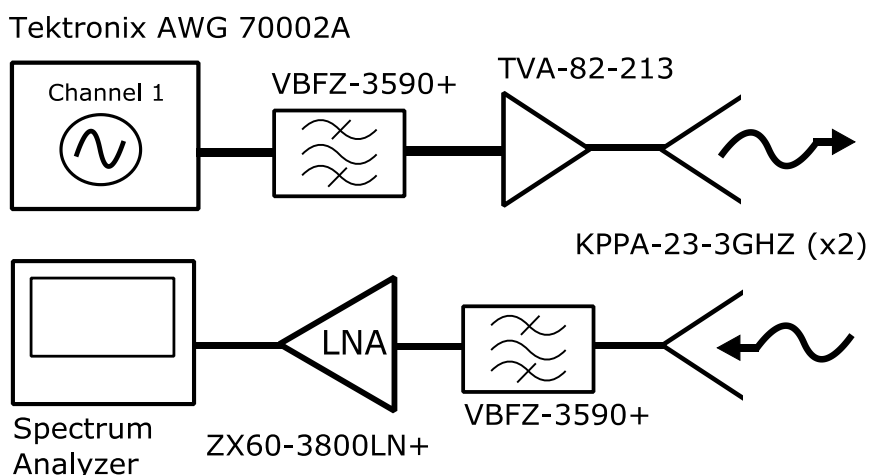
Figure 69: Diagram of experimental testbed used for MTI operation [83]

All radar waveforms tested are generated physically on a Tektronix 70002A arbitrary waveform generator (AWG) at a sample rate of 10 gigasamples/second (GS/s) and transmitted at a center frequency of 3.55 GHz. Subsequent backscatter is collected by a Rohde & Schwarz real-time spectrum analyzer (RSA), downconverted to complex baseband and sampled at a rate of 200

MS/s I/Q. Loopback captures (minus the transmit/receive antennas) for each radar waveform are captured and used to perform pulse compression matched filtering and generate NIMPC filters. Three radar waveform test sets are physically transmitted: 1) LFM, 2) PRO-FM, and 3) Notched PRO-FM, each with $BT = 200$ (with $B = 100$ MHz and $T = 2$ µs), $K = 2$ (so $N = 400$ baseband samples per waveform) and CPIs of $M = 125$ pulses each at a PRF of 1.25 kHz (resulting in a CPI length of 100 ms). The two PRO-FM radar waveform test cases are interleaved together and transmitted as a single CPI, while the LFM radar waveform is transmitted as a separate CPI directly afterwards, during the same emission. This provides a consistent comparison across the same illuminated scene, with the assumption that the moving vehicles velocities have changed a negligible amount during the length of a CPI (i.e., no hard accelerating or braking). Processing is performed on the backscatter collected for each test case both with and without the presence of narrowband interference. Two methods of processing are considered to generate a RD map for each test case, 1) standard matched filter pulse compression with Doppler processing (no windowing/tapering) and a projection-based clutter notch with $Z = 5$ principal singular values, and 2) joint-domain processing with clutter cancellation is performed via NIMPC using $Q = 3$ clutter notches.

Narrowband interference takes the form of OFDM with 8 subcarriers (randomly modulated with 4-QAM symbols) and 10 MHz instantaneous bandwidth. The center frequency of the OFDM signal is changed on every single pulse, representing a random hopping throughout the radar 3-dB operating band B. The OFDM interference is not transmitted through an antenna, but rather captured in a loopback configuration using the same testbed and subsequently power scaled and synthetically added with the captured backscatter of the radar test waveform, simulating an environment where hopping narrowband interference is present in the radar operating band and

must be accommodated by the radar system. Each OFDM interference signal is power scaled such that the SIR is 20 dB (over the entire signal/interference time duration of each PRI) before being synthetically added with the captured backscatter of the radar test waveform. It should be noted that the "signal" in this case will also include thermal noise from the radar receiver.

Figure 70 shows the heat map of the transmit LFM waveform spectrum for each pulse for the physical radar MTI experiment. As expected, the spectral energy is concentrated compactly into the 100 MHz 3-dB bandwidth. Figure 71 shows the heat map of the transmit PRO-FM (notch-free) waveform spectrum for each pulse for the physical radar MTI experiment. The spectral energy is not as compacted into the 3-dB bandwidth, which agrees with results observed thus far. Figure 72 shows the heat map of the spectrally notched PRO-FM waveform spectrum for each pulse for the physical radar MTI experiment. The spectral notch is hopping its location each pulse/PRI to accommodate the spectrally hopping narrowband interference present in the radar operating band. Finally, Figure 73 shows an example spectrum plot of the backscatter collected at the radar receiver for a single PRI for each radar waveform test case in the MTI experiment. The spectrum of the loopback-captured and power scaled OFDM interference for the corresponding PRI is shown on each plot also before synthetic combination of the two signals. The OFDM interference signal is not as spectrally compact as the OFDM interference of the simulation in Section 4, because a real OFDM signal is being represented here which has a degree of spectral-off when physically generated and captured. Still, the spectral notch in the PRO-FM waveform is able to accommodate most of the interference signal's power spectrum, with the expectation that more degradation to the processed RD map with the presence of interference will be experienced than the simulation cases of Section 4, due to the spectral roll-off of the OFDM interference.
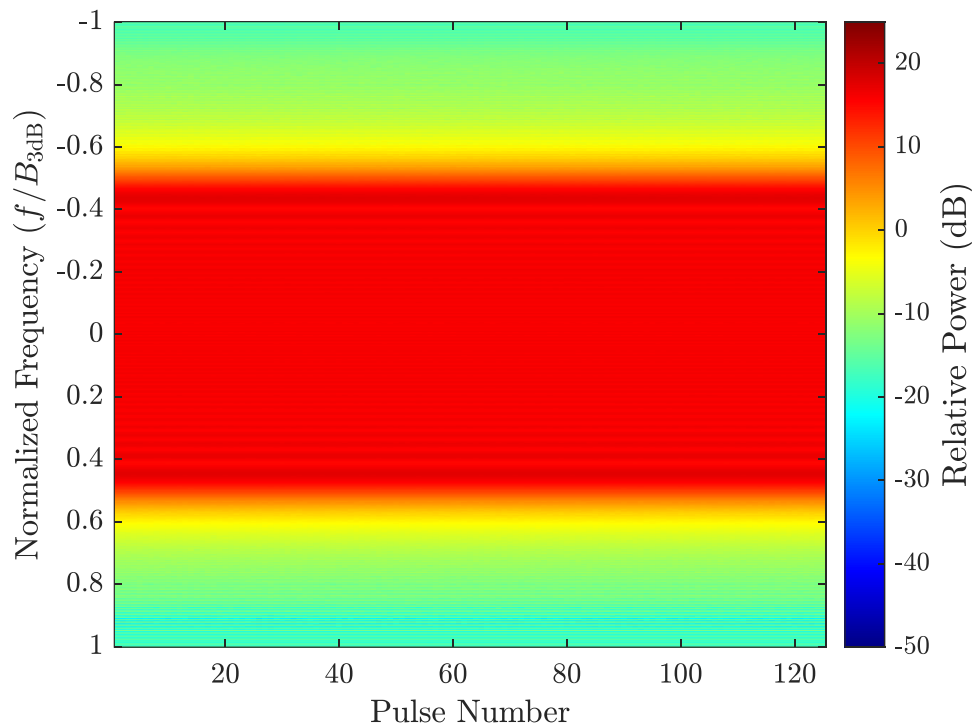
Figure 70: Transmit spectrum heat map of LFM waveform in physical radar MTI experiment
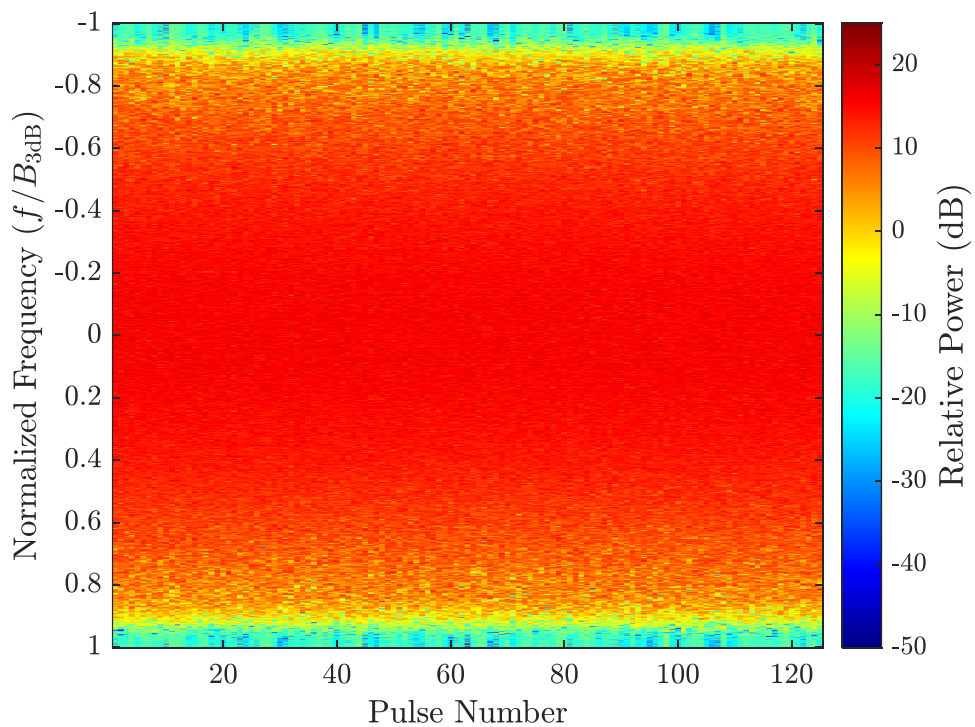
Figure 71: Transmit spectrum heat map of notch-free PRO-FM waveform in physical radar MTI experiment
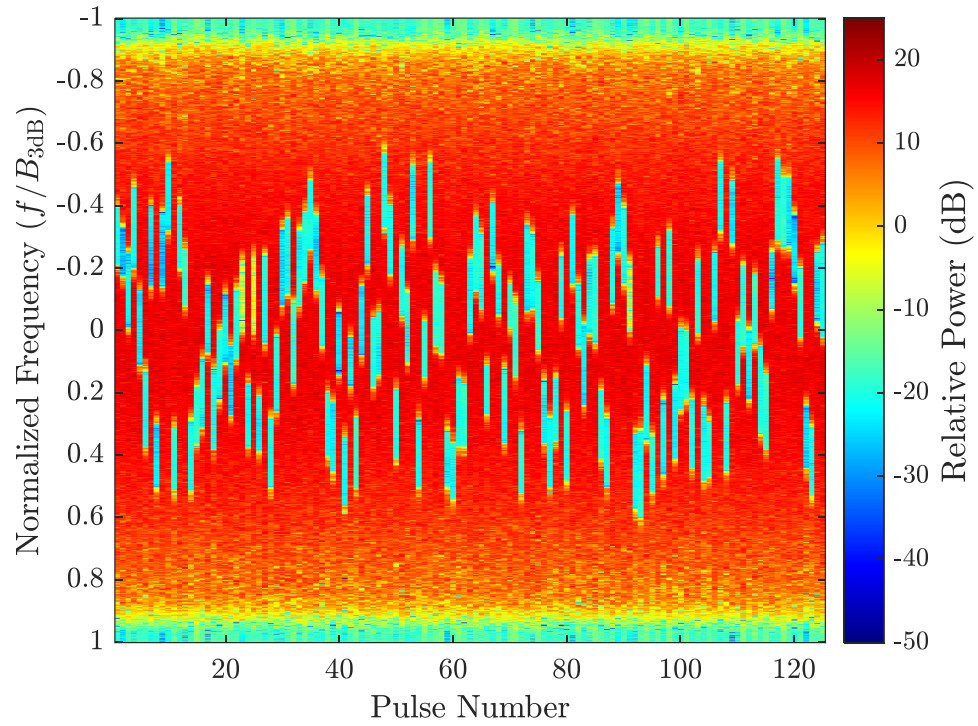
Figure 72: Transmit spectrum heat map of spectrally notched PRO-FM waveform accommodating spectrally hopping narrowband OFDM interference in physical radar MTI experiment
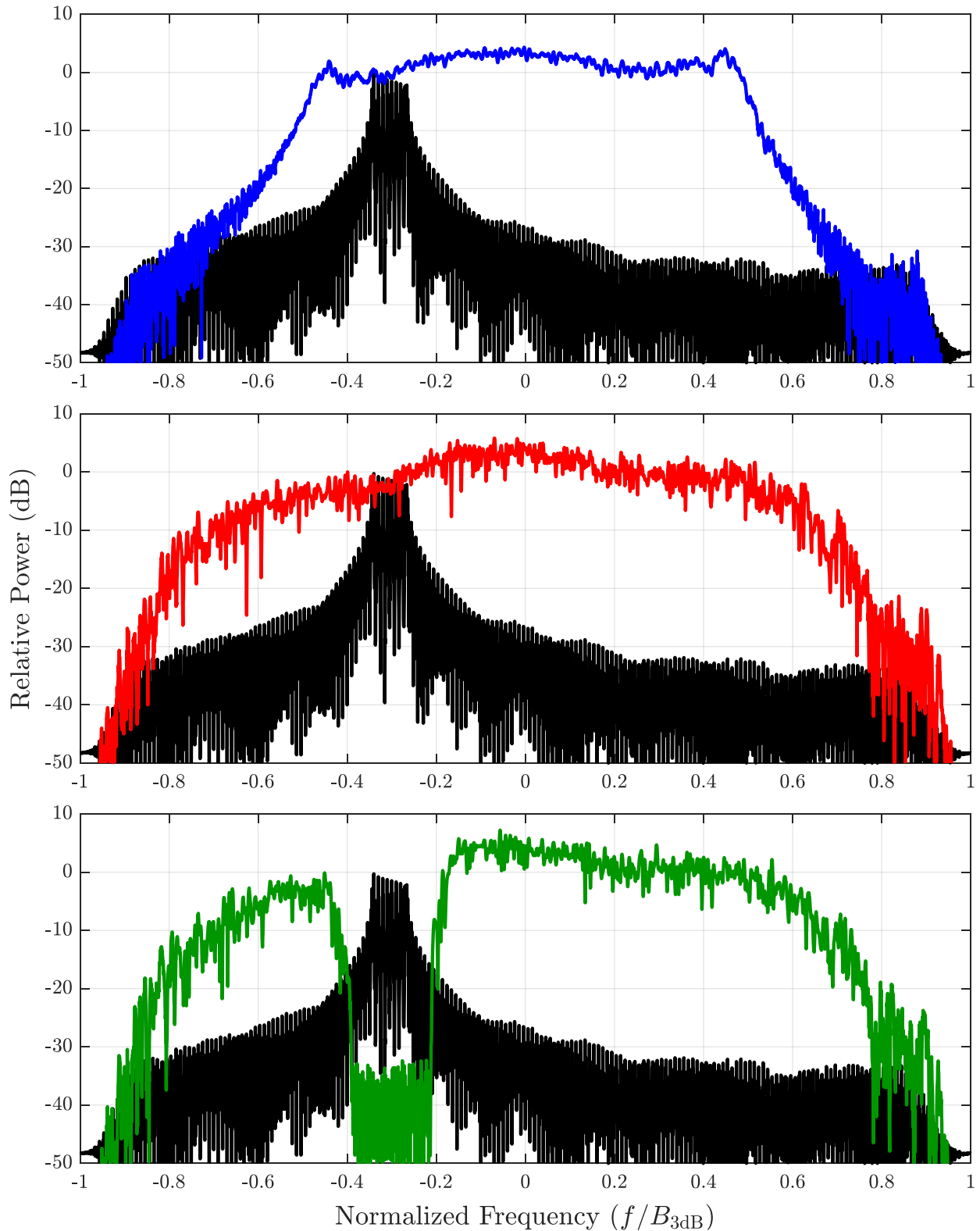
Figure 73: Example spectrum plots of captured backscatter in radar MTI experiment for LFM (top, blue), PRO-FM (middle, red) and notched PRO-FM (bottom, green) with power scaled, loopback captured OFDM interference signal (black)

Figure 74 shows the RD map formed for the case of a LFM transmit waveform CPI without the introduction of OFDM interference using standard processing and no clutter cancellation. This case is shown to illustrate the presence of large power clutter scatterers in the traffic intersection caused by large near-by buildings. All subsequent results shown will incorporate clutter cancellation. Figure 75 shows the RD map formed for the case of a transmit LFM waveform CPI without the introduction of OFDM interference using standard processing and projection-based clutter cancellation. This result will provide a baseline comparison for the remainder of the test cases for the MTI experiment. Many moving vehicles are present, travelling both towards and away from the radar testbed at varying velocities, in the traffic intersection located ~ 1.1 km away from the radar testbed, as indicated by their scattering power present in Figure 75. Next, Figure 76 shows the RD map for the LFM transmit waveform CPI with the synthetic combination of the in-band OFDM interference to the collected backscatter. The addition of interference has completely obscured all moving scatterers, as expected, since the LFM waveform is not capable of mitigating the in-band interference.

A modified version of the PSF metric, δ, in (3.5) can once again be used here as a means for comparison across each test case by measuring the amount of residual energy in the RD map in specified regions. The regions considered here are the range swath of 950 meters to 1250 meters and Doppler velocities greater than 16 m/s and less than -16 m/s. These regions exclude the scattering of vehicles in the traffic intersection but do include possible smearing of clutter in the traffic intersection across all Doppler velocities due to the presence of large buildings in the intersection, as demonstrated by Figure 74. The value of δ for Figure 75 is -97.9 dBm and for Figure 76 is -75.3 dBm. Note that the LFM transmit waveform CPI test case was not processed using NIMPC, as no benefit was observed applying NIMPC to LFM waveforms in Section 3.
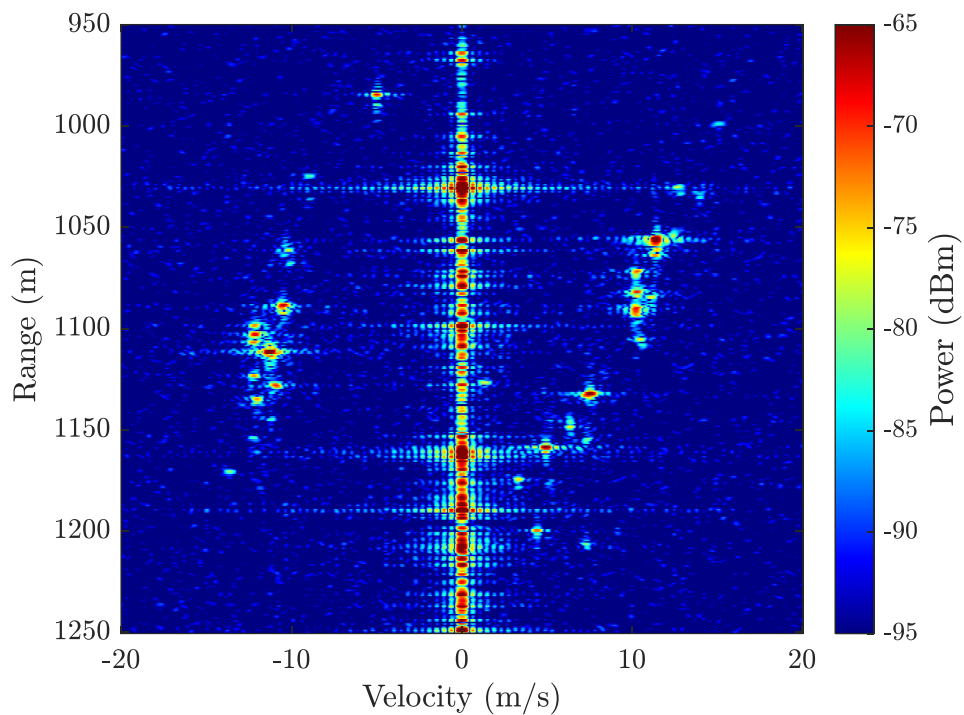
Figure 74: RD map of LFM transmit waveform case for physical radar MTI experiment using standard processing without clutter cancellation
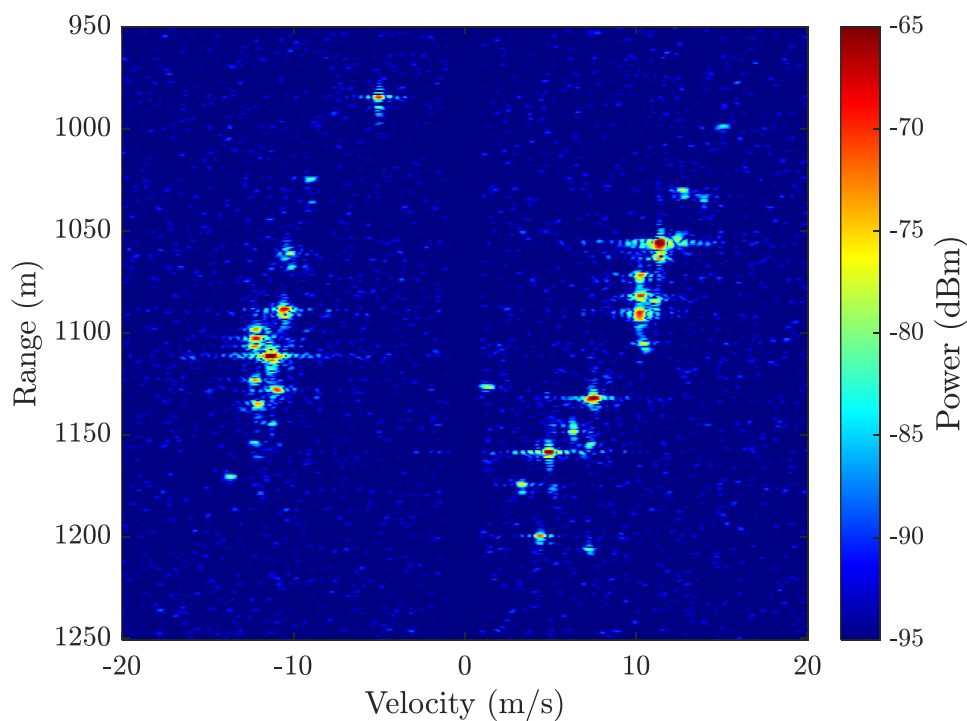
Figure 75: RD map of LFM transmit waveform case for physical radar MTI experiment using standard processing with projection-based clutter cancellation
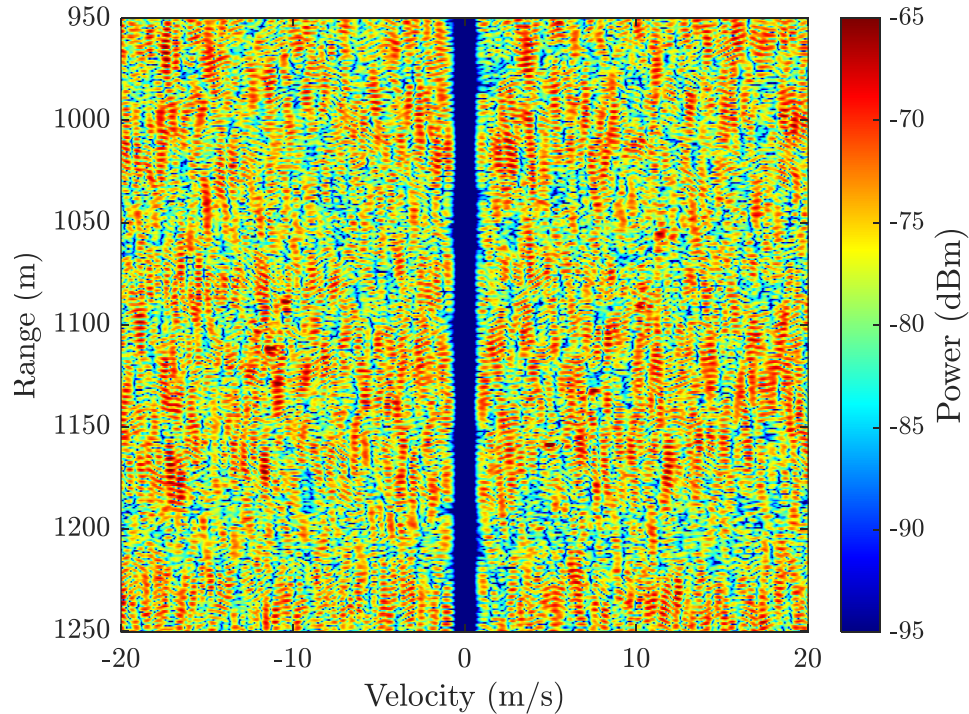
Figure 76: RD map of LFM transmit waveform case for physical radar MTI experiment, with the introduction of in-band interference, using standard processing with projection-based clutter cancellation

Next, Figure 77 shows the RD map formed for the case of a transmit notch-free PRO-FM waveform CPI without the introduction of OFDM interference using standard processing and projection-based clutter cancellation. The same moving vehicles as the LFM test case are visible in the illuminated scene, with a noticeable increase in the background floor power level for the PRO-FM waveform case when comparing Figure 77 to Figure 75. The value of δ for Figure 77 is -96.2 dBm, representing an increase of 1.7 dBm over the LFM test case due to introduction of RSM from the PRO-FM CPI with unique waveforms emitted every pulse. Figure 78 shows the RD map formed for the case of a transmit notch-free PRO-FM waveform CPI without the introduction of OFDM interference using NIMPC in clutter cancellation. There is a noticeable reduction in the background floor using NIMPC, and the value of δ for Figure 78 is -97.5 dBm, an improvement of 1.3 dBm over Figure 77 and only 0.4 dB higher than the LFM case of Figure 75, showing that NIMPC has successfully eliminated almost all of the RSM caused by the PRO-FM waveform CPI.
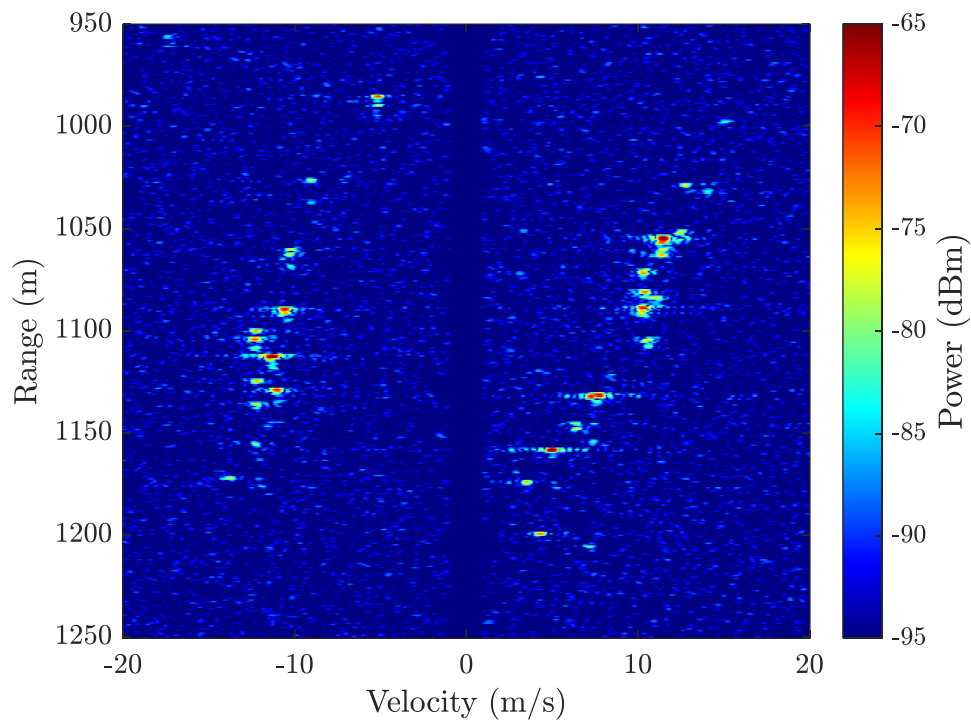
Figure 77: RD map of notch-free PRO-FM transmit waveform case for physical radar MTI experiment using standard processing with projection-based clutter cancellation
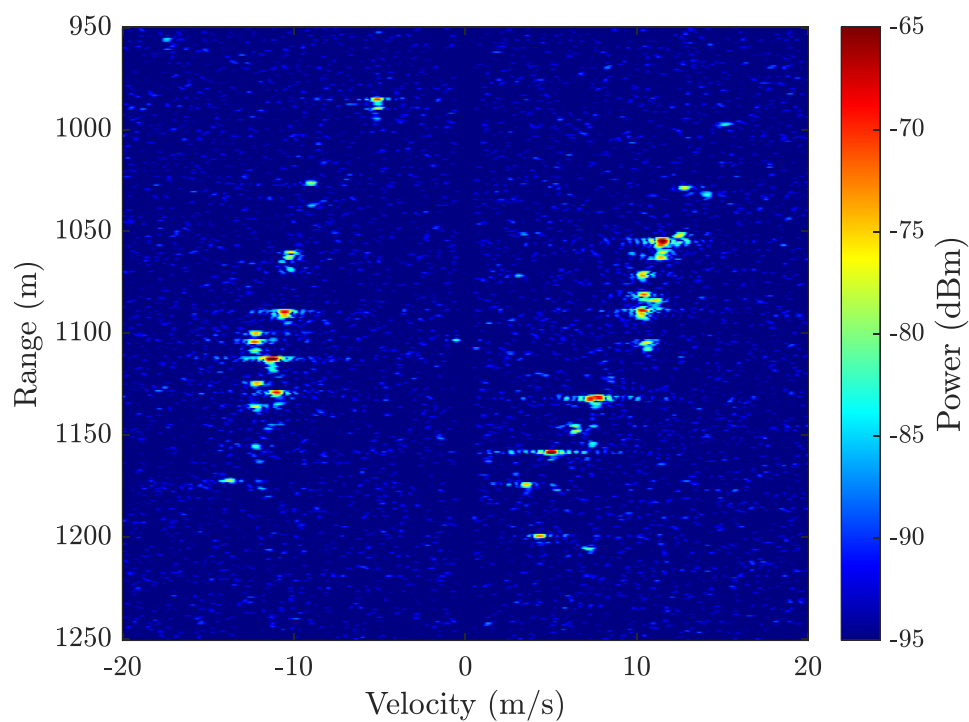
Figure 78: RD map of notch-free PRO-FM transmit waveform case for physical radar MTI experiment using NIMPC with clutter cancellation

Figure 79 shows the RD map formed for the case of a transmit notch-free PRO-FM waveform CPI with the synthetic combination of the in-band OFDM interference to the collected backscatter using standard processing and projection-based clutter cancellation. Figure 80 shows the same RD map but using NIMPC with clutter cancellation. The addition of interference has completely obscured all moving scatterers, regardless of processing method, with the exception of maybe some of the very high-power scatterers, however their distinction as true scatterers versus just unmitigated interference power smeared across the RD map cannot be made. This result is expected since the PRO-FM waveform is not designed with spectral notches to mitigate the in-band interference. The value of δ for Figure 79 is -76.5 dBm and for Figure 80 is -76.4 dBm.
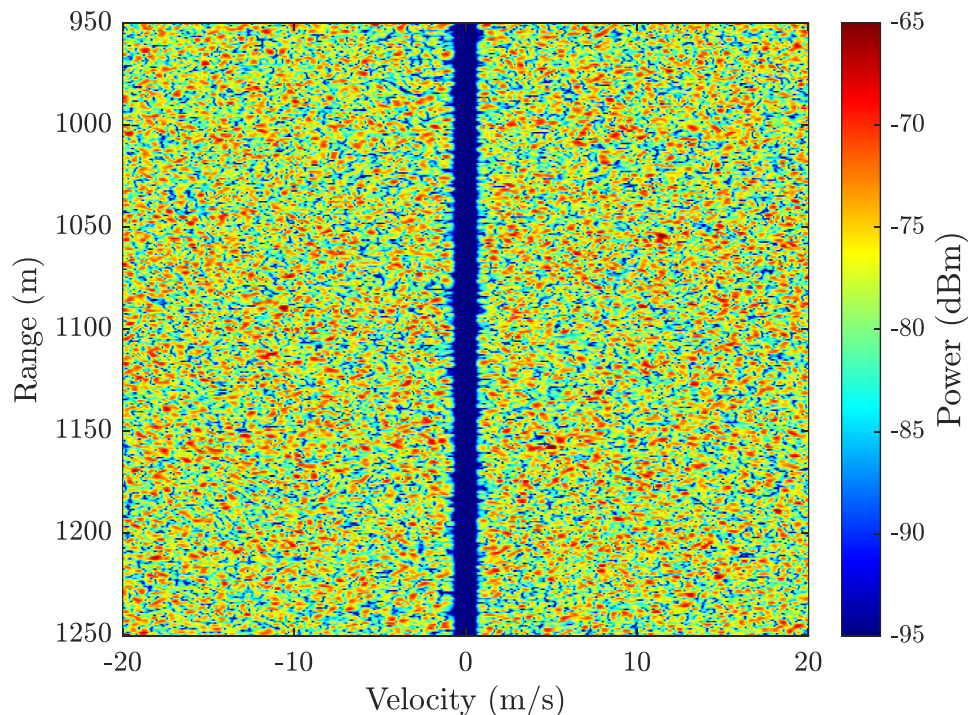
Figure 79: RD map of notch-free PRO-FM transmit waveform case for physical radar MTI experiment, with the introduction of in-band interference, using standard processing with projection-based clutter cancellation
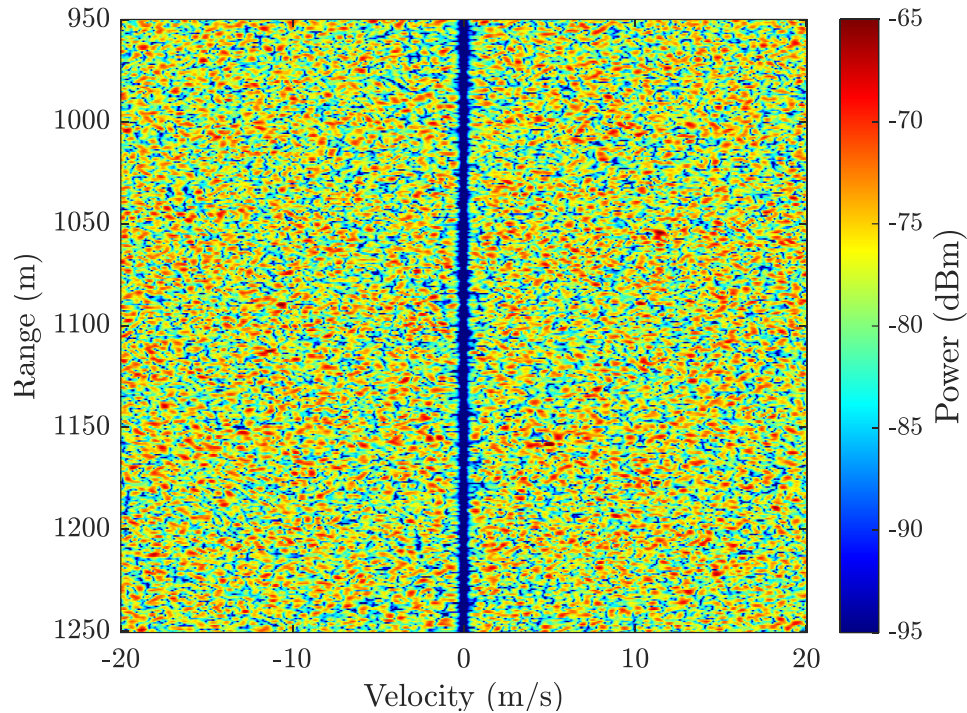
Figure 80: RD map of notch-free PRO-FM transmit waveform case for physical radar MTI experiment, with the introduction of in-band interference, using NIMPC with clutter cancellation

Figure 81 shows the RD map formed for the case of a spectrally notched PRO-FM waveform CPI, where the spectral notch changes location every pulse in response to hopping in-band interference, without the introduction of OFDM interference, using standard processing and projection-based clutter cancellation. Many of the same moving vehicles as the notch-free PRO-FM test case are visible in the illuminated scene, but now with noticeable "streaking" of energy across Doppler in many of the range cells of the illuminated scene. These streaks correspond to the high-power clutter (buildings) shown in Figure 74, where clutter cancellation was not utilized, and have obscured the presence of many of the lower RCS moving vehicles. Figure 82 shows the same RD map but using NIMPC with clutter cancellation. The Doppler streaking due to high-power clutter has essentially been eliminated by utilizing joint-domain processing via NIMPC. Some streaking in Doppler associated with the higher power moving vehicles is still present, and a method to mitigate this is a topic of future research. The value of δ for Figure 81 is -91.3 dBm and for Figure 82 is -97.3 dBm, representing degradations of 4.9 dBm and 0.2 dBm, respectively,

over the notch-free PRO waveform transmit case. This shows that NIMPC has essentially eliminated all of the RSM due to the hopping spectral notch.
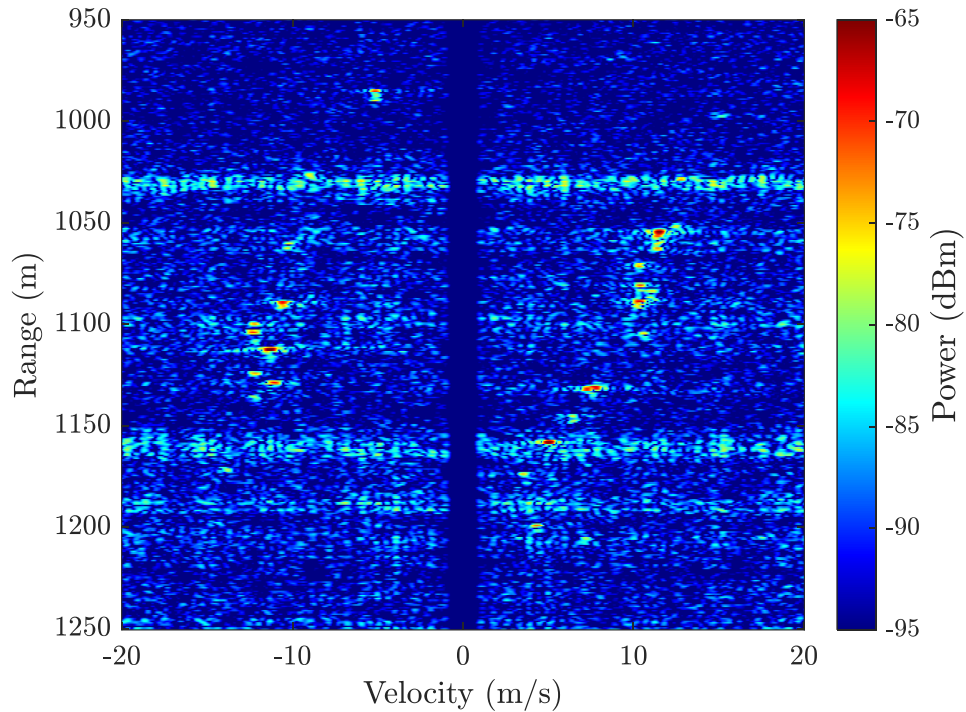
Figure 81: RD map of notched PRO-FM transmit waveform case, where the spectral notch changes location every pulse, for physical radar MTI experiment using standard processing with projection-based clutter cancellation
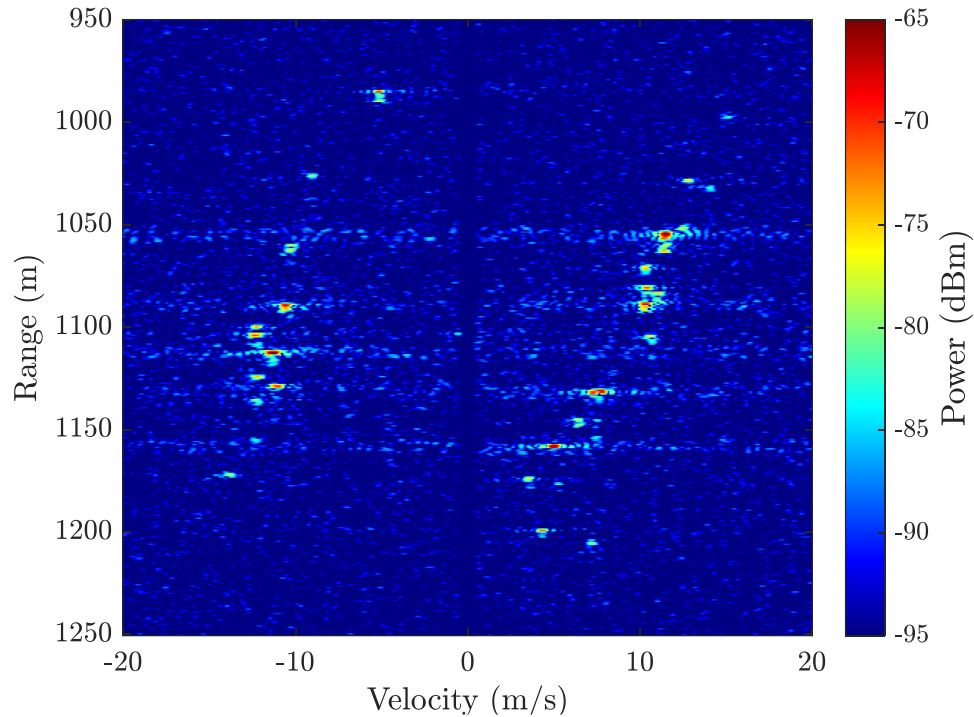
Figure 82: RD map of notched PRO-FM transmit waveform case, where the spectral notch changes location every pulse, for physical radar MTI experiment using NIMPC with clutter cancellation

Figure 83 shows the RD map formed for the case of a spectrally notched PRO-FM waveform CPI, where the spectral notch changes location every pulse in response to hopping in-band interference, with the synthetic combination of the in-band OFDM interference to the collected backscatter, using standard processing and projection-based clutter cancellation. Many of the higher power vehicles are discernible with the same "streaking" of energy across Doppler noticeable as in Figure 81. Also present now is an increased background floor when compared to the interference-free case of Figure 81, caused by interference power which has not been completely mitigated by the spectral notch due to the spectral roll-off of the interference shown in Figure 73. This leaked interference energy causes obfuscation of many of the lower RCS vehicles in the scene.

Figure 84 shows the same RD map but using NIMPC with clutter cancellation. The Doppler streaking due to high-power clutter has essentially been eliminated by utilizing joint-domain processing via NIMPC, but the increased background floor is still present due to the unmitigated

interference. The value of δ for Figure 83 is -87.1 dBm and for Figure 84 is -88.8 dBm, representing degradations of 4.2 dBm and 8.5 dBm, respectively, over the interference free case, and improvements of 10.6 dBm and 12.4 dBm, respectively, over the notch-free PRO-FM case with interference. This shows that while NIMPC can eliminate RSM caused by a spectrally hopped notched PRO-FM waveform, performance is still limited by the ability of the radar system to sufficiently mitigate the in-band interference via spectral notches of sufficient depth.
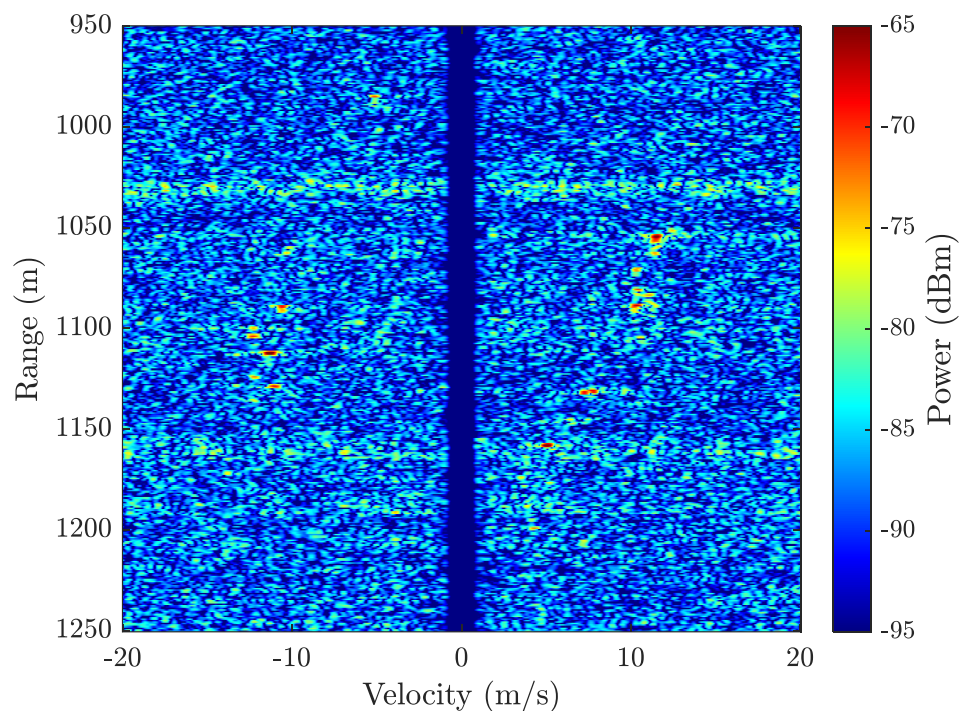
Figure 83: RD map of notched PRO-FM transmit waveform case, where the spectral notch changes location every pulse, with the introduction of in-band interference, for physical radar MTI experiment using standard processing with projection-based clutter cancellation
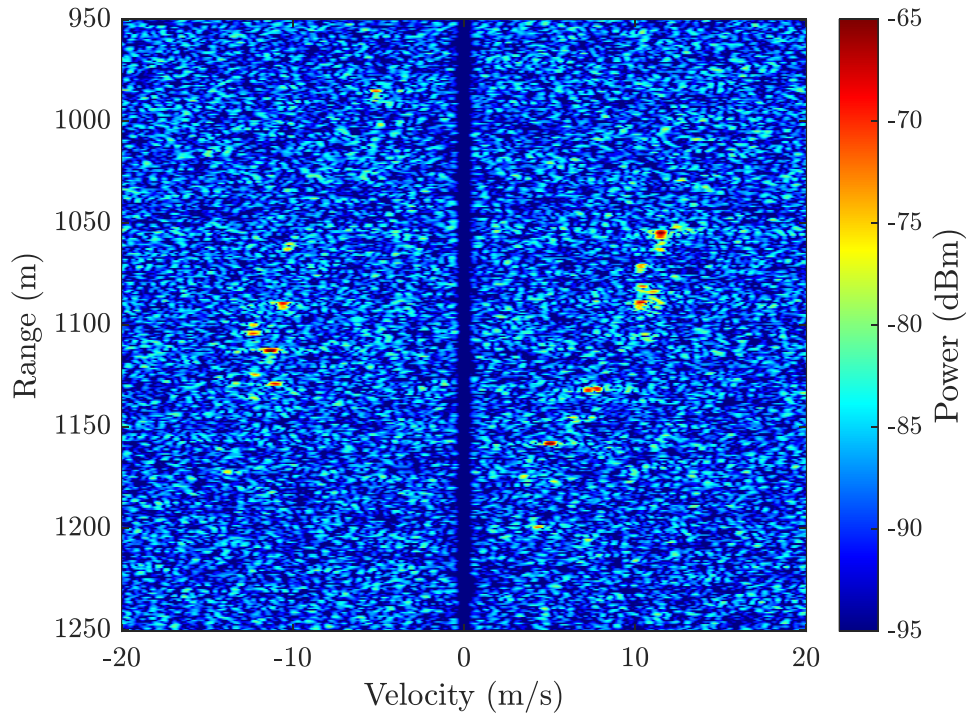
Figure 84: RD map of notched PRO-FM transmit waveform case, where the spectral notch changes location every pulse, with the introduction of in-band interference, for physical radar MTI experiment NIMPC with clutter cancellation

Investigation of spectral notch preservation in physically generated PRO-FM waveforms is given by Figure 85, where the spectrum is plotted for two pulses of the loopback captured transmit waveform CPI with hopped spectral notches and the spectrum of their associated NIMPC filters. For the first pulse, the NIMPC filter has a spectral notch which is about 10 dB shallower than what the associated optimized waveform has after loopback capture on hardware. This is on par with the result noticed in Figure 54 for the simulation conducted in Section 3. For the second pulse in Figure 85, the NIMPC filter has a notch depth essentially identical to that of its associated optimized waveform after loopback capture on hardware. The NIMPC filter of each pulse could theoretically mitigate more narrowband interference, if the interference had a tighter spectral roll-off than that observed for this test scenario as shown in Figure 73. Table 4 provides a summary of the δ values for each test case of the physical radar MTI experiment shown in this section.
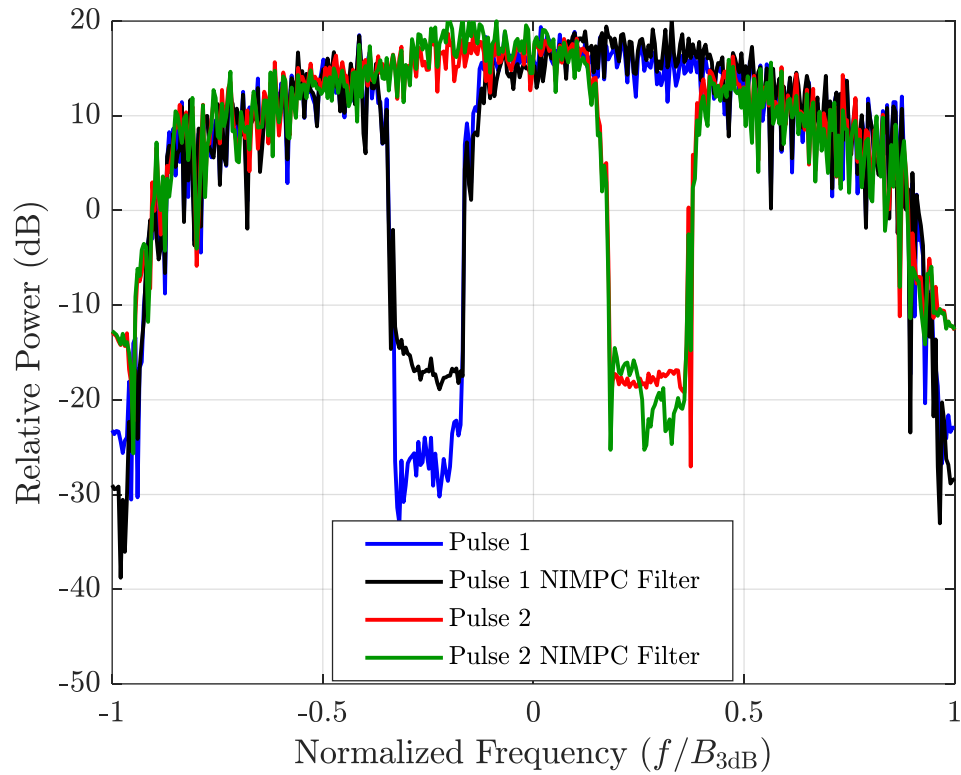
Figure 85: Example spectrum plots of two pulses of the spectrally notched PRO-FM waveforms used in the physical radar MTI experiment, along with their associated NIMPC filters

Table 4: Summary of δ values for each test case of the physical radar MTI experiment

	Matched Filter	NIMPC
LFM w/o Hopping Interference	-97.9	
LFM w/ Hopping Interference	-75.3	
PRO-FM w/o Hopping Interference	-96.2	-97.5
PRO-FM w/ Hopping Interference	-76.5	-76.4
Notched PRO-FM w/o Hopping Interference	-91.3	-97.3
Notched PRO-FM w/ Hopping Interference	-87.1	-88.8

Chapter 5: Tandem Hopped Radar and Communications

5.1 Introduction

The idea of tandemly hopping the spectral notch in a PRO-FM waveform with narrowband communications in the form of OFDM was first set about in [14]. In this work, a strategy known as THoRaCs was used to accommodate a cooperative communications system transmitting narrowband OFDM signals from a separate emitter than the radar waveform, the goal being a communications receiver in the illuminated operating environment being able to receive and demodulate the communications signal with little to no interference from the spectrally notched PRO-FM radar transmit waveform. It was shown in [14] how the combination of the collected radar backscatter from the illuminated environment and the coexisting OFDM signal could be used to perform radar processing across the full coherent band of the two signals, achieving performance fairly close to that of a transmit PRO-FM waveform without a spectral notch. Of course, this requires the radar system to have knowledge of the transmitted OFDM signal for each pulse, which is reasonable given cooperation of the systems.

The primary drawbacks to this approach are 1) the requirement of two separate transmitters to perform the dual radar and communications functions, and 2) the high peak-to-average power (PAPR) ratio known to be inherent to OFDM signals, which precludes their use in high power amplification. These drawbacks were addressed in [105-107] with creation of a new form of THoRaCs denoted as power efficient THoRaCs (PE-THoRaCs). In this new power-efficient approach, an optimization procedure was used to embed an OFDM communications signal into a PRO-FM radar waveform to create a single emission with little to no degradation to either function, while remaining the power efficient FM structure. The efficacy of this new approach was demonstrated via simulation in [106] and physical open-air experimentation in [108]. This new

approach was found to perform both functions so well that the older, dual signal approach was essentially "retired" in favor of the new, power-efficient approach and the acronym THoRaCs has subsequently been used to address the newer approach.

The remainder of this chapter is laid out as follows. Section 2 provides an overview of the THoRaCs optimization procedure. Section 3 shows simulation results for several different test cases demonstrating THoRaCs performance in both the radar and communications functions. Section 4 validates the utility of THoRaCs waveforms for radar operation via physical experimentation on a radar testbed in an MTI operating mode. Section 5 then provides experimental demonstration of the THoRaCs waveform for the communications function in both loopback and open-air hardware experiments.

5.2 Optimization of THoRaCs Waveforms

THoRaCs optimization is a two-stage procedure which considers the design of M unique pulsed FM waveforms with 3-dB bandwidth B and pulse duration T which is also required to embed N OFDM subcarriers modulated with arbitrary QAM constellation communications symbols. The two-stage optimization procedure serves to produce FM noise waveforms with good spectral containment and favorably low autocorrelation sidelobes like those produced with PRO-FM optimization in Chapter 2, while also containing communications symbols which can be demodulated at a communications receiver. The primary advantage of embedding an OFDM communications signal into the radar waveform is that only a single transmitter is required to perform the dual functions of radar and communications. THoRaCs optimization is a two-stage procedure, having many similarities to the single-stage, two-step PRO-FM optimization procedure of (3.1) and (3.2), which uses the degrees of design freedom afforded by the radar waveform BT to optimize a good radar FM noise waveform with an OFDM signal embedded within.

With proper choice of communications signal design parameters, THoRaCs retains all of the advantages of PRO-FM as a radar waveform, namely good spectral containment, FM structure and low autocorrelation sidelobes that are further reduced by coherent processing across the M waveforms in the CPI. Furthermore, with knowledge of the subcarrier locations in the waveform spectrum, the embedded communications signal in the optimized THoRaCs waveform can be demodulated with standard OFDM receiver processing. Simple OFDM receive processing requires an IFFT to be performed on the received signal, followed by estimation of the complex symbol modulated onto the OFDM subcarrier. It should be noted that this approach is different to that of constant envelope OFDM (CE-OFDM) presented in [109-111], which requires a more complex communications demodulation scheme on receive.

The first optimization stage consists of three sequential projection steps which serve to 1) shape the spectrum to a desired template, 2) place a notch in the spectral regions where communications carriers are to be located and then embed them and 3), enforce constant amplitude. Drawing comparison to the PRO-FM optimization of Chapter 3, the first and third steps of the stage-one optimization of THoRaCs are very similar to that of PRO-FM. The second optimization stage of THoRaCs consists of two more sequential projection steps with the goal of 1) embedding the communications carriers and 2) enforcing constant amplitude. The spectral shaping step of stage one is removed in stage two since a good approximation to the desired spectrum is generally obtained after first stage, thus allowing the second stage to focus on embedding the communications signal.

The THoRaCs optimization procedure is initialized with a random FM waveform $s_{0,m}(t)$ via either random phase codes or the PCFM framework, like with PRO-FM described in Chapter 3. The waveform initialization $s_{0,m}(t)$ is defined over time interval $-T/2 \leq t \leq +T/2$ for the mth

pulse. The communications signal which is desired to be embedded into the optimized waveform is denoted as $r_m(t)$, also defined over the same time interval of $-T/2 \leq t \leq +T/2$ as

$$r_m(t) = \sum_{n=0}^{N-1} a_{m,n} |c_{m,n}| \exp\left[j\left(2\pi f_{m,n} t + \angle c_{m,n}\right)\right]. \tag{5.1}$$

The frequency of the nth subcarrier for the mth pulse is represented by $f_{m,n}$, the QAM symbol (complex in general) embedded onto the nth subcarrier is $c_{m,n}$, $\angle(\bullet)$ produces the phase of the argument and $|\bullet|$ produces the amplitude of the argument. The term $a_{m,n}$ shapes the amplitude of the nth subcarrier for the mth pulse such that it is well-matched to the local spectrum energy around the subcarrier, thus avoiding spectral discontinuities. The form given in (5.1) is essentially the same as the definition of an OFDM signal given in (2.26), with the addition of the $a_{m,n}$ term.

The first projection step of stage one takes the form of

$$b_{k,m}(t) = \mathbb{F}^{-1}\left\{|G(f)| \exp\left(j\angle\mathbb{F}\{s_{k,m}(t)\}\right)\right\}, \tag{5.2}$$

in which the spectrum of $s_{k,m}(t)$ is matched to the power spectrum template $|G(f)|^2$ (which is super Gaussian) much like the first step of the PRO-FM optimization procedure. F and F^{-1} denote the Fourier and inverse Fourier transforms, respectively. Next, the second projection step enforces a (shallow) notch in the radar spectrum and inserts the communication signal $r_m(t)$ via

$$\tilde{b}_{k,m}(t) = P_{\perp r_m}\{b_{k,m}(t)\} + r_m(t), \tag{5.3}$$

where the operation $P_{\perp r_m}\{\bullet\}$ projects the argument onto the orthogonal complement of the frequencies where the subcarriers reside in the communications signal. Finally, since the output of the second stage will not be time-limited or constant amplitude, this can be enforced by the third, and final, step in the first stage by

$$s_{k+1,m}(t) = \begin{cases} \exp\left(j\angle\tilde{b}_{k,m}(t)\right) & |t| \leq T/2 \\ 0 & |t| > T/2 \end{cases}. \tag{5.4}$$

Steps one through three of the first optimization stage are repeated for K iterations such that the resultant optimized constant amplitude waveform $s_{K,m}(t)$ has a spectral shape that well approximates the desired template. It has been found that communications performance (i.e., ability to demodulate the carriers at the communications receiver) is improved by conducting the second optimization stage.

The second optimization stage is performed for L iterations and is initialized with $\tilde{s}_{l=0,m}(t) = s_{K,m}(t)$. This stage contains only two steps, which serve to 1) embed the communications signal, and 2) enforce constant amplitude and pulse duration via sequential application of

$$d_{l,m}(t) = P_{\perp r_m}\left\{\tilde{s}_{l,m}(t)\right\} + r_m(t) \tag{5.5}$$

and

$$\tilde{s}_{l+1,m}(t) = \begin{cases} \exp\left(j\angle d_{l,m}(t)\right) & |t| \leq T/2 \\ 0 & |t| > T/2 \end{cases}. \tag{5.6}$$

After L iterations of the second optimization stage, the final set of M optimized waveforms, denoted as $\tilde{s}_{L,m}(t)$ for the mth waveform, will, with careful selection of communications parameters, have a spectrum shape that is a good approximation of the desired spectrum template and contain subcarriers with QAM symbols that can be demodulated at the communications receiver. The final optimized THoRaCs signal can be represented by

$$s(t) = e^{j\theta(t)} = r(t) + e(t), \tag{5.7}$$

where $e(t)$ corresponds to an "excess" signal term that is required for the OFDM communications signal $r(t)$ to be embedded into the FM structure of the optimized waveform. The last step of the second stage of the THoRaCs optimization routine enforces constant amplitude, which may cause

some distortion to the embedded OFDM communications signal $r(t)$ if the excess signal $e(t)$ does not possess sufficient degrees of design freedom in order to compensate for the discrepancy between an FM waveform and the OFDM communications signal, which is known to have AM.

When creating the communications signal $r_m(t)$ to be embedded into the optimized waveform set for the mth pulse, three primary design parameters are considered. The first of these is the symbol constellation from which the QAM symbols are drawn. Three QAM constellations are considered: 4-QAM, 16-QAM and 64-QAM as shown in Figure 14. A 4-QAM constellation consists of a single energy level, represented by $|c_{m,n}|$ in (5.1). Both 16-QAM and 64-QAM constellations contain multiple values of $|c_{m,n}|$ (3 and 8, respectively). These energy levels are shown in Figure 14 as constant amplitude "phase rings" on each constellation.

It has been found ([106]) that the number of energy levels contained in the constellation from which to draw communications symbols has an impact on the both the spectrum and autocorrelation of the optimized waveform $\tilde{s}_{L,m}(t)$. Specifically, a larger number of amplitude values in the constellation can cause distortion in the spectrum around the frequencies where the subcarriers are embedded, which causes a degradation to the autocorrelation sidelobe response. Also, use of constellations with multiple energy levels results in decreased communications demodulation performance of the optimized waveform at the receiver. The primary advantage to larger constellations is an increase in achievable data rate for the communications function, as more bits are represented by each constellation symbol.

The second design parameter considered for the communications waveform is the number of subcarriers embedded during the optimization procedure, denoted as N. This number is designated as a fraction of the time-bandwidth product of the waveform, BT. It has been observed that embedding N subcarriers representing a large fraction of the waveform time-bandwidth

product causes degradation to both the waveform spectrum and autocorrelation response, as well as a decrease in communications demodulation performance, due to a lack of design degrees of freedom for the optimization procedure by fixing the spectrum phase and amplitude values for a large number of subcarriers as compared to the available BT. Once again, the primary advantage in embedding more communications subcarriers in the waveform is an increase in achievable data rate for the communications function.

Finally, the third design parameter considered is the placement strategy of the OFDM subcarrier frequencies within the waveform spectrum. Three different strategies are examined, all of which restrict all N subcarriers to reside within the normalized 3-dB bandwidth, B, of the waveform spectrum. For the first strategy, denoted as "contiguous fixed", all subcarriers occupy N contiguous frequencies at fixed spectral locations for all M pulses. For the second strategy, denoted as "contiguous hopped", the subcarriers occupy N contiguous frequencies, but their spectral location changes randomly within B for each pulse. In the last strategy, denoted as "non-contiguous hopped", the subcarriers occupy N non-contiguous random frequencies which also change locations randomly on each pulse. It should be noted that for the "contiguous hopped" and "non-contiguous hopped" strategies, the communications receiver needs to be aware of the pattern in which the OFDM subcarriers change on a pulse-wise basis such that the communications information can be demodulated.

5.3 THoRaCs Simulation

A series of simulations are conducted to assess the efficacy of THoRaCs waveforms in both the radar and communications functions. Functionality as a good radar waveform is shown via assessment of the RMS spectrum, mean and RMS autocorrelations and PSF (to assess RSM) of the optimized waveform set. Communications performance is assessed through symbol error rate

(SER) Monte Carlo simulations by demodulating the THoRaCs waveforms and determining whether or not the estimated communications symbols are the same as what was actually modulated onto each subcarrier of the waveform. For each optimized THoRaCs waveform set, the waveforms have $BT = 200$ with oversampling of 4 (so 800 discrete points in each waveform) with a CPI being composed of $M = 1000$ optimized THoRaCs pulses. The power spectrum template $|G(f)|^2$ is super Gaussian with four different orders, $\eta = 2, 4, 8$ and 16. This represents the same four templates utilized for the PRO-FM waveform optimization of Chapter 3 which were displayed in Figure 16. In each test case, stage one of the optimization procedure of (5.2) – (5.4) is performed for $K = 100$ iterations and stage two of the optimization procedure of (5.5) – (5.6) is performed for $L = 50$ iterations, values which have been observed to produce satisfactory results.

Several values of each of the embedded communications signal parameterizations are considered. Communications symbol constellations considered are 4-QAM, 16-QAM and 64-QAM. Numbers of embedded subcarriers tested are 25%, 50% and 75% of the waveform BT, corresponding values of $N = 50, 100$ and 150 subcarriers per waveform, respectively. Finally, all three placement strategies of the OFDM subcarrier frequencies within the waveform spectrum are considered: contiguous fixed, contiguous hopped and non-contiguous hopped. The possible combinations of these three design parameters amounts to 27 different possibilities (108 when considering each value of η). Figures are not provided for each of these cases, but rather for three different combinations of these parameters. However, metrics are calculated for all 108 possible cases and summarized in tables contained in Appendix A, as will described in more detail later in this section.

The first simulation case considered is that of a THoRaCs waveform set with embedded OFDM signal parameters of a 4-QAM constellation, contiguous fixed subcarrier placement

strategy, and 25% *BT* subcarriers embedded, corresponding to $N = 50$ subcarriers per pulse. Figure 86 shows the RMS power spectrum across all $M = 1000$ optimized waveforms in this set for each value of η, along with their respective SG optimization templates. Adherence to the spectral template within the 3-dB bandwidth is almost the same as with the PRO-FM waveforms observed in Figure 17, with the THoRaCs waveform set of this case matching slightly worse than the PRO-FM waveforms. The spectral roll-off of the THoRaCs waveform spectra is degraded when compared to that of their PRO-FM counterparts, with increases in spectral roll-off floor of about 1.2 dB, 3.8 dB, 3.7 dB and 3.4 dB for values of $\eta = 2$, 4, 8 and 16, respectively. Figure 87 shows a detail view of the RMS spectra in the 3-dB bandwidth. Use of the contiguous fixed placement strategy has caused a deformation to the area of the spectrum where the subcarriers are embedded, being more pronounced for the lower values of η, and causing worse coherence to the spectral template than what was observed in the PRO-FM waveform case.
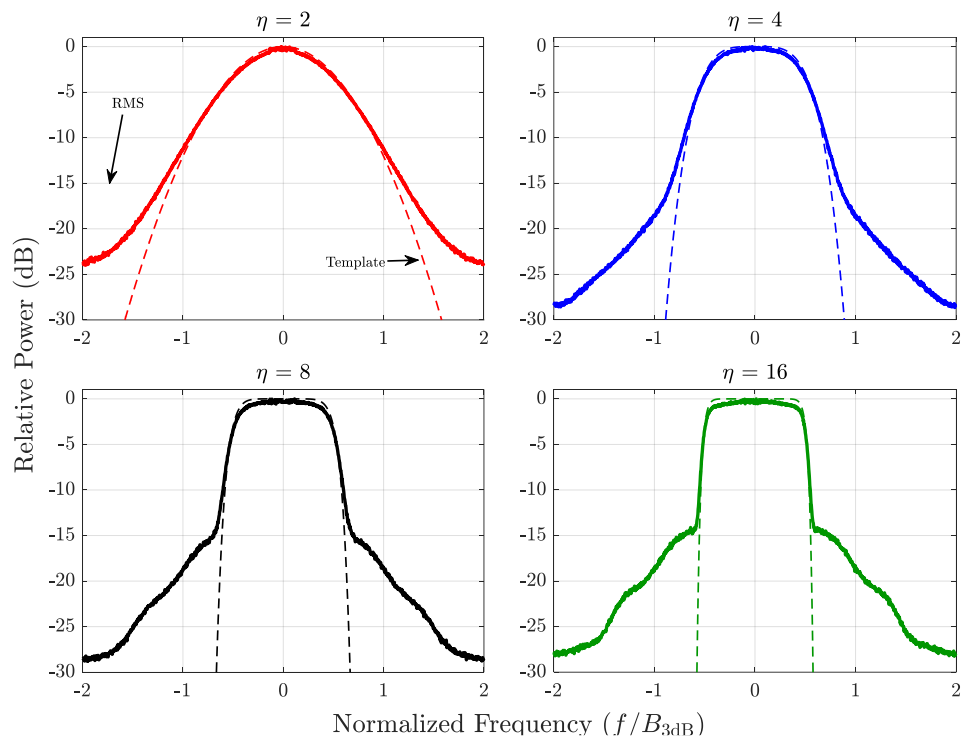
Figure 86: RMS power spectrum plots for a set of $M = 1000$ THoRaCs waveforms with embedded communications parameters of a 4-QAM constellation with $N = 50$ (25% *BT*) subcarriers using the contiguous fixed placement strategy, along with the associated SG template for $\eta = 2$, 4, 8 and 16
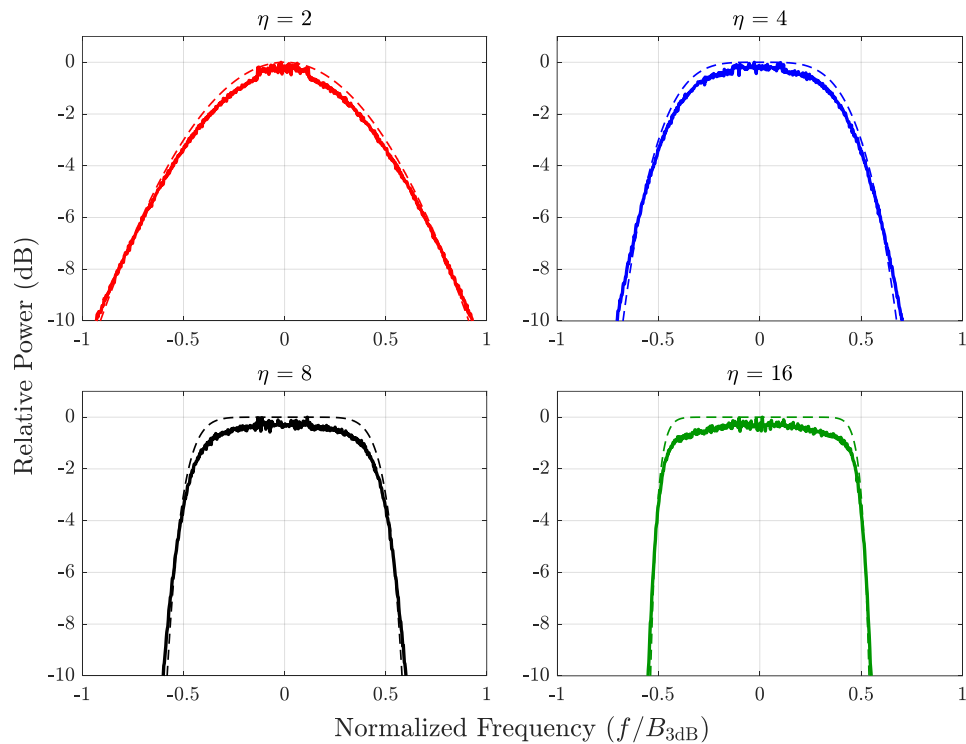
Figure 87: RMS power spectrum detail view plots for a set of $M = 1000$ THoRaCs waveforms with embedded communications parameters of a 4-QAM constellation with $N = 50$ (25% BT) subcarriers using the contiguous fixed placement strategy, along with the associated SG template for $\eta = 2, 4, 8$ and 16

Figure 88 shows the mean and RMS autocorrelation plots across all $M = 1000$ optimized waveforms in this test case set. The peak sidelobe levels of the RMS autocorrelation are about 1.8 dB. 1.6 dB, 1.0 dB and 1.2 dB higher for values of $\eta = 2, 4, 8$ and 16, respectively, compared to that of the PRO-FM waveforms observed in Figure 19. The peak sidelobe level of the mean autocorrelation of the THoRaCs waveforms is increased by about the same amount when comparing to PRO-FM in Figure 19. However, the THoRaCs waveforms still achieve the expected approximate 30 dB reduction in sidelobe level with coherent combination across the optimized waveform set. The autocorrelation mainlobe regions for the THoRaCs waveforms appear to be slightly wider than those of the PRO-FM waveforms, which is confirmed with the mean and RMS autocorrelation mainlobe detail plots in Figure 89. Embedding of the communications signal in this case has introduced slightly more shoulder lobing structure for each value of η.
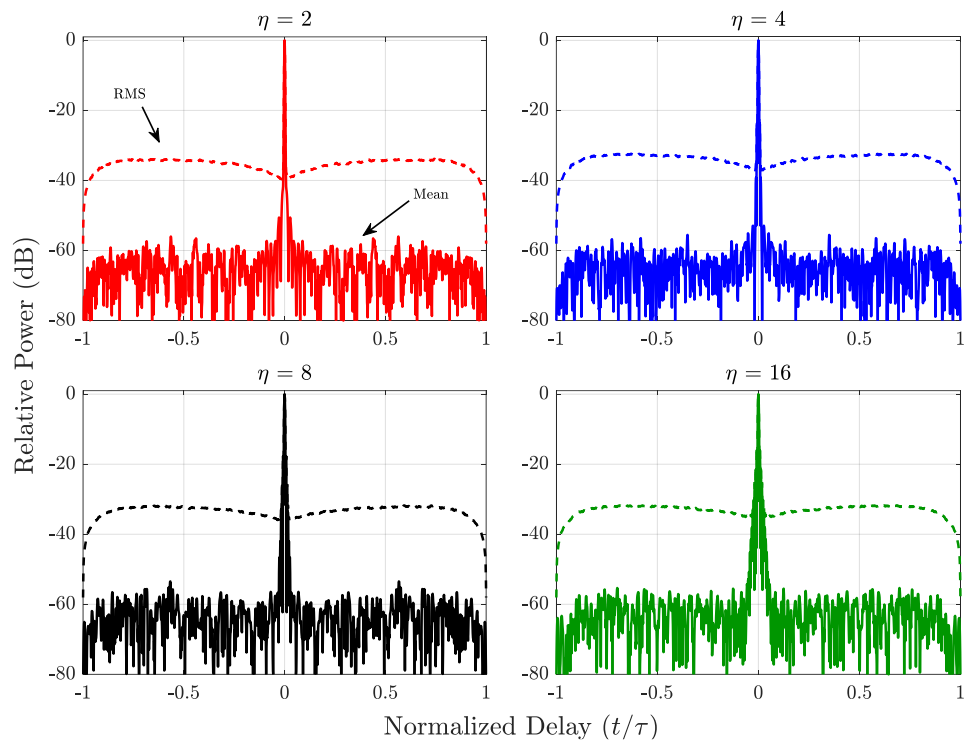
Figure 88: Mean and RMS autocorrelation plots for a set of $M = 1000$ THoRaCs waveforms with embedded communications parameters of a 4-QAM constellation with $N = 50$ (25% BT) subcarriers using the contiguous fixed placement strategy for $\eta = 2, 4, 8$ and 16
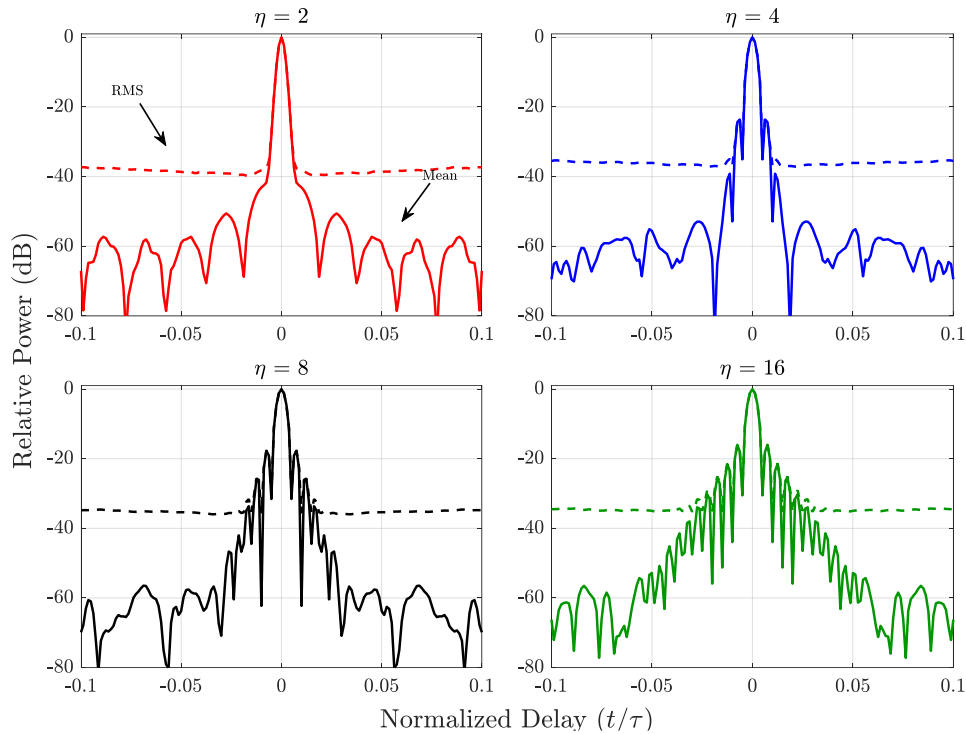
Figure 89: Mean and RMS autocorrelation mainlobe detail plots for a set of $M = 1000$ THoRaCs waveforms with embedded communications parameters of a 4-QAM constellation with $N = 50$ (25% BT) subcarriers using the contiguous fixed placement strategy for $\eta = 2, 4, 8$ and 16

Figure 90 shows the mainlobe detail region of the PSF formed for each THoRaCs waveform optimized in this test case. Noticeably higher background floor can be observed in the PSF for each test case when compared to PRO-FM. This is confirmed by once again applying the PSF metric of (3.5) to the THoRaCs waveforms. For this test case, the values of δ are -66.5 dB, -65.0 dB, -64.5 dB and -64.2 dB for values of $\eta = 2, 4, 8$ and 16, respectively, representing increases over the PRO-FM PSFs observed in Figure 23 of 4.0 dB, 2.9 dB, 2.4 dB and 2.3 dB, respectively. The results of this test case show that the optimized THoRaCs waveform set still operates as a good radar waveform, with modest performance degradation over the respective PRO-FM waveforms. The values of δ for all 108 possible test cases are given in Table 5 of Appendix A.
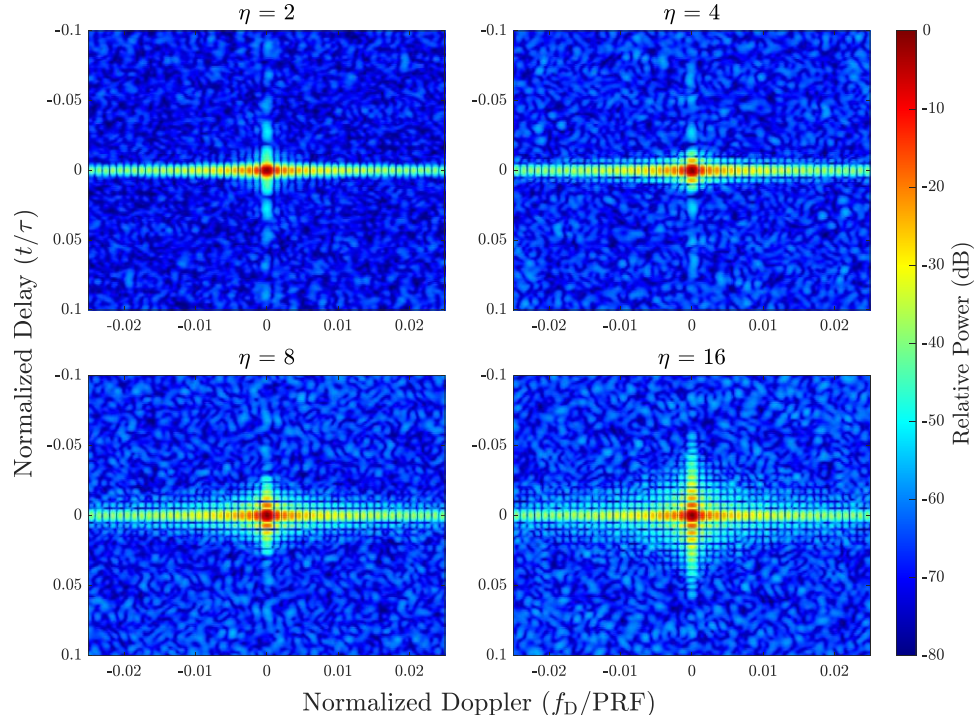
Figure 90: PSF plots for a set of $M = 1000$ THoRaCs waveforms with embedded communications parameters of a 4-QAM constellation with $N = 50$ (25% BT) subcarriers using the contiguous fixed placement strategy for $\eta = 2, 4, 8$ and 16

In order to assess the communications capability of the THoRaCs waveform in this test case, the embedded symbols on each subcarrier of every pulse in the optimized CPI are demodulated and plotted against the true constellation symbols used to form the OFDM communications signal prior to THoRaCs optimization, as shown in Figure 91. The demodulated symbols form tight clusters around their respective true constellation points, showing that the THoRaCs optimization procedure has caused minimal distortion to the embedded OFDM subcarriers. A useful metric in measuring the discrepancy between the demodulated symbols and their true constellation points is the error vector magnitude (EVM) [112]. The RMS of the EVM across all N subcarriers embedded into the M optimized waveforms of the set can be expressed mathematically as

$$\text{EVM}_{\text{RMS}} = \left(\frac{1}{NM} \sum_{m=1}^{M} \sum_{n=1}^{N} \left| \hat{x}_{n,m} - x_{n,m} \right|^2 \right)^{1/2}, \qquad (5.8)$$

where $\hat{x}_{n,m}$ and $x_{n,m}$ are the demodulated estimate and true value, respectively, of the complex communications symbol for the nth subcarrier of the mth pulse. This error vector is normalized by the average symbol amplitude of the true constellation (which is always scaled to be unity), before the RMS operation is performed in (5.8), and then represented on a decibel scale. A smaller error vector is desired, so lower values of the RMS EVM are desired, indicating little distortion caused to the embedded communications symbols. The RMS value of the EVM values in Figure 91 are -46.6 dB, -43.7 dB, -45.2 dB and -42.4 dB for values of η = 2, 4, 8 and 16, respectively. Table 6 of Appendix A provides a summary of the RMS EVM values for all 108 possible test cases.

Finally, the true measure of successful communications is whether or not the demodulated communications symbol is actually estimated correctly. Estimation for a communication symbol taken from a constellation is typically performed by finding the closest constellation point (known as the Euclidian distance [113]) to the demodulated communication symbol. The number of estimation errors accumulated over each waveform test case set is represented by the SER, which is simply the total number of errors divided by the total number of demodulated and estimated symbols. The test case shown in Figure 91 resulted in no symbol errors for each value of η, meaning a SER of 0. Table 7 of Appendix A provides a summary of the SER values for all 108 possible test cases. Note that the PSF, RMS EVM and SER values presented in this section and summarized in Table 7 of Appendix A represent single instantiations for BT and M in each optimization test case and are provided for general comparisons across different test cases. An adequate number of communications symbols are tested in each case in order to make these general comparisons, but Monte Carlo simulations across many instantiations of each test case would reduce the variation in RMS EVM and SER and yield results closer to the true value for each.
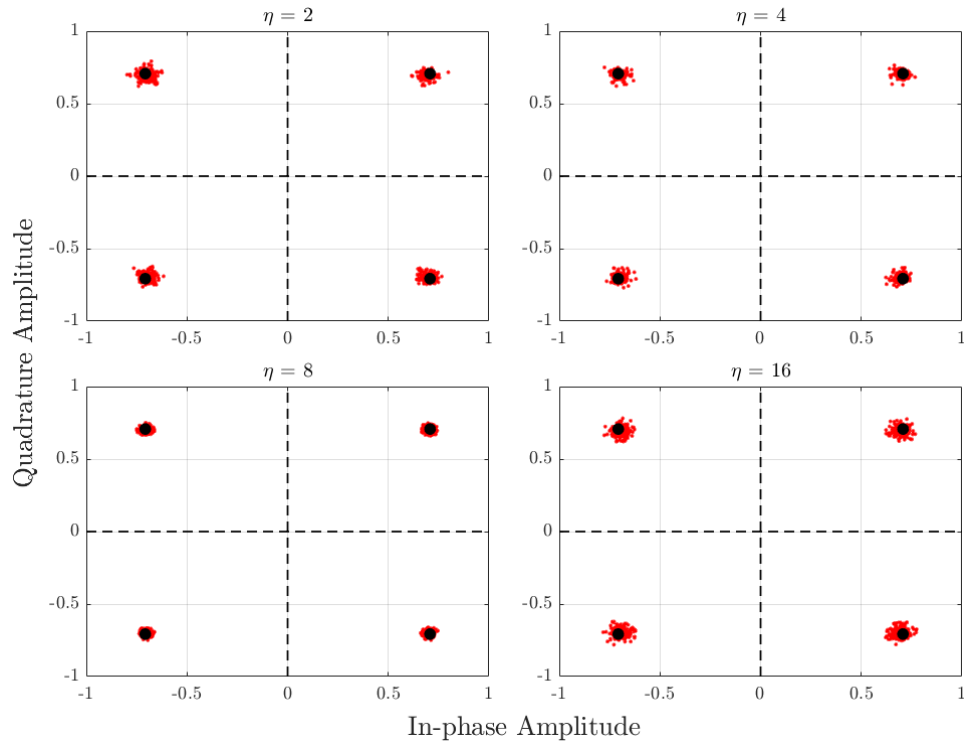
Figure 91: Plots of true (black) constellation and demodulated (red) communications symbols for a set of $M = 1000$ THoRaCs waveforms with embedded communications parameters of a 4-QAM constellation with $N = 50$ (25% BT) subcarriers using the contiguous fixed placement strategy for $\eta = 2$, 4, 8 and 16

The next simulation case considered is that of a THoRaCs waveform set with embedded OFDM signal parameters of a 16-QAM constellation, contiguous hopped subcarrier placement strategy, and 25% BT subcarriers embedded, corresponding to $N = 50$ subcarriers per pulse. Figure 92 shows the RMS power spectrum across all $M = 1000$ optimized waveforms in this set for each value of η, along with their respective SG optimization templates. Adherence to the spectral template within the 3-dB bandwidth is almost the same as with the PRO-FM waveforms observed in Figure 17, with the THoRaCs waveform set of this case matching slightly worse than the PRO-FM waveforms. The spectral roll-off of the THoRaCs waveform spectra is degraded when compared to that of their PRO-FM counterparts, with increases in spectral roll-off floor of about 1.5 dB, 4.3 dB, 5.3 dB and 5.5 dB for values of $\eta = 2$, 4, 8 and 16, respectively. These values are slightly higher than that of the previous THoRaCs test case in Figure 86, and are caused by the introduction of additional energy levels in the 16-QAM constellation. Figure 93 shows a detail

view of the RMS spectra in the 3-dB bandwidth. Use of the contiguous hopped placement strategy has yielded better adherence to the SG spectrum template in the 3-dB band than what was observed with the contiguous fixed strategy shown in Figure 87, and is qualitatively the same as the PRO-FM waveform cases shown in Figure 17.
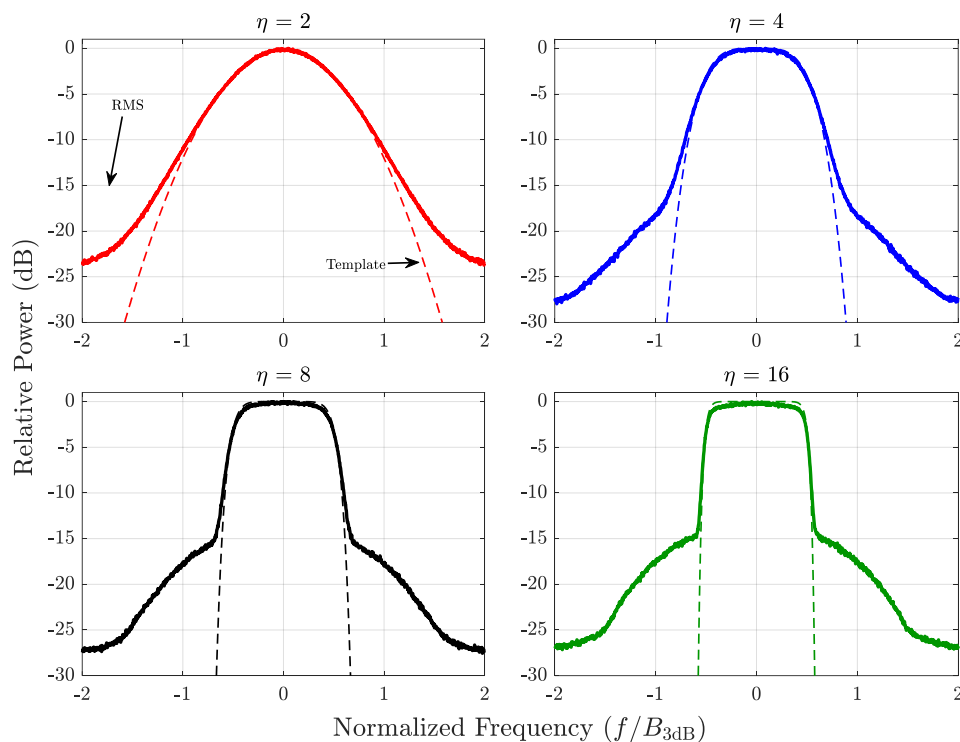
Figure 92: RMS power spectrum plots for a set of $M = 1000$ THoRaCs waveforms with embedded communications parameters of a 16-QAM constellation with $N = 50$ (25% BT) subcarriers using the contiguous hopped placement strategy, along with the associated SG template for $\eta = 2, 4, 8$ and 16
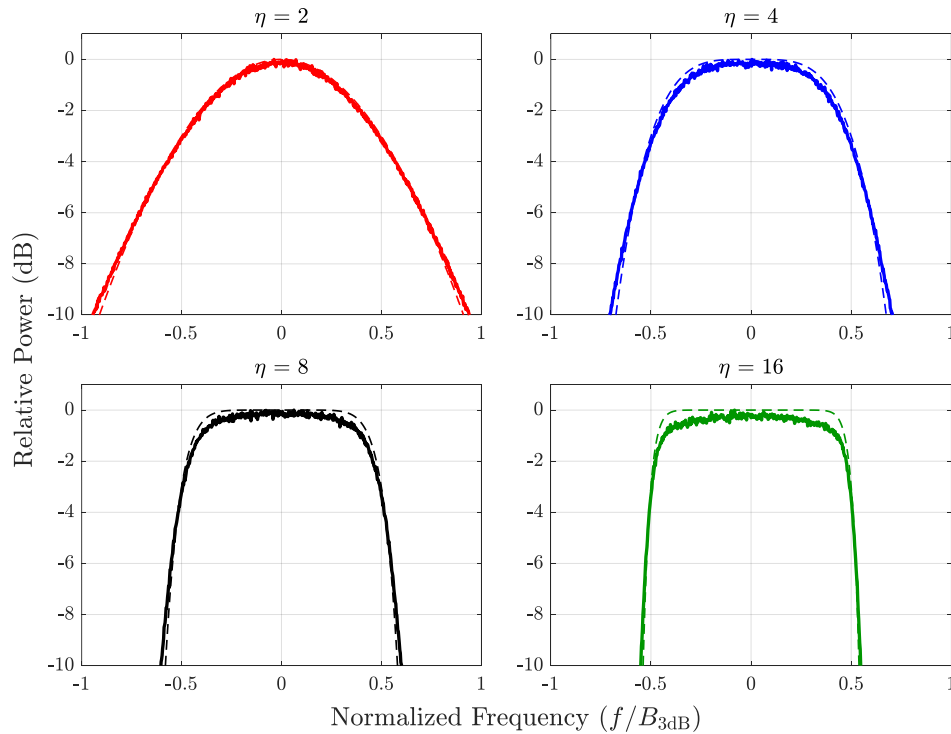
Figure 93: RMS power spectrum detail view plots for a set of $M = 1000$ THoRaCs waveforms with embedded communications parameters of a 16-QAM constellation with $N = 50$ (25% BT) subcarriers using the contiguous hopped placement strategy, along with the associated SG template for $\eta = 2, 4, 8$ and 16

Figure 94 shows the mean and RMS autocorrelation plots across all $M = 1000$ optimized waveforms in this test case set. The peak sidelobe levels of the RMS autocorrelation are increased by about the same amount for all η as the previous test case when compared to that of the PRO-FM waveforms observed in Figure 19. The RMS sidelobe level floor of this test case is flatter than what was observed in the previous case in Figure 88, which has been found to be caused by the different placement strategy (contiguous hopped over contiguous fixed). The peak sidelobe level of the mean autocorrelation of the THoRaCs waveforms is increased by about the same amount when comparing to PRO-FM in Figure 19. However, the THoRaCs waveforms still achieve the expected approximate 30 dB reduction in sidelobe level with coherent combination across the optimized waveform set. The autocorrelation mainlobe regions for the THoRaCs waveforms appear to be slightly wider than for the PRO-FM waveforms, which is confirmed with the mean and RMS autocorrelation mainlobe detail plots in Figure 94. Embedding of the communications

signal in this case has introduced slightly more shoulder lobing structure for each value of η, but to a much less degree than the previous test case shown in Figure 89, showing that the contiguous hopped placement strategy produces an optimized waveform with better autocorrelation properties than that of the contiguous fixed placement strategy.
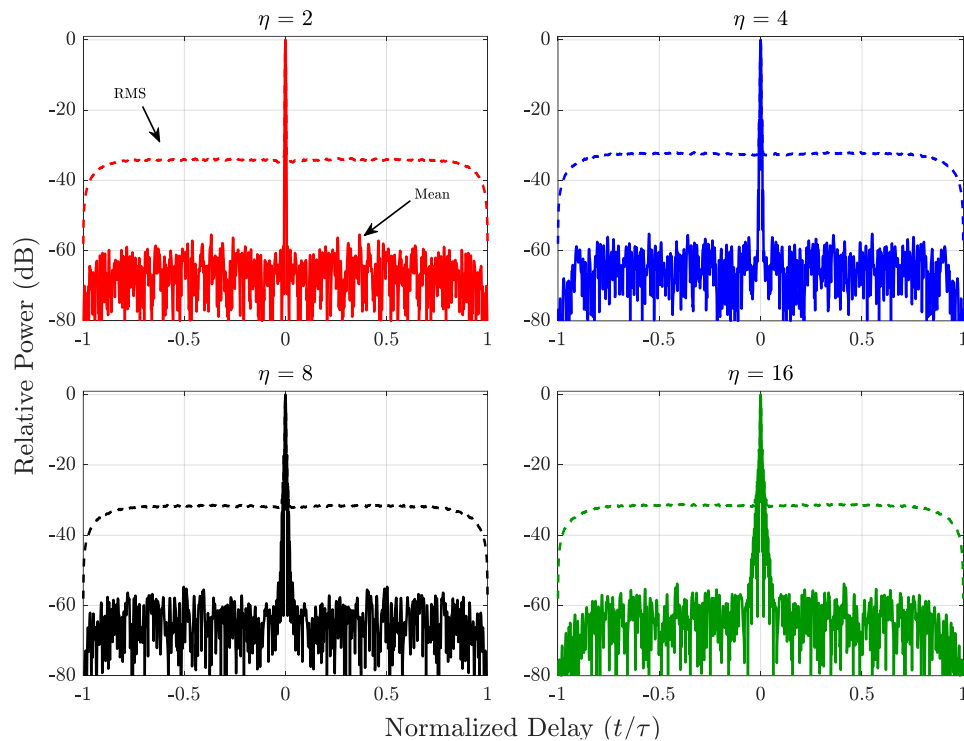
Figure 94: Mean and RMS autocorrelation plots for a set of $M = 1000$ THoRaCs waveforms with embedded communications parameters of a 16-QAM constellation with $N = 50$ (25% BT) subcarriers using the contiguous hopped placement strategy for $\eta = 2$, 4, 8 and 16
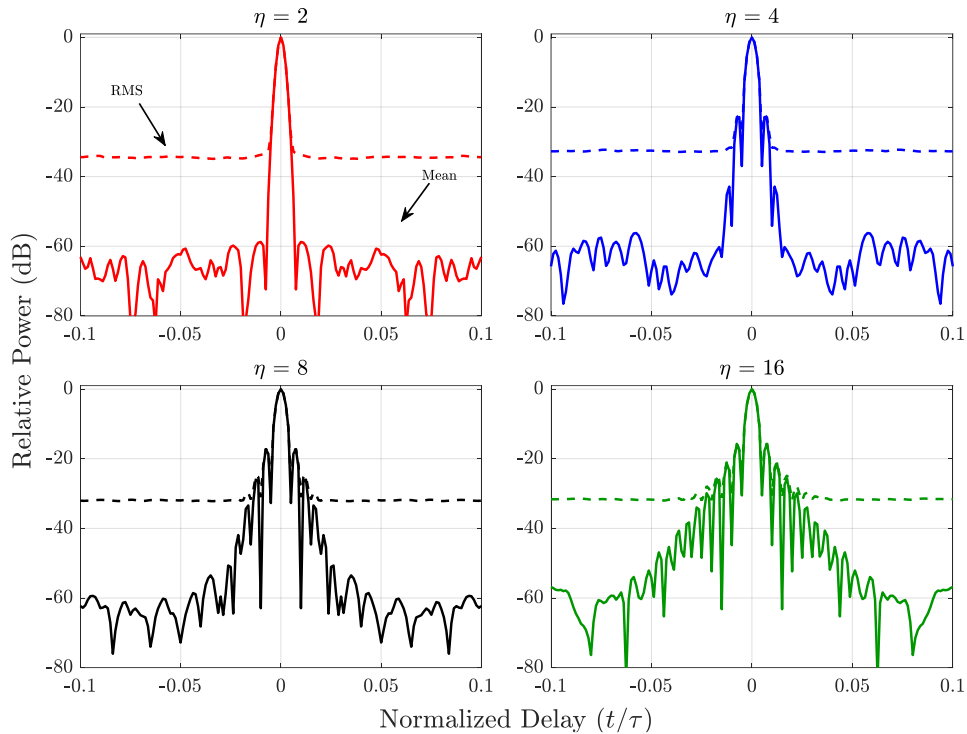
Figure 95: Mean and RMS autocorrelation mainlobe detail plots for a set of M = 1000 THoRaCs waveforms with embedded communications parameters of a 16-QAM constellation with N = 50 (25% BT) subcarriers using the contiguous hopped placement strategy for η = 2, 4, 8 and 16

Figure 96 shows the mainlobe detail region of the PSF formed for each THoRaCs waveform optimized in this test case. Noticeably higher background floor can be observed in the PSF for each test case when compared to PRO-FM. For this test case, the values of δ are -65.7 dB, -64.0 dB, -63.4 dB and -63.2 dB for values of η = 2, 4, 8 and 16, respectively, representing increases over the PRO-FM PSFs observed in Figure 23 of 4.8 dB, 3.9 dB, 3.5 dB and 3.3 dB, respectively. These values also represent increases of about 1 dB for all values of η compared to the previous THoRaCs test case, which has been found to be caused by the use of a 16-QAM constellation that has more energy levels than 4-QAM. The results of this test case show that the optimized THoRaCs waveform set still operates as a good radar waveform, with modest performance degradation over the respective PRO-FM waveforms.
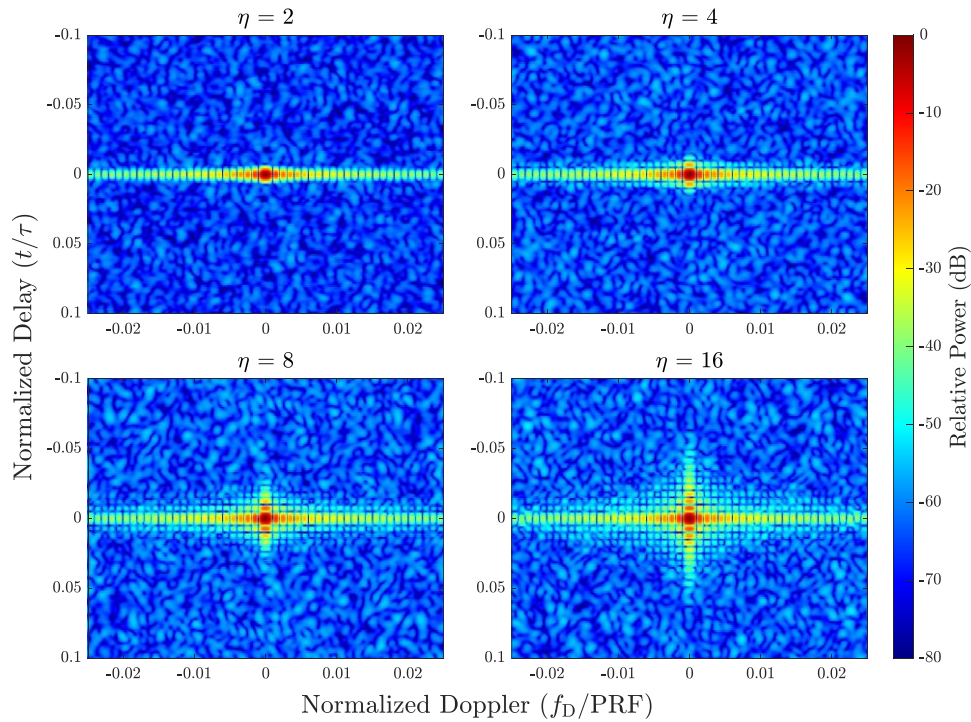
Figure 96: PSF plots for a set of $M = 1000$ THoRaCs waveforms with embedded communications parameters of a 16-QAM constellation with $N = 50$ (25% BT) subcarriers using the contiguous hopped placement strategy for $\eta = 2$, 4, 8 and 16

Figure 97 shows the demodulated symbols for the optimized THoRaCs waveform CPI test case plotted against the true constellation symbols used to form the OFDM communications signal prior to THoRaCs optimization. The demodulated symbols once again form tight clusters around their respective true constellation points, showing that the THoRaCs optimization procedure has caused minimal distortion to the embedded OFDM subcarriers. The RMS value of the EVM values in Figure 91 are -48.6 dB, -44.4 dB, -43.0 dB and -42.5 dB for values of $\eta = 2$, 4, 8 and 16, respectively, representing changes of 2.0 dB, 0.7 dB, -2.2 dB and 0.1 dB, respectively, over the previous THoRaCs test case, showing that use of the contiguous hopped placement strategy has in general improved the EVM for the embedded communications symbols. The test case shown in Figure 97 once again resulted in no symbol errors for each value of η, meaning a SER of 0 in each case.
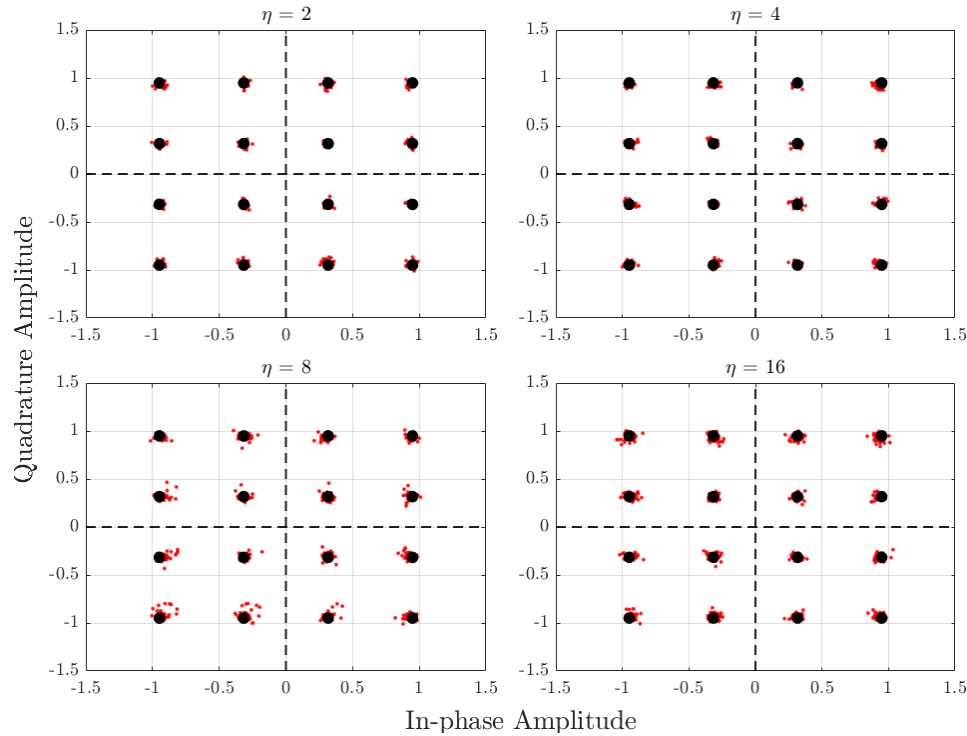
Figure 97: Plots of true (black) constellation and demodulated (red) communications symbols for a set of $M = 1000$ THoRaCs waveforms with embedded communications parameters of a 16-QAM constellation with $N = 50$ (25% BT) subcarriers using the contiguous hopped placement strategy for $\eta = 2, 4, 8$ and 16

The next simulation case considered is that of a THoRaCs waveform set with embedded OFDM signal parameters of a 64-QAM constellation, non-contiguous hopped subcarrier placement strategy, and 75% BT subcarriers embedded, corresponding to $N = 150$ subcarriers per pulse. Figure 98 shows the RMS power spectrum across all $M = 1000$ optimized waveforms in this set for each value of η, along with their respective SG optimization templates. Figure 99 shows a detail view of the RMS spectra in the 3-dB bandwidth. The spectral roll-off is severely degraded, rolling off to about -15 dB for all η, in this case as compared to the two previous THoRaCs test cases. This degradation is caused by the introduction of additional energy levels in the 64-QAM constellation, as well as a threefold increase in the number of embedded subcarriers per waveform, leaving insufficient degrees of design freedom to achieve a spectral roll-off on par with that of the previous two test cases. The optimized RMS spectra do not adhere as well to their spectral templates as they did in the previous test case, as shown in Figure 99. Some slight deformation in

the spectrum around the 3-dB normalized frequencies for the cases of $\eta = 2$ and 4 is noticeable and is smoothed out for $\eta = 8$ and 16.
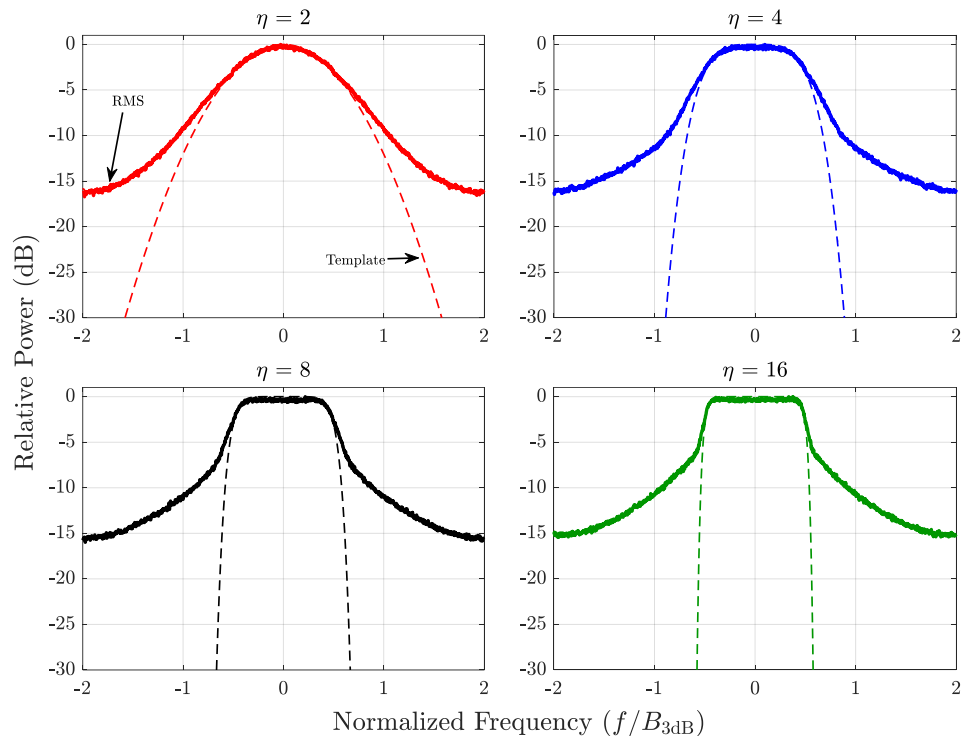
Figure 98: RMS power spectrum plots for a set of $M = 1000$ THoRaCs waveforms with embedded communications parameters of a 64-QAM constellation with $N = 150$ (75% BT) subcarriers using the non-contiguous hopped placement strategy, along with the associated SG template for $\eta = 2, 4, 8$ and 16
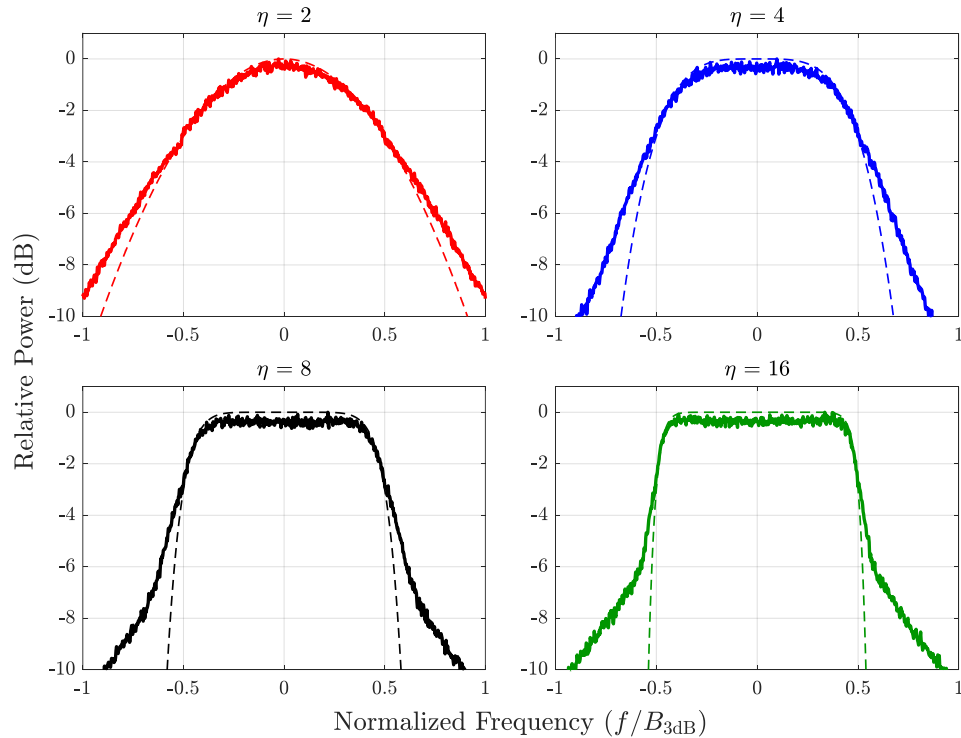
Figure 99: RMS power spectrum detail view plots for a set of $M = 1000$ THoRaCs waveforms with embedded communications parameters of a 64-QAM constellation with $N = 150$ (75% BT) subcarriers using the non-contiguous hopped placement strategy, along with the associated SG template for $\eta = 2, 4, 8$ and 16

Figure 100 shows the mean and RMS autocorrelation plots across all $M = 1000$ optimized waveforms in this test case set. The peak sidelobe levels of the RMS autocorrelation are increased by about 4-5 dB for all η as compared to the previous test case in Figure 94. The sidelobe floor level is also not quite as flat. The mean autocorrelation sidelobe levels experience a similar increase. This degradation in sidelobe level is once again caused by introduction of additional energy levels in the 64-QAM constellation, as well as a threefold increase in the number of embedded subcarriers per waveform. However, the THoRaCs waveforms still achieve the expected approximate 30 dB reduction in sidelobe level with coherent combination across the optimized waveform set. The autocorrelation mainlobe regions for the THoRaCs waveforms in this case are also wider than the previous case, which is confirmed with the mean and RMS autocorrelation mainlobe detail plots in Figure 101. Embedding of the communications signal in this case has introduced more shoulder lobing structure than for the previous case.
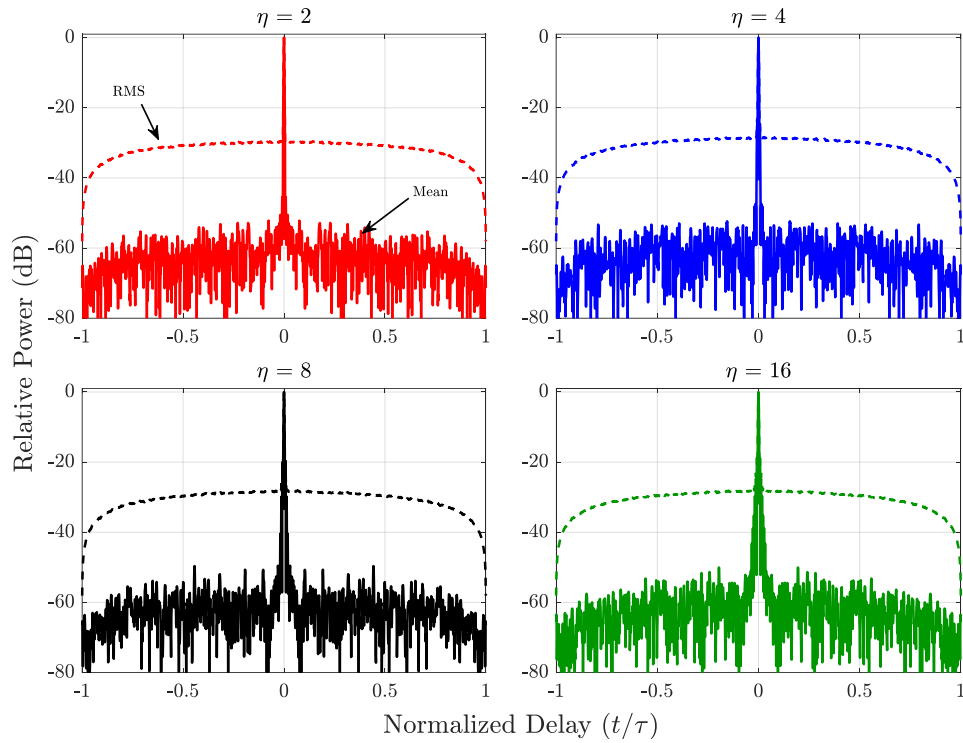
Figure 100: Mean and RMS autocorrelation plots for a set of $M = 1000$ THoRaCs waveforms with embedded communications parameters of a 64-QAM constellation with $N = 150$ (75% BT) subcarriers using the non-contiguous hopped placement strategy for $\eta = 2$, 4, 8 and 16
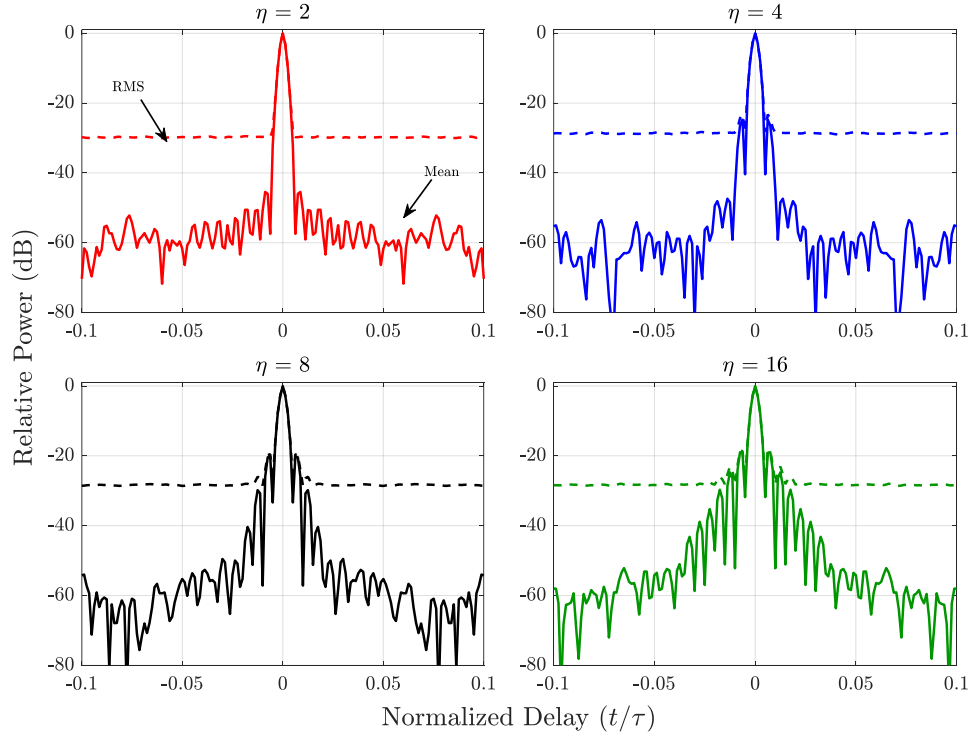
Figure 101: Mean and RMS autocorrelation mainlobe detail plots for a set of $M = 1000$ THoRaCs waveforms with embedded communications parameters of a 64-QAM constellation with $N = 150$ (75% BT) subcarriers using the non-contiguous hopped placement strategy for $\eta = 2$, 4, 8 and 16

Figure 102 shows the mainlobe detail region of the PSF formed for each THoRaCs waveform optimized in this test case. The values of δ are -62.7 dB, -61.7 dB, -61.5 dB and -61.4 dB for values of $\eta = 2$, 4, 8 and 16, respectively, representing increases over the PSFs observed in the previous case in Figure 96 of 3.0 dB, 2.3 dB, 1.9 dB and 1.8 dB, respectively. The results of this test case show that the optimized THoRaCs waveform is not as good of a radar waveform, suffering from worse spectral containment, higher autocorrelation sidelobes and higher PSF floor, indicating a higher degree of RSM, due to the embedding of a large percentage of subcarrier as a fraction of the waveform BT.
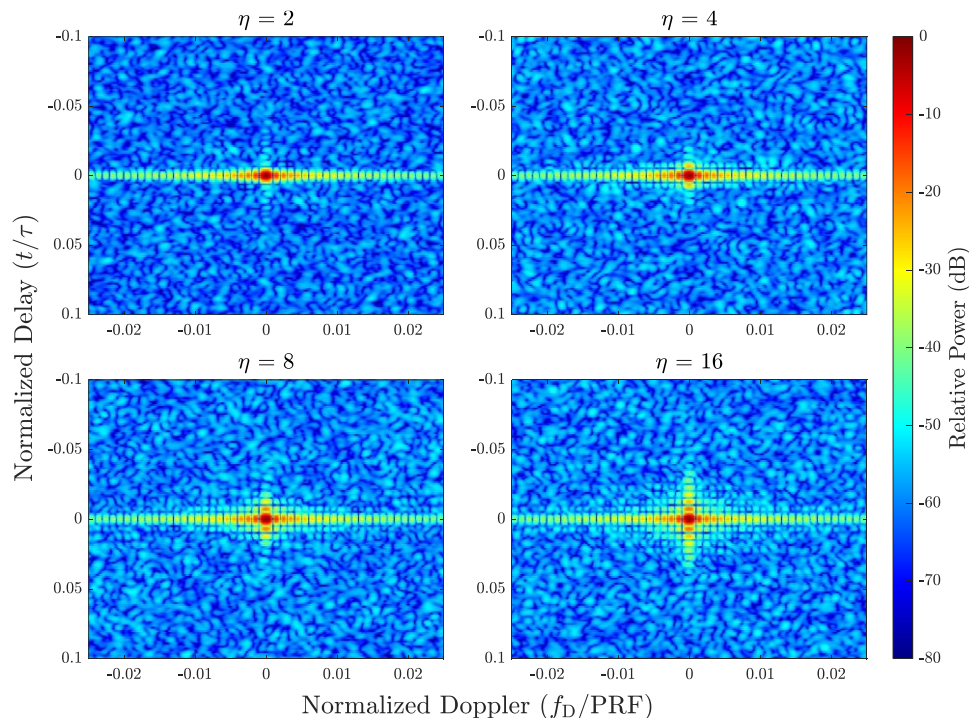
Figure 102: PSF plots for a set of $M = 1000$ THoRaCs waveforms with embedded communications parameters of a 64-QAM constellation with $N = 150$ (75% BT) subcarriers using the non-contiguous hopped placement strategy for $\eta = 2$, 4, 8 and 16

Figure 103 shows the demodulated symbols for the optimized THoRaCs waveform CPI for this test case plotted against the true constellation symbols used to form the OFDM communications signal prior to THoRaCs optimization. The demodulated symbols are no longer as tightly packed around their respective true constellation points, representing RMS EVM values

of -29.8 dB, -24.1 dB, -22.2 dB and -21.5 dB for values of $\eta = 2, 4, 8$ and 16, respectively. These

values are significantly worse than the previous two test cases. The test case shown in Figure 103

contains SER values of 6.67 x 10^{-6}, 3.0 x 10^{-3}, 1.21 x 10^{-2}, and 1.79 x 10^{-2} for values of $\eta = 2, 4, 8$

and 16, respectively. This shows that this optimized THoRaCs waveform would not serve the

communications function well, as significant degradation to the embedded communications

subcarriers has occurred due to the amount being embedded. This degradation is caused solely by

the inadequacy of the optimization procedure before any channel propagation or thermal noise

corruption is considered.
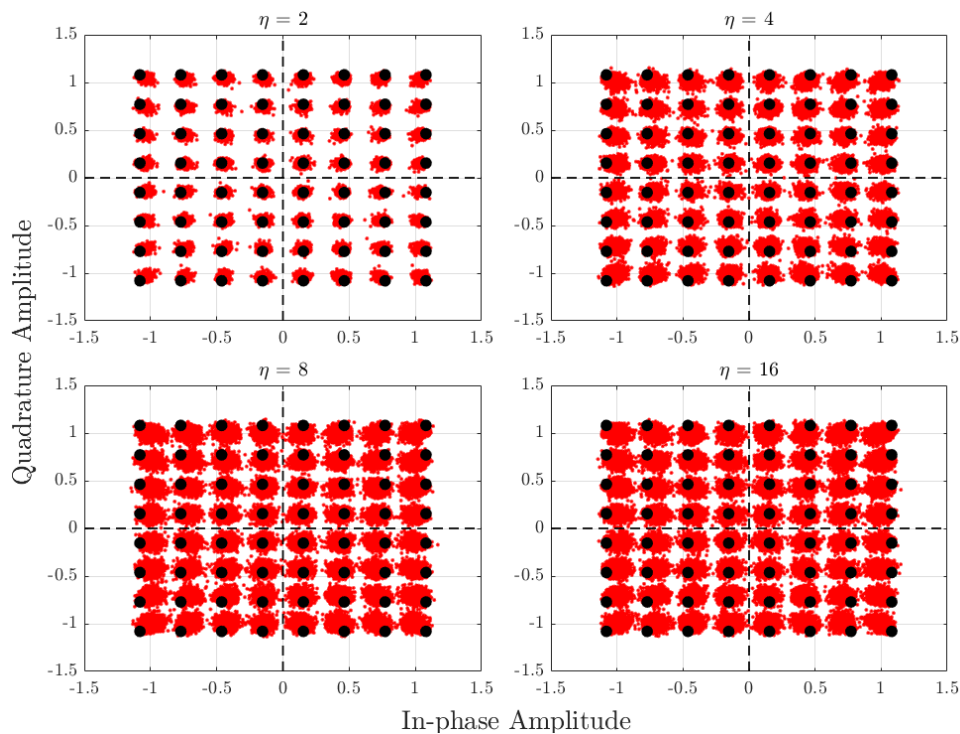
Figure 103: Plots of true (black) constellation and demodulated (red) communications symbols for a set of $M = 1000$ THoRaCs waveforms with embedded communications parameters of a 64-QAM constellation with $N = 150$ (75% BT) subcarriers using the non-contiguous hopped placement strategy for $\eta = 2, 4, 8$ and 16

A quick summary of the values in Table 5, Table 6 and Table 7 is given here to provide a

general idea of which communications signal parameterizations result in optimized THoRaCs

waveforms with the best radar and communications functions, as indicated by the δ, RMS EVM,

and SER metrics. Lower values of δ are obtained in general when using constellations with fewer

energy levels, with 4-QAM giving the lowest values. Additionally, lower values of δ are obtained in general for the non-contiguous hopped placement strategy, with contiguous hopped being the next best and contiguous fixed being the worst choice for δ value. Lower values of δ are obtained in general for a fewer number of embedded subcarriers as a percentage of the waveform BT. Of the cases tested and summarized in Table 5, 25% BT provides the best performance while 75% BT provides the worst performance. Finally, lower values of δ are obtained in general for smaller orders of super Gaussian template, η, with $\eta = 2$ giving the best performance and the $\eta = 16$ worst. Combining these generalities, it is not surprising that the lowest values of δ occur for the case of a 4-QAM constellation with the non-contiguous hopped placement strategy and 25% BT subcarriers. These values are -68.2 dB, -66.0 dB, -65.1 dB and -64.8 dB, for values of $\eta = 2$, 4, 8 and 16, respectively, which represent increases over the respective PRO-FM waveform cases of 2.3 dB, 1.9 dB, 1.8 dB and 1.7 dB. While this THoRaCs parameterization provides the best radar waveform, achieving PSF performance close to that of PRO-FM, using a smaller number of embedded subcarriers with a smaller constellation will decrease the available data rate of the communications function.

Now considering communications performance, the same generalities observed for δ hold true for the RMS EVM, with the case of a 4-QAM constellation with the non-contiguous hopped placement strategy and 25% BT subcarriers having RMS EVM values of -130.2 dB, -117.0 dB, -111.8 dB and -109.2 dB, respectively. This represents negligible distortion caused to the communications subcarriers caused by the THoRaCs optimization procedure. While not enough trials were conducted to observe symbol errors in many of the test cases, the same general trends observed for the RMS EVM are expected as well for the SER. It is convenient that the same communications signal parameterization provides the best radar and communications performance

for THoRaCs waveforms (in the absence of thermal noise and channel distortion), assuming the desired communications data rate can be achieved with this parameterization.

Further evaluation of the communications performance of THoRaCs waveforms is performed via Monte Carlo SER simulations with introduction of AWGN, simulating a noisy propagation channel for the communications waveform. Every possible parameterization of communications signal is tested for each value of η (108 total test cases). For each optimized THoRaCs waveform set, the waveforms once again have $BT = 200$ with oversampling of 4 (so 800 discrete points in each waveform) with a CPI being composed of $M = 1000$ optimized THoRaCs pulses. Complex AWGN is generated and added to each optimized test waveform set and varied in power to form average per-sample SNR values ranging from -10 dB to + 30 dB. Each SNR value for each test case (all 108 combinations) is repeated until at least 10^6 symbols have been generated and at least 300 total symbol errors are observed unless the SER is observed to be less than 10^{-4} once 10^6 symbols have been generated. The SER results are presented as "waterfall" plots with SER plotted on a semi-log scale against SNR represented with the decibel operation.

Figure 104 shows the SER waterfall plots for all parameterizations of the embedded communications signal for $\eta = 2$. Several important trends can be ascertained from Figure 104. First, using QAM constellations with fewer energy levels (and thus lower constellation density) results in better SER performance for all placement strategies, which is expected given the EVM results summarized in Table 6. Second, for lower SNR values, the contiguous fixed placement strategy has better SER performance followed by contiguous hopped then non-contiguous hopped, which is not surprising since the subcarriers reside in the middle of the waveform band for the contiguous fixed strategy where the spectral energy is highest. This trend seems to conflict with the generalizations previously made for communications performance, until it is realized that those

test cases did not have noise included, and thus represented a very high SNR regime where relative spectral locations of the embedded subcarriers, and thus varying symbol power, were not a factor. Third, for larger numbers of embedded subcarriers, the contiguous fixed and contiguous hopped placement strategies have SERs that level off to a floor for high values of SNR for the constellations with more than one energy level. However, the non-contiguous hopped placement strategy does not experience this same floor in SER performance. This interference limitation floor in the SER is caused by attempting to embed too many subcarriers into the THoRaCs waveform. The SER results of Figure 104 indicate that careful consideration must be made when choosing communications signal parameterizations for design of THoRaCs waveforms, lest the communications function be severely hindered.

Figure 105, Figure 106 and Figure 107 show the SER waterfall plots for all parameterizations of the embedded communications signal for $\eta = 4$, 8 and 16, respectively. The SER performance for each of these plots is essentially the same as for the case of $\eta = 2$. A slight decrease in SER performance is noted for increased values of η, but the difference is essentially insignificant when comparing across $\eta = 2$ (Figure 104) to $\eta = 16$ (Figure 107). The most notable difference is that high values of η tend to make the SER performance more similar across all placement strategies for a given constellation size and number of embedded subcarriers.
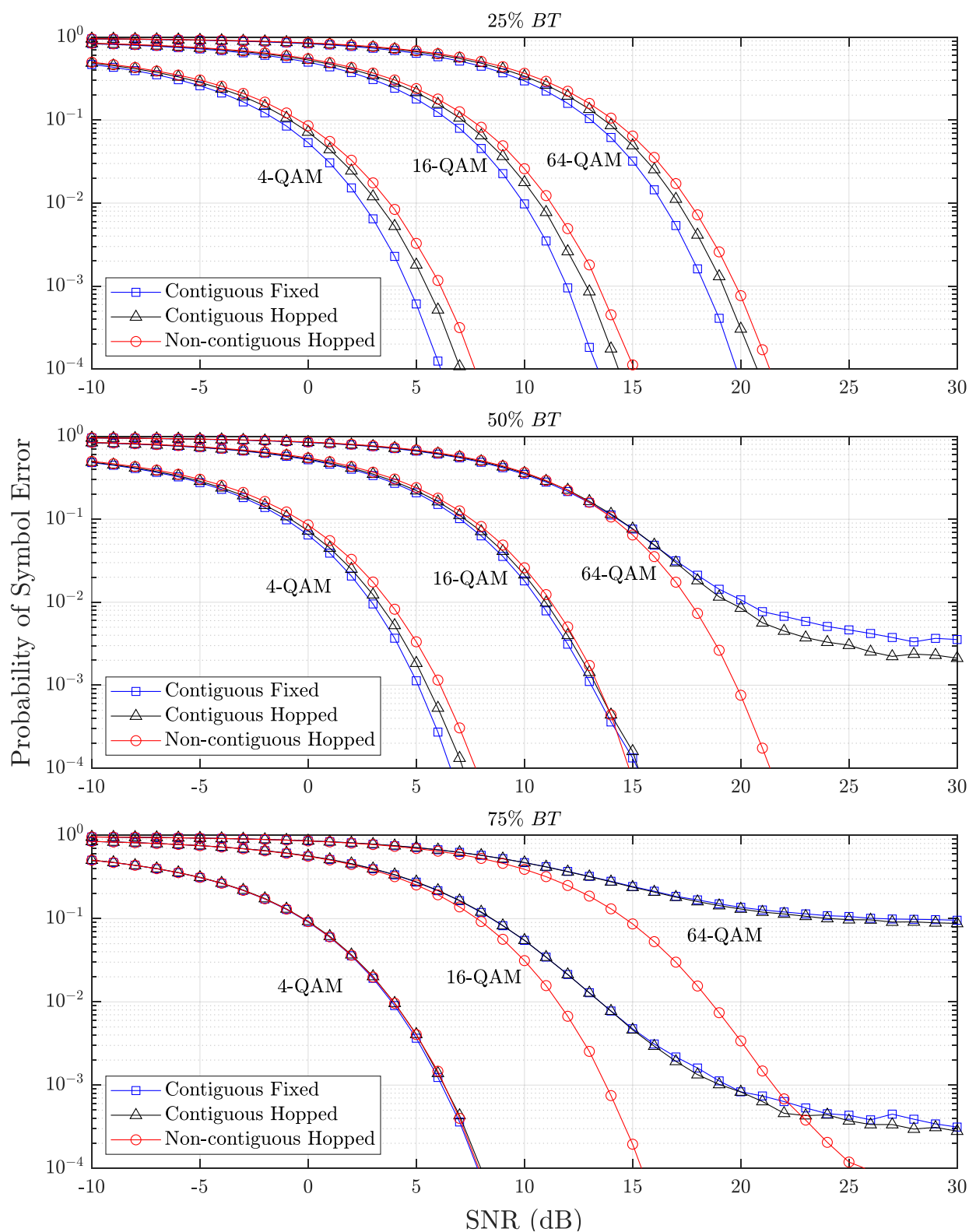
Figure 104: SER waterfall plots of Monte Carlo simulation assessing communications performance in a noisy channel for all possible parameterizations of the communication signal for $\eta = 2$
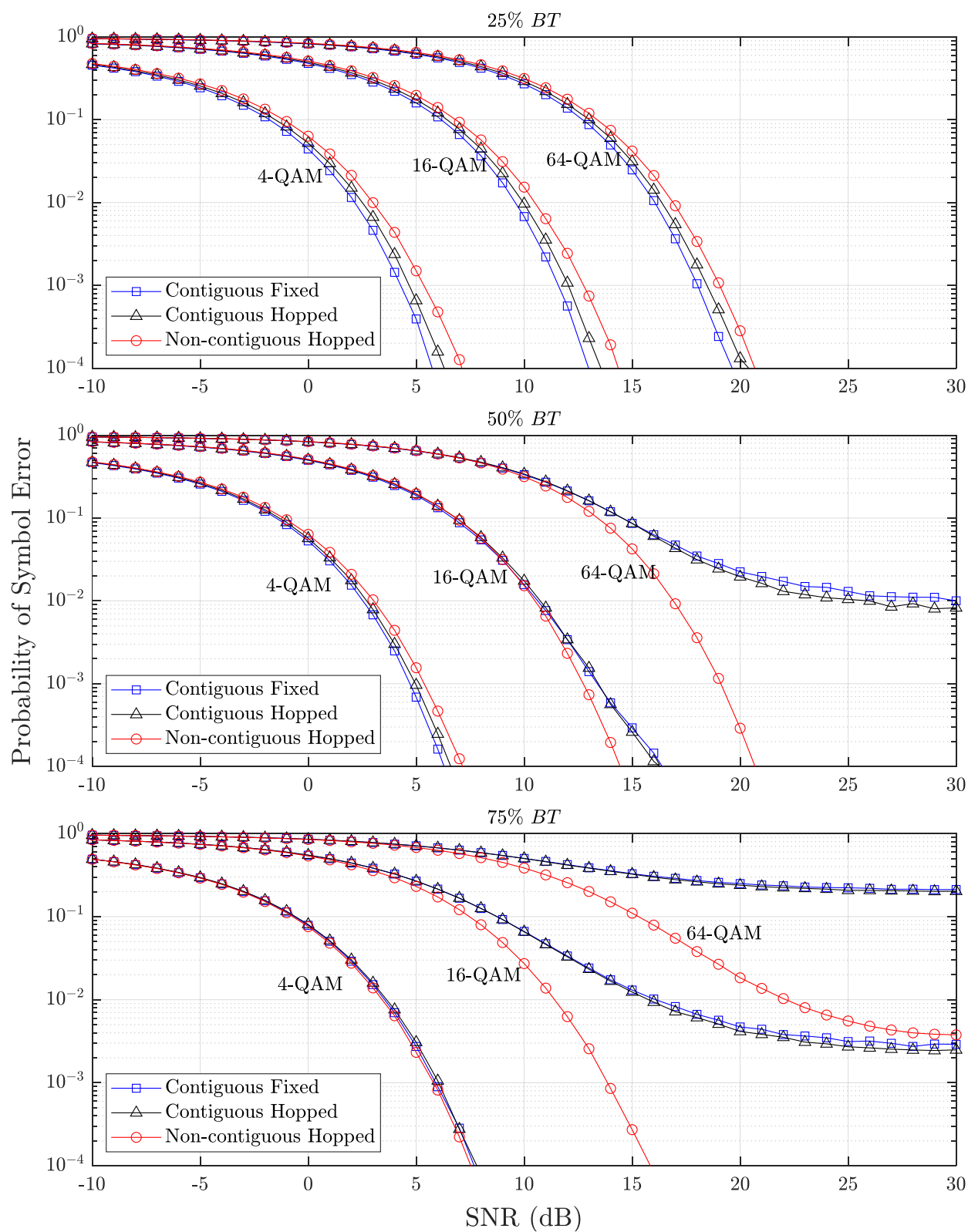
Figure 105: SER waterfall plots of Monte Carlo simulation assessing communications performance in a noisy channel for all possible parameterizations of the communication signal for $\eta = 4$
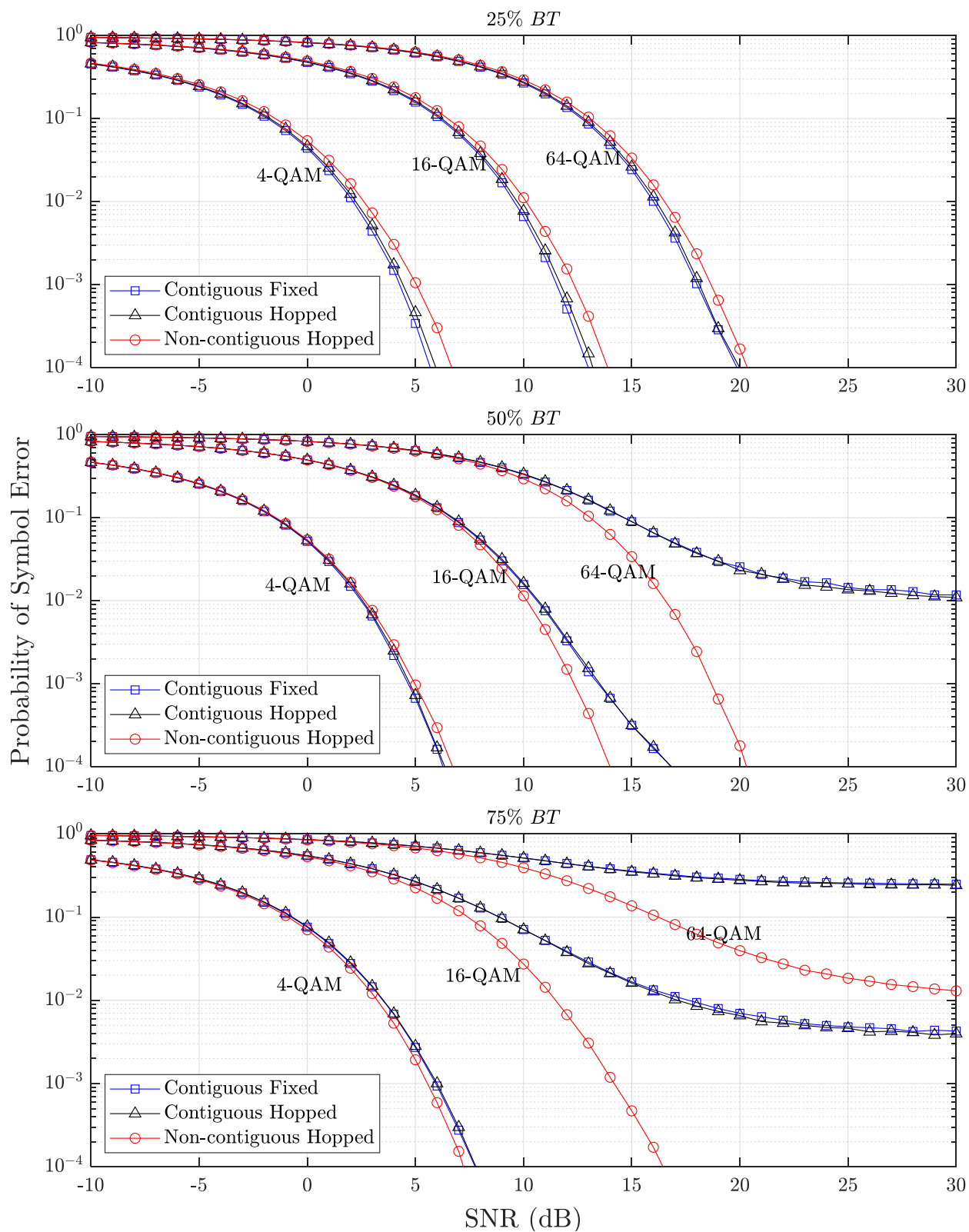
Figure 106: SER waterfall plots of Monte Carlo simulation assessing communications performance in a noisy channel for all possible parameterizations of the communication signal for $\eta = 8$
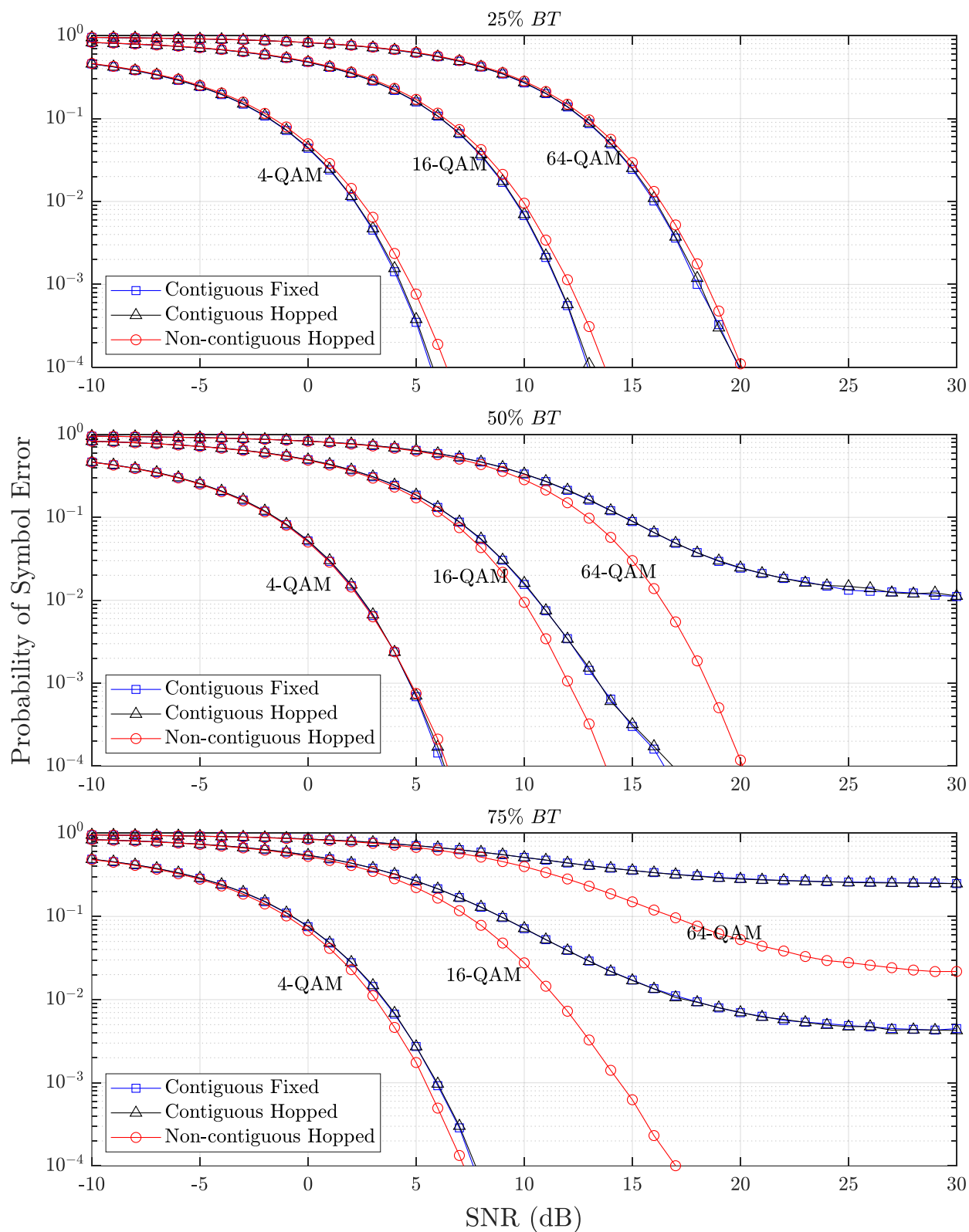
Figure 107: SER waterfall plots of Monte Carlo simulation assessing communications performance in a noisy channel for all possible parameterizations of the communication signal for $\eta = 16$

5.4 Experimental Evaluation of THoRaCs Waveforms for Radar Operation

Open-air testing was performed to assess the capability of the THoRaCs waveforms for radar function in an MTI scenario. The radar testbed hardware setup and illuminated intersection are identical to that described for the NIMPC experimental test in Section 4.5 and depicted in Figure 68 and Figure 69. Three sets of optimized THoRaCs waveforms were generated with $BT = 200$ ($B = 66.7$ MHz and pulse width $T = 3\mu s$) and oversampling factor of 3. Each set contains three different optimized THoRaCs waveform CPIs concatenated to one another in order to illuminate a nearly identical scene at the traffic intersection. Each CPI contains $M = 1000$ pulses and is 40 ms in duration with a PRF of 25 kHz. The first waveform set contains THoRaCs waveforms optimized with communications signals drawn from 4-QAM constellations with 25% BT ($N = 50$) subcarriers per pulse and placement strategies of contiguous fixed, contiguous hopped, and non-contiguous hopped. The second waveform set contains THoRaCs waveforms optimized with communications signals drawn from 16-QAM constellations with 25% BT ($N = 50$) subcarriers per pulse and placement strategies of contiguous fixed, contiguous hopped, and non-contiguous hopped. The third waveform set contains THoRaCs waveforms optimized with communications signals drawn from 64-QAM constellations with 25% BT ($N = 50$) subcarriers per pulse and placement strategies of contiguous fixed, contiguous hopped, and non-contiguous hopped. Hardware loopback versions of each waveform were captured and used for matched filter pulse compression, which was performed on the collected backscatter of each emission, followed by Doppler processing and projection-based clutter cancellation. The Taylor Doppler window taper shown in Figure 9 was used to suppress Doppler sidelobes.

Figure 108 shows the RD maps formed for the first THoRaCs waveform set optimized with communications signals drawn from 4-QAM constellations with 25% BT ($N = 50$) subcarriers per

pulse and placement strategies of contiguous fixed, contiguous hopped, and non-contiguous hopped. Many moving vehicles are discernible in the traffic intersection and each RD map is qualitatively the same. Figure 109 shows the RD maps formed for the second THoRaCs waveform set optimized with communications signals drawn from 16-QAM constellations with 25% *BT* (N = 50) subcarriers per pulse and placement strategies of contiguous fixed, contiguous hopped, and non-contiguous hopped. Many moving vehicles are discernible once again in the traffic intersection and each RD map is qualitatively the same once again. Figure 110 shows the RD maps formed for the third THoRaCs waveform set optimized with communications signals drawn from 64-QAM constellations with 25% *BT* (N = 50) subcarriers per pulse and placement strategies of contiguous fixed, contiguous hopped, and non-contiguous hopped. Many moving vehicles are discernible once again in the traffic intersection and each RD map is qualitatively the same once again. A reduction in Doppler sidelobe levels, and broadening of the Doppler mainlobes, due to the Taylor window can be observed when comparing these open-air results to those presented in Section 4.5. The results shown in this section demonstrate the efficacy of optimized THoRaCs waveforms for radar operation.
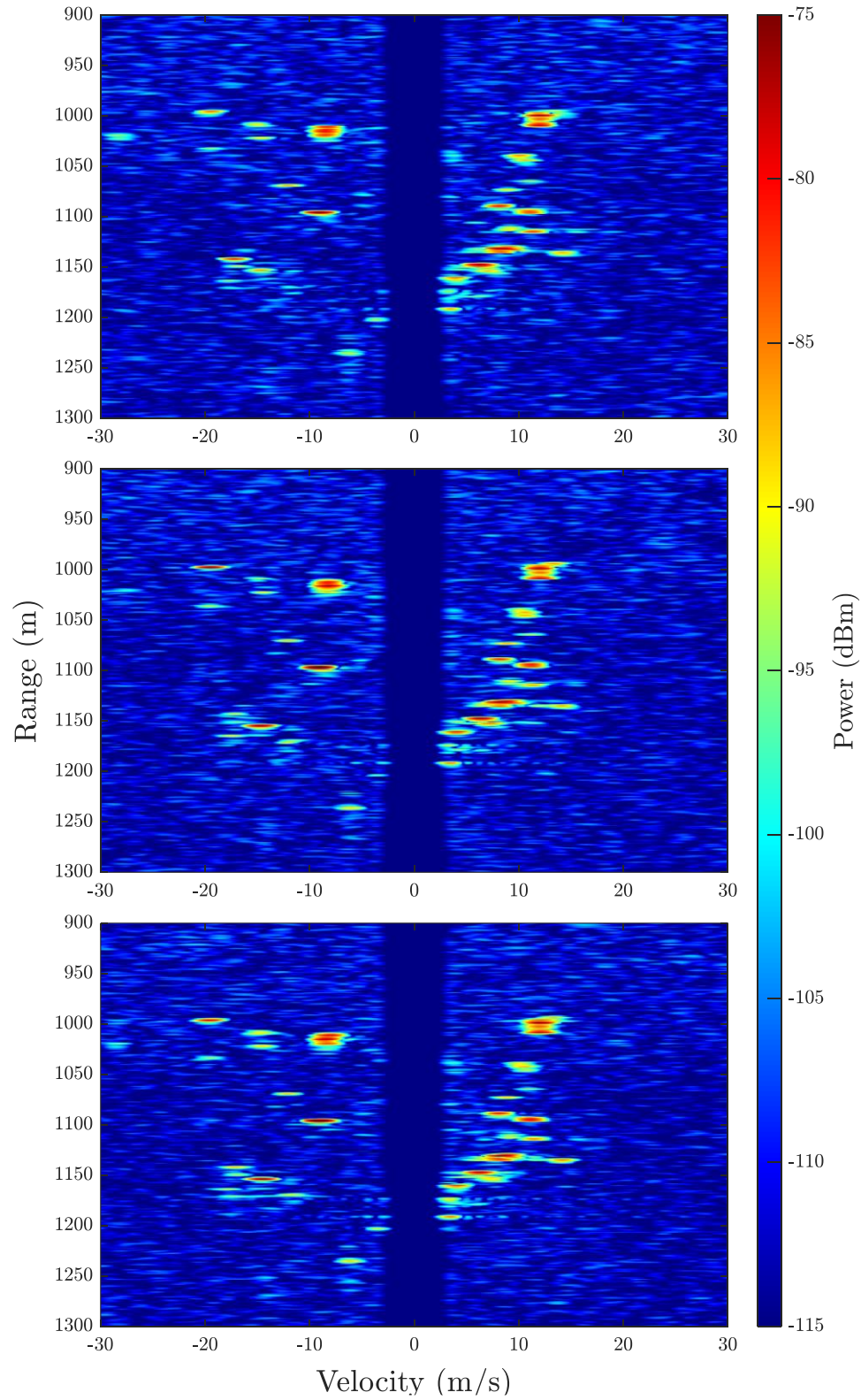
Figure 108: RD maps of THoRaCs transmit waveform set optimized with communications signals drawn from 4-QAM constellations with 25% *BT* (*N* = 50) subcarriers per pulse and placement strategies of contiguous fixed (top), contiguous hopped (middle), and non-contiguous hopped (bottom) for physical radar MTI experiment
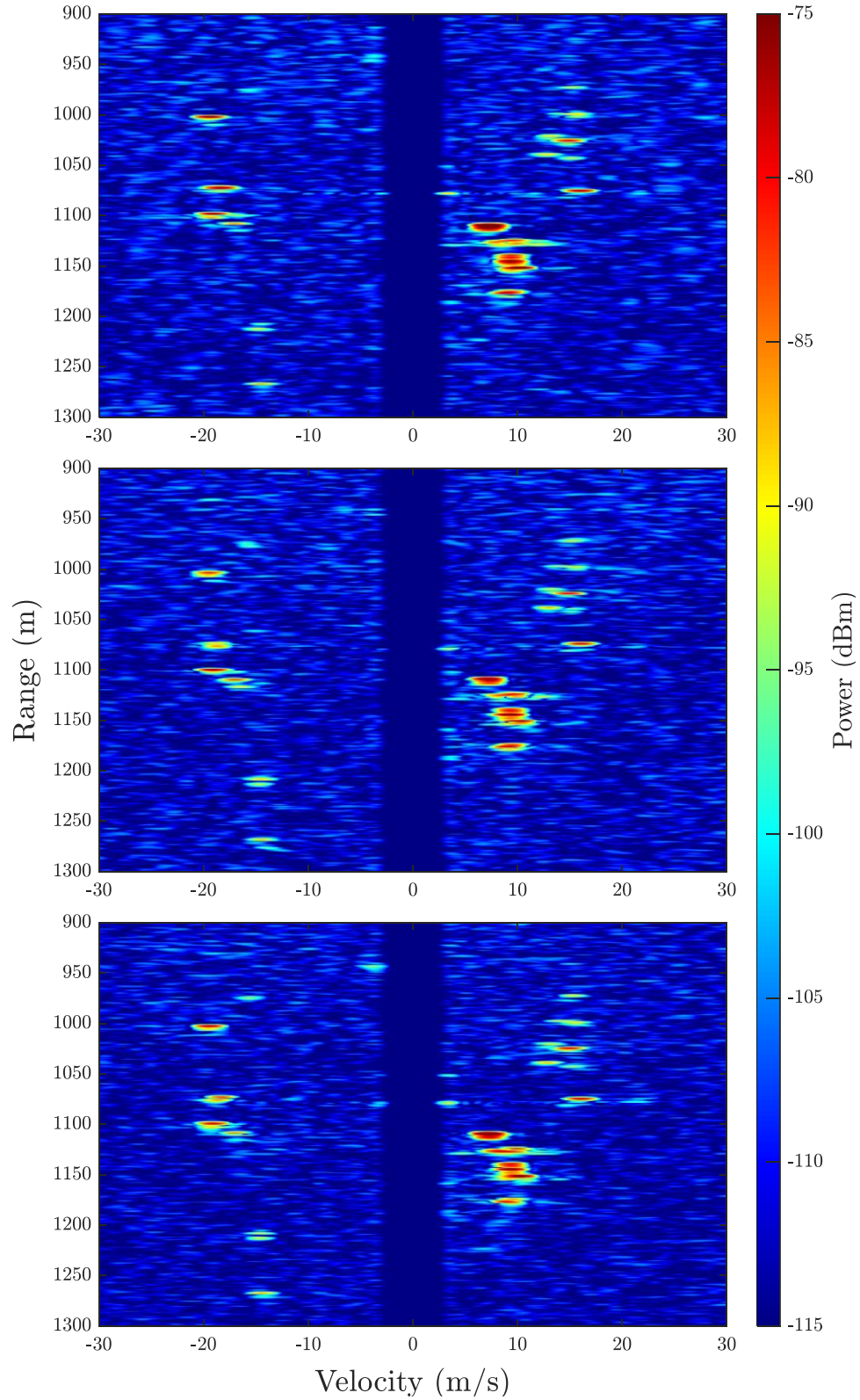
Figure 109: RD maps of THoRaCs transmit waveform set optimized with communications signals drawn from 16-QAM constellations with 25% *BT* (*N* = 50) subcarriers per pulse and placement strategies of contiguous fixed (top), contiguous hopped (middle), and non-contiguous hopped (bottom) for physical radar MTI experiment
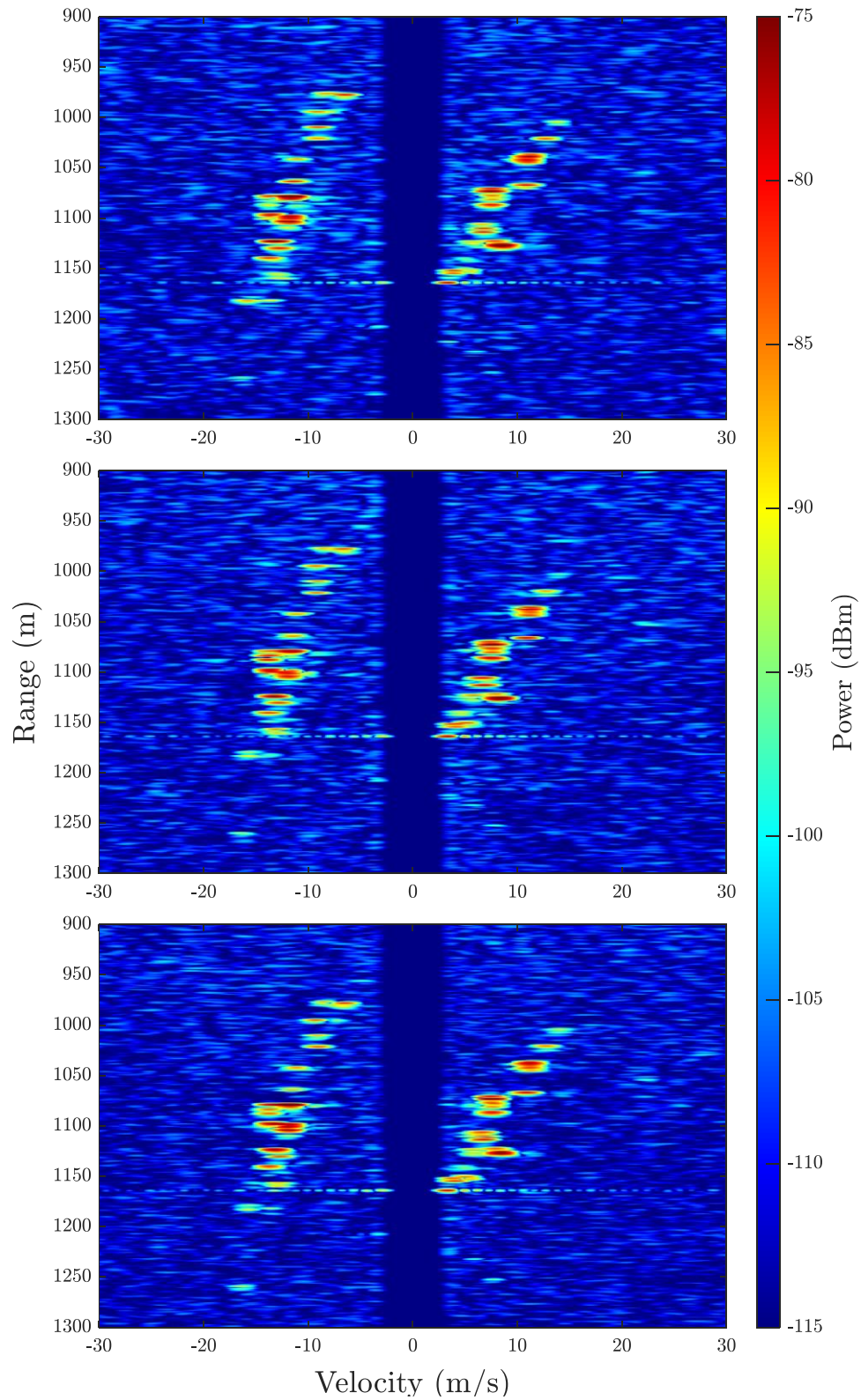
Figure 110: RD maps of THoRaCs transmit waveform set optimized with communications signals drawn from 64-QAM constellations with 25% *BT* (*N* = 50) subcarriers per pulse and placement strategies of contiguous fixed (top), contiguous hopped (middle), and non-contiguous hopped (bottom) for physical radar MTI experiment

5.5 Experimental Evaluation of THoRaCs Waveforms for Communications Operation

Experimental assessment of the communication function of optimized THoRaCs is demonstrated first using loopback capture of the transmitted signals, thus representing a high SNR environment. Each THoRaCs test waveform is physically generated on the same AWG used in the radar testbed and captured on the same RSA, which are connected directly together. The clocks of the transmit AWG and receive RSA are not reference locked to one another, thus a phase drift will be present across the collection interval of each test waveform. The waveform parameters for each test case are the same as described in Section 5.4 for the open-air radar experiment.

In order for the THoRaCs waveforms to operate in a real communications scenario, it is necessary for the communication receiver to perform synchronization and channel estimation/equalization based on a priori known pilot symbols before demodulation and estimation of the embedded communications signal can be accomplished. Although the communications signal embedded into the optimized THoRaCs signal is OFDM, a cyclic prefix is not present, thus traditional OFDM frequency domain equalization [42] cannot be performed without introducing error. Therefore, channel equalization is conducted using a Wiener Filer (WF) to estimate the inverse response of the channel and then creating an inverse filter in the form of a zero-forcing (ZF) equalizer. The signal received at the communications receiver, $y(t)$, can be modeled as

$$y(t) = s(t) * g(t) + n(t),\qquad(5.9)$$

for the transmitted THoRaCs waveform $s(t)$, impulse response of the communications channel, $g(t)$, and AWGN present in the receive channel $n(t)$. The discretized WF estimate of the channel inverse is formed by [114]

$$\hat{\mathbf{g}} = \mathbf{R}^{-1}\mathbf{p},\qquad(5.10)$$

where $\mathbf{R}$ is the autocorrelation matrix formed from $s(t)$ and $\mathbf{p}$ is the cross-correlation vector between the transmitted signal $s(t)$ and the received signal captured at the communications receiver $y(t)$. The WF estimate of the channel inverse is performed using a pilot waveform (a pulse of the transmitted CPI) where the symbol sequence is assumed to be known at the communications reviver (needed to form $\mathbf{p}$ in (5.10)). This estimate is formed using every 50th pulse as a pilot pulse (starting with the first pulse), which then serves as the estimate for the next 49 pulses in the signal. Once the WF channel estimate is determined, the ZF equalizer is formed as [42]

$$\mathbf{c} = (\mathbf{A}^{H}\mathbf{A} + \sigma\mathbf{I})^{-1}\mathbf{A}^{H}\mathbf{e}. \tag{5.11}$$

In (5.11), $\mathbf{e}$ is an elementary vector with a '1' in the middle element and zeros elsewhere, $\mathbf{I}$ is an identity matrix and σ is a diagonal loading factor used to prevent an ill-conditioned matrix inverse. The matrix $\mathbf{A}$ is formed with delay-shifted versions of the WF estimate formed from (5.10) as

$$\mathbf{A} = \begin{bmatrix} \hat{\mathbf{g}} & 0 & \cdots & 0 \\ 0 & \hat{\mathbf{g}} & \ddots & \vdots \\ \vdots & \ddots & \ddots & 0 \\ 0 & \cdots & 0 & \hat{\mathbf{g}} \end{bmatrix}. \tag{5.12}$$

The generated ZF equalizer is applied, via convolution, to a discretized version of the receive signal $y(t)$ in an attempt to remove as much of the channel impulse response as possible, resulting in an estimate of the transmitted THoRaCs signal.

In addition to channel estimation and equalization, synchronization also needs to be performed since the transmitter and receiver are not reference locked to a common clock. This lack of reference will cause the relative phases of the transmit and receive signals to drift over time (due to both open-air propagation and phase offset in the hardware clocks), thus corrupting the phase estimate of the QAM symbols embedded into the waveform. The first and second pulses in the waveform set were used as pilots to estimate the phase offset of the transmitted and received

signals. This phase offset is expected to remain nearly constant and persist for each pulse in the signal in a predictable manner. The phase offset is thus compensated in a progressive manner for all pulses after the 2nd, with a reset occurring every 50th pulse to address minor errors in the phase offset estimation.

Figure 111 shows the demodulated symbols, along with the true constellation values, for a CPI of $M = 1000$ THoRaCs waveforms captured in loopback with $N = 50$ (25% of BT) subcarriers per pulse modulated from a 4-QAM constellation using the "contiguous fixed" placement strategy. It is observed that all demodulated symbols are fairly tightly grouped around their respective constellation values and no symbol errors occur upon demodulation (not surprising considering the high SNR inherent to the loopback test setup). There is a noticeable phase-orientated behavior of the spreading of the demodulated symbols that can likely be attributed to the simplistic approach taken for frequency offset estimation and subsequent synchronization. The RMS EVM for the demodulated symbols in Figure 111 is -25.9 dB.

Figure 112 shows the demodulated symbols, along with the true constellation values, for a CPI of 1000 THoRaCs waveforms with $N = 50$ (25% of BT) subcarriers per pulse modulated from a 16-QAM constellation using the "contiguous fixed" placement strategy. It is observed that once again all demodulated symbols are fairly tightly grouped around their respective constellation values and no symbol errors occur upon demodulation. The noticeable phase-orientated behavior of the spreading of the demodulated symbols is again visible, but to a lesser degree than what was observed in Figure 111. The RMS EVM for the demodulated symbols in Figure 112 is -26.3 dB.

Figure 113 shows the demodulated symbols, along with the true constellation values, for a CPI of 1000 THoRaCs waveforms with $N = 50$ (25% of BT) subcarriers per pulse modulated from a 64-QAM constellation using the "contiguous fixed" placement strategy. The demodulated

symbols are not quite as tightly packed around their respective constellation values as the previous two cases, and the phase-orientated behavior of the spreading of the demodulated symbols is more severe for the higher energy phase rings on the constellation, indicating a dependence on the associated approach taken for channel estimation/equalization and phase synchronization. The RMS EVM for the demodulated symbols in Figure 113 is -24.8 dB and 50 symbol errors have occurred upon demodulation, yielding an SER of 1×10^{-3}.
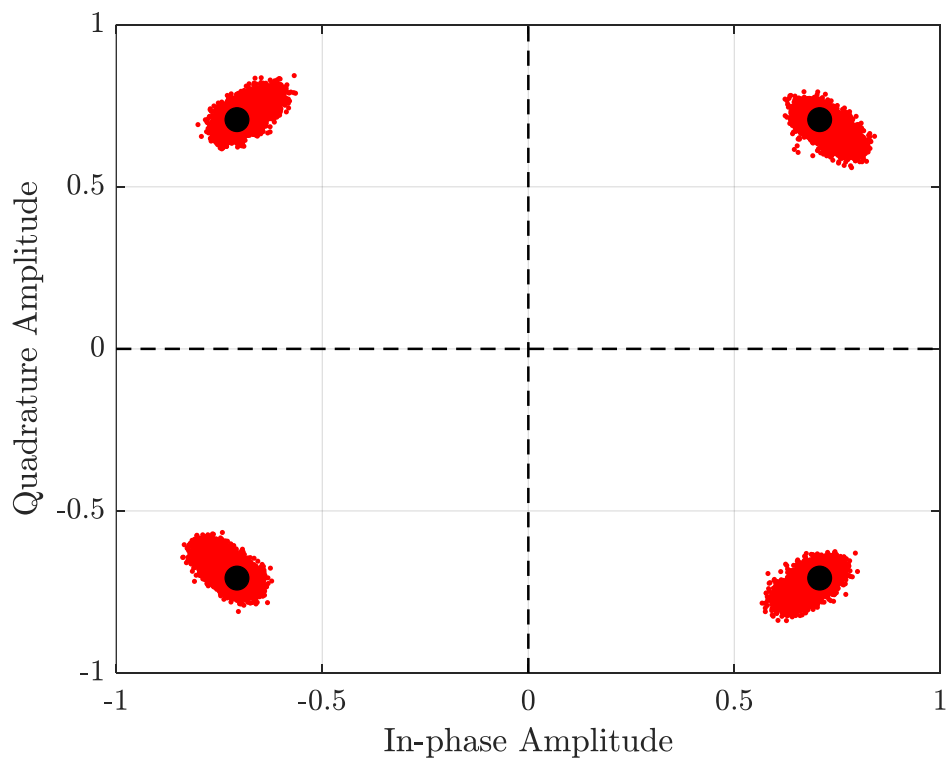
Figure 111: Plot of true (black) constellation and demodulated (red) communications symbols for a set of $M = 1000$ loopback captured THoRaCs waveforms with embedded communications parameters of a 4-QAM constellation with $N = 50$ (25% BT) subcarriers using the contiguous fixed placement strategy
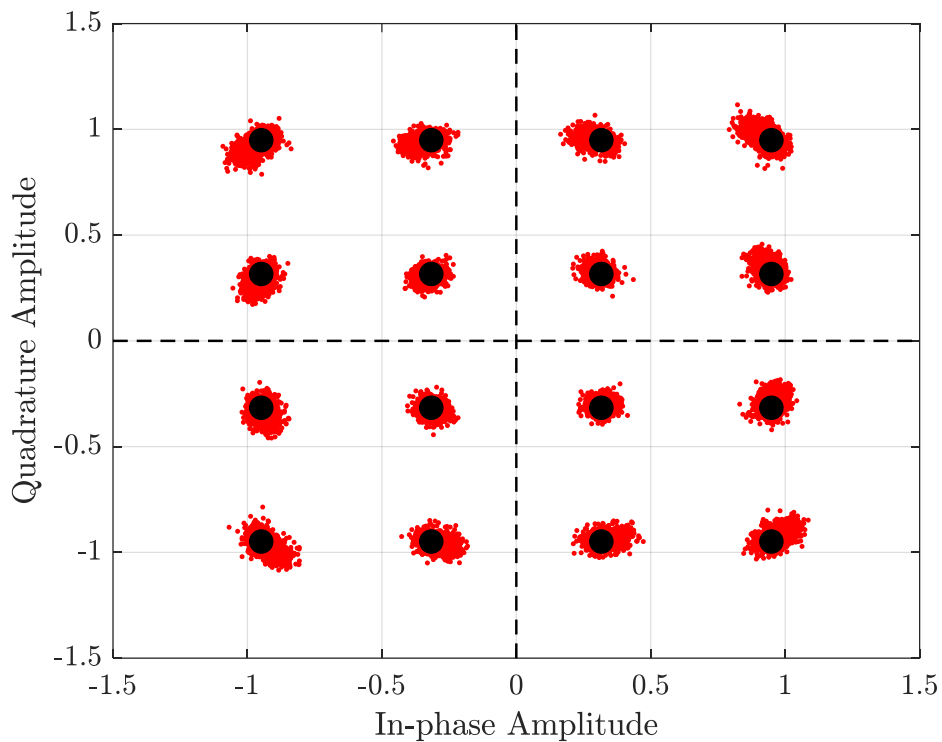
Figure 112: Plot of true (black) constellation and demodulated (red) communications symbols for a set of $M = 1000$ loopback captured THoRaCs waveforms with embedded communications parameters of a 16-QAM constellation with $N = 50$ (25% BT) subcarriers using the contiguous fixed placement strategy
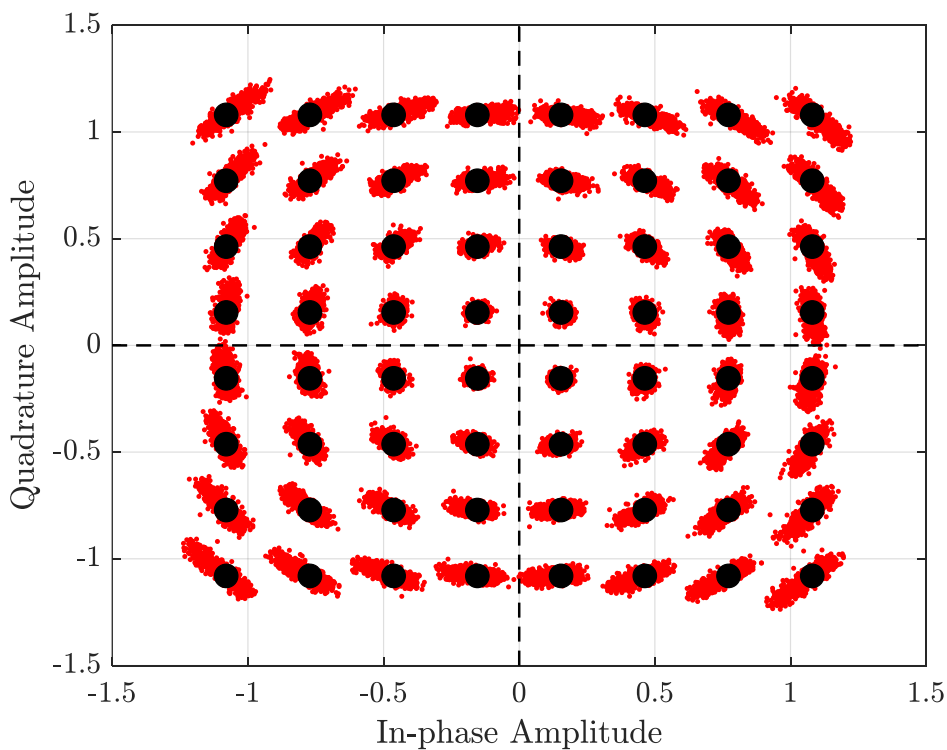
Figure 113: Plot of true (black) constellation and demodulated (red) communications symbols for a set of $M = 1000$ loopback captured THoRaCs waveforms with embedded communications parameters of a 64-QAM constellation with $N = 50$ (25% BT) subcarriers using the contiguous fixed placement strategy

Experimental assessment of the communication function of optimized THoRaCs is demonstrated next in an open-air communications collection scenario, as shown in Figure 114. The transmit and communications receive antennas are separated by approximately 50 meters on the lawn of Nichols Hall at the University of Kansas and have a clear line-of-sight (LOS) with one another. In this test configuration, the transmit AWG and receive RSA are once again not synchronized to a common reference clock and multipath will be present at the receive antenna due to reflections from the surrounding environment. The transmit AWG is connected to the transmit antenna and the receive RSA is connected to the receive antenna. The transmit and receive amplifiers utilized for the radar testbed experiment are used here as well.
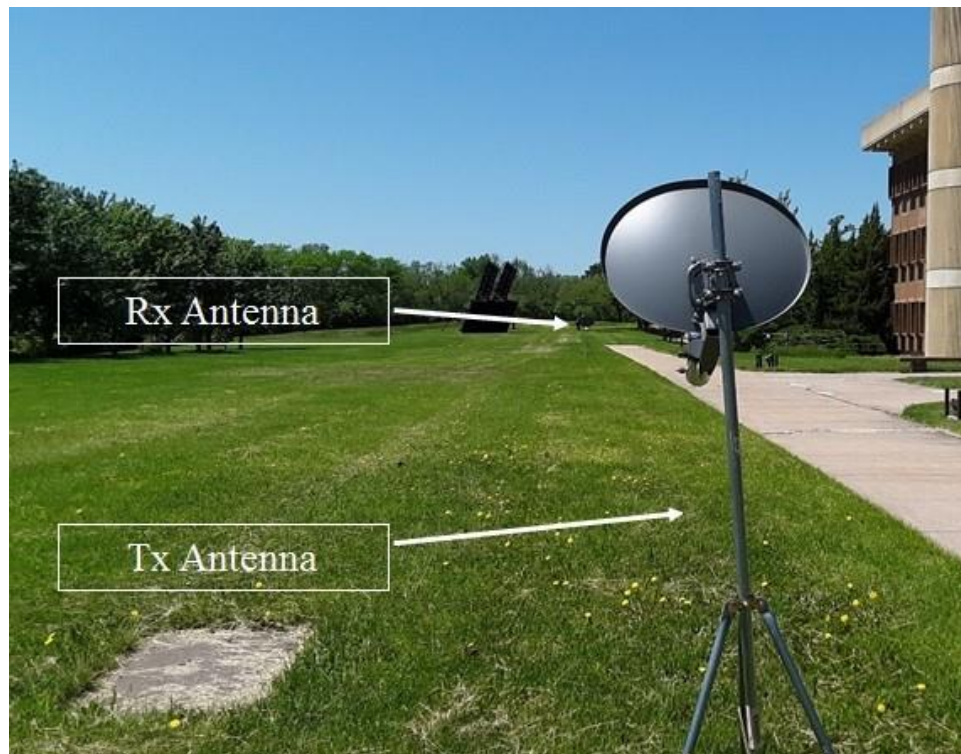
Figure 114: Open-air communications antenna configuration for experimental validation of THoRaCs waveforms in a LOS communications scenario

Figure 115 shows the demodulated symbols, along with the true constellation values, for a CPI of 1000 THoRaCs waveforms with $N = 50$ (25% of BT) subcarriers per pulse modulated from a 4-QAM constellation using the "contiguous fixed" placement strategy. The demodulated constellation symbols are not as tightly packed around their respective constellation points as the loopback capture of Figure 111, but this is not surprising given the migration to an open-air collection scenario. This result shows that the equalization and demodulation procedure has performed sufficiently well in an open-air communications test scenario. The RMS EVM for the demodulated symbols in Figure 115 is –21.2 dB, representing an increase of 4.7 dB over the loopback capture test of the same waveform in Figure 111, a modest increase for a much more challenging propagation channel. No symbol errors were observed in this test case.
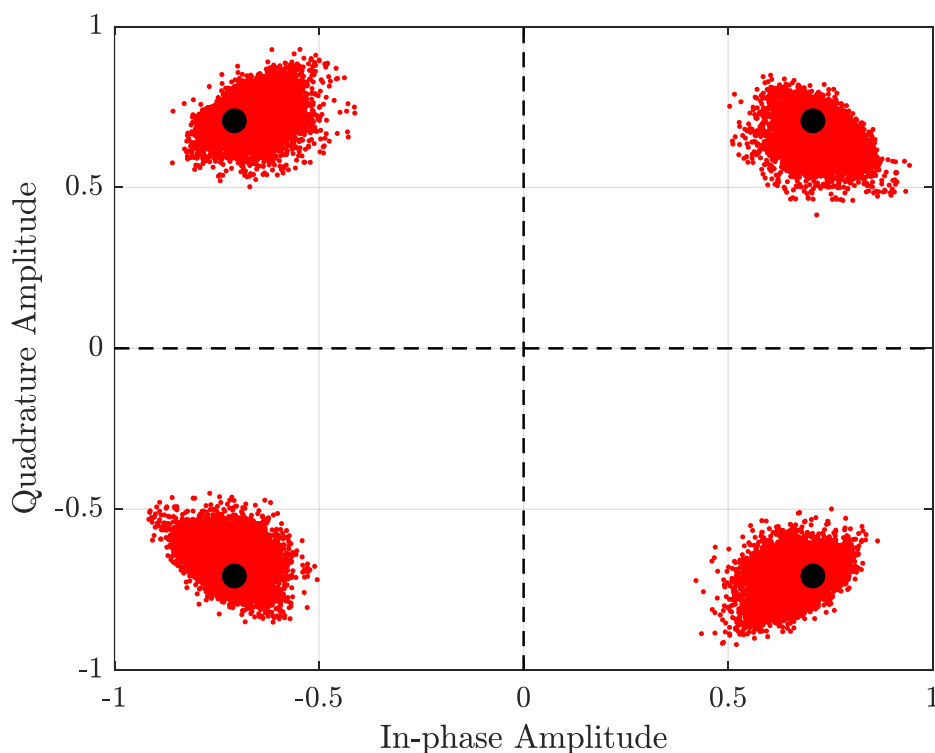
Figure 115: Plot of true (black) constellation and demodulated (red) communications symbols for a set of $M = 1000$ THoRaCs waveforms tested in an open-air configuration with embedded communications parameters of a 4-QAM constellation with $N = 50$ (25% BT) subcarriers using the contiguous fixed placement strategy

Figure 116 shows the demodulated symbols, along with the true constellation values, for a CPI of 1000 THoRaCs waveforms with $N = 50$ (25% of BT) subcarriers per pulse modulated from

a 16-QAM constellation using the "contiguous fixed" placement strategy. Once again, the demodulated constellation symbols are not as tightly packed around their respective constellation points as the loopback capture of Figure 112, and there is more a phase-oriented nature to the symbol spread, but this is again not surprising given the migration to an open-air collection scenario. The RMS EVM for the demodulated symbols in Figure 116 is –25.0 dB, representing an increase of 1.3 dB over the loopback capture test of the same waveform in Figure 112, a small increase for a much more challenging propagation channel. No symbol errors were observed in this test case.
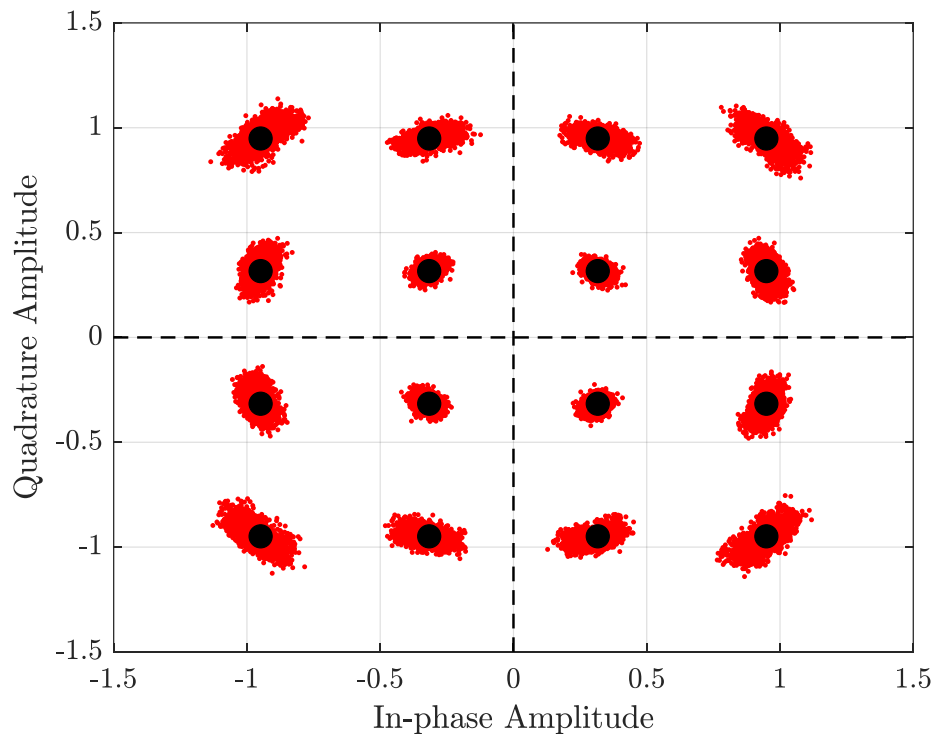
Figure 116: Plot of true (black) constellation and demodulated (red) communications symbols for a set of $M = 1000$ THoRaCs waveforms tested in an open-air configuration with embedded communications parameters of a 16-QAM constellation with $N = 50$ (25% BT) subcarriers using the contiguous fixed placement strategy

Figure 117 shows the demodulated symbols, along with the true constellation values, for a CPI of 1000 THoRaCs waveforms with $N = 50$ (25% of BT) subcarriers per pulse modulated from a 64-QAM constellation using the "contiguous fixed" placement strategy. Once again, the demodulated constellation symbols are not as tightly packed around their respective constellation

points as the loopback capture of Figure 113, and there is more a phase-oriented nature to the symbol spread, but this is again not surprising given the migration to an open-air collection scenario. The RMS EVM for the demodulated symbols in Figure 117 is –25.6 dB, representing a decrease of 0.8 dB over the loopback capture test of the same waveform in Figure 113, which is actually an improvement over the loopback capture, though likely not a statistically significant difference give the single test case. A total of 88 symbol errors occurred upon demodulation for this test case, yielding an SER of 1.8 x 10^{-3}, a moderate degradation compared to the loopback test case.
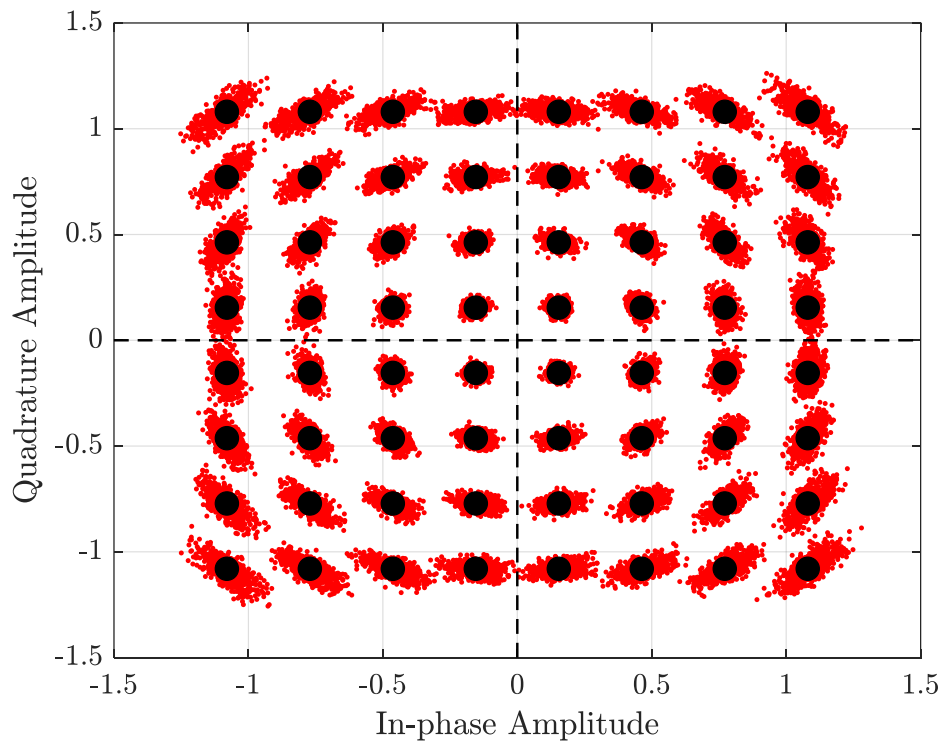
Figure 117: Plot of true (black) constellation and demodulated (red) communications symbols for a set of $M = 1000$ THoRaCs waveforms tested in an open-air configuration with embedded communications parameters of a 64-QAM constellation with $N = 50$ (25% BT) subcarriers using the contiguous fixed placement strategy

Chapter 6: Conclusions and Future Work

Results presented in this document have demonstrated the capability of a radar system to spectrally cohabitate with in-band communications systems. Simulation and physical experimentation demonstrated this capability thoroughly. Even with successful demonstration of cohabitation, there is room for improvement and expansion upon the techniques presented here.

PRO-FM waveforms were shown to be excellent waveforms for radar functionality while readily incorporating hopping spectral notches to accommodate in-band interference. They possess constant amplitude, good spectral containment, and favorably low autocorrelation sidelobes due to proper design and optimization, even with varying orders of super Gaussian functions acting as the power spectrum templates. The primary drawback to PRO-FM waveforms was shown to be RSM introduced by incoherent combination of sidelobes when performing pulse compression. RSM was shown to be exacerbated by the introduction of hopping spectral notches throughout the waveform CPI due to additional modulation of the pulse compression mainlobe.

Joint-domain processing via NIMPC with clutter cancellation was shown as an effective means to mitigate this RSM, at the cost of increased computation complexity. NIMPC was demonstrated to mostly preserve the spectral notch in PRO-FM waveforms for the purpose of mitigating in-band interference. The capability of hopping notched PRO-FM waveforms to avoid and accommodate hopping interference in the radar waveform band was demonstrated through simulation results and physical experimentation with a radar testbed. The capability of NIMPC was also proven through simulation and physical experimentation.

THoRaCs waveforms were shown to be an effective dual-function radar waveform with embedded communications. Extensive simulation showed their utility as a radar waveform with communications capability only limited by the choice of embedded communications signal

parameterization and available degrees of design freedom available within the waveform. Physical experimentation on a radar testbed demonstrated their potential as good radar waveforms. Hardware experimentation in both loopback and open-air communications scenarios showed that THoRaCs waveforms can successfully embed a communications signal that can be successfully demodulated at a communications receiver when proper channel estimation, equalization and phase synchronization is performed.

Future work for notched PRO-FM waveforms will include physical experimentation with higher order super Gaussian templates, which has been performed for notch-free PRO-FM waveforms but not their notched counterpart. Simulation results shown in this work lend confidence in the transition from simulation to physical experimentation. Future work with NIMPC will include examination of the preservation of spectral notches and determination of the ability to always preserve the entire notch depth in the waveform spectrum, which was shown to be inconsistent in simulation and physical experimentation. A method of performing Doppler windowing in joint-domain NIMPC processing is also a topic of future interest, as the application of such will take a different form that of sequential pulse compression followed by Doppler processing, which performs the filtering operation sequentially in each domain, as opposed to jointly with NIMPC.

Physical experimentation of THoRaCs waveforms optimized with higher order super Gaussian templates is another topic of future interest. This includes validation of both the radar and communications capabilities of the waveform in open-air experiments for both functionalities. Again, simulation results shown in this work lend confidence in the transition from simulation to physical experimentation. Finally, investigation of alternative channel estimation and equalization techniques, as well as phase synchronization, or expansion of the approaches taken in this work

are topics of future interest. Finally, testing of the communications capability in more realistic open-air communications propagation environments, including non-line-of-sight (NLOS) is also desired. This could possibly necessitate more robust estimation and equalization techniques than what was explored here.

Appendix A: Tables Summarizing Metrics in Chapter 5

This appendix contains tables providing summaries for values of the PSF δ metric (Table 5), RMS

EVM (Table 6) and SER (Table 7) for all communications signal parameterizations and values of

η for the THoRaCs simulations conducted in Section 5.3.

Table 5: Summary of PSF δ values (dB) for all communication signal parameterizations and values of η for THoRaCs simulation in Section 5.3

Constellation	Placement Strategy	Subcarriers (% BT)	$\eta = 2$	$\eta = 4$	$\eta = 8$	$\eta = 16$
4-QAM	Contiguous Fixed	25	-66.5	-65.0	-64.5	-64.2
4-QAM	Contiguous Fixed	50	-64.5	-63.1	-62.7	-62.6
4-QAM	Contiguous Fixed	75	-64.0	-63.0	-62.7	-62.6
4-QAM	Contiguous Hopped	25	-67.0	-65.1	-64.5	-64.2
4-QAM	Contiguous Hopped	50	-64.6	-63.2	-62.8	-62.7
4-QAM	Contiguous Hopped	75	-64.0	-63.0	-62.7	-62.6
4-QAM	Non-contiguous Hopped	25	-68.2	-66.0	-65.1	-64.8
4-QAM	Non-contiguous Hopped	50	-66.0	-64.2	-63.5	-63.2
4-QAM	Non-contiguous Hopped	75	-64.2	-63.3	-63.1	-63.1
16-QAM	Contiguous Fixed	25	-65.2	-63.8	-63.3	-63.2
16-QAM	Contiguous Fixed	50	-63.3	-61.8	-61.5	-61.4
16-QAM	Contiguous Fixed	75	-62.6	-61.7	-61.4	-61.3
16-QAM	Contiguous Hopped	25	-65.7	-64.0	-63.4	-63.2
16-QAM	Contiguous Hopped	50	-63.2	-62.0	-61.6	-61.5
16-QAM	Contiguous Hopped	75	-62.6	-61.7	-61.4	-61.4
16-QAM	Non-contiguous Hopped	25	-67.0	-65.0	-64.3	-64.0
16-QAM	Non-contiguous Hopped	50	-64.6	-62.9	-62.3	-62.1
16-QAM	Non-contiguous Hopped	75	-62.9	-61.9	-61.7	-61.6
64-QAM	Contiguous Fixed	25	-64.9	-63.6	-63.2	-63.0
64-QAM	Contiguous Fixed	50	-62.8	-61.6	-61.3	-61.3
64-QAM	Contiguous Fixed	75	-62.4	-61.5	-61.2	-61.1
64-QAM	Contiguous Hopped	25	-65.5	-63.9	-63.2	-63.0
64-QAM	Contiguous Hopped	50	-63.1	-61.9	-61.4	-61.3
64-QAM	Contiguous Hopped	75	-62.4	-61.5	-61.3	-61.2
64-QAM	Non-contiguous Hopped	25	-66.9	-64.9	-64.1	-63.8
64-QAM	Non-contiguous Hopped	50	-64.4	-62.7	-62.1	-61.9
64-QAM	Non-contiguous Hopped	75	-62.7	-61.7	-61.5	-61.4

Table 6: Summary of EVM values (dB) for all communication signal parameterizations and values of η for THoRaCs simulation in Section 5.3

Constellation	Placement Strategy	Subcarriers (% BT)	$\eta = 2$	$\eta = 4$	$\eta = 8$	$\eta = 16$
4-QAM	Contiguous Fixed	25	-46.6	-43.7	-45.2	-42.4
4-QAM	Contiguous Fixed	50	-26.6	-24.4	-23.9	-24.1
4-QAM	Contiguous Fixed	75	-19.5	-17.3	-16.7	-16.8
4-QAM	Contiguous Hopped	25	-54.0	-46.2	-43.9	-44.7
4-QAM	Contiguous Hopped	50	-27.8	-24.6	-23.8	-24.1
4-QAM	Contiguous Hopped	75	-19.6	-17.4	-16.9	-16.7
4-QAM	Non-contiguous Hopped	25	-130.2	-117.0	-111.8	-109.2
4-QAM	Non-contiguous Hopped	50	-66.6	-54.4	-49.9	-48.0
4-QAM	Non-contiguous Hopped	75	-30.1	-24.3	-22.4	-21.6
16-QAM	Contiguous Fixed	25	-45.5	-43.2	-42.4	-43.6
16-QAM	Contiguous Fixed	50	-26.3	-24.0	-23.9	-23.8
16-QAM	Contiguous Fixed	75	-19.4	-17.2	-16.7	-16.6
16-QAM	Contiguous Hopped	25	-48.6	-44.4	-43.0	-42.5
16-QAM	Contiguous Hopped	50	-27.7	-24.7	-23.9	-23.9
16-QAM	Contiguous Hopped	75	-19.7	-17.5	-16.8	-16.8
16-QAM	Non-contiguous Hopped	25	-130.2	-115.9	-111.2	-108.2
16-QAM	Non-contiguous Hopped	50	-64.9	-53.2	-49.4	-47.1
16-QAM	Non-contiguous Hopped	75	-29.7	-24.2	-22.0	-21.5
64-QAM	Contiguous Fixed	25	-46.0	-42.9	-45.0	-45.2
64-QAM	Contiguous Fixed	50	-26.4	-24.2	-23.9	-24.1
64-QAM	Contiguous Fixed	75	-19.3	-17.2	-16.8	-16.8
64-QAM	Contiguous Hopped	25	-53.2	-43.1	-41.8	-42.5
64-QAM	Contiguous Hopped	50	-27.2	-24.6	-23.9	-23.9
64-QAM	Contiguous Hopped	75	-19.5	-17.4	-16.8	-16.7
64-QAM	Non-contiguous Hopped	25	-129.5	-116.3	-110.6	-108.2
64-QAM	Non-contiguous Hopped	50	-64.6	-52.8	-48.4	-46.6
64-QAM	Non-contiguous Hopped	75	-29.8	-24.1	-22.2	-21.5

Table 7: Summary of SER values for all communication signal parameterizations and values of η for THoRaCs simulation in Section 5.3

Constellation	Placement Strategy	Subcarriers (% BT)	$\eta = 2$	$\eta = 4$	$\eta = 8$	$\eta = 16$
4-QAM	Contiguous Fixed	25	0	0	0	0
4-QAM	Contiguous Fixed	50	0	0	0	0
4-QAM	Contiguous Fixed	75	0	0	0	0
4-QAM	Contiguous Hopped	25	0	0	0	0
4-QAM	Contiguous Hopped	50	0	0	0	0
4-QAM	Contiguous Hopped	75	0	0	0	0
4-QAM	Non-contiguous Hopped	25	0	0	0	0
4-QAM	Non-contiguous Hopped	50	0	0	0	0
4-QAM	Non-contiguous Hopped	75	0	0	0	0
16-QAM	Contiguous Fixed	25	0	0	0	0
16-QAM	Contiguous Fixed	50	0	0	0	1.00E-05
16-QAM	Contiguous Fixed	75	3.40E-04	2.60E-03	4.50E-03	4.40E-03
16-QAM	Contiguous Hopped	25	0	0	0	0
16-QAM	Contiguous Hopped	50	0	0	0	1.00E-05
16-QAM	Contiguous Hopped	75	1.53E-04	2.10E-03	3.90E-03	3.20E-03
16-QAM	Non-contiguous Hopped	25	0	0	0	0
16-QAM	Non-contiguous Hopped	50	0	0	0	0
16-QAM	Non-contiguous Hopped	75	0	0	0	0
64-QAM	Contiguous Fixed	25	0	0	0	0
64-QAM	Contiguous Fixed	50	3.40E-03	8.30E-03	1.01E-02	9.50E-03
64-QAM	Contiguous Fixed	75	9.36E-02	2.09E-01	2.40E-01	2.44E-01
64-QAM	Contiguous Hopped	25	0	0	0	0
64-QAM	Contiguous Hopped	50	2.20E-03	7.30E-03	8.90E-03	1.16E-02
64-QAM	Contiguous Hopped	75	8.66E-02	1.98E-01	2.38E-01	2.44E-01
64-QAM	Non-contiguous Hopped	25	0	0	0	0
64-QAM	Non-contiguous Hopped	50	0	0	0	0
64-QAM	Non-contiguous Hopped	75	6.67E-06	3.00E-03	1.21E-02	1.79E-02

Appendix B: List of Acronyms

Acronym	Definition
4G	4th Generation
5G	5th Generation
AM	Amplitude Modulation
AWG	Arbitrary Waveform Generator
AWGN	Additive White Gaussian Noise
CE-OFDM	Constant Envelope OFDM
CNR	Clutter-to-Noise Ratio
CPI	Coherent Processing Interval
CPM	Continuous Phase Modulation
CW	Continuous Waveform
DFRC	Dual-function Radar and Communications
DFT	Discrete Fourier Transform
EVM	Error Vector Magnitude
FFT	Fast Fourier Transform
FM	Frequency Modulation
IFFT	Inverse Fast Fourier Transform
ISI	Intersymbol Interference
LFM	Linear Frequency Modulation
LOS	Line-of-Sight
LS-MMF	Least Squares Mismatched Filter
LTI	Linear Time Invariant
MF	Matched Filter
MIMO	Multiple Input Multiple Output
MTI	Moving Target Indication
NIMPC	Non-identical Multiple Pulse Compression
NLOS	Non-Line-of-Sight
OFDM	Orthogonal Frequency Division Multiplexing
PCFM	Polyphase Coded FM
PE-THoRaCs	Power Efficient Tandem Hopped Radar and Communications
PRF	Pulse Repetition Frequency
PRI	Pulse Repetition Interval
PRO-FM	Pseudo Random Optimized FM
PSF	Point Spread Function
QAM	Quadrature Amplitude Modulation
RCS	Radar Cross Section
RD	Range Doppler
RF	Radio Frequency

Acronym	Definition
RFI	Radio Frequency Interference
RFM	Random FM
RMS	Root-Mean-Square
RNG	Random Number Generator
RSA	Real-time Spectrum Analyzer
RSM	Range Sidelobe Modulation
RUWO	Reiterative Uniform Weighting Optimization
SER	Symbol Error Rate
SG	Super Gaussian
SIR	Signal-to-Interference Ratio
SNR	Signal-to-Noise Ratio
SS-MA	Spread Spectrum Multiple Access
SVD	Singular Value Decomposition
THoRaCs	Tandem Hopped Radar and Communications
WF	Wiener Filter
ZF	Zero-Forcing

References

[1]   H. Griffiths *et al.*, "Radar Spectrum Engineering and Management: Technical and Regulatory Issues," *Proceedings of the IEEE,* vol. 103, no. 1, pp. 85-102, 2015.

[2]   J. M. Peha, "Approaches to spectrum sharing," *IEEE Communications Magazine,* vol. 43, no. 2, pp. 10-12, 2005.

[3]   H. Griffiths, S. Blunt, L. Cohen, and L. Savy, "Challenge problems in spectrum engineering and waveform diversity," in *2013 IEEE Radar Conference (RadarCon13)*, 29 April-3 May 2013 2013, pp. 1-5.

[4]   FCC. "Auctions." https://www.fcc.gov/auctions (accessed 19 Apr. 2023).

[5]   S. D. Blunt and E. S. Perrins, Eds. *Radar and Communication Spectrum Sharing*. London, UK: Scitech Publishing, 2018.

[6]   M. S. Greco, F. Gini, P. Stinco, and K. Bell, "Cognitive Radars: On the Road to Reality: Progress Thus Far and Possibilities for the Future," *IEEE Signal Processing Magazine,* vol. 35, no. 4, pp. 112-125, 2018.

[7]   A. Hassanien, M. G. Amin, E. Aboutanios, and B. Himed, "Dual-Function Radar Communication Systems: A Solution to the Spectrum Congestion Problem," *IEEE Signal Processing Magazine,* vol. 36, no. 5, pp. 115-126, 2019.

[8]   L. Zheng, M. Lops, Y. C. Eldar, and X. Wang, "Radar and Communication Coexistence: An Overview: A Review of Recent Methods," *IEEE Signal Processing Magazine,* vol. 36, no. 5, pp. 85-99, 2019.

[9]   A. F. Martone, K. I. Ranney, K. Sherbondy, K. A. Gallagher, and S. D. Blunt, "Spectrum Allocation for Noncooperative Radar Coexistence," *IEEE Transactions on Aerospace and Electronic Systems,* vol. 54, no. 1, pp. 90-105, 2018.

[10]   P. Stinco, M. S. Greco, and F. Gini, "Spectrum sensing and sharing for cognitive radars," *IET Radar, Sonar & Navigation,* vol. 10, no. 3, pp. 595-602, Feb. 2016.

[11]   M. Labib, V. Marojevic, A. F. Martone, J. H. Reed, and A. I. Zaghloui, "Coexistence between communications and radar systems: A survey," *URSI Radio Science Bulletin,* vol. 2017, no. 362, pp. 74-82, 2017.

[12]   H. Deng and B. Himed, "Interference Mitigation Processing for Spectrum-Sharing Between Radar and Wireless Communications Systems," *IEEE Transactions on Aerospace and Electronic Systems,* vol. 49, no. 3, pp. 1911-1919, 2013.

[13]   G. Meager, R. A. Romero, and Z. Staples, "Estimation and cancellation of high powered radar interference for communication signal collection," in *2016 IEEE Radar Conference (RadarConf)*, 2-6 May 2016 2016, pp. 1-4.

[14]   B. Ravenscroft, P. M. McCormick, S. D. Blunt, J. Jakabosky, and J. G. Metcalf, "Tandem-hopped OFDM communications in spectral gaps of FM noise radar," in *2017 IEEE Radar Conference (RadarConf)*, 8-12 May 2017 2017, pp. 1262-1267.

[15]   B. Ravenscroft, S. D. Blunt, C. Allen, A. Martone, and K. Sherbondy, "Analysis of spectral notching in FM noise radar using measured interference," in *International Conference on Radar Systems (Radar 2017)*, 23-26 Oct. 2017 2017, pp. 1-6.

[16]   J. Jakabosky, B. Ravenscroft, S. D. Blunt, and A. Martone, "Gapped spectrum shaping for tandem-hopped radar/communications & cognitive sensing," in *2016 IEEE Radar Conference (RadarConf)*, 2-6 May 2016 2016, pp. 1-6.

[17]   J. Jakabosky, S. D. Blunt, and A. Martone, "Incorporating hopped spectral gaps into nonrecurrent nonlinear FMCW radar emissions," in *2015 IEEE 6th International*

Workshop on Computational Advances in Multi-Sensor Adaptive Processing (CAMSAP), 13-16 Dec. 2015 2015, pp. 281-284.

[18] R. A. Romero and K. D. Shepherd, "Friendly Spectrally Shaped Radar Waveform With Legacy Communication Systems for Shared Access and Spectrum Management," *IEEE Access,* vol. 3, pp. 1541-1554, 2015.

[19] C. Sturm and W. Wiesbeck, "Waveform Design and Signal Processing Aspects for Fusion of Wireless Communications and Radar Sensing," *Proceedings of the IEEE,* vol. 99, no. 7, pp. 1236-1259, 2011.

[20] C. Sahin, J. G. Metcalf, A. Kordik, T. Kendo, and T. Corigliano, "Experimental Validation of Phase-Attached Radar/Communication (PARC) Waveforms: Radar Performance," in *2018 International Conference on Radar (RADAR)*, 27-31 Aug. 2018 2018, pp. 1-6.

[21] C. Sahin, J. G. Metcalf, and B. Himed, "Reduced complexity maximum SINR receiver processing for transmit-encoded radar-embedded communications," in *2018 IEEE Radar Conference (RadarConf18)*, 23-27 April 2018 2018, pp. 1317-1322.

[22] C. Sahin, J. G. Metcalf, and S. D. Blunt, "Filter design to address range sidelobe modulation in transmit-encoded radar-embedded communications," in *2017 IEEE Radar Conference (RadarConf)*, 8-12 May 2017 2017, pp. 1509-1514.

[23] C. Sahin, J. G. Metcalf, and S. D. Blunt, "Characterization of range sidelobe modulation arising from radar-embedded communications," in *International Conference on Radar Systems (Radar 2017)*, 23-26 Oct. 2017 2017, pp. 1-6.

[24] C. Sahin, P. M. McCormick, J. G. Metcalf, and S. D. Blunt, "Power-Efficient Multi-Beam Phase-Attached Radar/Communications," in *2019 IEEE Radar Conference (RadarConf)*, 22-26 April 2019 2019, pp. 1-6.

[25] C. Sahin, P. M. McCormick, and S. D. Blunt, "Optimized Stretch Processing Compensation for FMCW Phase-Attached Radar-Communications," in *2019 International Radar Conference (RADAR)*, 23-27 Sept. 2019 2019, pp. 1-5.

[26] C. Sahin, J. Jakabosky, P. M. McCormick, J. G. Metcalf, and S. D. Blunt, "A novel approach for embedding communication symbols into physical radar waveforms," in *2017 IEEE Radar Conference (RadarConf)*, 8-12 May 2017 2017, pp. 1498-1503.

[27] P. M. McCormick, C. Sahin, S. D. Blunt, and J. G. Metcalf, "FMCW Implementation of Phase-Attached Radar-Communications (PARC)," in *2019 IEEE Radar Conference (RadarConf)*, 22-26 April 2019 2019, pp. 1-6.

[28] J. B. Anderson, T. Aulin, and C. Sundberg, Eds. *Digital Phase Modulation*. New York, NY: Plenum Press, 1986.

[29] S. D. Blunt, M. Cook, J. Jakabosky, J. D. Graaf, and E. Perrins, "Polyphase-coded FM (PCFM) radar waveforms, part I: implementation," *IEEE Transactions on Aerospace and Electronic Systems,* vol. 50, no. 3, pp. 2218-2229, 2014.

[30] B. Ravenscroft, A. Fontes, P. M. McCormick, S. D. Blunt, and C. Musgrove, "Physically Realizable Multi-User Radar/Communications (MURC)," presented at the IEEE Radar Conference, San Antonio, TX, May 2023.

[31] D. J. Torrieri, Ed. *Principles of Spread-Spectrum Communication Systems*. Springer Nature, 2022.

[32] P. M. McCormick, "Spatially Diverse Dual-Function Radar-Communications with Reduced Self-Interference," in *2022 IEEE Radar Conference (RadarConf22)*, 21-25 March 2022 2022, pp. 1-6.

[33] P. M. McCormick, C. Sahin, S. D. Blunt, and J. G. Metcalf, "Physical Waveform Optimization for Multiple-Beam Multifunction Digital Arrays," in *2018 52nd Asilomar Conference on Signals, Systems, and Computers*, 28-31 Oct. 2018 2018, pp. 1036-1041.

[34] P. M. McCormick, B. Ravenscroft, S. D. Blunt, A. J. Duly, and J. G. Metcalf, "Simultaneous radar and communication emissions from a common aperture, Part II: Experimentation," in *2017 IEEE Radar Conference (RadarConf)*, 8-12 May 2017 2017, pp. 1697-1702.

[35] P. M. McCormick, S. D. Blunt, and J. G. Metcalf, "Simultaneous radar and communications emissions from a common aperture, Part I: Theory," in *2017 IEEE Radar Conference (RadarConf)*, 8-12 May 2017 2017, pp. 1685-1690.

[36] M. A. Richards, J. A. Scheer, and W. A. Holm, Eds. *Principles of Modern Radar: Basic Principles*. Edison, NJ: Scitech Publishing, 2010.

[37] M. A. Richards, Ed. *Fundamentals of Radar Signal Processing*. McGraw-Hill Education, 2014.

[38] J. R. Klauder, A. C. Price, S. Darlington, and W. J. Albersheim, "The theory and design of chirp radars," *The Bell System Technical Journal,* vol. 39, no. 4, pp. 745-808, 1960.

[39] B. P. Lathi, Ed. *Signal Processing & Linear Systems*. New York, NY: Oxford University Press, 1998.

[40] I. W. Selesnick and C. S. Burrus, Eds. *Fast convolution and filtering* (The Digital Signal Processing Handbook). CRC Press, 2017.

[41] MathWorks, *taylorwin*. [Online]. Available: https://www.mathworks.com/help/signal/ref/taylorwin.html

[42]   U. Madhow, Ed. *Fundamentals of Digital Communication*. Cambridge, UK: Cambridge University Press, 2008.

[43]   T. K. Moon, Ed. *Error Correction Coding: Mathematical Methods and Algorithms*. Hoboken, NJ: John Wiley & Sons, Inc., 2005.

[44]   *IRIG standard 106-20: Telemetry Standards,* Range Commanders Council Telemetry Group, 2020.

[45]   M. Ergen, Ed. *Mobile Broadband: Including WiMax and LTE*. New York, NY: Springer, 2009.

[46]   J. Jakabosky, S. D. Blunt, and B. Himed, "Waveform design and receive processing for nonrecurrent nonlinear FMCW radar," in *2015 IEEE Radar Conference (RadarCon)*, 10-15 May 2015 2015, pp. 1376-1381.

[47]   J. Jakabosky, S. D. Blunt, and B. Himed, "Spectral-shape optimized FM noise radar for pulse agility," in *2016 IEEE Radar Conference (RadarConf)*, 2-6 May 2016 2016, pp. 1-6.

[48]   S. D. Blunt, J. Jakabosky, M. Cook, J. Stiles, S. Seguin, and E. L. Mokole, "Polyphase-coded FM (PCFM) radar waveforms, part II: optimization," *IEEE Transactions on Aerospace and Electronic Systems,* vol. 50, no. 3, pp. 2230-2241, 2014.

[49]   P. M. McCormick and S. D. Blunt, "Nonlinear conjugate gradient optimization of polyphase-coded FM radar waveforms," in *2017 IEEE Radar Conference (RadarConf)*, 8-12 May 2017 2017, pp. 1675-1680.

[50]   C. A. Mohr, P. M. McCormick, C. A. Topliff, S. D. Blunt, and J. M. Baden, "Gradient-Based Optimization of PCFM Radar Waveforms," *IEEE Transactions on Aerospace and Electronic Systems,* vol. 57, no. 2, pp. 935-956, 2021.

[51]   T. Peng Seng, J. Jakabosky, J. M. Stiles, and S. D. Blunt, "On higher-order representations of Polyphase-Coded FM radar waveforms," in *2015 IEEE Radar Conference (RadarCon)*, 10-15 May 2015 2015, pp. 0467-0472.

[52]   Y. Sun, H. Fan, J. Wang, L. Ren, E. Mao, and T. Long, "Optimization of Diverse PCFM Waveforms and Joint Mismatched Filters," *IEEE Transactions on Aerospace and Electronic Systems,* vol. 57, no. 3, pp. 1840-1854, 2021.

[53]   P. S. Tan, J. Jakabosky, J. M. Stiles, and S. D. Blunt, "Higher-Order Implementations of Polyphase-Coded FM Radar Waveforms," *IEEE Transactions on Aerospace and Electronic Systems,* vol. 55, no. 6, pp. 2850-2870, 2019.

[54]   D. Zhao, Y. Wei, and Y. Liu, "PCFM Radar Waveform Design With Spectral and Correlation Considerations," *IEEE Transactions on Aerospace and Electronic Systems,* vol. 53, no. 6, pp. 2885-2898, 2017.

[55]   C. A. Mohr and S. D. Blunt, "Analytical Spectrum Representation for Physical Waveform Optimization Requiring Extreme Fidelity," in *2019 IEEE Radar Conference (RadarConf)*, 22-26 April 2019 2019, pp. 1-6.

[56]   C. A. Mohr, J. W. Owen, S. D. Blunt, and C. T. Allen, "Zero-Order Reconstruction Optimization of Waveforms (ZOROW) for Modest DAC Rates," in *2020 IEEE International Radar Conference (RADAR)*, 28-30 April 2020 2020, pp. 111-116.

[57]   P. M. McCormick, S. D. Blunt, and J. G. Metcalf, "Joint spectrum/beampattern design of wideband FM MIMO radar emissions," in *2016 IEEE Radar Conference (RadarConf)*, 2-6 May 2016 2016, pp. 1-6.

[58] P. M. McCormick, S. D. Blunt, and J. G. Metcalf, "Wideband MIMO Frequency-Modulated Emission Design With Space-Frequency Nulling," *IEEE Journal of Selected Topics in Signal Processing,* vol. 11, no. 2, pp. 363-378, 2017.

[59] G. Zook, P. M. McCormick, S. D. Blunt, C. Allen, and J. Jakabosky, "Dual-polarized FM noise radar," in *International Conference on Radar Systems (Radar 2017)*, 23-26 Oct. 2017 2017, pp. 1-5.

[60] C. A. Mohr and S. D. Blunt, "FM Noise Waveforms Optimized According to a Temporal Template Error (TTE) Metric," in *2019 IEEE Radar Conference (RadarConf)*, 22-26 April 2019 2019, pp. 1-6.

[61] C. A. Mohr, P. M. McCormick, S. D. Blunt, and C. Mott, "Spectrally-efficient FM noise radar waveforms optimized in the logarithmic domain," in *2018 IEEE Radar Conference (RadarConf18)*, 23-27 April 2018 2018, pp. 0839-0844.

[62] C. A. Mohr, P. M. McCormick, and S. D. Blunt, "Optimized complementary waveform subsets within an FM noise radar CPI," in *2018 IEEE Radar Conference (RadarConf18)*, 23-27 April 2018 2018, pp. 0687-0692.

[63] J. Owen, S. D. Blunt, K. Gallagher, P. McCormick, C. Allen, and K. Sherbondy, "Nonlinear radar via intermodulation of FM noise waveform pairs," in *2018 IEEE Radar Conference (RadarConf18)*, 23-27 April 2018 2018, pp. 0951-0956.

[64] J. Owen, C. Mohr, S. D. Blunt, and K. Gallagher, "Nonlinear Radar via Intermodulation of Jointly Optimized FM Noise Waveform Pairs," in *2019 IEEE Radar Conference (RadarConf)*, 22-26 April 2019 2019, pp. 1-6.

[65]   C. A. Mohr and S. D. Blunt, "Design and Generation of Stochastically Defined, Pulsed FM Noise Waveforms," in *2019 International Radar Conference (RADAR)*, 23-27 Sept. 2019 2019, pp. 1-6.

[66]   T. B. Whiteley and D. J. Adrian, "Random FM Autocorrelation Fuze System," Patent #4 220 952, Sep. 2, 1980.

[67]   G. Liu, H. Gu, X. Zhu, and W. Su, "The present and the future of random signal radars," *IEEE Aerospace and Electronic Systems Magazine,* vol. 12, no. 10, pp. 35-40, 1997.

[68]   S. R. J. Axelsson, "Noise radar using random phase and frequency modulation," *IEEE Transactions on Geoscience and Remote Sensing,* vol. 42, no. 11, pp. 2370-2384, 2004.

[69]   L. Pralon, B. Pompeo, and J. M. Fortes, "Stochastic analysis of random frequency modulated waveforms for noise radar systems," *IEEE Transactions on Aerospace and Electronic Systems,* vol. 51, no. 2, pp. 1447-1461, 2015.

[70]   F. D. Palo, G. Galati, G. Pavan, C. Wasserzier, and K. Savci, "Introduction to Noise Radar and Its Waveforms," *Sensors*, vol. 20, no. 18.

[71]   S. D. Blunt *et al.*, "Principles and Applications of Random FM Radar Waveform Design," *IEEE Aerospace and Electronic Systems Magazine,* vol. 35, no. 10, pp. 20-28, 2020.

[72]   S. D. Blunt and E. L. Mokole, "Overview of radar waveform diversity," *IEEE Aerospace and Electronic Systems Magazine,* vol. 31, no. 11, pp. 2-42, 2016.

[73]   M. Wicks, E. Mokole, S. Blunt, V. Amuso, and R. Schneible, Eds. *Principles of Waveform Diversity and Design*. SciTech Publishing, 2010.

[74]   S. D. Blunt, M. R. Cook, and J. Stiles, "Embedding information into radar emissions via waveform implementation," in *2010 International Waveform Diversity and Design Conference*, 8-13 Aug. 2010 2010, pp. 000195-000199.

[75] R. W. Gerchberg and W. O. Saxton, "A Practical Algorithm for the Determination of Phase from Image and Diffraction Plane Pictures," *OPTIK,* vol. 35, no. 2, pp. 237-246, 1972.

[76] M. B. Heintzelman, T. J. Kramer, and S. D. Blunt, "Experimental Evaluation of Super-Gaussian-Shaped Random FM Waveforms," in *2022 IEEE Radar Conference (RadarConf22)*, 21-25 March 2022 2022, pp. 1-6.

[77] A. Parent, M. Morin, and P. Lavigne, "Propagation of Super-Gaussian Field Distributions," *Optical and Quantum Electronics,* vol. 24, no. 9, pp. S1071-S1079, 1992.

[78] C. A. Mohr and S. D. Blunt, "Designing Random FM Radar Waveforms with Compact Spectrum," in *ICASSP 2021 - 2021 IEEE International Conference on Acoustics, Speech and Signal Processing (ICASSP)*, 6-11 June 2021 2021, pp. 8473-8477.

[79] B. Ravenscroft, J. W. Owen, S. D. Blunt, A. F. Martone, and K. D. Sherbondy, "Optimal Mismatched Filtering to Address Clutter Spread from Intra-CPI Variation of Spectral Notches," in *2019 IEEE Radar Conference (RadarConf)*, 22-26 April 2019 2019, pp. 1-6.

[80] T. Higgins, T. Webster, and A. K. Shackelford, "Mitigating interference via spatial and spectral nulls," in *IET International Conference on Radar Systems (Radar 2012)*, 22-25 Oct. 2012 2012, pp. 1-6.

[81] I. W. Selesnick, S. U. Pillai, and R. Zheng, "An iterative algorithm for the construction of notched chirp signals," in *2010 IEEE Radar Conference*, 10-14 May 2010 2010, pp. 200-203.

[82] I. W. Selesnick and S. U. Pillai, "Chirp-like transmit waveforms with multiple frequency-notches," in *2011 IEEE RadarCon (RADAR)*, 23-27 May 2011 2011, pp. 1106-1110.

[83] B. Ravenscroft, J. W. Owen, J. K. Jakabosky, S. D. Blunt, A. F. Martone, and K. D. Sherbondy, "Experimental demonstration and analysis of cognitive spectrum sensing and notching for radar," *IET Radar, Sonar & Navigation,* vol. 12, no. 12, pp. 1466-1475.

[84] J. W. Owen, G. B. Ravenscroft, and S. D. Blunt, "Devoid Clutter Capture and Filling (DeCCaF) to Compensate for Intra-CPI Spectral Notch Variation," Patent Appl. #62/903,618, Sept. 20, 2019.

[85] J. W. Owen, B. Ravenscroft, and S. D. Blunt, "Devoid Clutter Capture and Filling (DeCCaF) to Compensate for Intra-CPI Spectral Notch Variation," in *2019 International Radar Conference (RADAR)*, 23-27 Sept. 2019 2019, pp. 1-6.

[86] T. Higgins, K. Gerlach, A. K. Shackelford, and S. D. Blunt, "Aspects of Non-Identical Multiple Pulse Compression," in *2011 IEEE RadarCon (RADAR)*, 23-27 May 2011 2011, pp. 895-900.

[87] B. Ravenscroft *et al.*, "Experimental Assessment of Joint Range-Doppler Processing to Address Clutter Modulation from Dynamic Radar Spectrum Sharing," in *2020 IEEE International Radar Conference (RADAR)*, 28-30 April 2020 2020, pp. 448-453.

[88] C. Jones *et al.*, "Computationally Efficient Joint-Domain Clutter Cancellation for Waveform-Agile Radar," in *2021 IEEE Radar Conference (RadarConf21)*, 7-14 May 2021 2021, pp. 1-6.

[89] A. F. Martone *et al.*, "Closing the Loop on Cognitive Radar for Spectrum Sharing," *IEEE Aerospace and Electronic Systems Magazine,* vol. 36, no. 9, pp. 44-55, 2021.

[90] A. F. Martone, "Cognitive radar demystified," *URSI Radio Science Bulletin,* vol. 2014, no. 350, pp. 10-22, 2014.

[91]   S. Haykin, "Cognitive radar: a way of the future," *IEEE Signal Processing Magazine,* vol. 23, no. 1, pp. 30-40, 2006.

[92]   B. H. Kirk *et al.*, "Cognitive Software-Defined Radar: Evaluation of Target Detection with RFI Avoidance," in *2019 IEEE Radar Conference (RadarConf)*, 22-26 April 2019 2019, pp. 1-6.

[93]   A. Egbert, A. Goad, C. Baylis, A. F. Martone, B. H. Kirk, and I. R. J. Marks, "Continuous Real-Time Circuit Reconfiguration to Maximize Average Output Power in Cognitive Radar Transmitters," *IEEE Transactions on Aerospace and Electronic Systems,* vol. 58, no. 3, pp. 1514-1527, 2022.

[94]   J. W. Owen, C. A. Mohr, B. H. Kirk, S. D. Blunt, A. F. Martone, and K. D. Sherbondy, "Demonstration of Real-time Cognitive Radar using Spectrally-Notched Random FM Waveforms," in *2020 IEEE International Radar Conference (RADAR)*, 28-30 April 2020 2020, pp. 123-128.

[95]   W. W. Howard, A. F. Martone, and R. M. Buehrer, "Distributed Online Learning for Coexistence in Cognitive Radar Networks," *IEEE Transactions on Aerospace and Electronic Systems,* vol. 59, no. 2, pp. 1202-1216, 2023.

[96]   J. W. Owen *et al.*, "Experimental demonstration of cognitive spectrum sensing & notching for radar," in *2018 IEEE Radar Conference (RadarConf18)*, 23-27 April 2018 2018, pp. 0957-0962.

[97]   J. Roessler *et al.*, "A Fast Impedance Tuner Implementation in a Cognitive Radar for Synchronous Real-Time Optimization in a Congested Environment," in *2022 IEEE/MTT-S International Microwave Symposium - IMS 2022*, 19-24 June 2022 2022, pp. 645-648.

[98] A. F. Martone *et al.*, "Metacognition for Radar Coexistence," in *2020 IEEE International Radar Conference (RADAR)*, 28-30 April 2020 2020, pp. 55-60.

[99] T. D. Ridder, A. F. Martone, B. H. Kirk, and R. M. Narayanan, "Multiple Criteria Operational Reliability Performance Metric of a Metacognitive Tracking Radar," *IEEE Transactions on Aerospace and Electronic Systems,* pp. 1-10, 2023.

[100] S. Z. Gurbuz, H. D. Griffiths, A. Charlish, M. Rangaswamy, M. S. Greco, and K. Bell, "An Overview of Cognitive Radar: Past, Present, and Future," *IEEE Aerospace and Electronic Systems Magazine,* vol. 34, no. 12, pp. 6-18, 2019.

[101] A. F. Martone *et al.*, "Practical Aspects of Cognitive Radar," in *2020 IEEE Radar Conference (RadarConf20)*, 21-25 Sept. 2020 2020, pp. 1-6.

[102] J. Owen, C. Mohr, B. Ravenscroft, S. Blunt, B. Kirk, and A. Martone, "Real-Time Experimental Demonstration and Evaluation of Open-Air Sense-and-Notch Radar," in *2022 IEEE Radar Conference (RadarConf22)*, 21-25 March 2022 2022, pp. 1-6.

[103] J. A. Kovarskiy, J. W. Owen, R. M. Narayanan, S. D. Blunt, A. F. Martone, and K. D. Sherbondy, "Spectral Prediction and Notching of RF Emitters for Cognitive Radar Coexistence," in *2020 IEEE International Radar Conference (RADAR)*, 28-30 April 2020 2020, pp. 61-66.

[104] J. M. Christiansen, G. E. Smith, and K. E. Olsen, "USRP based cognitive radar testbed," in *2017 IEEE Radar Conference (RadarConf)*, 8-12 May 2017 2017, pp. 1115-1118.

[105] G. B. Ravenscroft, P. M. McCormick, S. D. Blunt, E. S. Perrins, and J. G. Metcalf, "Power-Efficient Formulation of Tandem-Hopped Radar & Communications," Patent Appl. #62/737,074, Sept. 26, 2018.

[106] B. Ravenscroft, P. M. McCormick, S. D. Blunt, E. Perrins, and J. G. Metcalf, "A power-efficient formulation of tandem-hopped radar & communications," in *2018 IEEE Radar Conference (RadarConf18)*, 23-27 April 2018 2018, pp. 1061-1066.

[107] T. J. Kramer, C. C. Jones, G. B. Ravenscroft, E. R. Biehl, E. A. Ramos, and S. D. Blunt, "Methods for Embedding Communications into Physical Radar Waveforms," Patent Appl. #63/279,062, Nov. 12, 2021.

[108] B. Ravenscroft, P. M. McCormick, S. Blunt, E. S. Perrins, C. Sahin, and J. G. Metcalf, "Experimental Assessment of Tandem-Hopped Radar and Communications (THoRaCs)," in *2019 International Radar Conference (RADAR)*, 23-27 Sept. 2019 2019, pp. 1-6.

[109] S. C. Thompson, A. U. Ahmed, J. G. Proakis, J. R. Zeidler, and M. J. Geile, "Constant Envelope OFDM," *IEEE Transactions on Communications,* vol. 56, no. 8, pp. 1300-1312, 2008.

[110] S. C. Thompson and J. P. Stralka, "Constant envelope OFDM for power-efficient radar and data communications," in *2009 International Waveform Diversity and Design Conference*, 8-13 Feb. 2009 2009, pp. 291-295.

[111] E. R. Biehl, C. A. Mohr, B. Ravenscroft, and S. D. Blunt, "Assessment of Constant Envelope OFDM as a Class of Random FM Radar Waveforms," in *2020 IEEE Radar Conference (RadarConf20)*, 21-25 Sept. 2020 2020, pp. 1-6.

[112] S. R. Bullock, Ed. *Transceiver and System Design for Digital Communications*. SciTech Publishing, 2009, p. 58.

[113] S. Haykin and M. Moher, Eds. *Introduction to Analog and Digital Communications*. John Wiley & Sons, Inc., p. 433.

[114] S. Haykin, Ed. *Adaptive Filter Theory*. Upper Saddle River, NJ: Pearson Education, 2014.